X-RAY SPECTROMICROSCOPY STUDY OF PROTEIN ADSORPTION

X-RAY SPECTROMICROSCOPY STUDY OF PROTEIN ADSORPTION ONTO A CHEMICALLY PATTERNED SURFACE.

By

LI LI, M.Sc.

A Thesis

Submitted to the School of Graduate Studies

in Partial Fulfillment of the Requirements

for the Degree of

Doctor of Philosophy

McMaster University

DOCTOR OF PHILOSOPHY (2006)
(Chemistry)

McMaster University
Hamilton, Ontario

TITLE: X-ray Spectromicroscopy Study of Protein Adsorption onto a Chemically Patterned Surface

AUTHOR: Li Li, M.Sc. (University of New Brunswick)

SUPERVISOR: Professor A. P. Hitchcock

NUMBER OF PAGES: xxi, 200

ABSTRACT

Protein adsorption, the first event in the interaction of tissue with a foreign material, is a complex process. Understanding and controlling protein adsorption is an important issue in biomaterials. Many different techniques have been developed to study protein adsorption from different aspects. In this work, two soft X-ray spectromicroscopy techniques, photoemission electron microscopy (X-PEEM) and scanning transmission x-ray microscopy (STXM) were used to map the interaction of blood proteins on a phase segregated polymer film — polystyrene/ polymethylmethacrylate (PS/PMMA) blend. The two techniques provide high chemical sensitivity, through near edge X-ray absorption fine structure (NEXAFS) spectroscopy, and high spatial resolution (~50 nm).

As a surface sensitive technique, X-PEEM was used to study adsorption of albumin onto a PS/PMMA blend under different conditions (concentration, adsorption time, pH, temperature and ionic strength), as well as to compare adsorption of albumin and fibrinogen. STXM, a less surface sensitive technique, was used to study albumin adsorption in the presence of a overlayer protein solution, a study which can not be conducted using X-PEEM.

The results give quantitative spatial distributions of adsorbed protein on chemically different regions of the PS/PMMA blend at the studied conditions. This helps understand protein adsorption in a way different from other techniques. Through technique development and an intensive study of the albumin covered PS/PMMA system, this work has made a contribution to development of biomaterials.

ACKNOWLEDGEMENTS

I would like to give my deepest thanks to my supervisor Dr. Adam Hitchcock for his continuous encouragement, numerous guidance and suggestions through the years. I especially appreciate his positive attitude and efforts to solve problems when we were in conflict with different opinions.

I would also like to thank my supervisory committee members, Dr. John Brash and Dr. Alex Andronov, for their comments and suggestions for my work. Especially thanks to Dr. John Brash for his extensive contributions to the papers. Also thanks to Rena Cornelius who is working in Dr. Brash's group for performing the radio-labeling experiments for me, for providing protein samples and advice.

Thanks to Dr. Harald Stover for his always quick reply to all my questions about polymers. He always explained everything so clear to me! Also thanks to the support from his group.

Thanks to the two scientists responsible for the ALS X-PEEM beamline, Andreas Scholl, and Andrew Doran for their great support, especially for the great job done by Andreas to help me optimize the PEEM microscope. I would have had a hard time to get good PEEM data without his help.

Thanks to Andy Duft who helped me a lot with operating the AFM machine in BIMR, and his hot hot chocolate in the winter time.

Thanks to all members (former and current) from Hitchcock group, especially to Cynthia Morin, Daniel Hernández Cruz, and Sherry Zhang, and Glyn Copper.

Thanks to Dr. Kari Dalnoki-Veress for letting me use his lab.

Thanks to all my friends. They are the Sun in my life!

感谢爸爸妈妈对我一惯的支持和宠爱。不论我是怎样或将是怎样，我总是他们心中的乖乖女。他们让我永远有个依靠的方向，和一个心系的地方。感谢我的兄弟们，他们的问侯总让我感动不已。

TABLE OF CONTENTS

DESCRIPTIVE NOTE ii
ABSTRACT iii
ACKNOWLEDGEMENTS iv
TABLE OF CONTENTS vi
LIST OF FIGURES x
LIST OF TABLES xv
LIST OF ABBREVIATIONS AND SYMBOLS xvii

Chapter 1 Introduction 1
§ 1.1 Why " Protein Adsorption"? 1
§ 1.2 Capabilities of Techniques Commonly Used in Biomaterials Development 8
§ 1.3 Why X-ray Spectromicroscopy for Protein Adsorption 19
§ 1.4 Outline of Thesis Chapters 25

Chapter 2 Methods 27
§ 2. 1 NEXAFS 27
§ 2. 1. 1 Theory of Inner Shell Excitation Spectra 28
§ 2. 1. 2 Chemical Sensitivity 31
§ 2. 1. 3 Detection Methods 33
§ 2. 2 PEEM Principles and Instrumentation 36
§ 2. 2. 1 Instrumental Description of X-PEEM 2: Beamline 7.3.1.1 37
§ 2. 2. 2 Instrumental Description of X-PEEM2: PEEM 2 Microscope 40
§ 2. 3 STXM Principles and Instrumentation 42
§ 2. 3. 1 STXM Beamline 5.3.2 44
§ 2. 3. 2 STXM Microscopes 46
§ 2. 4 Atomic Force Microscopy 47

§ 2. 4. 1 Imaging Modes 49
§ 2. 4. 2 AFM Study in This Work 52

Chapter 3 Sample preparation, AFM and ^{125}I-labeling study 53
§ 3.1 Sample Preparation and AFM Study of Corresponding Samples 53
§ 3.1.1 Polystyrene Films 53
§ 3.1.2. Polystyrene/ polymethylmethacrylate (PS/PMMA) Blend Substrate 56
§ 3. 1. 3 Protein Exposure Methods for STXM and PEEM Samples 59
§ 3.2 AFM Study of Protein Covered PS/PMMA Blend 62
§ 3.3 ^{125}I-labeling Adsorption Isotherm 63

Chapter 4 Data acquisition and analysis in X-PEEM and STXM 71
§ 4.1 Data Acquisition in PEEM 71
§ 4.1.1 Images 71
§ 4.1.2 Spectra 72
§ 4.1.3 Stacks 73
§ 4.2 PEEM Measurements of Protein Covered PS/PMMA Blend Surfaces 74
§ 4.3. Principle of Data Acquisition in STXM 77
§ 4.3.1 Single Energy Images 77
§ 4.3.2 Point Spectra 78
§ 4.3.3 Stacks (Image Sequences) 79
§ 4.4 STXM Measurements of Protein Covered PS/PMMA Blend Surfaces 80
§ 4.5 Procedure of Spectromicroscopy Data Analysis 80
§ 4.6 Optimization of Spectromicroscopy Data Analysis 96
§ 4.6.1 Normalization of X-PEEM Signals to The Total Sampling Depth 96
§ 4.6.2 Protein Distribution On a Region 99
§ 4.6.3 C1s Stacks: Different Mapping Fitting Approaches 101
§ 4.6.4 N1s Stacks: Different Fitting Approaches 105
§ 4.6.5 O 1s Stacks: Different Fitting Approaches 109

§ 4.6.6 Comparison of Results from C 1s, N 1s, and O 1s Signal. 112

Chapter 5 Concentration and exposure-time dependence for albumin adsorption 116

§ 5.1 Introduction 117
§ 5.2 Experimental Section 118
§ 5.2.1 Materials 118
§ 5.1.2 Protein Exposure 118
§ 5.1.3 X-PEEM 118
§ 5.3. Data Analysis 118
§ 5.3.1 Reference Spectra 118
§ 5.3.2 Chemical Mapping 119
§ 5.3.3 Histogram Analysis of the Albumin Distributions 120
§ 5.3.4 Verification of Precision and Accuracy 120
§ 5.4 Results 122
§ 5.4.1 Concentration Dependence of Albumin Adsorption 122
§ 5.4.2 Exposure-Time Dependence 122
§ 5.5 Discussion 122
§ 5.6 Summary 126

Chapter 6 Effect of pH on albumin adsorption 128

§ 6. 1 Introduction 128
§ 6. 2 Experimental 131
§ 6. 3 Results 132
§ 6. 4 Discussion 136

Chapter 7 Effect of incubation temperature on albumin adsorption.. 139

§ 7.1 Introduction 139
§ 7.2 Experimental 140

§ 7.3 Data analysis and results 141
§ 7.4 Discussion 147

Chapter 8 Comparison of albumin and fibrinogen adsorption 151

§ 8. 1 Introduction 151
§ 8. 2 Experimental 153
§ 8. 3 Data analysis 153
§ 8. 4 Results and Discussions 156
§ 8. 4. 1 ^{125}I-labeled Adsorption Isotherms of HSA and Fibrinogen 156
§ 8. 4. 2 X-PEEM Study of Adsorption of HSA and Fibrinogen 159
§ 8. 4. 3 Comparison of ^{125}I-label and X-PEEM Studies 161
§ 8. 4. 4 Discussion 163

Chapter 9 Albumin adsorption in presence of solution 166

§ 9.1 Introduction 166
§ 9.2 Experimental 167
§ 9.2.1 Sample Preparation 167
§ 9.2.2 STXM 168
§ 9.3 Results and Discussions 171

Chapter 10 Summary and further work 177

§ 10. 1 Summary 177
§ 10. 2 Suggestion for Further Work 178
§ 10. 2. 1 Clarification of Issues Raised in Thesis 178
§ 10. 2. 2 Extension in New Direction 178

References 183

Appendix A 199

LIST OF FIGURES

Chapter 1

Fig. 1.1 (A) A patterned gold surface with fibrinection absorbed [KTO&99] 7
Fig. 1.2 TOF-SIMS images of a patterned tetreathylene glycol thiol 16
Fig. 1.3 X-ray adsorption spectrum of albumin. 21

Chapter 2

Fig. 2.1 Schematic potentials (bottom) and K-shell spectra (top) of diatomic molecules. 30
Fig. 2.2 NEXAFS spectra of unsaturated polymers [AU00] 32
Fig. 2.3 NEXAFS spectra of some saturated polymers [AU00] 33
Fig. 2.4 Schematic diagram of a photon absorption process 34
Fig. 2.5 Sketch of physical processes of X-ray excited electrons. 37
Fig. 2.6 Layout of PEEM 2 beamline (7.3.1.1) (modified from [M04]). 39
Fig. 2.7 Schematics of PEEM2. 41
Fig. 2.8 Beamline 5.3.2 layout (Plan view) [M04] 44
Fig. 2.9 Focusing scheme of STXM. 45
Fig. 2.10 5.3.2 STXM components a) schematically, b) top view picture [M04] 46
Fig. 2.11 (a) The original set-up for AFM constructed by Bining et al. (b) the most popular design of atomic force microscope [SMC&96] 48
Fig. 2.12 The tapping-mode atomic force microscope. (a) The necessary hardware; (b) illustration of the signal in the tip engagement process. 50

Chapter 3

Fig. 3.1 Measurement of the thickness of a PS film by AFM: a) a scanning height image (tapping mode) of PS film with a scratch; b) the height profile. 55
Fig. 3.2 Setup of a home-built vacuum oven. 56
Fig. 3.3 Phase image of PS/PMMA (30/70 mass ratio) blend. 57
Fig. 3.4 AFM measurement of PS/PMMA (30/70 mass ratio) blend. (a) Height image (b) Profile at while line defined in (a) 58

Fig. 3.5 AFM image of albumin covered PS/PMMA surface, compared with X-PEEM color-coded maps. 63

Fig. 3.6 Isotherms for adsorbing albumin onto PS, PMMA and PS/PMMA blend surfaces from PBS solutions, as determined by ^{125}I-labeling. 66

Fig. 3.7 Isotherms for adsorbing albumin onto PS, PMMA and PS/PMMA blend surfaces from de-ionized water solutions, as determined by ^{125}I-labeling. 67

Fig. 3.8 Comparison of ^{125}I-labeling adsorption isotherm of albumin onto PS, PMMA and PS/PMMA blend surfaces from PBS and de-ionized water solutions. 69

Chapter 4

Fig. 4.1 X-PEEM images of a PS/PMMA blend imaged at 285.1 eV (a), 288.5 eV (b), and 296 eV (c) 72

Fig. 4.2 a) Spectra of PS, PMMA and albumin recorded from pure material using STXM. b) PMMA spectra in a sequence of continuous scanning measured using X-PEEM. 75

Fig. 4.3 a) Io signal as a function of chopper at a fixed mask; b) the effects of chopper setting on the spectral resolution of PMMA. 76

Fig. 4.4 STXM images of a PS/PMMA blend at three energies in transmitted mode (top row) and OD mode (bottom row). 78

Fig. 4.5 A stack on a PS/PMMA blend 79

Fig. 4.6 Scheme of the steps used to analyze an image sequence in STXM and PEEM.. 81

Fig. 4.7 Misalignment of the C1 stack of the 0.01 mg/ml albumin covered PS/PMMA.. 83

Fig. 4.8 a) Image at 295.15 eV of a stack. b) comparison of external I_0 and internal I_0; c) comparison of the spectra normalized to external and internal I_0 85

Fig. 4.9 Ring current of 2-bunch and multi-bunch of X-PEEM [Note different Y-axis scales are used for multi-bunch (left) and 2-bunch (right)]. 86

Fig. 4.10 a) Stack average image before the illumination correction; b) image used for the illumination correction; c) stack average image after the illumination correction. 88

Fig. 4.11 C 1s, N 1s and O 1s X-ray absorption reference spectra of PS, PMMA, albumin and fibrinogen recorded from pure materials. 90

Fig. 4.12 SF of the C1s stack of 0.005mg/ml albumin covered PS/PMMA 93

Fig. 4.13 The mask of PS (a), PMMA (b), the PS/PMMA interface (c), and the color-coded map of the three different regions. 94

Fig. 4.14 Linear regression curve fit of the masked spectra on different regions from the C1s stack of 0.005mg/ml albumin covered PS/PMMA 95

Fig. 4.15 a) Spectra of PS films with different thicknesses used for sampling depth measuremt. 97

Fig. 4.16 Generation of color-coded albumin distribution map..... 101

Fig. 4.17 Histograms of albumin thickness on different regions, obtained by different mapping approaches..... 104

Fig. 4. 18 The stack-fit and SVD maps of the N1s stack of 0.005mg/ml albumin covered PS/PMMA..... 106

Fig. 4.19 Experimental N 1s spectra and fitting curves by linear regression and CGO fittings in different regions (PS, PMMA and interface). 107

Fig. 4.20 Curve fit of the masked spectra from the N 1s stack of 0.005mg/ml albumin covered PS/PMMA.. 108

Fig. 4. 21 Composition maps of the O1s stack of 0.005mg/ml albumin covered PS/PMMA..... 110

Fig. 4.22 Experimental O1s spectra and fitting curves by linear regression and CGO fittings in different regions..... 111

Fig. 4.23 Interface mask (green) from the C1s stack superimposed on a N1s and O1s stack. 113

Fig. 4.24 Masks of PMMA from two different ways: a) from the N1s stack; b) from the C1s image, and c) the comparison of the two masks. 113

Chapter 5

Fig. 5.1 (a) C 1s X-ray absorption spectra of polystyrene, poly(methyl methacrylate), and human serum albumin recorded from pure materials... 119

Fig. 5.2 Component maps of a C 1s stack of a PS/PMMMA blend substrate exposed to a 0.005 mg/mL HSA aqueous solution for 20 min... 120

Fig. 5.3 (a) Color-coded component map for the albumin-covered PS/PMMA blend sample. (b) Masks used to extract spectra of specific regions. (c-e) Curve fits to the average C 1s spectra extracted from the masked regions. 121

Fig. 5.4 Concentration dependence of albumin adsorption on PS/PMMA: Color-coded component maps of albumin-covered PS/PMMA. 123

Fig. 5.5 Exposure-time dependence of albumin adsorption on PS/PMMA: Color-coded component maps of albumin covered PS/PMMA.. 125

Fig. 5.6 Histograms of the albumin thickness on different regions for adsorption from a 0.01 mg/mL solution for exposure times of 5, 20, and 60 min..... 125

Fig. 5.7 Log-log plots of the albumin thickness on different regions of PS/PMMA. (a) concentration and (b) exposure-time dependences.. 126

Chapter 6

Fig. 6.1 (a) Names of conformations of albumin at different pH and corresponding transition points [F77]; (b) Structures of albumin [CH94] 129

Fig. 6.2 Top: X-ray crystallographic structure of HSA at neutral pH condition. Bottom: schematic representation of conformational transitions [QZO&06]. 130

Fig. 6.3 Component maps of for a PS/PMMMA blend substrate exposed to a 0.05 mg/ml HSA at pH 4, derived from a C 1s image sequence.. 134

Fig. 6.4 (a) Masks used to extract spectra of specific regions. (b-d) Curve fits to the average C1s spectra extracted from the masked regions. 134

Fig. 6.5 Color-coded component maps of albumin covered PS/PMMA for the indicated pH media. 136

Fig. 6.6 Albumin adsorption on different regions as a function of pH. The numbers are mean thickness (nm) on each region..... 137

Chapter 7

Fig. 7.1 Experimental setup of protein adsorption at a controlled temperature..... 141

Fig. 7.2 Component maps of a C 1s image sequence of a PS/PMMMA blend substrate exposed to a 0.004 mg/ml HSA at 15°C.. 142

Fig. 7.3 Color-coded component maps of albumin covered PS/PMMA for the indicated adsorption temperature..... 145

Fig. 7.4 Curve fits of a C 1s image sequence of a PS/PMMMA blend substrate exposed to a 0.004 mg/ml HSA at 15°C. 145

Fig. 7.5 Adsorbed amount thickness (nm/pixel) on different regions of the PS/PMMA blend surface. 147

Chapter 8

Fig. 8.1 Maps of PS, PMMA and albumin produced by stack fit of a C1s image sequence of 0.01 mg/ml PBS fibrinogen adsorption. 155

Fig. 8.2 Curve fit of a C1s image sequence of 0.01 mg/ml PBS fibrinogen adsorption.. 155

Fig. 8.3 Isotherms for adsorption of fibrinogen and albumin on pure PS, pure PM and the blend measured using ^{125}I radiolabeling.. 158

Fig. 8.4 Color-coded component maps of albumin and fibrinogen covered PS/PMMA at concentrations of 0.01 and 0.05 mg/ml..... 159

Fig. 8.5 (a) Radio-label measurement of albumin and fibrinogen adsorption from 0.01 and 0.05 mg/ml PBS solutions. (b) X-PEEM measurement of albumin and fibrinogen adsorption from 0.01 and 0.05 mg/ml PBS solutions.. 162

Fig. 8.6 Adsorption process of albumin and fibrinogen. 165

Chapter 9

Fig. 9.1 Diagram of making a wet cell for STXM measurement. 168

Fig. 9.2 Measurement of solution layer in the wetcell..... 170

Fig. 9.3 Component maps of a C 1s image sequence of a PS/PMMMA blend substrate in presence of a 0.05 mg/ml HSA unbuffered water solution..... 173

Fig. 9.4 Curve fit of a C1s image sequence of a PS/PMMMA blend substrate in presence of a 0.05 mg/ml HSA unbuffered water solution..... 173

Fig. 9.5 The scheme of the phase separation of PS/PMMA blend. 175

LIST OF TABLES

Chapter 1

Table 1.1 Various fields or events in which adsorption of protein onto a solid surface plays an important role [NSI01]. 2

Table 1.2 Techniques used to investigate protein adsorption behavior [NSI01] [KH02]. .8

Table 1.3 Comparison of the capacities of different techniques with those of XRM..... 23

Chapter 2

Table 2.1 Comparison of different STXMs in ALS (see http://www-als.lbl.gov) 43

Chapter 3

Table 3.1 Thickness of a series of PS films. 54

Table 3.2 List of protein covered PS/PMMA samples. 61

Table 3.3 Fitting parameters of albumin adsorption from PBS buffered and unbuffered de-ionized water solutions. 68

Chapter 4

Table 4.1 Thickness of each component from a C 1s image sequence of 0.005 mg/ml albumin covered PS/PMMA. 98

Table 4.2 Albumin thickness of 0.005mg/ml albumin covered PS/PMMA, obtained by different mapping and curve fit approaches..... 102

Table 4.3 a) Io signal as a function of chopper at a fixed mask; b) the effects of chopper setting on the spectral resolution of PMMA 114

Chapter 5

Table 5.1 Concentration dependence of adsorption of HSA on PS/PMMA from De-ionized water Solution). 122

Table 5.2 Exposure-time dependence of adsorption of HSA on PS/PMMA from de-ionized water Solution. 124

Chapter 6

Table 6.1 Adsorptions of albumin on PS/PMMA film from different pH solutions: protein thickness. 135

Chapter 7

Table 7.1 Temperature dependence of adsorption of HSA on PS/PMMA from de-ionized water solution..... 148

Chapter 8

Table 8.1 Adsorption of albumin on PS/PMMA film from 0.01mg/ml PBS solution: Composition of PS, PMMA and PS/PMMA interfaces..... 156

Table 8.2 Adsorptions of albumin and fibrinogen on PS/PMMA film from PBS solutions: thickness (nm/pixel) of each component 160

Chapter 9

Table 9.1 Adsorption of HSA on PS/PMMA in presence of 0.05 mg/ml unbuffered de-ionized water solution: composition of PS, PMMA and PS/PMMA interfaces.. 174

LIST OF ABBREVIATIONS AND SYMBOLS

AEY	Auger electron yield
AFM	Atomic force microscope
ALS	Advanced Light Source
AOI	Area-of-interest
BCE	Bovine capillary endothelial
BIMR	Brockhouse Institute for Material Research
BSA	Bovine serum albumin
°C	Degree of Celsius
CaPeRS	Canadian Photoelectron emission Research Spectroscope
CCD	Charge coupled device
CD	Circular dichroism
CLS	Canadian Light Source
cm	center meter
CGO	Conjugate gradient optimization
δ	Polydispersity, Mw/Mn
DSC	Differential scanning calorimetry
ELISA	Enzyme-linked immunosorbent assay
EPR	Ethylene propylene rubber
EPU	Elliptically polarized undulator
EXAFS	Extended X-ray absorption fine structure

FOV	Field of view
FTIR	Fourier transform infrared spectroscopy
G	Gibbs energy
HSA	Human serum albumin
H	enthalpy
I_0	Incident photon energy
I_t	Transmitted photon energy
K	1000
λ	Wavelength of light
δ_r	Outmost ring of the zone plate
LEEM	Low-energy electron microscopy
$\mu(E)$	Energy dependent mass absorption coefficient
MALDI-TOF-MS	Matrix-assisted laser desorption ionisation time-of-flight mass spectrometry
MDI	Methylene bis phenyl isocyanate
Mn	Number average molecular weight
Mw	Weight average molecular weight
MW	Molecular weight
NEXAFS	Near-edge X-ray absorption fine structure
NP	Neoprene
OD	Optical density
OD_{max}	Maximum optical density

OSA	Order sorting aperture
PBD	Poly(butadiene)
PBrS	Poly brominated styrene
PBS	Phosphate Buffered Saline
PC	Polycarbonate
PE	Polyethylene
PEO	Poly ethylene oxide
PET	Poly (ethylene terephthalate)
PEY	Photoelectron yield
PGM	Plane grating monochromator
PI	Polyisoprene
PIB	Polyisobutylene
PMT	Photomultiplier
PP	Polypropylene
PPO	Poly (propylene oxide)
PS	Polystyrene
PSF	Polysulfone
QCM	Quartz crystal microbalance
rpm	Revolution per minute
ρ	Density
σ	Linear absorption coefficent
S	entropy

SAN	Poly(styrene-ran-acrylonitrile)
SDS-PAGE	Sodium dodecyl sulphate polyacrylamide gel electrophoresis
SEY	Secondary electron yield
SF	Stack fit
SFG	Sum frequency generation
SPM	Scanning probe microscopy
SPR	Surface plasmon resonance
SVD	Singular value decomposition
STXM	Scanning transmission X-ray microscopy
T	absolute temperature
TEY	Total electron yield
TDI	Toluene diisocyanate
TIRF	Total internal reflection fluorescence
TOF-SIMS	Time-of-flight secondary ion mass spectrometry
wt%	Weight percent
XANES	X-ray Absorption Near Edge Structure
XAS	X-ray Adsorption Spectroscopy
XMCD	X-ray magnetic circular dichroism
XMLD	X-ray magnetic linear dichroism
X-PEEM	X-ray photoemission electron microscopy
XPS	X-ray photoelectron spectroscopy
XRM	X-ray microscope

θ	Fraction of surface coverage
ZP	Zone-plate

Chapter 1

Introduction

This chapter presents a general introduction to protein adsorption and the motivation for this thesis. Some major techniques employed in the study of protein adsorption are reviewed and then the major technique I have used, soft X-ray spectromicroscopy, is presented. This chapter ends with an outline of the whole thesis.

§ 1.1 Why "Protein Adsorption"?

Artificial medical devices implanted into people are important in that they have increased the length and quality of life. During the past several decades, polymer materials have become widely used as components of medical devices. Many medical devices involve blood contact. The first event which occurs after exposure of a device to blood is the adsorption of blood proteins, such as albumin and fibrinogen.

When a surface is exposed to a protein solution, it will quickly be covered by proteins. Protein adsorption will result in significant changes in the physicochemical and biological properties of the surface-solution interface. It is the first step in the biological response to materials and one that may ultimately determine biocompatibility in the end use [CR02]. The study of protein adsorption and interactions between proteins and surfaces is a major concern to various fields such as biology, medicine, biotechnology, and food processing [NSI01]. **Table 1.1** lists various fields concerned with the adsorption of proteins and categorizes them with regard to several important factors [NSI01].

Table 1.1 Various fields or events in which adsorption of protein onto a solid surface plays an important role [NSI01].

Various fields or events	**Important factors**		
	Adsorbed amount	Selectivity for adsorption	Orientation/ conformation of the adsorbed protein
Design of biocompatible materials	+	+	
Adsorption chromatography	+		+
Membrane separation	+		
Foods/bioproducts manufacturing processes	+		
Biosensors	+	+	+
Cultivation of animal cells	+	+	
Drug delivery systems	+		

For the factors that are primarily important in the function or efficiency, a "plus" symbol is given.

Protein adsorption on solid surfaces is a very complex process that depends on the nature of various interactions between protein and substrate, as well as the state of hydration of the protein and the surface, and the structural arrangement of the protein [M03]. Adsorption is very sensitive to many variables. Small changes in pH, temperature or ionic strength can make a large difference in the amount of adsorbed protein or which protein in a mixture is preferentially adsorbed. However, all protein adsorption phenomena share a common feature in the initial stages in that the process is only possible if the Gibbs energy, G, of the system decreases:

$$\Delta G_{ads} = \Delta H_{ads} - T\Delta S_{ads} < 0 \qquad (1)$$

where H, S, and T refer to the enthalpy, entropy, and absolute temperature, respectively, and ΔX_{ads} indicates the change of the thermodynamic state functions resulting from the adsorption process [NL91]. During the adsorption process, a number of interactions in the system contribute to the enthalpy and entropy changes and thus drive the process of protein adsorption. These driving forces include Lifshitz-van der Waals forces (i.e., dispersive, and induction forces), Lewis acid-base forces (including hydrogen bonding), electrostatic forces (including ion pairing), hydrophobic forces, and steric effects [KH02]. Among these interactions, enthalpic contributions include van der Waals interactions and electrostatic interactions whereas entropic contributions may involve release of counterions and /or solvation water (dehydration) as well as reduction of amount of ordered structure due to adsorption-induced conformation changes ([M03], [M98], [N86]).

Hydrophobic interactions have been reported to play an important role in protein adsorption. For instance, hydrophobic interactions were found to be the main driving forces in the adsorption of collagen on hydrophobic polystyrene surfaces [DBS&97]. The amount of bovine serum albumin (BSA) adsorbed on polystyrene was found to decrease when the surface was modified by hydrophilic substances such as saccharide [REC&96] or 2-hydroxyethyl methacrylate [PB62]. These examples indicate the importance of hydrophobic interactions in protein adsorption. The most important factor accounting for hydrophobic interaction between a hydrophobic surface and protein in water environment is the dehydration of hydrophobic surfaces and proteins. This

dehydration promotes adsorption of proteins from aqueous solution by lowering the Gibbs energy of the system as a result of a large entropy gain [NL91]. This can cause spontaneous adsorption.

When a charged surface is exposed to a protein solution, electrostatic attraction forces are important. This is because protein molecules are charged to an extent and polarity that depends on pH. Most proteins have a net negative charge at neutral pH, thus adsorption at positively charged surfaces can be expected to be particularly strong [KH02]. However, it is not always true that opposing charges promote strong interactions between proteins and surfaces. Sometimes a protein can absorb to a greater extent on a surface with the same net charge than on a surface with opposite charge. It was reported that "hard" proteins (proteins that almost do not change conformation upon adsorption) hardly adsorb on a surface when the proteins and surface have opposite charges ([NSI01] [N86] [HN94]). For a situation where both the protein and the surface are negatively charged, the adsorption of the protein to the surface may be promoted by positively charged groups of the protein interacting with the negatively charged surface. Therefore in order to fully understand the interactions involved in the adsorption process one needs to consider the individual interactions between charged groups of the protein and the solid surface, not just the net charge of the protein and surface.

It was believed that hydrogen bonding and/or dipolar interaction between groups of the protein molecule and the surface contribute only to a minor extent, because such interactions would occur at the expense of the same type of interaction inside the protein molecules, between protein and water, and between the surface and water [NL91].

However, hydrogen bonding can be a favorable force for protein adsorption when it leads to an overall increased conformational entropy [M03]. For instance, it was found that increasing the acrylic acid or methacrylic acid comonomer content in polystyrene microspheres resulted in increased BSA adsorption which was attributed to hydrogen bonding [SSS89].

In most cases protein adsorption is driven by a combination of different forces. For example, many surfaces contain both hydrophobic domains and charged or chargable groups. Protein adsorption on such surfaces will be driven by a combination of hydrophobic interactions and electrostatic attractions.

Apart from hydrophobic interactions, electrostatic attractions, hydrogen bonding and/or dipolar interaction, protein adsorption is influenced by factors such as the degree of conformational flexibility of the protein, the ability of the surface to rearrange in order to expose different groups, etc [KH02].

Protein adsorption could be a desired event or not. Many medical and biotechnological techniques are based on specific interactions between proteins in solution and surface-bound molecules such as antigens, antibodies, haptens, affinity ligands, etc. Uncontrolled (non-specific) adsorption of proteins at solid surfaces is a problem in many biotechnological applications. If nonspecific adsorption competes favorably with the specific interactions, it would be hard to achieve a high sensitivity (signal-to-noise ratio) in analytical procedures and a high efficiency in therapeutic applications ([KH02], [M03]). For example, in chromatographic separation of proteins, the ion-exchange and size-exclusion mechanisms of separation require minimizing

interactions between the protein and the chromatographic support matrix to prevent unwanted nonspecific interactions ([C87], [GW87], [HU92])

Protein adsorption on heterogeneous surfaces rather than homogeneous surfaces is important in many practical cases, such as a biomaterial implant in a living body, cell growth in a culture, or the functionality of biosensors [K02]. A homogeneous surface with only one component is modified in different ways in order to achieve different surface properties. For example, oligoethylene glycol monolayers have been used to modify gold ([PSP&91], [OYW99]), SiO_2 ([SJD99], [FSL&04]), silicon and diamond surfaces [LCA&04] in order to resist the nonspecific adsorption of proteins and cells. This is important for the design of biocompatible coatings for implants and for biosensors ([CR02], [LCH04]). Rather than modifying the surfaces with one glycol, it was demonstrated that mixed monolayers of amine and triethylene glycol on silicon and diamond surface can optimize the ratio of specific to nonspecific binding in a model protein sensing assay [LCA&04].

Despite the clear motivation to eliminate or reduce the non-specific adhesion of proteins on surfaces, in some cases the ability to enable protein adhesion to certain restricted regions on a device surface is very desirable. Such spatially controlled heterogeneous surfaces can be advantageous in the operation of some biomicroelectromechanical systems (bioMEMS) [PHL&01]. Therefore it is useful to achieve precisely patterned surfaces consisting of protein adhesive and non-adhesive micro-domains designed to enhance electrochemical sensors [PHL&01], protein microarrays [MS00], and control of cell growth on surfaces [KKH&88]. For example,

Kane et al [KTO&99] patterned a gold surface into regions of hexadecanethiolate and undecanethiolate terminated with tri(ethyleneglycol) by microcontact printing. As shown in **Fig.1.1 (A)**, it was found that fibronectin (light) adsorbed on the hydrophobic squares of hexadecanethiolate but not on the tri(ethyleneglycol) terminated undecanethiolate (dark). Fibronectin is an extracellular matix protein of bovine capillary endothelial (BCE)

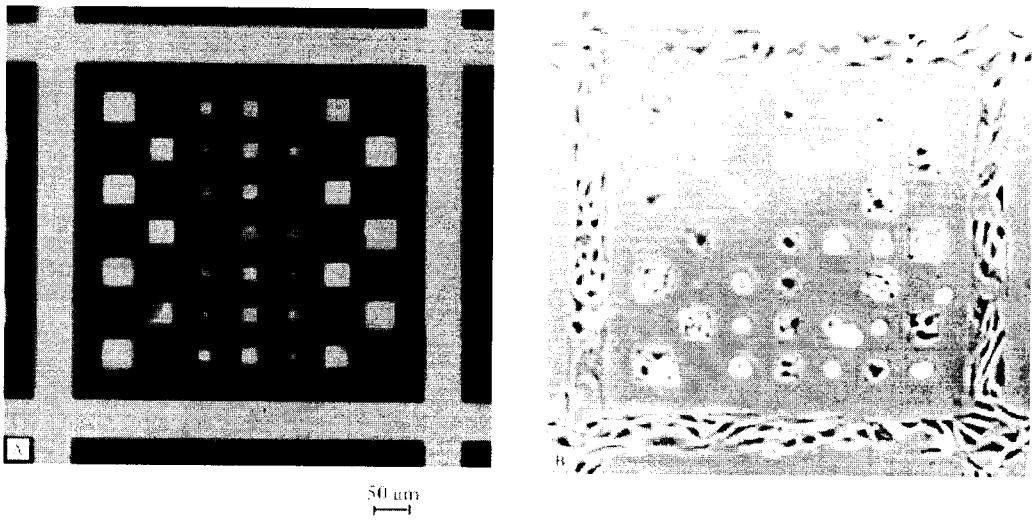

Fig. 1.1 (A) A gold surface was patterned into regions of hexadecanethiolate (I) and undecanethiolate terminated with tri(ethylene glycol) (II). Fibronectin (light) adsorbed on the hydrophobic squares of (I) but not on the region of (II) (dark). (B) Bovine capillary endothelial (BCE) cells patterned by culturing on a substrate presenting hydrophobic squares of varying sizes that were coated with fibronectin, prior to incubation with cells [KTO&99][1]

[1] Reprinted from *Biomaterials 20*, R. S. Kane, S. Takayama, E. Ostuni, D. E. Ingber, G. M. Whiteside, "Patterning proteins and cells using soft lithography", Page 2363-2376, Copyright Elsevier (**1999**), with permission from Elsevier.

cells and it can promote the adhesion of BCE cells to substrates. As shown in **Fig.1.1 (B)**, the control of the adsorption of adhesive protein of fibronectin enables the patterning of BCE cells on the substrate. BCE only adheres to the hydrophobic squares coated with fibronectin.

§ 1.2 Capabilities of Common Techniques for Biomaterials Development

Due to its significance in various fields, protein adsorption has been extensively studied for decades with different experimental techniques in an attempt to understand the complex process of protein adsorption. However, a broader understanding of protein adsorption still remains a challenge in order to improve existing materials. In addition to developing new methods of assessing protein adsorption, a multi-technique analysis approach is necessary. Individual methods are not capable of providing a complete picture of the process. The methods should be capable of providing different types of information about the adsorption process, including the amount of adsorbed protein, the rate of adsorption, the conformation and/or orientation of the adsorbed protein layer, investigations of competitive adsorption from complex biological media, and the time-dependent change in the structure of the protein layers. **Table 1.2** gives an overview of some major techniques for assessing protein adsorption [NSI01] [KH02]. This table does not include X-ray spectromicroscopy which is discussed in the following section.

Table 1.2 Techniques used to investigate protein adsorption behavior [NSI01] [KH02]. (Note that in the column of 'Information to be obtained', I refers to imaging mode, Q refers to quantitative, C refers to competition of multiple proteins, O refers to orientation (or conformation) and S refers to substrate.)

Technique	Principle	Information					Ref.
		I	Q	C	O	S	
Depletion	Decrease in solute concentration after incubation with solid surface		√				FJ80, KL89, KMH93, INT&95
Radiotracer	Decrease in concentration of radioisotope-labeled molecules in solution radioactivity on surface due to readiosiotope-labeled molecules adsorbed		√	√			EDL84,YPC88, DN83
Quartz crystal microbalance (QCM)	Change in oscillating frequency of piezoelectric devices upon mass loading		√				HRB&98, HK01
Enzyme-linked immunosorbent assay (ELISA)	Epitope recognition by primary antibodies		√	√			SHK95
Ellipsometry	Change in the state of polarized light upon reflection		√	√	√		GK88, WAL95
Reflectometry	changes in the state of polarized light upon reflections at an interface		√	√	√		NA92, NGP95, BBL&96, BWN97
Total internal reflection fluorescence (TIRF)	Fluorescence due to surface-adsorbed molecules excited by evanescent field		√				HRA86, SL92
Fluorescence spectroscopy	Change in fluorescence spectrum of protein on adsorption				√		MNV&97
Neutron reflection	Reflectivity of neutrons at solid-water interface		√		√	√	SLT&98
Fourier transform infrared spectroscopy (FTIR)	Change in fluorescence spectrum of protein on adsorption		√				LP91
X-ray photoelectron spectroscopy (XPS)	Element-specific photoelectron		√				PR85, GMC&93, MMJ&01, EBC&97
Matrix-assisted laser desorption ionisation time-of-flight mass spectrometry (MALDI-TOF-MS)	Mass of macromolecules	√	√	√			KSC&00
Time-of-flight secondary ion mass spectrometry (TOF-SIMS)	Mass analysis of segments of macromolecules	√	√	√		√	BGC03, LWT&01, MRC&93
Differential scanning calorimetry (DSC)	Shifts in heat capacity of samples undergoing a controlled temperature increase.						M03
Surface plasmon resonance (SPR)	Reduction in the intensity of internally reflected light and the angle of excitation of the surface plasmon.		√				GFS&00, SMW98, HK01
Raman scattering	Change in Amide I, II, III bands to quantify the secondary structure contents of absorbed proteins.				√		CA85
Circular dichroism (CD)	differences in the absorption of left-handed versus right-handed polarized light which arise due chirality				√		MW74
Atomic force microscopy (AFM)	Atomic interaction between surface and scanning probe	√			√		SM98, TM00

The goals of different techniques developed for the study of protein adsorption can be classified into two groups: adsorbed amount and conformational changes upon adsorption. Some techniques have the capacity of achieving both goals but other techniques are capable of only one goal. For the measurement of adsorbed amount of proteins, detection limits, precision and accuracy are important issues due to the low amounts on the surface, especially when the surface of interest has small area.

Depletion method is a conventional adsorption experiment. The amount of adsorbed proteins is determined based on the decrease in the protein concentration in the solution after exposure to the surface. This method requires a large surface area to be sufficiently accurate but may not require any labeling ([NSI01], [FJ80], [KL89], [KMH93], [INT&95]).

The radiotracer technique labels the adsorbate in the solution using a radioisotope such as ^{125}I ([CB84], [AB04]). Then the adsorption is measured as the decrease in radioactivity in the solution. In this method, one assumes that the radio label does not affect the adsorption behavior of the protein. It can be used to study the competitive adsorption of various components of a mixture of proteins [AN86].

Several techniques can be used for direct measurement of proteins adsorbed on the surface. They include enzyme-linked immunosorbent assay (ELISA) [SHK95], radiolabeling [DN83], and quartz crystal microbalance (QCM) ([HRB&98], [HK01]). The QCM technique is based on the change in the oscillating frequency of piezoelectric devices upon mass loading. This technique can monitor both adsorption and desorption processes [MD00].

Ellipsometry and reflectometry are two optical techniques used to measure the amount of protein absorbed on a surface ([GK88], [WAL95]). These two techniques are closely related, both detect the changes in the state of polarized light upon reflection at an interface [KH02]. There are some restrictions on the surfaces used for ellipsometry and reflectometry investigations for protein adsorption. The surface must be smooth and highly reflective and optical isotropic. The most common substrate is silica. However, metal surfaces ([AN88], [CHH78], [MA95]) have also been found to be suitable for ellipsometric investigations. Moreover, mineral surfaces [NAG97] and ceramic materials [[BMA&96]] have also proved to be practical substrates. Most interestingly, polymers such as polystyrene and poly (methacrylic acid) [MLW&96] are also used as substrates for ellipsometric measurement. Ellipsometry and reflectometry can not only detect the static absorbed amount but they can also monitor in situ adsorption and desorption of proteins ([ABN86], [EPS&96]). Ellipsometry is good at monitoring the total amount of proteins at the solution/substrate interface with time but it has no structural sensitivity.

Total internal reflection fluorescence (TIRF) is also an optical technique ([GK88], [WAL95]). In this technique, a beam of light is shone on an interface between two transparent media, starting from the media with the higher refractive index. The light is completely reflected at the interface and becomes an evanescent wave penetrating into the medium with a lower refractive index. This evanescent wave excites fluorescent molecules attached to proteins at the surface, and the fluorescent intensity is detected. This technique can provide rich information on protein adsorption including competitive

adsorption, interfacial conformational changes of proteins and mobility of adsorbed proteins [LM96].

Neutron reflection is a technique for probing the structural details of both protein and surfactant involved in the interfacial interaction ([L98], [PT90], [LLT96], [LT98]). The principles and applications of neutron reflection have been reviewed by Jian R. Lu [L98]. The essence of a neutron reflection experiment is to measure the specular reflection of a neutron beam as a function of the momentum transfer perpendicular to the reflecting surface. This can be related to the neutron refractive index profile normal to the interface. The resulting scattering length density yields information about the composition and density gradients of surfaces and interfaces [PT90]. Therefore neutron reflectivity offers the opportunity of measuring not only adsorbed amounts, but the surface/ interfacial structure of the adsorbed protein at a high resolution [SLT&99]. Neutron scattering amplitudes vary from element to element, and isotopic substitution can be used to produce large contrasts in scattering amplitude. Of particular importance is the large difference in scattering powers of hydrogen and deuterium. The characteristic feature of neutron reflection is that its signal can be altered by isotopic substitution. Isotopic substitution is used to vary the contrast between water, protein, and solid substrate. Variation between H_2O and D_2O allows a reliable determination of the extent to which water penetrates the protein layer. This information combined with the known dimensions of proteins often provides useful insights into the physical state of an adsorbed protein layer.

X-ray photoelectron spectroscopy (XPS) is a technique which detects photoelectrons ejected from the atoms after X-ray adsorption. The photoelectron energy is element specific and sensitive to the chemical state of the element. XPS can provide information about the chemical composition and chemical structure of surface layers [BS90]. This technique has high surface sensitivity with a sampling depth of 1-2 nm (with a detection limit of 10^{-2} of a monolayer [B94]) typically and as good as 0.3 nm if one uses grazing emission and a photon energy such that the electron kinetic energy is around 50 – 100 eV [S92]. Angle dependent XPS allows the analysis depth to be varied between 0.3 – 2 nm, enabling detection of very small amounts (~10 ng/cm^2) of surface adsorbed protein [M03]. XPS has been used to monitor adsorption of protein ([GMC&93], [MMJ&01]) and quantify amounts of protein ([EBC&97], [FLE&92]). This technique is incapable of identifying particular proteins.

Matrix-assisted laser desorption ionisation time-of-flight mass spectrometry (MALDI-TOF-MS) is a technique that was developed by Karas et al [KH88]. MALDI-TOF-MS detects the parent molecule as an ion rather than detecting only fragments of the parent molecule. To prepare the sample for conventional MALDI-TOF-MS, analyte molecules such as protein molecules are pre-adsorbed on a solid surface. Then matrix solution (a solution typically with aromatic acids or aromatic carbonyl compounds dissolved in an appropriate mixture of organic solvent/water solvent) is added to the analyte-covered surface. The solvent is allowed to evaporate and matrix crystals are formed with analyte included. The sample is then irradiated with nitrogen laser pulses (3ns). The matrix molecules absorb the energy and act as proton donors, which results in

the rapid ejection of protonated analyte molecules which are evaporated and analysed by a time-of-flight mass spectrometer.

MALDI-TOF-MS can directly detect adsorbed proteins on various synthetic material surfaces and has been used to determine the mass of biological macromolecules ([WTL99], [BH99]) with an accuracy of 0.1 – 0.001% [OKH91]. The high mass resolution makes MALDI-TOF-MS unique at characterization of complex adsorbed protein layers and competitive adsorptions of different proteins. There are some issues/limits in the MALDI-TOF-MS technique. The upper mass limit of the detector is such that it can only detect ions up to mass of 550, 000 [CCD92]. The most critical issue is that MALDI-TOF-MS is not capable for detecting some specific adsorbed proteins which are detectable by other techniques such as XPS and ELISA for some unknown reasons. The second issue is that the protein-surface interaction has to be in the 'right' range – strong enough to resist removed in rinsing but not too strong to prevent laser desorption from the surface. There are several cases in which proteins bind too tightly to the surface so that the protein signals detected are weaken or negligible. One case is protein denaturation, which often happens after a long time of adsorption for some proteins. The other is that some sticky proteins have very strong surface affinity to many surfaces in a natured state. Sometimes a protein does not incorporate well into the matrix crystals due to incompatibility. This also causes the problem of losing protein signals. A recent review by Griesser et al [GKM&04] discusses different aspects of the MALDI-TOF-MS technique.

Static time-of-flight secondary ion mass spectrometry (TOF-SIMS) can be used to study the conformation of adsorbed proteins due to its extreme surface sensitivity (sampling depth of 1-1.5 nm) ([BGC03], [WHC03], [R95], [LDA&98], [TCG&01]). The TOF-SIMS technique has been reviewed by Belu et al [BGC03]. In this technique, an absorbed protein layer is bombarded with ions, breaking off short segments (as much as several peptides) from the upper nanometer of the adsorbed layer. After identifying these segments using mass spectroscopy, the orientation of the protein or its state of unfolding can be inferred [G04]. This technique can also discriminate between different adsorbed proteins ([WC01], [WTC02]) and quantify the composition of several binary adsorbed protein films ([LWT&01], [WSH&03]). Using the imaging mode of TOF-SIMS it is possible to characterize patterned protein films at spatial resolutions on the micrometer scale [M03]. As an example, TOF-SIMS was used to image patterned alkanethiols on gold by two monolayer films: **A**= tetraethylene glycol thiol ($HS\text{-}(CH_2)_{11}\text{-}(OCH_2CH_2)_4\text{-}OH$), **B**= $(S\text{-}(CH_2)_{11}\text{-}CH_3)_2$. **Fig. 1.2** shows negative ion images of O^- (left) and S^- (right). The O^- signals represent **A** and the S^- signals represent **B**. Since oxygen is unique to **A** the high contrast image is seen in the O^- image. Both **A** and **B** contain sulfur but **B** has higher sulfur density. This is why much weaker contrast is seen in the S^- image and the contrast is reversed compared with the O^- image. There are some challenges in current TOF-SIMS. One is to relate the information present in static TOF-SIMS spectra to surface molecular structure since the intensity of a given fragment depends on its surrounding environment and is not unique to its concentration on the surface. This is called "matrix effect" but this effect seems to be minimal for most organic surfaces such

as polymeric biomaterials and adsorbed protein films. The second challenge is related to the data analysis technique, especially for imaging. It is now possible to acquire high-mass resolution images at spatial resolutions of better than 1 μm. Each spectrum can contain hundreds of peaks but each peak may contain only a few counts. An efficient data analysis method is needed to analyze this low signal-to-noise data to identify and quantify all the chemical components present in a TOF-SIMS image.

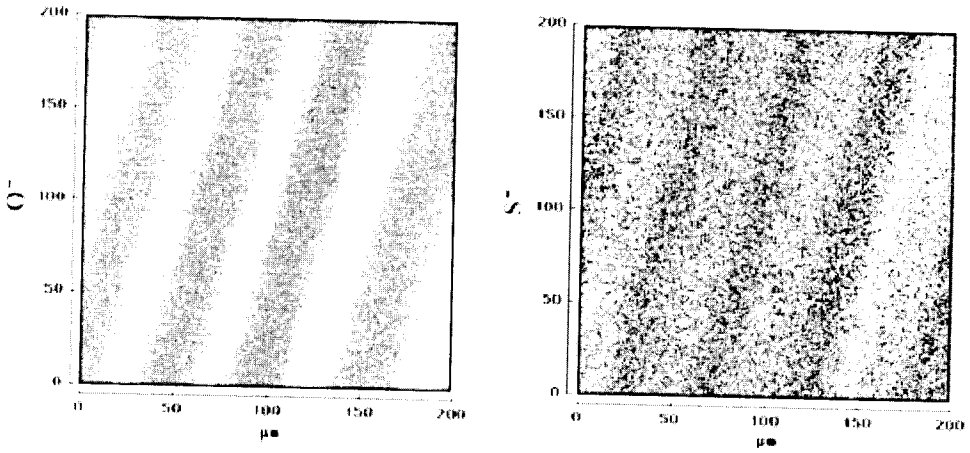

Fig. 1.2 TOF-SIMS images of a patterned tetreathylene glycol thiol ($HS\text{-}(CH_2)_{11}\text{-}(OCH_2CH_2)_4\text{-}OH$) SAM backfilled with $(S\text{-}(CH_2)_{11}\text{-}CH_3)_2$SAM [BGC03][1].

Differential scanning calorimetry (DSC) measures shifts in the heat capacity of samples undergoing a controlled temperature increase. From DSC measurements, one can obtain the transition enthalpy from the native state to the denatured state induced by heat. The change in the environment of proteins can be associated with a change in

[1]Reprinted from *Biomaterials 24*, A. M. Belu, D. J. Graham, D. G. Castner, "Time-of-flight secondary ion mass spectrometry: techniques and applications for the characterization of biomaterial surfaces" , Page 3635-3653, Copyright Elsevier (**2003**), with permission from Elsevier.

enthalpy [M03]. This technique is not substrate-sensitive and the only requirement for the substrate is that it is thermally stable in the temperature range examined.

Many spectroscopic techniques are used for characterizing protein conformation changes upon adsorption. These spectroscopic techniques include fourier transform infrared absorption (FTIR) ([BNL96], [LP91]), Raman scattering [CA85], fluorescence emission [M03], XPS and circular dichroism (CD) ([MW74], [KF98], [ELC&97]). They rely on the interaction of photons with the species present in the interfacial region to detect molecular events at the interface.

FTIR provides information regarding changes in the peptide backbone [BNL96], while fluorescence studies can indicate polarity shifts in the environment of a fluorescent probe, whether intrinsic or introduced, that occur as a result of the protein's interaction with the surface [M03]. Circular dichroism is informative regarding changes in protein secondary structure, as it reports the relative contents of α-helix, β-sheet, β-turn, and random structure in the protein under examination [F96]. CD can also study the conformational stability of a protein under stress: thermal stability, pH stability, and stability to denaturants, and how this stability is altered by buffer composition or addition of stabilizers. Although these techniques are powerful and provide valuable information on the change in α-helical and β-sheet content, they are unable to distinguish between individual protein molecules on the surface.

Surface plasmon resonance (SPR) [GFS&00] is a real-time technique capable of monitoring not only the adsorption of compounds to transition metal surfaces but also subsequent binding to these layers. SPR requires a metal surface to couple with the

incident light at a specific angle to excite surface plasmon resonantly. The metal can be silver, gold, copper and aluminum and silver and gold are more commonly used. The excitation of surface plasmon causes energy loss of incident light to the metal film. This results in a reduction in the intensity of reflected light which is detected by a two-dimensional array of photodiodes or charge coupled detectors. The signal of surface plasmon is depend on the refractive index of the water/air medium above the silver film, and a change in the refractive index of above the metal surface will result in a change in the angle incidence required to excite a surface plasmon. The metal surface can be modified with a surface used for protein adsorption study. A SPR profile can be obtained by monitoring the angle at which resonance occur during a protein adsorption process with respect to time. The signals within 500nm above the metal surface can be detected by SPR.

SPR has been used to study the adsorption of protein molecules ([SBY93], [GDD&97]) and antibody-antigen interactions at sensor surfaces [KPE&96]. SPR has the potential to provide valuable information regarding protein interactions with model chromatography surfaces ([BO93], [NLS&94]). Two disadvantages of SPR are: (1) that it lacks sensitivity for the adsorption of low molecular weight proteins; and (2) the rate-limiting mass transport can affect kinetic analysis.

As a nanoscale imaging technique, atomic force microscope (AFM), invented by Binnig et al [BQG86], has been employed to study protein adsorption at surfaces ([KBR02], [JYL00]) and observe surface denaturation [SFJ02]. AFM has also become a popular technique to observe the dynamics of the adsorption process on the molecular

level ([SGF98], [KM99]). The principles and applications of AFM are discussed in more detail in **Chapter 2**.

Above I gave an overview of many popular techniques used for protein adsorption studies. As mentioned earlier, none of them are capable of determining all aspects of protein adsorption and it is usually advantageous to combine different techniques. For example, Wagner et al [WHC03] combined ToF-SIMS, XPS and ^{125}I-radiolabel to study protein films formed from binary and ternary mixtures of albumin, fibrinogen, and immunoglobulin G. The study provides information about the composition, conformation and orientation of such complex protein films absorbed on mica substrates.

§ 1.3 Why X-ray Spectromicroscopy for Protein Adsorption?

My work uses two types of X-ray spectomicroscopies in combination with other techniques: X-ray photoemission electron microscopy (X-PEEM) and scanning transmission X-ray microscopy (STXM). As discussed above, there are already many techniques available to study protein adsorption. Why do we bother to develop X-PEEM and STXM for the study of protein adsorption? What is the benefit of these two microscopies relative to other techniques?

The details about the principles and operations of X-PEEM and STXM are discussed in **Chapters 2 and 4**. PEEM images the spatial distribution of electrons emitted by photoionization from a region illuminated by a beam of light. The contrast in a PEEM image is a combination of topographical features, work function effects and chemical composition. PEEM was initially developed using low energy light sources such as a Hg arc lamp. The energy of Hg lamp light (~6 eV) is lower than the work

function of many materials thus the contrast of UV-PEEM is the variations of work function. X-PEEM combines the characteristics of X-ray adsorption and electron microscopy. X-ray absorption is element-specific since the interaction of X-rays with matter depends on not only wavelength but also atomic number [M04]. The energy of an X-ray is much larger than the work function so all materials produce at least some electrons. Due to the properties of the magnification lens, it is the low energy secondary electrons that form the image in X-PEEM. The contrast of X-PEEM depends on the surface composition through the adsorption coefficient and, for layers thinner than the sampling depth, the thickness. The sampling depth of X-PEEM is 5-10 nm [S92], which is much larger than that of other photo-emission techniques. The specific sampling depth of X-PEEM enables it to image adsorbed layers up to 5-10 nm thick and the substrate underneath simultaneously [MHC&04]. Furthermore the X-ray energy is tuneable and it is possible to choose only the inner shell absorption edge of interest (within the energy range limitations of the synchrotron beam line). As known, most biomaterials and proteins contain atoms of C, N and O. **Fig. 1.3** shows an example of characteristic X-ray adsorption of albumin at C1s, N1s and O1s edges.

Samples and sample-supported substrates for X-PEEM must be conductive. In this work I have used silicon wafers with native oxide intact. X-PEEM requires an ultra high-vacuum environment and thus it can only measure dry samples, which raises questions about possible conformation change on drying. In that regard, STXM is a good complementary technique since it can make protein adsorption measurements in wetcell samples [HMH&02]. STXM uses a focused X-ray beam and raster scanning of the

sample to make an image. It detects X-ray light transmitted through a sample. It is a bulk technique but has some surface sensitivity since samples are very thin (50-200 nm). It is less surface-sensitive than X-PEEM. STXM can operate either in vacuum or atmospheric environment. The substrates for supporting STXM samples are usually Si_3N_4 windows or 3mm electron microscopy grids. This may cause some problems for sample preparation due to the fragility of Si_3N_4 windows.

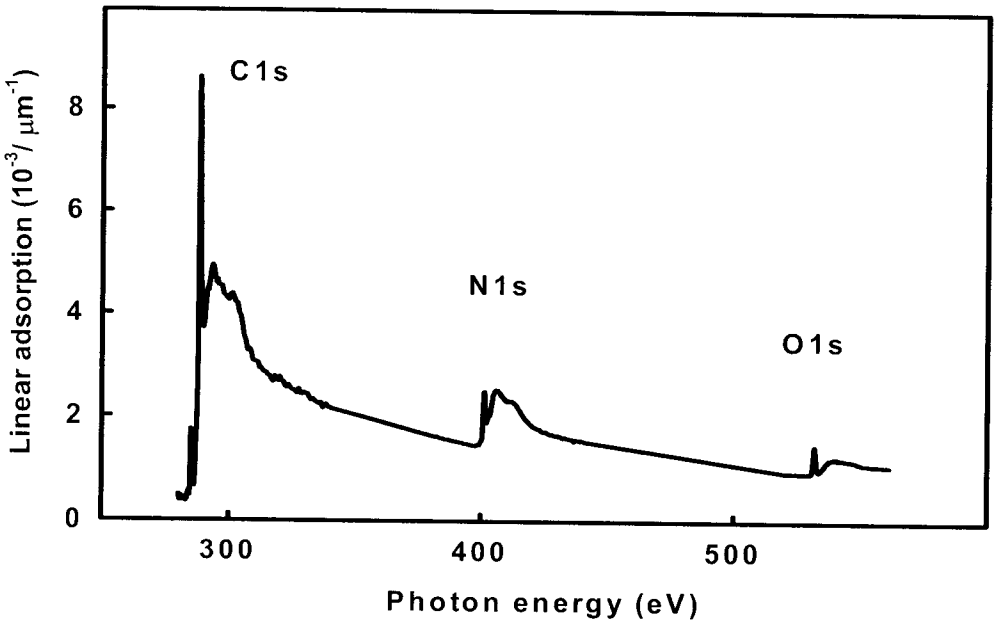

Fig. 1.3 X-ray adsorption spectrum of albumin.

The X-ray microscopes (XRM) used in this work have a spatial resolution of 50-80 nm. The resolving power (E/ΔE) is ~1000 (X-PEEM) and ~5000 (STXM). By tuning the x-ray energy to a particular absorption edge, XRM gives both image and spectra information.

Compared with other techniques discussed in § **1.3**, X-PEEM and STXM have advantages and disadvantages. Their strength is chemically sensitive imaging at a spatial resolution of 50-80 nm. Furthermore they are complementary techniques in the senses of surface-sensitive (X-PEEM) vs. bulk property (STXM), dry measurements (X-PEEM) vs. wet measurements (STXM). The capacities of other techniques are compared with those of XRM in **Table 1.3**. If XRM is capable of providing the functions listed, a "√" sign is assigned. If XRM is only potentially or partially capable to provide the functions listed, a "∞" sign is assigned. If the technique listed is better than the XRM, a "+" sign is assigned; if it is worse, a "–" sign is assigned and if it is similar, a "~" is assigned. This table shows that, while some techniques outperform XRM in one or the other aspect, there is no other technique which surpasses XRM in all aspects simultaneously. The other advantage of X-PEEM/STXM is that it can detect adsorbents and substrates simultaneously. This feature is extremely important for studying protein adsorption on a patterned surface. An example is the adsorption of fibronectin and adhesion of BCE cells on the patterned surface shown in **Fig. 1.1** [KTO&99]. In that work, complicated labeling processes were used in order to visualize absorbed fibronectin and BCE cells, whereas XRM would be capable of direct detection and identification of the absorbed fibronectin and BCE cells without labeling.

The importance of protein adsorption studies and the increasing complexity of surfaces being developed for controlling protein adsorption require a technique to monitor protein adsorption on nano-patterned heterogeneous surfaces. X-PEEM and STXM is developed and optimized for this purpose in this work.

Table 1.3 Comparison of the capacities of different techniques with those of XRM. (Q refers to quantitative, C refers to competition of multiple proteins, O refers to orientation (or conformation) and S refers to substrate.)

Technique	Chemical sensitive	imaging	Q	C	O	S
X-PEEM	√*	√	√	∞*	∞	√
STXM	√	√	√	∞	∞	√
Depletion	–*	–	–	–	–	–
Radiotracer	–	–	–	+*	–	–
QCM	–	–	–	–	+	–
ELISA	+	–	–	+	–	–
Ellipsometry	+	–	–	+	+	–
Reflectometry	+	–	–	+	+	–
TIRF	~*	–	–	–	–	–
Fluorescence spectroscopy	–	–	–	–	+	–
Neutron reflection	–	–	–	–	+	~
FTIR	~	–	–	–	–	–
XPS	~	–	–	–	+	–
MALDI-TOF-MS	+	–	–	+	–	–
TOF-SIMS	+	–	–	+	+	–
DSC	–	–	–	–	+	–
SPR	–	–	–	–	–	–
Raman scattering	~	–	–	–	+	–
CD	–	–	–	–	+	–
AFM	–	+	–	–	+	–

*see text for details.

This work is not the first study of protein adsorption using XRM. Cynthia Morin [M04] did the first study of this type. Cynthia Morin used X-PEEM to study fibrinogen adsorption onto a patterned PS/PMMA surface under different concentrations from buffered and unbuffered water solutions [MHC&04]. Cynthia Morin also used STXM to study fibrinogen adsorption on the same type of PS/PMMA blend surface [HMZ&05]. For these studies, color-coded maps of PS, PMMA and fibrinogen were generated to visualize fibrinogen adsorption preference on PS, PMMA or PS/PMMA interface regions. The relative percentages of absorbed fibrinogen were also calibrated on different regions.

Although the initial studies showed the potential of XRM for biomaterials analysis, there are lots of aspects requiring further optimization as well as developing new application. Starting from this point, my work was mainly focused on the following aspects:

1. Optimizing data acquisition strategies to minimize radiation damage but keep good quality of spectra and images.
2. Optimizing data analysis procedures in the following aspects: procedure, how to generate a good mask for a region, making X-PEEM signals quantitative, generating protein distribution curves.
3. Studying adsorption of albumin and fibrinogen on a PS/PMMA blend under different conditions using XRM, AFM and radio-label techniques.
4. Exploring different substrates for protein adsorption studies.

§ 1.4 Outline of Thesis Chapters

Chapter 2 outlines the fundamental principles of synchrotron radiation, near edge X-ray absorption fine structure (NEXAFS), X-ray spectromicroscopy (scanning transmission microscopy, STXM, and X-ray photoemission electron microscopy, X-PEEM) , atomic force microscopy (AFM) and ^{125}I-labeling technique.

Chapter 3 describes in detail how the samples were prepared and how AFM and ^{125}I-labeling measurement were done.

Chapter 4 discusses how X-PEEM and STXM measurements were performed and optimized, along with the data analysis, including principle and exploring effects of different parameters such as energy calibration, radiation damage, different mapping methods, etc. In the end of this chapter, the optimized strategy for data acquisition and analysis is summarized.

Chapter 5 presents X-PEEM results on the concentration and exposure time effects on the adsorption of albumin on a PS/PMMA blend. This work has been published in Journal of Physical Chemistry B.

Chapter 6 presents X-PEEM results of the effect of pH on the adsorption of albumin on a PS/PMMA blend. The pH ranges from 2 to 10. A paper based on these results is in preparation.

Chapter 7 presents X-PEEM results of the effect of solution temperature on the adsorption of albumin on a PS/PMMA blend. The temperatures studied are 15, 38 and 65 C.

Chapter 8 compares adsorption of albumin and fibrinogen on a PS/PMMA blend at two concentrations: 0.01 and 0.05 mg/ml from de-ionized water solutions. The comparison is based on the X-EEM measurement and ^{125}I-labeling. A paper based on these results is in preparation.

Chapter 9 presents results of the STXM wet-cell measurement of albumin on a PS/PMMA blend. A paper is under preparation.

Chapter 10 summarizes the thesis and proposes future work.

Chapter 2

Methods

This chapter describes fundamental principles of near edge X-ray absorption fine structure (NEXAFS), X-ray spectromicroscopy, and atomic force microscopy (AFM) and the instruments used to carry out my experiments.

§ 2. 1 NEXAFS

X-ray absorption spectroscopy (XAS) is a term covering all techniques involving the excitation of atoms of a particular element in a material by X-rays. When passing through a material, a proportion of the X-rays will be absorbed. When an X-ray has sufficient energy to excite an inner-shell (or core) electron within the material, the level of absorption increases suddenly. This is called an absorption edge. Therefore X-ray absorption spectra show a steep rise at the onset of absorption, exhibit a structured region associated with the electronic structure of target electron and then attenuate gradually with increasing X-ray energy. X-ray absorption spectra are usually divided in two energy regions: 1) the X-ray Absorption Near Edge Structure (XANES) or near-edge X-ray absorption fine structure (NEXAFS), which covers the energy range within 40 eV near the edge, and 2) the extended X-ray absorption fine structure (EXAFS), which covers the energy range from 40 eV to 1000 eV or more above the edge. My work used NEXAFS spectroscopy.

There is a comprehensive book [S92] on the principles and experimental techniques of near edge X-ray absorption fine structure (NEXAFS) spectroscopy which includes many examples of applications of NEXAFS. The description of NEXAFS in this thesis is mostly taken from that book. There are also some other more recent books about X-ray absorption spectroscopy ([NM01], [GNJ&03], [TIG04])

NEXAFS is a technique developed in the 1980's with the goal of elucidating the electronic and geometric structure of molecules bonded to surfaces. NEXAFS selects a specific atomic species by tuning the X-ray photon energy to that needed to excite a particular inner shell electronic level of the atom. Upon X-ray absorption, the excited inner shell (core) electron can be promoted to an unoccupied energy level (excitation) or it can be removed completely (ionization). NEXAFS detects the photoabsorption cross-section for the excitation or ionization of the core electrons. Each element has a characteristic core binding energy: Carbon 1s (C 1s): ~290 eV, Calcium 2p (Ca 2p): ~350 eV, Nitrogen 1s (N 1s): ~400 eV, Oxygen 1s (O 1s): ~530 eV, etc. NEXAFS spectra reflect chemical composition, through the various core edges that can be excited, and the bonding environment of the core excited atom, through details of the unoccupied electronic structure of the system.

§ 2. 1. 1 Theory of Inner Shell Excitation Spectra

The X-ray absorption cross section $\sigma(E)$ of an atom or molecule is defined as the number of electrons excited per unit time divided by the number of incident photons per unit time per unit area. The cross section for photoionization can be calculated from the

probability per unit time P_{if} for the transition from an initial state typically the (1s shell) $|\, i \,\rangle$ to a final continuum state $|\, f \,\rangle$ corresponding to a free electron in the potential of an ion [S92].

$$P_{if} = \frac{2\pi}{\hbar}\left|\left\langle f\left|\overline{V}\right|\, i\right\rangle\right|^2 \alpha_f(E)\,. \tag{2.1}$$

where $\alpha_f(E)$ is the energy density of final continuum states.

For photoexciation, the cross section can be calculated in terms of an optical oscillator strength f, the energy integral of the cross section, as shown in equation (2.2) [S92]

$$\sigma_x(E) = C\frac{df}{dE}\,. \tag{2.2}$$

where C is a constant. The oscillator strength is a measure of the intensity of a transition. The intensities of bound state transitions are typically quoted as an "*f number*" [S92].

$$f = \frac{2}{m\hbar\omega}\left|\left\langle f\left|\mathbf{e}\cdot\mathbf{p}\right|i\right\rangle\right|^2, \tag{2.3}$$

where $\boldsymbol{e}$ is the unit vector of electric field, $\boldsymbol{p}$ is the sum of the linear momentum operators of the electrons, $\hbar\omega$ is the photon energy.

The calculated oscillator strength for a bound state transition can be converted to cross section by equation (2.4).

$$\sigma(E) = \frac{2\pi^2 e^2\hbar}{mc} f\alpha_x(E)\ \text{[S92]}, \tag{2.4}$$

where $\alpha_x(E)$ is the bound state energy density of final states.

The 1s (K-shell) spectra of atoms and molecules contain a few pronounced resonances which correspond to electronic transitions of an inner shell electron to states

near the vacuum level and therefore fall at an excitation energy just below the ionization potential (IP) of the inner shell electron. **Fig 2.1** shows the typical potential (bottom) and 1s edge spectrum (top) of a diatomic molecule (assuming the molecule is multiply bonded).

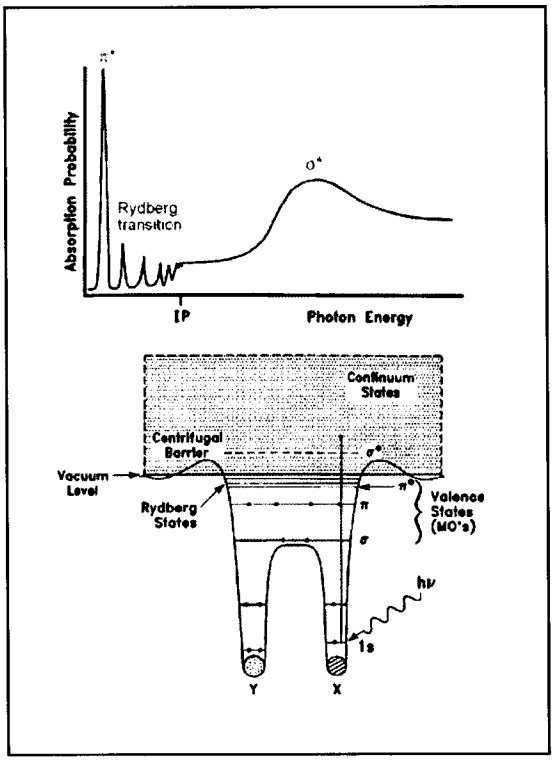

Fig. 2.1 Schematic potentials (bottom) and K-shell spectra (top) of diatomic molecules [S92], reproduced with permission from Springer-Verlag Berlin Heidelberg 1992 (page 85).

Usually the most pronounced feature is the lowest energy peak, which corresponds to a transition to a π^* antibonding orbital of the molecule ($1s \rightarrow \pi^*$). Between the π^* resonance and the IP several sharp but weak features can be observed which correspond to excitations to Rydberg orbitals or, in the presence of bonds to hydrogen atoms, to a mixture of Rydberg and antibonding orbitals of the same symmetry. Mixing of Rydberg orbitals with valence orbitals increases the the intensity of the corresponding resonance because of the more compact nature of the valence orbitals. Rydberg orbitals have a large spatial extent and thus are strongly perturbed and often quenched in condensed states.

Above the IP, there are often one or more broad peaks. These are called "σ* resonance" or "σ* shape resonance" ([S92], [VDS&05]). The σ* resonance is usually described as a two step process where the 1s electron is first excited to a virtual molecular orbital of σ symmetry, followed rapidly by the emission of a photoelectron. The higher the virtual σ-symmetry molecular orbital(s) is located in the continuum, the larger the decay probability of the electron to the energy-equivalent continuum state, which results in a broader σ* resonance.

§ 2. 1. 2 Chemical Sensitivity

NEXAFS is both element specific and sensitive to the local chemical environment. Since this work deals with polymers and proteins (which can also be considered as polymers), the NEXAFS spectra of some polymers are used as an example. These spectra are taken from the work of Ade and Urquhart [AU00]. **Fig. 2.2** presents the C 1s NEXAFS spectra of a range of polymers containing unsaturated functional groups including phenyl rings and double bonds. All spectra are dominated by one or more low energy C 1s $\rightarrow \pi^*_{C=C}$ transitions. The shape and energy of these transitions vary with the chemical and electronic structure of the different polymers. For example, the π^* resonances of toluene diisocyanate (TDI) polyurethane and TDI polyurea are split into two features, associated with the C 1s (C-H) $\rightarrow \pi^*_{C=C}$ (~285 eV) and C 1s (C-R)$\rightarrow$ $\pi^*_{C=C}$ (286.5 eV) transitions. "C-H" refers to the phenyl carbon atoms attached to the hydrogen atoms while "C-R" refers to the phenyl carbon atoms attached to the amide groups. The energy shift of the two π^* resonances is due to the inductive effect of the

amine group, which shifts the C 1s IP of the C-R phenyl carbon to lower energy. This is an example of the chemical sensitivity of NEXAFS spectroscopy.

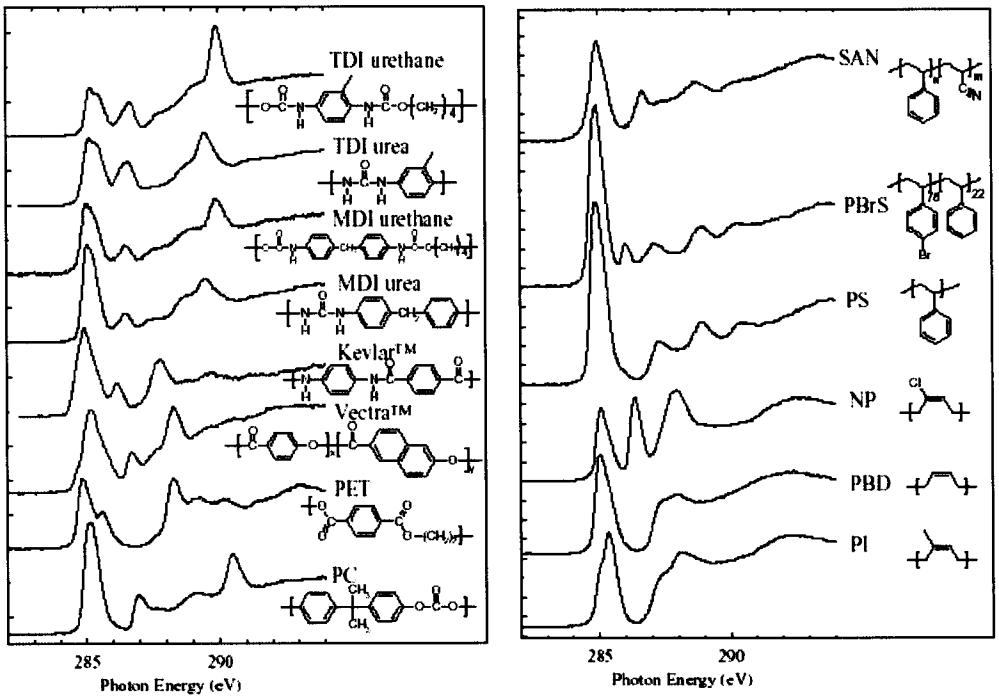

Fig. 2.2 NEXAFS spectra of unsaturated polymers (adapted from [AU00]. TDI = Toluene diisocyanate; MDI = Methylene bis (phenyl isocyanate); Vectra^{TM}: x=0.73, y=0.27; PET = Poly (ethylene terephthalate) ; PC= Polycarbonate; SAN = Poly(styrene-ran-acrylonitrile); PBrS = Poly brominated styrene; PS =Polystyrene; NP = Neoprene ; PBD = Poly(butadiene); PI = Polyisoprene [Taken from page 291 of [AU00] with permission from World Scientific (2000), Ade and Urquhart).

Another example is the energy shift in the π^* resonances of TDI polyurea (~289.5 eV) and vectra^{TM} (~288.3 eV) associated with C 1s (C-X) $\rightarrow \pi^*_{C=O}$ transition. X

represents different atoms connected to the core excited atom in the two different polymers. For vectra^{TM}, X is a N atom while X is a carbon atom for TDI polyurea.

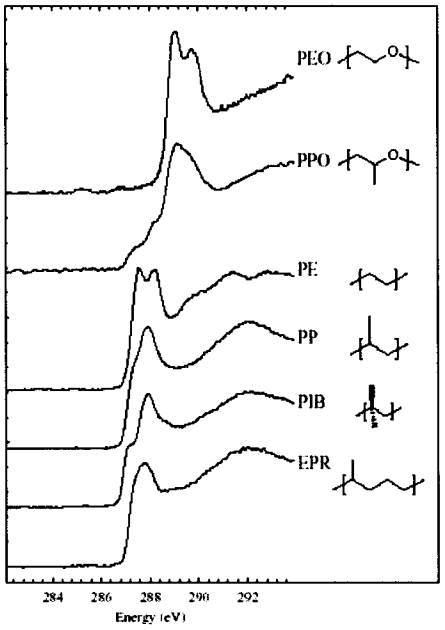

Fig. 2.3 NEXAFS spectra of some saturated polymers: PEO=Poly ethylene oxide; PPO = Poly (propylene oxide); PE= Polyethylene; PP= Polypropylene; PIB=Polyisobutylene ; EPR=Ethylene propylene rubber [Taken from page 292 of [AU00] with permission from World Scientific (2000), Ade and Urquhart].

Fig. 2.3 presents the C 1s NEXAFS spectra for some saturated polymers. All of these spectra are dominated by C 1s $\rightarrow\sigma^*$ electronic transitions with mixture of some Rydberg character. The main difference in chemistry between these polymers is the number and arrangement of methyl groups bound to the $(CH_2)_x$ backbone. The spectra of PEO and PPO are shifted to higher energy by the core binding energy shift induced by the oxygen atom. The differences in the NEXAFS spectra of different chemicals form the chemical contrast for chemically sensitive imaging in X-ray microscopy.

§ 2. 1. 3 Detection Methods

NEXAFS spectra can be recorded in different ways. The main requirement is that the detected signal must be proportional to the X-ray absorption cross section. he most direct method to detect X-ray absorption is by monitoring the change in X-ray intensity as

an X-ray beam passes through a sample. The detected transmitted light is related to the incident photon intensity, the energy-dependent mass absorption coefficient [μ(E)], the sample density (ρ), and the sample thickness (t), through Beers-Law [H48]:

$$I_t = I_0 e^{-\mu\rho t} \tag{2.5}$$

Rearranging this equation, one gets:

$$OD = \ln(I_0 / I_t) = \mu(E)\rho t \tag{2.6}$$

The optical density (OD), also called absorbance, is the log of inverse transmittance, which is the ratio of the transmitted intensity to the incident intensity.

For transmission detection, samples must be partly transparent at the X-ray energy of interest. This means a sample thickness of 20 to 200 nm for carbon 1s studies of unit density organic material, ranging up to 1-2 microns thick for higher energy edges or low density samples such as hydrated polymer gels or biological samples [M04].

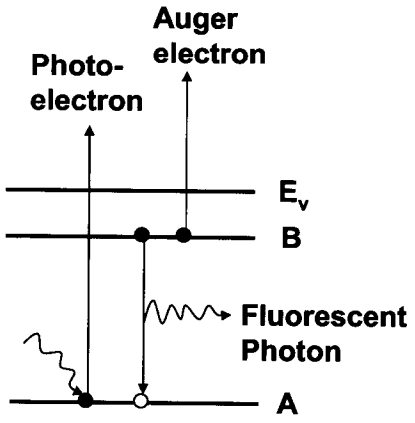

Fig. 2.4 Schematic diagram of a photon absorption process

However, for non-translucent samples, or for other reasons, it is often useful to measure NEXAFS spectra using indirect methods involving detection of a product of the initial X-ray absorption process. **Fig. 2.4** is a diagram of a photon absorption process resulting in creation of a photoelectron and a core hole. The core hole is filled by an electron from a higher energy shell, either

radiatively, by emission of a fluorescent photon, or nonradiatively, by emission of an Auger electron. NEXAFS can be measured by monitoring the intensity of the photo-electrons which constitute the primary excitation channel. However, this detection method can not detect structure below the IP since only free photoelectrons are measured in photoemission. Alternatively, one can measure the yield of Auger electrons or X-ray fluorescence photons associated with the secondary process of core hole decay. For C, N, and O atoms the Auger electron yield is higher than the fluorescence yield by more than two orders of magnitude [S92]. Thus Auger yield detection is much more practical than fluorescence detection in the soft X-ray regime. Other alternatives include various other electron yield methods such as total, secondary and partial electron yield, ion yield, luminescent yield etc.

Different modes are used for electron yield detection: Auger yield mode, partial electron yield mode and total electron yield mode. In the Auger yield mode the detector window is set around the energy of the Auger peak. For partial yield detection only electrons with a kinetic energy larger than a threshold energy are detected. All electrons are collected in the total electron yield mode.

The major technique used in X-PEEM is a type of total electron yield detection. Both photoelectrons and Auger electrons are scattered inelastically by electron-electron, and electron-phonon interactions on their way to the surface. Only the electrons having the correct trajectory and a kinetic energy at the surface greater than the work function escape from the surface and can be detected. Since the inelastic scattering and work

function are highly material dependent, the sampling depth of total electron yield varies from material to material.

§ 2. 2 PEEM Principles and Instrumentation

PEEM evolved from low-energy electron microscopy (LEEM) [B98], a technique which uses an incident electron beam as source. In PEEM, a UV (UV-PEEM) or soft x-ray light source (X-PEEM) replaces the incident electron beam, and photoemission electrons provide the chemical and surface potential contrast. For UV-PEEM, the image contrast for different compositions is mainly the difference in their work function. The image contrast in X-PEEM is due to a combination of topographical features, work function, and chemical composition. X-ray absorption depends on the latter.

X-PEEM detects the total electron yield for electrons emitted from the surface. The physical processes of an X-ray excited electron in a material are sketched in **Fig. 2.5**. The total electron signal is dominated by secondary electrons whose yield depends upon the composition both through the absorption coefficient $\mu(E)$ and the amount of a substance absorbing X-rays within the sampling depth.

X-PEEMs have been constructed by several different groups ([TDD&95], [WLH&97], [DCL&98], [TR91], [EKR&91], [MBL&97], [APD99]). The PEEM2 instrument [APD99] installed on beamline 7.3.1 of the Advanced Light Source (ALS) in Berkeley was used for this thesis, as well as the Canadian Photoelectron Emission Research Spectromicroscope (CaPeRs), (purchased from Elmitec GmbH) when it was located at the Synchrotron Radiation Center (SRC) in Wisconsin, Madison. CaPeRs was

moved to Canadian Light Source (CLS) in 2005. All results presented in this thesis were acquired using the ALS PEEM2, thus only this instrument will be described here.

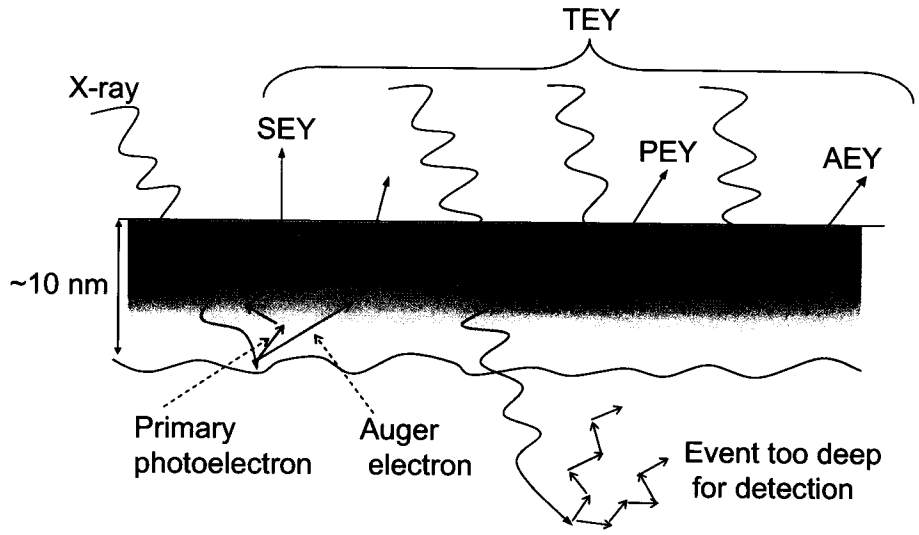

Fig. 2.5 Sketch of physical processes of X-ray excited electrons. The shading is used to indicate the probability of electron escape. The darker the higher probability. SEY = secondary electron yield; PEY = photoelectron yield; AEY = Auger electron yield, TEY = total electron yield.

§ 2. 2. 1 Instrumental Description of X-PEEM 2: Beamline 7.3.1.1

This description of beamline 7.3.1.1 and the PEEM 2 microscope is taken from Anders et al. [APD&99] (the team who designed and built the beamline and microscope) and from communications with Andreas Scholl (the PEEM 2 beamline scientist at ALS).

PEEM 2 at the ALS bending magnet beamline 7.3.1.1 was developed by the ALS in collaboration with the IBM Almaden Research Center (Joachim Stöhr). It is designed specifically for surface and magnetism analysis. It emphasizes X-ray magnetic circular dichroism (XMCD), and X-ray magnetic linear dichroism (XMLD) measurements.

PEEM 2 studies based on chemical contrast have been carried out for a wide range of materials such as semi-conductors [H97], superconductors [DMT&97], polymers ([SM97], [SSK&97]) and biomaterials ([SSK&97], [AWS&98]) .

XMCD contrast comes from differences in the adsorption of left and right circularly polarized radiation due to the relative orientation of the magnetic moment of a sample relative to the handedness of the light. It can be used to study magnetic structures. Detailed analysis of XMCD can distinguish spin and orbital contributions to element specific magnetism.

XMLD contrast arises when linearly polarized X-rays are absorbed by molecules oriented at different directions and by antiferromagnetic materials. For NEXAFS when the electric vectors of the light and transition moment direction are parallel, the absorption is strong. When the electric vector of the light and the transition moment are perpendicular, the absorption is weak. XMLD contrast has been used to study molecular orientation in fibers [SA96] and polymer thin films ([SSC&98], [CDL&98]). XMLD has also used to study antiferromagnetic materials [SSK&98].

The layout of beamline 7.3.1 is shown in **Fig. 2.6**. The source is a dipole bend magnet in the storage ring which deflects the electron beam and generates synchrotron radiation. The pinhole, aperture stop and quadrant position sensor are fixed and thus are not adjusted for the PEEM experiment. The aperture (mask) and chopper are used to select a fan of radiation from the bend magnet, either on the storage ring plane, or above or below the plane. On the storage ring plane the radiation is linearly polarized, above and below it is circularly or elliptically polarized. The chopper can be rotated to quickly

chop the beam and modulate the polarization. This function has never been used in our work. Mask and chopper can be moved relative to each other in the vertical direction to limit the transmitted radiation and reduce the X-ray flux. The spherical grating is the monochromator which vertically disperses the X-ray spectrum. It is rotated to change the photon energy. The elliptical refocus mirror demagnifies the X-ray beam by 10 to reduce the spot width on the sample to about 30 μm. The Ti foil suppresses radiation with energy above the Ti L edge, around 460 eV, reducing 2nd order light at the C 1s edge. The exit slit vertically limits the size of the X-ray beam on the sample. There are two different size slits: 50 μm and 100 μm. In this work, the 100 μm slit was used throughout. The slit is also used to define the photon energy scale so that it stays fixed when changing samples.

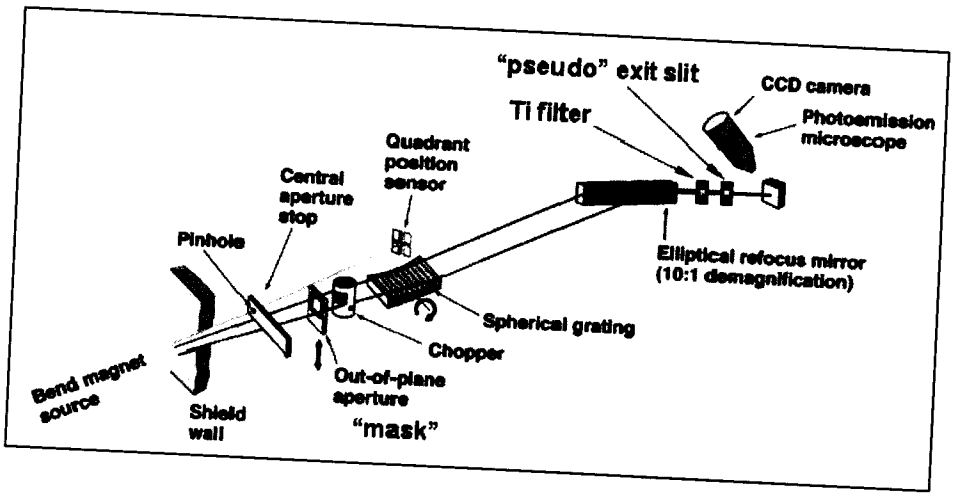

Fig. 2.6 Layout of PEEM 2 beamline (7.3.1.1) (modified from [M04]).

The photon energy range of beamline 7.3.1 is 175-1500 eV. The photon flux measured with an x-ray photodiode is 1 x 10^{11} photons/s at ~ 700 eV in a 30 ×30 μm spot when the storage ring is operated at 1.9 GeV with a ring current of 400 mA in a design bandpass of 1 eV at 1000 eV. A spherical-grating monochromator (SGM) with no entrance slit and a low line-density grating (200 lines/mm) is used to obtain high throughput while still achieving the desired spectral resolution. The flux is very high because the minimum number of optical components is used. The storage ring electron beam acts as the entrance slit while the PEEM acceptance is the pseudo exit slit [M04]. The resolving power of the beamline is $E/\Delta E$ = 1800. For the reduced flux beamline conditions used for studies of X-ray sensitive polymers, $E/\Delta E \sim 500$ at the C 1s edge, i.e., $\Delta E \sim 0.6$ eV [M04].

§ 2. 2. 2 Instrumental Description of X-PEEM2: PEEM 2 Microscope

The optical layout of the PEEM 2 microscope on beamline 7.3.1 is shown in **Fig. 2.7**. The angle between the sample surface and the incident X-ray beam is 30°. The microscope optical axis is oriented at an angle of 90° with respect to the electric field vector of the radiation for linearly polarized light. Secondary electrons emitted from the sample surface are extracted into an electron optical imaging system by a strong electric field that is applied between the sample and the objective, the first electrode of the electron optical system. The typical distance between the objective lens and the sample is 2 mm, and the maximum operating voltage is 30 kV. However most samples start to show considerable field emission at voltages of 20 kV. Field emission results in an

unstable image and then limits the applied voltage. The objective lens has a stigmator/deflection assembly located in its back focal plane. The stigmator setup is optimized by searching for symmetric motion of the image while wobbling the voltage of the transfer lens. The stigmator adjustment is important for good quality data, especially when detecting signals from a small region.

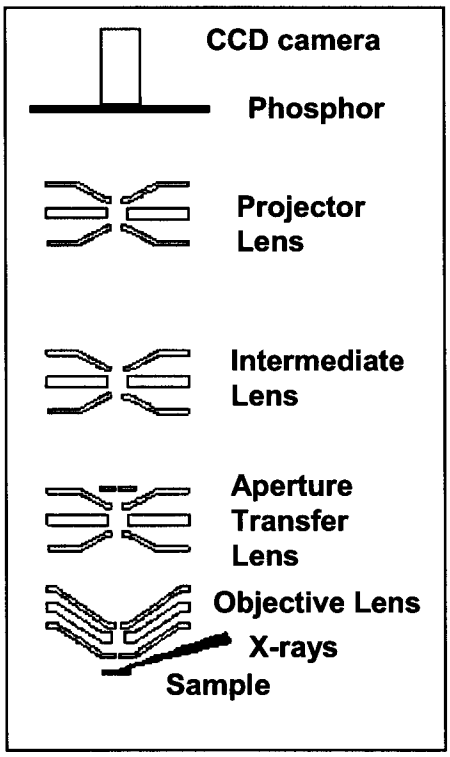

Fig. 2.7 Schematics of PEEM2 [M04].

The transfer lens produces a 1:1 image at the second objective back focal plane outside the lens where an aperture is located. There are four different apertures (2 mm, 50 μm, 20 μm, and 12 μm diameter) mounted on a small flexure stage and the four apertures can be switched from one to another in vacuum. The smaller the aperture, the better the spatial resolution, the lower the efficiency of the column, and thus for similar statistical quantity, a large statistical quantity, a larger dose and thus larger radiation damage. The 50 μm aperture was used in this work.

The intermediate lens (with another deflector) and projector lens form the final image on a phosphor screen deposited on a fiber optic plate which serves as the window separating vacuum and air where the CCD camera is mounted. The projector lens and intermediate lens are used to control the magnification of the microscope. For large fields of view (from a maximum of 200 μm down to 20-25 μm) only the intermediate lens is

used. The projector lens is turned on to magnify even more when fields of view lower than 20 μm are required [M04]. In our work, the projector lens is turned off in order to work with a column efficiency that allows adequate statistics when using the reduced x-ray flux required to avoid radiation damage.

The detector consists of an electron sensitive phosphor, a fiber bundle coupling the phosphor to the charge coupled device (CCD), and a cooled CCD camera (from Princeton Instrument).

X-PEEM samples must be adequately conductive, reasonably flat, UHV-compatible (i.e. non-outgassing) solids. The yield of electrons emitted from the entire illuminated area is imaged. By recording a sequence of images with incrementally increasing photon energy ('stack acquisition'), a NEXAFS spectrum can be extracted for each image point. **Chapter 4** describes the various modes of data acquisition at PEEM2 and how the data was actually recorded and analyzed for this thesis.

§ 2. 3 STXM Principles and Instrumentation

Scanning transmission X-ray microscopy (STXM), detects transmitted signals passing through the sample. The transmitted signal, when converted to optical density (OD), is sensitive to sample thickness, density and composition, according to **Equation 2.6**.

This work used a dedicated STXM [KTS&03] installed on beamline 5.3.2 [WAK&02] in ALS. STXM532 was designed specifically for the study of polymers. It is the first in the world with interferometric control. There is another STXM at the ALS.

It was installed on beamline 7.0.1 prior to 2001 and then moved to the molecular environmental science beamline 11.0.2. STXM 11.0.2 was not used for the work detailed in this thesis. Different STXMs are compared in **Table 2.1**.

Table 2.1 Comparison of different STXMs in ALS (see http://www-als.lbl.gov)

	STXM 532	**STXM 11 0 2**
Beamline	5. 3. 2	11. 0. 2
Source	Bend magnet	Elliptically polarized undulator (EPU)
Energy range	250-700 eV	90-2150 eV
Monochromator	Low-dispersion, spherical-grating monochromator, one grating	Variable-included-angle plane grating monochromator (PGM)
Flux in focused spot (1.9 Gev, 400mA)	1 x 10^7 photons/s at sample	~10^9 photons/s
Resolving power (E/ΔE)	≤ 3000	≤ 7000
Characteristics	Active servo-stabilized toroidal premirror	High performance beamline, full polarization control (linear, circular) by EPU
Spatial resolution	40 nm with current zone plates	30 or 40 nm with current zone plates.
Detectors	Phosphor (fine grained powder on fibre optic) converts to visible light, light pulses detected by high performance photomultiplier (PMT) system	(a) Phosphor PMT; (b) Fast avalanche photodiode.
Spot size at sample	40 nm	30 or 40 nm
Sample requirements	Thin sections, films, and particulates (20–100) nm thick), supported using Si_3N_4 windows or TEM grids.	Thin sections, films, and particulates (50–1000 nm thick); 3 x 3 mm in area
Sample environment	Helium up to 1 atm, vacuum to 10^{-2} Torr	Helium up to 1 atm, vacuum to 10^{-2} Torr, inert gas up to 1 atm
Scientific applications	polymers	Molecular environmental science STXM, materials sciences, life sciences, magnetic materials
Experimental techniques	NEXAFS spectromicroscopy at the C, N, and O K edges; electrochemical STXM; tomography.	X-ray images; NEXAFS spectra; Chemical mapping at 30-nm resolution; polarization studies.

§ 2. 3. 1 STXM Beamline 5.3.2

The principles of the optical design for BL 5.3.2 have been described in [WPA98]. **Figure 2.8** shows the layout of beamline 5.3.2. A spherical-grating monochromator (SGM) disperses the X-ray in the horizontal plane. The energy resolution is determined by the settings of the entrance slit and the dispersive exit slit. The STXM zone-plate (ZP) is a variable-line-spacing circular diffraction grating. It accepts only the coherent fraction of the illuminating beam when focusing at its diffraction limit.

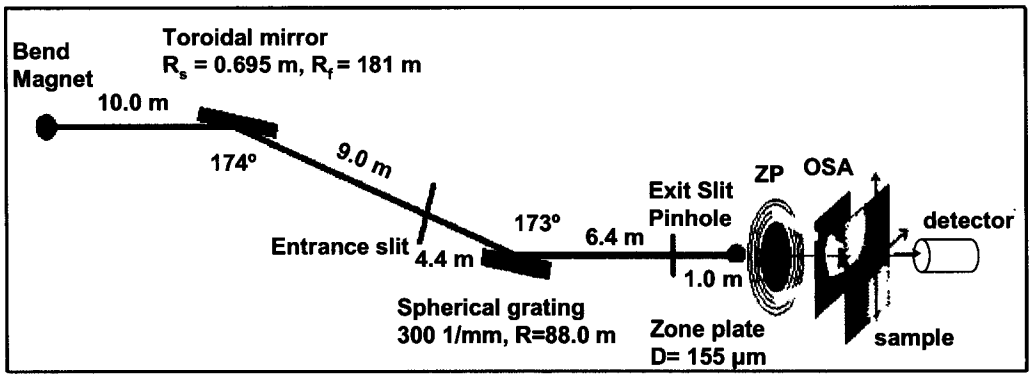

Fig. 2.8 Beamline 5.3.2 layout (Plan view) [M04]

There is a large central stop fabricated on the ZP (80 µm diameter in the ZP used in this work). When aligned with the 80 µm central stop, the 55 µm diameter order sorting aperture (OSA) allows only first order ZP diffracted light to pass and blocks the zeroth order light. Effective first order X-ray filtering only occurs when both OSA position and ZP focus are set properly. Schematic representations of zeroth and first order light are shown on **Fig. 2.9**. The zeroth order light is the light that is not diffracted

by the zone plate, and the first order light is the most intense diffracted light. The focus length f is given by

$$f = \frac{D \cdot \delta_r}{\lambda} \tag{2.7}$$

where D is the diameter of ZP (155 μm), δ_r is the outmost ring of the zone plate (35 nm), and λ is the wavelength.

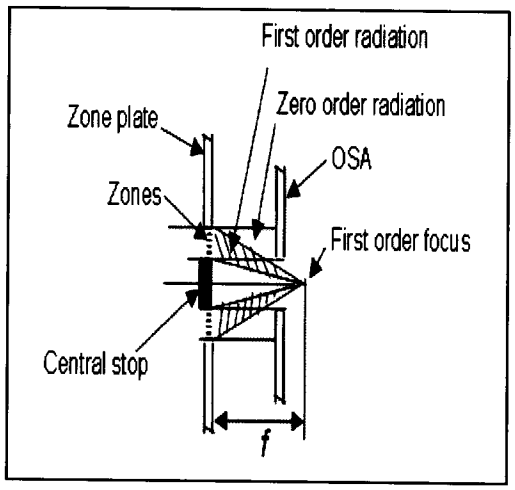

Fig. 2.9 Focusing scheme of STXM.

The OSA position, ZP focus, sample-OSA distance, sample focusing, and the accuracy of the energy scale all play a role in getting the highest spatial resolution and keeping it over an extended range of photon energies.

§ 2. 3. 2 STXM Microscopes

Fig. 2.10 shows a schematic of the mechanical components of STXM 532. The microscope contains the following major components: a) zone-plate *z* stage; b) OSA *x, y* stages; c) sample *x, y* coarse stage; d) sample *x, y* and *z* fine piezo stage; e) sample coarse *z* stage; f) detector *x, y, z* stage; g) interferometer system; h) mounting platform; i) passive vibration isolation to the floor and vacuum/He enclosure.

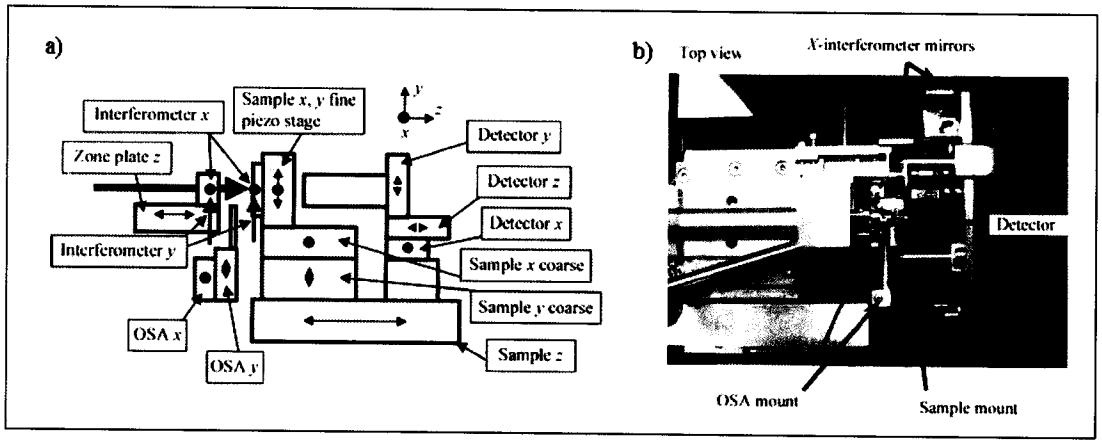

Fig. 2.10 5.3.2 STXM components a) schematically, b) top view picture [M04].

Transmission images are obtained by a raster scan of the sample through the focal point of the zone plate. Spectra are obtained in point, line or image mode by acquiring signal at multiple photon energies. The detector is a phosphor that converts X-rays to visible light. The visible photons are counted by a high performance photomultiplier (PMT) system which can count linearly up to ~20 MHz.

The requirements for sample preparation and measurement in STXM532 are shown in **Table 2.1**. For information about data acquisition modes and how my data was actually measured in STXM532, please see **Chapter 4**.

§ 2. 4 Atomic Force Microscopy

The atomic force microscope (AFM) is a well-known member of the so-called scanning probe microscopy (SPM) family. Different family members are different in the physical principle for probing. In the SPM technology, a sharp probe interacting locally with the specimen is raster scanned and an image providing three-dimensional information about the surface is obtained.

The basic AFM components include a probing tip and a detection system used to monitor the motion of the probe. Topological images can be obtained sequentially by controlled scanning either the tip or sample through a feedback mechanism. The detection system is a critical part of an AFM microscope and a soft cantilever is used in order to have sufficient force sensitivity. The first AFM microscope, invented by Binnig, Quate and Gerber [BQG86] in 1986, is shown in **Fig. 2.11 (a)**. In this instrument the cantilever was made of a thin strip of gold foil with a spring constant of about 100 N m^{-1} and a tunneling junction was used to detect the cantilever movement. Two types of image can be obtained: one with a constant deflection of the cantilever while recording the vertical position of the piezo scanner (constant-force mode), and the other with a constant vertical position of the piezo scanner while recording the deflection of the cantilever (constant-height mode). This design is not widely applied today due to several major

limitations, such as the vulnerability of a tunneling junction to surface contamination and the inability to operate in aqueous solutions.

A design based on optical detection was introduced in 1988 by Meyer and Amer [MA88] to overcome these shortcomings. As shown in **Fig.2.11 (b)**, when the cantilever is illuminated with a focused laser beam, the differential signal from a split diode allows the detection of minute movements of the cantilever. The vertical movement of the cantilever can be measured with a precision of 0.1 nm using an optical lever of a few centimeters long. Another advantage of this design is the use of a diode laser, which makes an AFM microscope compact.

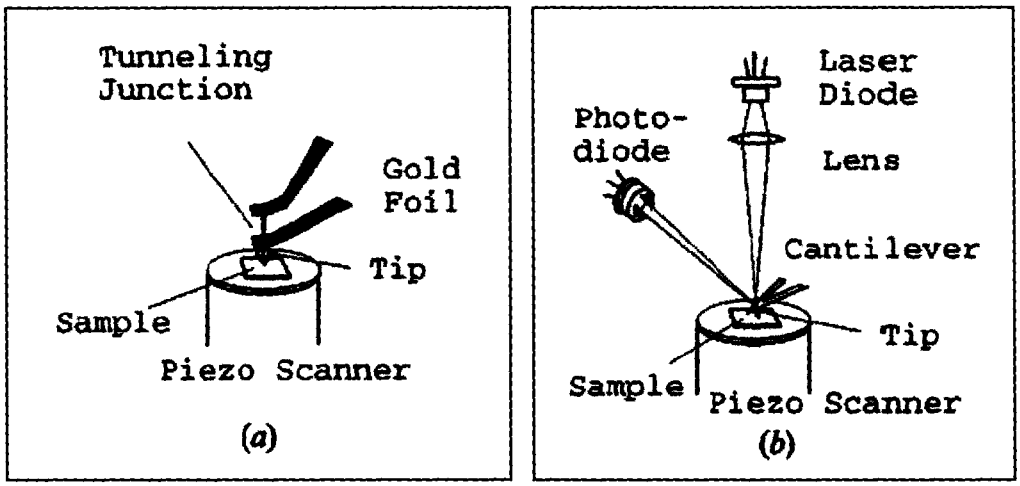

Fig. 2.11 (a) The original set-up for AFM constructed by Bining et al. (1986). A tunneling junction was used to sense the deflection of the cantilever, and the atomic force microscope probe is a piece of crushed diamond glued on a gold foil strip; (b) the most popular design of atomic force microscope. An optical lever is used to sense the deflection of the cantilever with the vertical sensitivity as high as 0.1 nm or better [SMC&96].

§ 2. 4. 1 Imaging Modes

The **contact mode** where the tip scans the sample in close contact with the surface is a common mode used in AFM. There are two contact modes of imaging: Constant height imaging and constant force imaging. In constant height imaging, the force between the tip and the sample vary with topography while the distance between the tip and the sample remain constant. The constant height mode is not good for imaging soft samples such as polymers since vertical forces can cause deformation of surfaces and shear forces can move delicate samples around or off a surface. However, these problems can be minimized in the constant force mode where a small constant force on the sample is maintained in order to insure reliable contact mode AFM operation. In the constant force mode of imaging, the force applied vertically to the surface is kept constant by monitoring the constant deflection of the cantilever through the signal in a feedback loop [SHA&00].

In contact mode AFM, the height of features on a surface is measured through the voltage of the feedback amplifier that applies to the piezotube. The voltage is applied when the sensed deflection of the cantilever deviates from the desired value of deflection (constant height or constant force). The deviation is amplified and then sent to the z-axis actuator of the piezotube which is a three-dimensional scanner. The distance between the sample and the cantilever will be adjusted to restore the desired value of deflection. Images taken in this mode are generally displayed in shades of gray where lighter gray implies higher features.

. **Non-contact** or **tapping mode**™ is a key advance in AFM. It makes it possible to acquire high resolution topographic imaging on a surface that is easily damaged, loosely attached to the substrate, or difficult to image by other AFM techniques. Tapping mode overcomes problems associated with friction, adhesion, electrostatic forces, and other difficulties that may be encountered in the contact mode due to its specific way of scanning. Different from the contact mode, the tip is only alternately in contact with the surface to provide high resolution and then the tip is lifted off the surface to avoid dragging the tip across the surface and thus deformation of the surface.

In ambient air, tapping mode imaging is operated by oscillating the cantilever assembly at or near the cantilever's resonant frequency using a piezoelectric crystal and then the cantilever oscillation amplitude is maintained constant by a feedback loop. The principle of tapping-mode AFM is shown in **Fig. 2.12**. Rather than having the tip in contact with the surface all the time, the cantilever is driven to oscillate at its resonance frequency, typically at a relatively high frequency (1-100 kHz). The amplitude of oscillation is a constant before the tip comes into contact with surface. However, as soon as the tip touches the surface, the amplitude is changed due to the damping introduced by the surface. This amplitude change can be used as the feedback signal to control how much the tip is allowed to 'feel' the sample in order to maintain constant oscillation amplitude. The tip is only transiently in contact with the surface at each pixel, and thus the lateral force exerted on the sample is reduced.

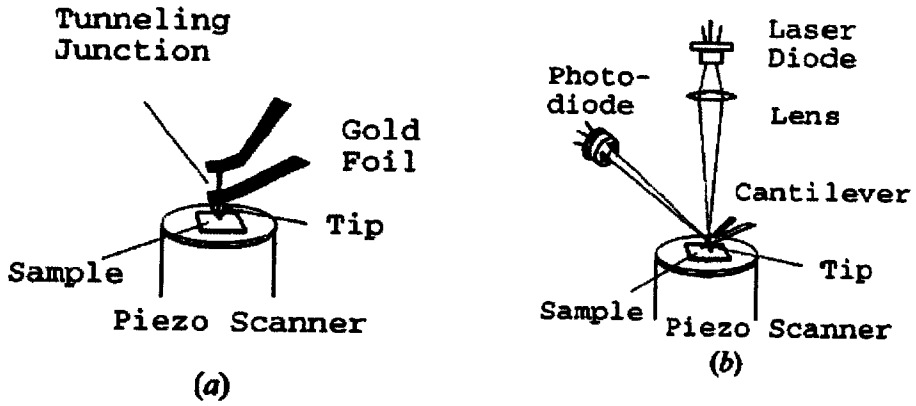

Fig. 2.12 The tapping-mode atomic force microscope. (a) The necessary hardware; (b) Illustration of the signal in the tip engagement process. The amplitude changes at the point of contacting surface. The amplitude change due to surface damping can be used as the feedback signal for imaging [SMC&96].

Tapping mode operation in fluid has the same advantages as in air or vacuum. However it is hard to maintain a constant oscillation in a fluid medium due to the frictional forces of the medium. In this case, instead of oscillating the cantilever itself, the entire fluid cell can be oscillated to drive the cantilever into oscillation. If the cantilever oscillates in an appropriate frequency (usually in the range of 5,000 to 40,000 cycles per second), when the tip contacts the sample, the amplitude of the cantilever will decrease in a way similar to tapping mode operation in air. Alternatively, very soft cantilevers (~0.1 N/m spring constant) can be used for imaging in fluid. The spring constant is typically in the range of 1-100 N/m for imaging in air [SMC&96].

In summary, in contact mode AFM, electrostatic and/or surface tension forces from the adsorbed gas layer pull the scanning tip toward the surface. Such forces can

cause damage to samples and distortion to image data. Tapping mode AFM was developed as a method to achieve high resolution without inducing destructive frictional forces both in air and fluid. The tapping mode technique makes it successful to image very soft and fragile samples. Also, when incorporated with *Phase Imaging*, tapping mode AFM can be used to analyze the components of the membrane. Phase imaging uses the changes in phase angle of the cantilever probe to produce an image, called a phase image or phase contrast image. Phase images often provides significantly more contrast than topographic images and are sensitive to material surface properties, such as stiffness, viscoelasticity, and chemical composition.

§ 2. 4. 2 AFM Study in This Work

All AFM images presented in this work were measured using tapping mode, with the DI-Nanoscope IIIA AFM instrument, located in Brockhouse Institute for Material Research (BIMR) at McMaster. There are three applications of AFM to my work. The first application is to detect the thickness of a series of PS films in order to measure the X-PEEM sampling depth of PS. The second application is to examine polymer substrate surfaces used for protein adsorption. The third application is to image absorbed proteins on the surfaces. The first two applications are relatively easy since the domain of patterned polymer substrates is large compared with the size of proteins. Furthermore the polymers in the substrate are relatively much more stable than the loosely adsorbed proteins.

The results of AFM study in this work are presented in **Chapter 3.**

Chapter 3

Sample preparation, Atomic force microscopy and ^{125}I-labeling study

This chapter describes sample preparation methods and presents the results of AFM and ^{125}I-labeling measurements. AFM was used to measure the thickness of polymer films, to monitor the morphology of PS/PMMA blend surfaces and to image proteins adsorbed on such surfaces. The ^{125}I-labelling technique was used to quantify the amount of proteins adsorbed onto PS, PMMA and PS/PMMA blend surfaces.

§ 3.1 Sample Preparation and AFM Study of Corresponding Samples

§ 3.1.1 Polystyrene Films

A series of polystyrene (PS) films with different thickness were prepared for characterization of sampling depth of X-PEEM. PS (Molecular weight: MW = 0.344 $\times 10^6$ Dalton, Molecular weight distribution index: δ = 1.05) was obtained from Polymer Source Inc. and was used without further purification. A series of PS solutions in toluene (Aldrich, 99.8% anhydrous) were prepared with different concentrations: 0.05%, 0.10%, 0.50%, 1.00%, and 2.00% (mass percentage). Each solution was spun cast with two different speeds between (1000~ 4000 rpm) and 40 seconds spinning time onto clean 1 cm x 1 cm native oxide Si wafers (111) (Wafer World, Inc.), which had previously been degreased with trichloroethylene (Aldrich, +99.5% pure), acetone (Burdick & Jackson,

HPLC grade), and methanol (Caledon), then rinsed under running de-ionized water. **Table 3.1** is the list of samples along with the thickness of each sample.

Table 3.1 Thickness of a series of PS films.

% PS (mass)	Spin Speed (rpm)	Thickness (± 0.5 nm*)
0.05	1K	**2.2**
	2K	--
0.10	1K	4.9
	2K	**3.7**
0.50	2K	16.4
	4K	**16.0**
1.00	4K	34.5
	6K	**33.1**
2.00	4K	95
	6K	--

(Note: no measurements were done on the samples labeled with '--'. *the error is derived from the variation of thickness along a scanning line, see **Fig. 3.1** for details)

As mentioned in Section 2.5.2, all AFM images presented in this work were measured under the guidance of Andy Duft (McMaster) using tapping mode, with the DI-Nanoscope IIIA AFM instrument, located in BIMR at McMaster. The thickness was measured at a scratch which exposed bare Si wafer. **Fig. 3.1** shows an example of the thickness measurement on the sample of a PS film (0.50 %, 4K rpm) by AFM. The film is not very flat as indicated by the dash line 1, while part of the slope of line 1 could be instrumental, it may also reflect real variation in film thickness. The scratch may contain some polymer residues as indicated by the variation on its height profile, but it is not hard

to find some clear areas – shown by arrows 6 and 7. The height difference between the two points pointed by arrows 6 and 7 is 0.06 nm. The height of the PS film measured by the two points (5 and 6) closest to the edge of the scratch is 15.62 nm. The uncertainty of the PS film thickness was estimated from the variation in the heights measured between point 6 and 4 points on the PS film: points 1, 2, 3, and 4. The height at the four points in order are: 15.85, 16.25, 16.61, and 17.09 nm. The average of the five heights is then 16.2 nm and the standard deviation is 0.5 nm.

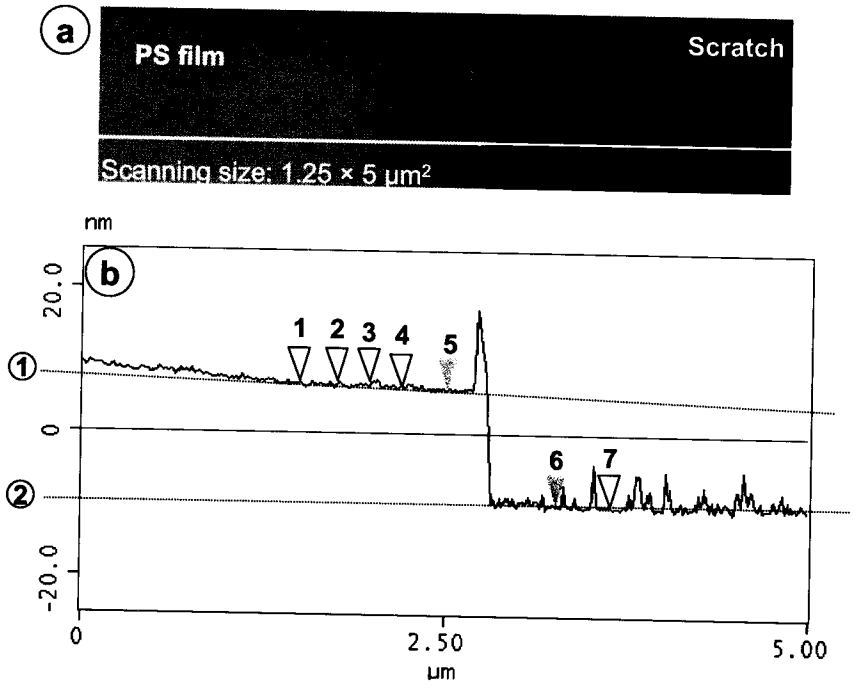

Fig. 3.1 Measurement of the thickness of a PS film (0.50 %, 4K rpm) by AFM: **a)** a scanning height image (tapping mode) of PS film with a scratch (1.25 ×5 μm^2); **b)** the height profile along the white line crossing PS film and the scratch defined in a), the height was measurement to be 16.2 ± 0.5 nm.

§ 3.1.2. Polystyrene/ polymethylmethacrylate (PS/PMMA) Blend Substrate

The procedure I used for preparing thin films of PS/PMMA blend is that developed by Morin et al [MIT&01]]. The recipe was optimized to have a flat surface with phase-separated PS and PMMA domains of a size (~1 μm) suitable X-PEEM study. The spatial resolution of XRM is around 50-70 nm and the ideal domain sizes should be about an order of magnitude larger than that.

Polymer thin films were prepared in the lab of Dr. Kari Dalnoki-Veress (Physics Department at McMaster). PS (MW = 1.07 $\times 10^6$ Dalton, δ = 1.06) and PMMA (MW =3.12 $\times 10^5$ Dalton, δ = 1.01) were obtained from Polymer Source Inc. and were used without further purification. A 30:70 w/w PS/PMMA (1% by weight) toluene (Aldrich, 99.8% anhydrous) solution was spun cast (4000 rpm, 40 s) onto clean 1x1cm (or 0.8x0.8cm) native oxide Si wafers (111). The PS/PMMA films were vacuum annealed at 160°C for 12 hours at a pressure of ~10^{-4} torr. The vacuum oven is shown in **Fig. 3.2**. It consists of a heater, a support heat plate and a vacuum dessicator pumped by a cryo-trapped turbo pump backed by an oil mechanical pump.

Fig. 3.2 Setup of a home-built vacuum oven.

Fig. 3.3 is an AFM image in phase contrast mode of one of the PS/PMMA blends prepared with this recipe. PS and PMMA are phase separated with islands of 500-800 nm width, separated by similar sized continuous domains. However at these molecular weights PS and PMMA do not phase separate completely. As seen in **Fig. 3.3**, there are black microdomains on the white islands and there are white microdomains on the black continuous phase. The different colors are used to emphasize the phase contrast. The size of the microdomains is around 10-200 nm. AFM does not have chemical sensitivity but the XRM results indicate that the continuous domain is PS while the discontinuous domains are PMMA. Why is PS the continuous phase with ~ 60% of surface area even though PS is only 30 (wt) % in the blend? Morin et al. [MIT01] did a rather systematic

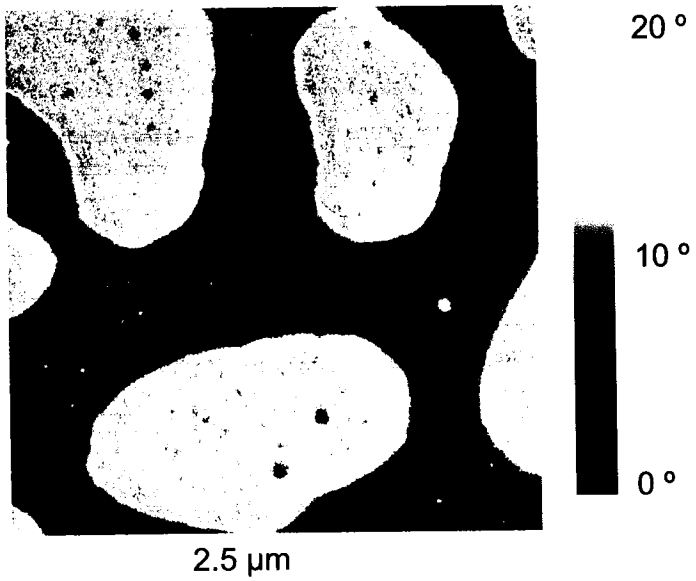

Fig. 3.3 Phase image of PS/PMMA (30/70 mass ratio) blend, annealed at 140°C for 12 hrs.

study of the PS/PMMA blend system using STXM and reported the same phenomenon. As mentioned in **Chapter 9**, there may be a PMMA underneath layer between the SiO_x wafer and the surface, which can explain why PS has a larger surface ratio than expected.

The PS/PMMA blend surface is very flat. **Fig. 3.4 (a)** is the height (topology) image of the blend. **Fig. 3.4 (b)** is the height profile at the white line defined in (a). The very small depressions at the interface of the PS and PMMA domains are 4-6 nm "deep" and the difference in height of the PS and PMMA domains is around 0-2 nm. Note that, relative to the 500 -800 nm domain sizes, this is a very flat surface. The width of the dips at the phase boundaries is ~ 80 nm, so the depressions at the interface are far from crevices.

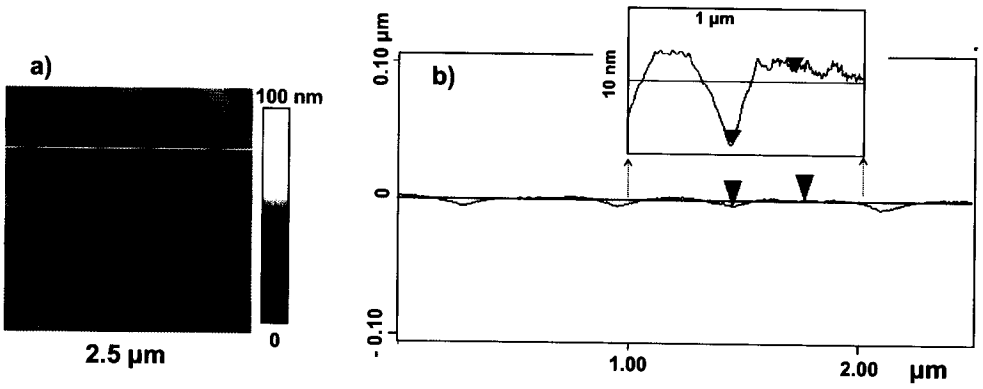

Fig. 3.4 AFM measurement of PS/PMMA (30/70 mass ratio) blend (annealed at 140°C for 12 hrs). (a) Height image (b) Profile at while line defined in (a) (the inserted profile is a magnified view of the 1 µm region between the two dash lines). The PS and PMMA domains are similar in height while the PS/PMMA interface is around 4-6 nm lower. The height difference between two points defined by the two red arrows is 5.2 nm.

The thickness of the PS/PMMA blend film is 40-50 nm, as measured from the height of a scratch through the film.

For AFM, X-PEEM and ^{125}I-labelling studies, the substrate for spin coating is a native oxide Si (111) wafer. Si wafers are not suitable for STXM since they are not X-ray transparent although Si would be ideal if thin enough. There are two methods to prepare polymer film for STXM measurements. The first method is to spin coat directly onto the Si_3N_4 membrane. The disadvantage is that the Si_3N_4 membrane is easily destroyed. The spin speed has to be limited to below 2000 RPM to avoid destroying the Si_3N_4 membrane. However it is hard to have a uniform film at spin speeds below 2000 RPM. The second method which was used in this work is to spin coat onto mica, then float the polymer film onto Si_3N_4. To transfer the polymer film onto a Si_3N_4 window, the polymer is floated onto the top of de-ionized water by immersing the polymer covered mica into water at an angle of ~45°. A Si_3N_4 window is held by a tweezer and approaches the polymer film floating on the top of the water. The Si_3N_4 window with the adhering polymer film is lifted quickly and removed from the water. The Si_3N_4 window can approach the film from the top or bottom.

§ 3. 1. 3 Protein Exposure Methods for STXM and PEEM Samples

The two different proteins used in this work, human serum albumin (HSA) and human plasma fibrinogen, were obtained from the Brash group (McMaster) and used without any further purification or other processes. The HSA is from Behringwerke AG, Marburg, Germany. It is homogeneous as judged by sodium dodecyl sulphate polyacrylamide gel electrophoresis (SDS-PAGE). Fibrinogen was plasminogen-free human plasma fibrinogen (Calbiochem). Dialysis is preformed to remove possible low-

molecular-weight impurities for the radiolabeling but not the PEEM samples. It is reported to be >95% clottable by thrombin, and pure as judged by SDS-PAGE.

Different methods were used to expose the PS/PMMA blend film to a protein solution. For a Si wafer supported polymer film, the exposure was done using 24-well cell culture plates. ~2 ml of protein solution was filled into one well and another 4 wells were filled with the phosphate buffered (or deionized water) used for preparing the protein solution. The whole polymer-coated Si wafer (0.8 cm×0.8 cm or 1 cm×1 cm) was immersed into the protein solution for a specific time. The substrate was then removed and put quickly into one well with the buffer or deionized water before the substrate dries. The substrate was left in the buffer or deionized water solutions for 2 minutes to rinse off the any weakly adhering and to dilute the solution. This rinse procedure was repeated four times for each substrate. Finally the substrate was taken out of the solution and dried by touching the edge carefully with lens paper[1].

For Si_3N_4 membrane supported polymer films, the exposure was done by putting a drop of protein solution onto the top of the entire membrane window. After a specific time for adsorption, the protein solution was removed carefully by a micro-pipet. A drop of buffer (or deionized water) solution was then put onto the membrane window to rinse weakly adhering and solution protein from the adsorbed protein. After two minutes, the solution was removed by a micro-pipet. Such rinsing was repeated four times for each polymer film and then the film was dried in the air for a few minutes. To have a uniform

[1] Such protein exposure and rinse procedure may have two issues. The protein solution interacts not only with PS/PMMA but also with the back side of the Si wafer. This issue needs to be considered particularly in dilute protein solution. When taking the samples out of protein solutions, the protein may deposit at the air-solution interface. It is better to rinse the protein solution under a gentle flow of solvent (micropipette) without taking out the samples.

protein layer over the whole polymer film, it is recommended that the protein solution should cover all of the polymer film not just one corner.

Table 3.2 summarizes the protein covered PS/PMMA samples used in this work.

Table 3.2 List of protein covered PS/PMMA samples.

Protein	Conc. (mg/ml)	Exposure time (min)	Temp. (C)	Solution	pH	Technique and date of beam time
Albumin	0.005	20	R. T.	Unbuffered de-ionized water	7.0	X-PEEM, March 2005
Albumin	0.01					
Albumin	0.05					
Albumin	0.01	5	R. T.	Unbuffered de-ionized water	7.0	X-PEEM, May 2005
		60				
Albumin	0.05	20	R. T.	HCl	2.0	X-PEEM, June-July 2005
				HCl	4.0	
				NaOH	8.6	
				NaOH	10	
Albumin	0.01	20	R. T.	Phosphate Buffered Saline (PBS)	7.4	X-PEEM, July 2005
Fibrinogen	0.01					
Albumin	0.05					
Albumin	0.05					
Mixture of albumin and fibrinogen (1:1 mass)	0.01					
Mixture of albumin and fibrinogen (1:1 mass)	0.05					
Albumin	0.004	20	15	Unbuffered de-ionized	7.0	X-PEEM, October 2005
			37			
			65			
Albumin	0.05*	--	R. T.	Unbuffered de-ionized	7.0	STXM, October 2005

- The measurement was done in presence of solution

§ 3.2 AFM Study of Protein Covered PS/PMMA Blend

Actually the first motivation of the AFM measurement of protein adsorption was to help understand a non-linear energy shift in X-PEEM data which ultimately was tracked down to an unannounced data format change which lead to incorrect read-in in the aXis2000 program.

At the beginning of my experience with X-PEEM data analysis (May 2003 ~ June 2004), all results showed albumin had a strong preference for PMMA regions. I will use the adsorption of albumin from 0.005 mg/ml unbuffered solution as an example. The X-PEEM result as initially analysed is shown in **Fig. 3.5 b)** panel as a color-coded map which visualizes the albumin distribution on a PS/PMMA blend surface. Red is used to represent PS, green represents PMMA and blue represents protein. The intensity of each color is proportional to the strength of signal at a given pixel. The discontinuous green PMMA domains are almost blue, which indicates protein has strong adsorption on PMMA domains. However the AFM image shown in **Fig.3.5 a)** does not agree with this result. Although AFM does not have chemical sensitivity, it is believed that the particles shown on the AFM image are adsorbed protein molecules. It is clear that most of the protein is located on the continuous PS domains.

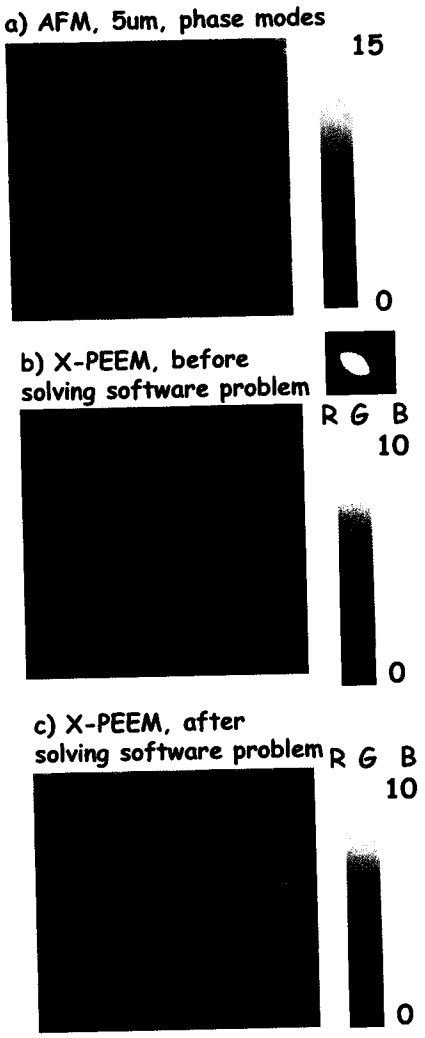

Fig. 3.5 AFM image of albumin covered PS/PMMA surface for the adsorption 0.005 mg/ml albumin from unbuffered water. The AFM image is compared with X-PEEM color-coded maps.

It was found that the apparently strong PMMA preference for albumin adsorption shown in **Fig.3.5 b)** was an artifact of the analysis of the X-PEEM data caused by a change in data file format which lead to the software assigning an incorrect energy scale. After correcting the analysis software to read both pre Dec 03 and post Dec 03 data formats, the X-PEEM map in **Fig.3.5 c)** shows that the continuous PS domains are 'pink rather than red' while the discontinuous PMMA domains are 'green rather than turquoise'. This color map shows that albumin has stronger preference to PS rather than PMMA, which is consistent with the AFM results.

§ 3.3 ^{125}I-labeling Adsorption Isotherm

For this study, I prepared the samples and Rena Cornelius (Chemical Engineering, McMaster) conducted the measurements of radio-labeling adsorption. Since the ^{125}I- labeling technique detects adsorbed proteins

on both sides of a substrate, the PS/PMMA blend polymer was spun coat onto both sides of the Si wafer. Therefore, it is quite possible to introduce some impurity into the polymer blend surface when the side of Si covered with the polymer film was put down on the supporting holder to spin coat on the other side of Si wafer, although the supporting holder for the Si wafer was cleaned with toluene every time and allowed to dry before spin coating.

The adsorption of albumin from phosphate buffered saline (pH 7.2) and unbuffered water solutions was studied at four different concentrations: 0.005, 0.01, 0.05, and 0.1 mg/ml.

Albumin and fibrinogen were labeled with ^{125}I (ICN Biomedicals, Mississauga, Ont., Canada) using the iodogen technique [RH90], a standard protocol for radioiodination of proteins by IODO-GEN® (Pierce Chemical Company, Rockford, IL) [PCC93]. The labeled protein was dialyzed overnight against isotonic Tris buffer to remove unbound radioactive iodide. Trichloroacetic acid precipitation [R84] of aliquots of protein solutions before and after completion of the experiments confirmed that >99% of the ^{125}I remained bound to the protein. The adsorption experiments were carried out in phosphate buffered saline (pH 7.2) or unbuffered water solutions with four repeats for 10 min exposures. For the radiolabeling experiments, the samples were rinsed statically for 2.5 min in a similar volume of buffer or deionized water solution. The radioactivity was counted with each sample placed in a plastic tube on the detector platform. The counts for each sample were averaged and the surface concentration (in mg/m^2) was calculated by **Equation 3.1** [LZZ98].

$$S.C.(mg/m^2) = \frac{counts(c.p.m)}{Sp.Ac.(cpm/mg) \times SA(m^2)} \qquad (3.1)$$

where the *counts* are the radioactivity of the sample; *Sp.Ac.* is the specific activity of the protein solution; and *SA* is the surface area of the sample. The results from four repeated samples give the uncertainty of the adsorption amount at each concentration.

The result from the ^{125}I radio-labeling study of albumin adsorption from PBS solution onto PS, PMMA and the PS/PMMA blend are shown in **Fig. 3.6**. The data are fit to neither the Langmuir adsorption 'isotherm equation' (**Equation 3.2**) [A90] or Freundlich isotherm (**Equation 3.3**) [NL91], the two common models for protein adsorption. The Langmuir equation is

$$\theta = \frac{KC}{1+KC}, \qquad K = \frac{k_a}{k_b} \qquad (3.2)$$

where θ is the fraction of surface coverage; k_a is the rate constant for adsorption and k_d is the rate constant for desorption; K is the equilibrium constant; C is concentration of protein solution. This assumes a dynamic equilibrium not irreversible adsorption. The Freundlich equation is

$$Log\theta = \log K + \frac{1}{n}\log C \qquad (3.3)$$

where θ is the fraction of surface coverage; K and n are empirical constants; C is concentration of protein solution. Instead the data are found to best fit to a logarithm 2nd order function (**Equation 3.4**).

$$\theta = \theta_0 + a\ln C + b(\ln C)^2 \qquad (3.4)$$

where θ is the fraction of surface coverage; θ_0, a, and b are constants; C is concentration of protein solution.

Albumin shows a stronger adsorption on the PS surface than the PMMA surface. The adsorption of albumin on the PS/PMMA blend surface is intermediate to those of PS and PMMA surface. This result is compared to the X-PEEM result for adsorption on PS/PMMA blend surface from the same solutions in **Chapter 8** in order to further understand the albumin adsorption.

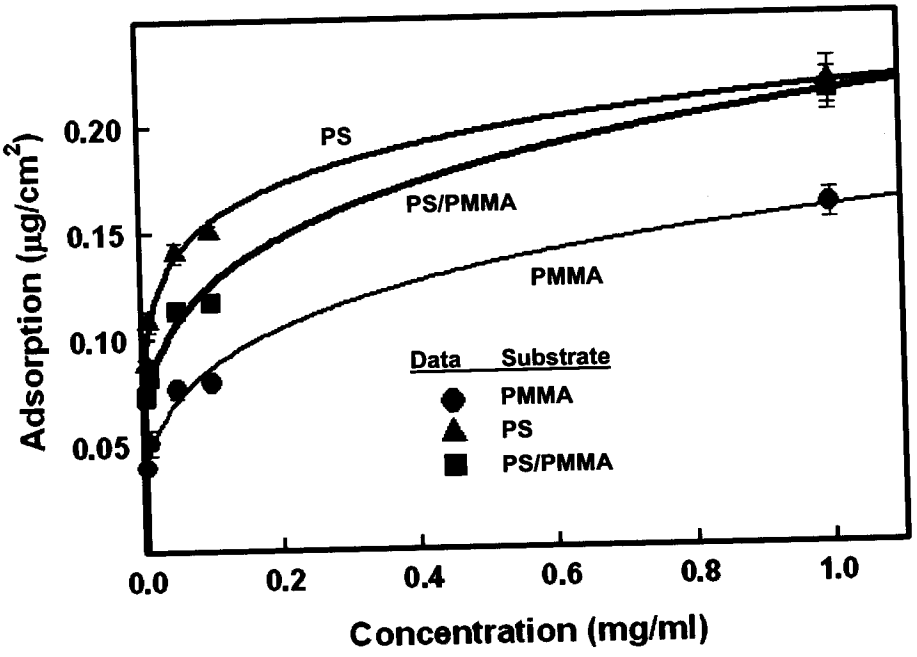

Fig. 3.6 Isotherms for adsorbing albumin onto PS, PMMA and PS/PMMA blend surfaces from PBS solutions, as determined by ^{125}I-labeling. The error bars are the standard deviation of four replicates.

The result for albumin adsorption from unbuffered water solutions is shown in **Fig. 3.7**. The data (points) are also found to best fit to a lonarithm 2nd order function

(**Equation 3.4**). Albumin shows a stronger adsorption onto the PS surface than the PMMA surface. The adsorption of albumin on PS/PMMA blend surface is intermediate to those of PS and PMMA surface.

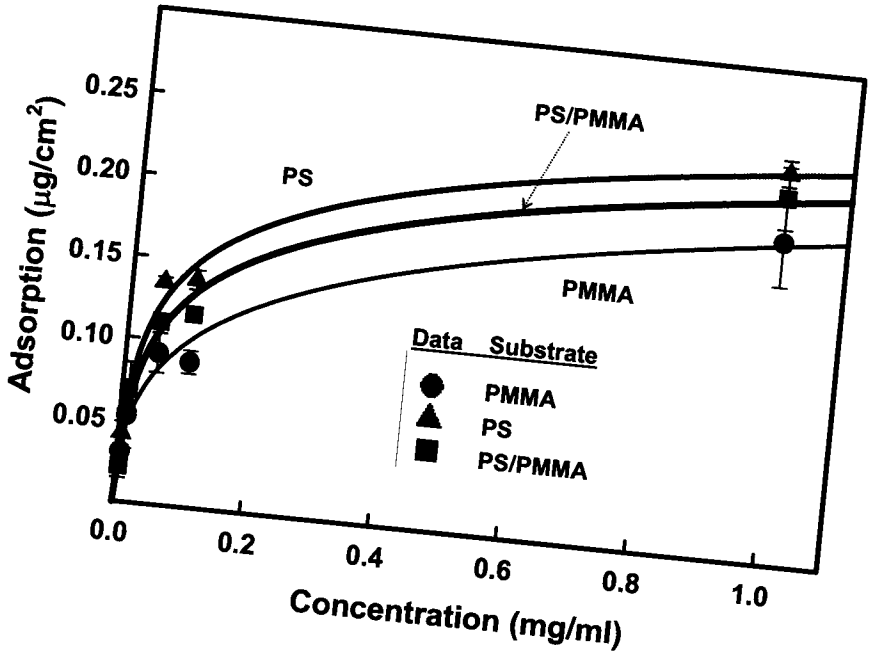

Fig. 3.7 Isotherms for adsorbing albumin onto PS, PMMA and PS/PMMA blend surfaces from de-ionized water solutions, as determined by ^{125}I-labeling. The error bars are the standard deviation of four replicates.

The fitting parameters of albumin adsorptions from PBS buffered and unbuffered de-ionized water solutions are summarized in **Table 3.3**.

Table 3.3 Fitting parameters of albumin adsorptions from PBS buffered and unbuffered de-ionized water solutions (fit to Equation 3.4).

	Substrates	θ_0^*	a^* ($\times 10^{-2}$)	b^* ($\times 10^{-4}$)	Rsqr
PBS	PS	0.22	2.9	11.1	0.99
	PMMA	0.16	3.8	31.4	0.99
	PS/PMMA blend	0.21	4.7	40.7	0.99
Unbuffered	PS	0.24	4.0	4.8	0.99
	PMMA	0.19	4.8	3.4	0.97
	PS/PMMA blend	0.22	4.2	13.2	0.97

*see the explanation about Equation 3.4.

The differences in adsorption of albumin from PBS buffer and unbuffered water solutions are explored in **Fig. 3.8**. At concentrations of 0.05 and 0.1 mg/ml, there is almost no difference in the amount of albumin adsorbed from PBS versus unbuffered water solutions on any of the studied surfaces: PS, PMMA and PS/PMMA surfaces. At concentrations of 0.005 and 0.01 mg/ml, albumin shows different amounts on PS and PS/PMMA blend surfaces when adsorbed from PBS versus unbuffered water solutions. The difference is most likely due to the change in ionic strength from PBS to unbuffered solutions. However the albumin shows similar adsorption at higher concentration when adsorbed from PBS and unbuffered solutions. This may suggest that electrostatic issues controlled by ionic strength are less important than other factors, such as relative hydrophobic or hydrophilic character, in controlling albumin adsorption on a PS/PMMA blend.

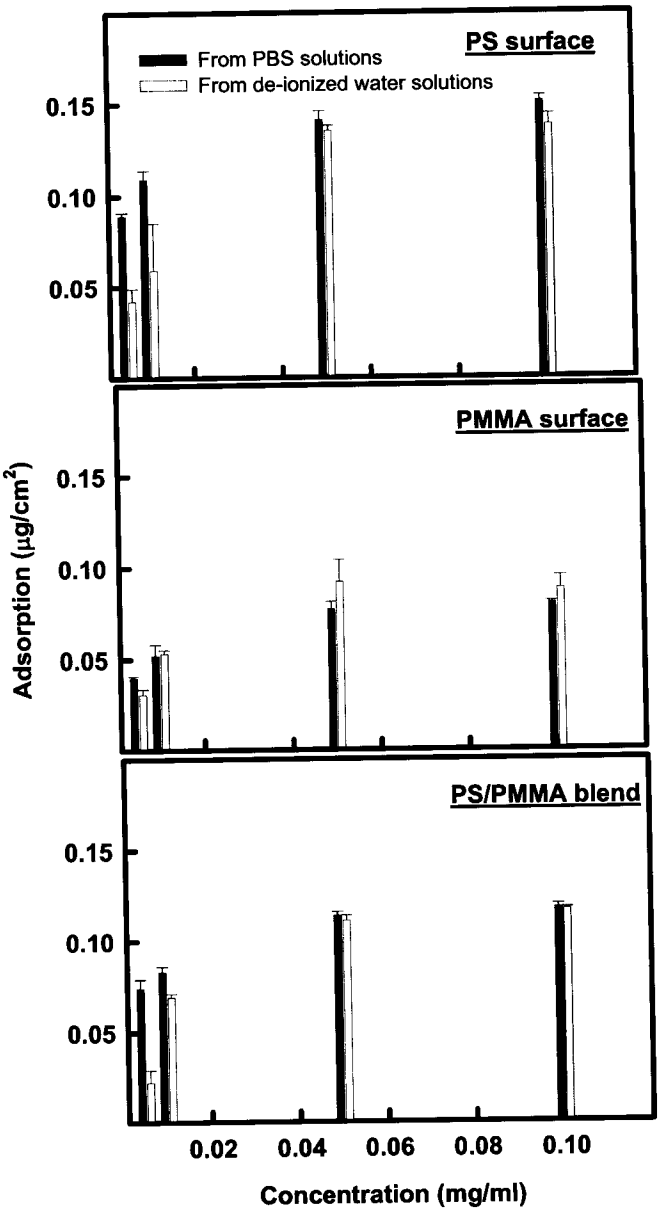

Fig. 3.8 Comparison of ^{125}I-labeling adsorption isotherm of albumin onto PS, PMMA and PS/PMMA blend surfaces from PBS and de-ionized water solutions. The error bars are the standard deviation of four replicates.

In most of our study of albumin adsorption, we used unbuffered solutions since albumin is hard to denature, unless it is heated above 70°C and under strong alkaline conditions [P95]. The unbuffered solutions can prevent the spectroscopically interference of the chemicals used for buffer. For the study of fibrinogen adsorption, a PBS buffer was used since fibrinogen is much easier to denature under unbuffered solution, extreme pH, high temperature, and etc. However we did not check whether the adsorbed proteins are denatured or not in our study, which can be done by testing the biological activity of the absorbed proteins.

Chapter 4
Data acquisition and analysis in X-PEEM and STXM

This chapter describes how I performed X-PEEM and STXM measurements of protein covered PS/PMMA surfaces. The data analysis methods are also described and evaluated.

§ 4.1 Data Acquisition in PEEM

There are three modes of data acquisition in PEEM: single energy images, spectra and stacks. Since PEEM is a parallel detection instrument, all modes of acquisition are similar and the main difference is what data are saved, and whether a single energy or a whole spectrum is scanned [M04].

§ 4.1.1 Images

When the components of a system have unique adsorption peaks, images acquired at the energies of each peak can locate each component. For example, the C1s $\rightarrow \pi^*$ transitions of PS and PMMA are 285.15 eV and 288.45 eV respectively. Images at these two photon energies can be used to visualize each species in a phase-segregated blend of PS/PMMA, as shown in **Fig. 4.1 a)** and **b)**. In contrast, there are many photon energies at which images show little or no chemical contrast (**Fig. 4.1 c)**). The patterned images are helpful to optimize the X-PEEM microscope, especially for optimization of spatial resolution and focusing.

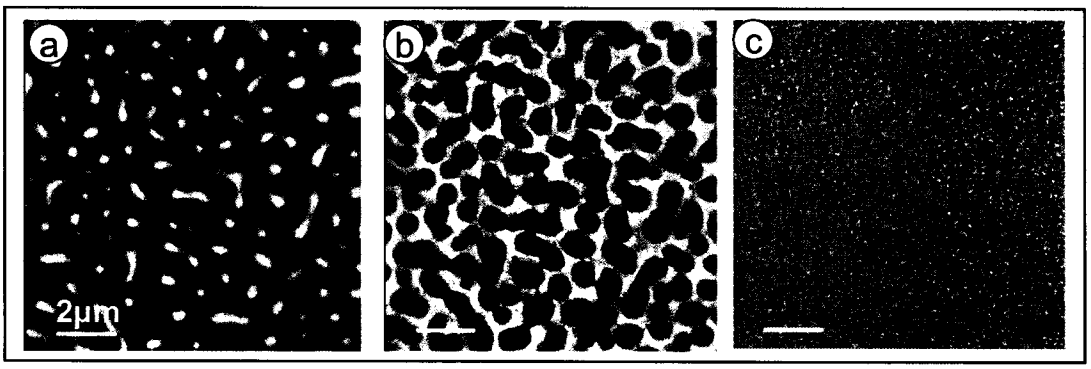

Fig. 4.1 X-PEEM images of a PS/PMMA blend imaged at 285.1 eV (a), 288.5 eV (b), and 296 eV (c).

The image can be recorded over the full field of view (FOV), or a smaller region by drawing a box onto a full image to select an area-of-interest (AOI). The physical size of the image depends on the magnification which is determined by the objective, intermediate and projector voltages. As discussed by Cynthia Morin [M04], there are two ways to identify the size of an image. The first one (used in this work) is to physically measure the FOV using a micrometer to measure the sample displacement as one feature of the sample is moved from one side to the other side of the image. The second method is from the voltages of the microscope, and a calibration table (see [M04] for details).

§ 4.1.2 Spectra

An X-PEEM spectrum is the detected photoemitted electron yield from a user defined area as a function of incident photon energy. Since there are no entrance and exit slits, the X-PEEM energy scale varies from day to day. Thus it is important to measure a spectrum even if the system examined is well known.

Radiation damage is a big issue for X-PEEM studies of soft materials such as polymers and proteins. Two major factors from radiation damage can affect these measurements. First, a chemical bond can be rearranged resulting in changes in NEXAFS spectra which can give errors in the analysis Second, mass loss can occur (eg loss of CO_2 from PMMA). This gives spectral changes as well. Ideally analytical measurements should be made with the least possible radiation damage. A series of spectra measured from the same location have been used to quantify radiation damage [WML&06], which then was used to guide the selection of data acquisition parameters such as number of points and dwell time.

In order to have the correct spectrum, it is necessary to normalize to the spectrum of the incident photon beam (I_0) recorded under the same experimental conditions and to correct for artifacts of the detection (bolometry, intrinsic absorption of the reference surface). In this work, I_0 spectra were recorded from an HF-etched Si wafer substrate.

§ 4.1.3 Stacks

Stacks (image sequences) [JWZ98] are a sequence of images recorded as a function of photon energy. Typically, for radiation sensitive polymer samples, the number of energy steps needs to be small to minimize damage but still sufficient to follow sharp spectral features. If two components of a system have very close spectral features, small energy steps (0.1 eV is the minimum because of the limited energy resolution of the beamline) are needed in the regions of such features in order to be sensitive to the signals of the two components. For regions without sharp features, a coarse energy step (0.5-1.0 eV) can be used. Different energy steps are used for different

energy ranges in order to reduce radiation dose. In general, one needs to optimize both dwell time for adequate statistics and energy steps for adequate spectral definition.

§ 4.2 PEEM Measurements of Protein Covered PS/PMMA Blend Surfaces

Albumin adsorption onto a PS/PMMA blend surface was performed under different conditions: concentration, exposure time, pH, temperature, and PBS buffer vs. deionized water. In addition, the adsorption of albumin and fibrinogen from PBS buffer solutions was compared at different concentrations.

The major challenge of X-PEEM measurements for this system is radiation damage. Of the three components, PMMA is most sensitive to radiation damage [WLM&06]. Radiation damage of PMMA causes the $\pi^*_{C=O}$ peak become weaker and broader and produces a new peak at 285.1 eV associated with $\pi^*_{C=C}$. Excessive damage makes it difficult to differentiate PMMA, PS and proteins due to the similarity of their spectra. The PS, PMMA and albumin spectra are compared in **Fig. 4.2 a)** while a series of PMMA spectra in a time sequence are plotted in **Fig. 4.2 b)** to show the radiation damage effects on the spectral shape of PMMA. Several strategies were used to reduce radiation damage.

A fast shutter was installed by ALS staff to reduce radiation exposure. The shutter blocks the light between each data point and thus reduces exposure. Typically it takes one second to transfer an image from the CCD camera to the computer and one second to change photon energies. While there is some temporal overlap of these steps, when one uses a typical one second image accumulation time at each photon energy, the

actual elapsed time is about 2.5 seconds. Thus the point-by-point shuttering (which was only implemented in late 2004), reduces exposure by more than 50% for the same 1s/point measurement protocol.

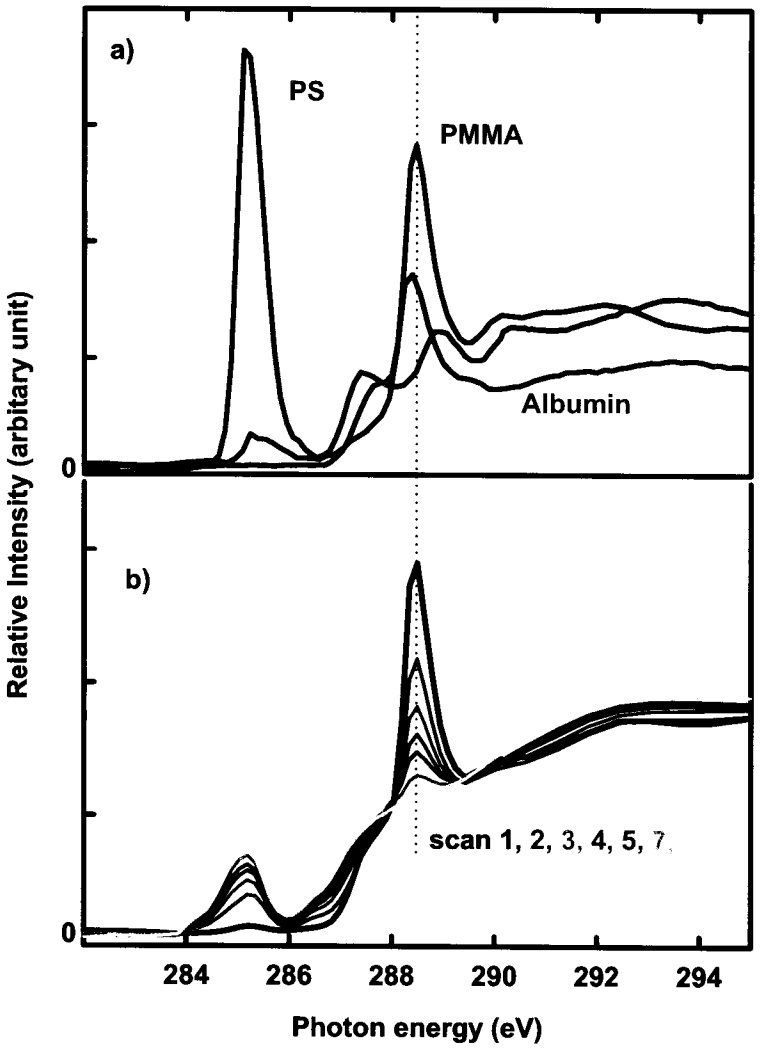

Fig. 4.2 a) Spectra of PS, PMMA and albumin recorded from pure material using STXM. b) PMMA spectra in a sequence of continuous scanning measured using X-PEEM. Different colors are used for the spectra recorded in different scanning sequences as indicated by the inserted scan numbers in corresponding colors.

Two devices located upstream of the grating called 'mask' and chopper' (See **Section 2.2.1** for details) are used to reduce the incident flux and hence radiation damage. The degree of flux reduction can be controlled by different mask or chopper settings. The reduction should not be too excessive since this reduces grating illumination which eventually loses spectral resolution. The mask/chopper settings were optimized to minimize dose without losing spectral resolution. The mask is fixed while the chopper varies. As shown in **Fig. 4.3a**, the I_0 signal responds linearly until the beam is fully blocked. The effect of flux reduction was evaluated by recording the C1s spectrum of PMMA (**Fig. 4.3b**). Based on this exploration, an optimized mask (-15.0) and chopper (17.5) setting were determined.

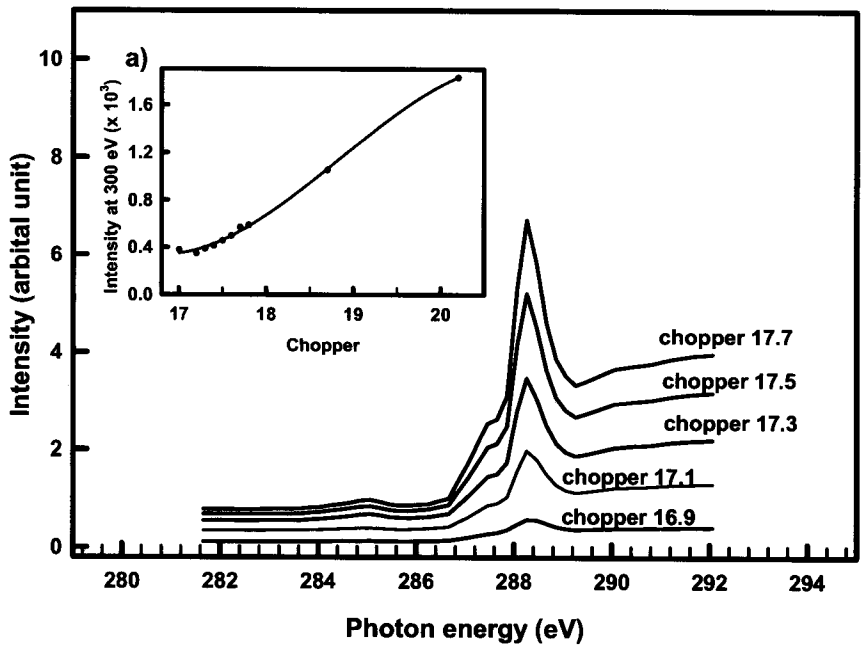

Fig. 4.3 a) Io signal as a function of chopper at a fixed mask; b) the effects of chopper setting on the spectral resolution of PMMA.

In order to minimize dose, short stacks (282-292 eV, ~35 points) rather than long stacks (282-320 eV, ~75 points) were used for most studies.

§ 4.3. Principle of Data Acquisition in STXM

The modes of data acquisition in STXM are similar to those in X-PEEM. The difference is that STXM is a serial (point-by-point) scanning technique so the different modes require different sample scanning procedures. The modes of data acquisition in STXM which I used are: images (single energy) and spectra (point spectrum, line scan, and image sequence).

§ 4.3.1 Single Energy Images

For the acquisition of single energy images, one needs to define the photon energy, the *x, y* dimensions of the image, the spacing in each dimension and the dwell time at each pixel. The size of an image can be defined by either drawing a box or typing the *x, y* scales. For a large size image (>120 μm on STXM 5.3.2, >60 μm on STXM 11.0.2), the coarse stepper motor is used to scan the sample, while for small size images, a piezo stage is used. The piezo stage has a higher scan speed and greater precision but has a restricted scan range.

Fig. 4.4 shows examples of STXM images of a PS/PMMA blend. The images were recorded at the characteristic energies of PS (285.15 eV) and PMMA (288.45 eV). The as-recoded images have opposite contrast to those acquired in X-PEEM (see **Fig. 4.1**). STXM detects transmitted light and more absorption means less transmission.

However when the STXM images are converted to an OD scale, the contrast of STXM and X-PEEM images is the same.

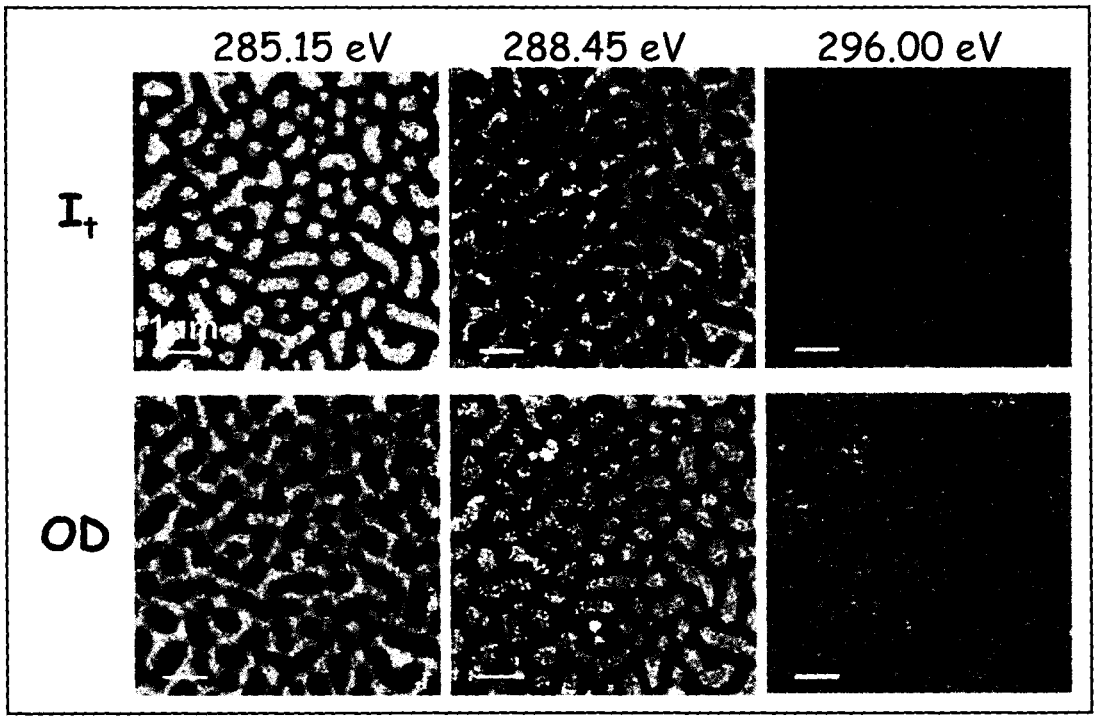

Fig. 4.4 STXM images of a PS/PMMA blend at three energies: 285.15 eV, 288.45 eV and 296 eV in transmitted mode (top row) and OD mode (bottom row) (123 ×104 pixel, 2ms dwell time).

§ 4.3.2 Point Spectra

Once a feature of interest is detected in a STXM image, it is possible to acquire a spectrum from a spot that is approximately the size of the focused beam [M04]. Different from X-PEEM, the STXM control software can acquire the spectra of up to 10 points 'simultaneously', i.e., the sample is moved from one point to the next, acquiring the signal at each point, before the monochromator moves to the next photon energy [M04].

One of the advantages of this multi-point mode is the "simultaneous" acquisition of I_0 spectra. It is important to have I_0 recorded under the same conditions since the incident photon flux has a strong spectral structure and its intensity decreases with the ring current decay. The I_0 is the signal from a region which does not contain the sample, but should contain any supporting substrate such as the Si_3N_4 window used in this work.

§ 4.3.3 Stacks (Image Sequences)

A STXM stack (image sequences) in STXM is a sequence of images recorded over a set of photon energies. An example of is shown in **Figure 4.5**. The top is a few images at the photon energies indicated by the dash lines, and the bottom is the spectrum from the white round dot as shown in the images.

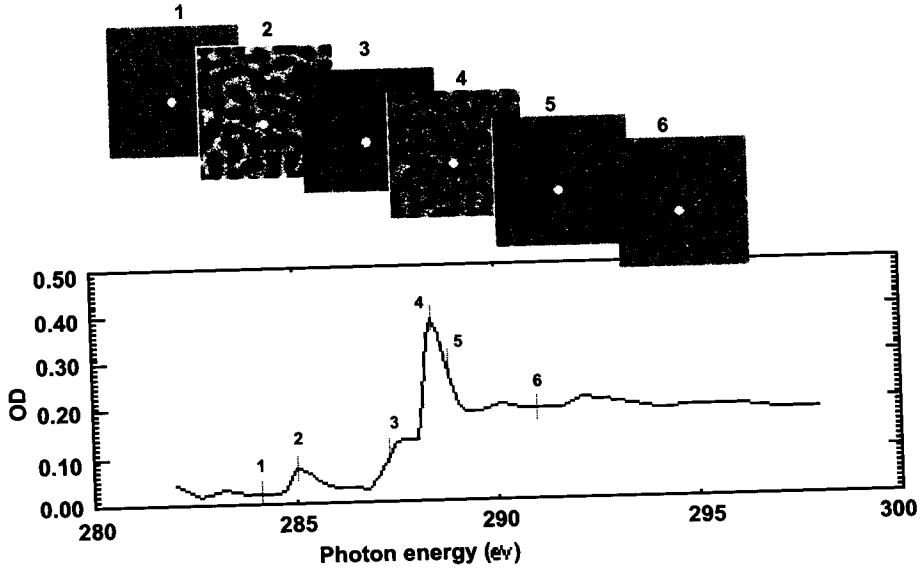

Fig. 4.5 (Top) A few images at the photon energies as indicated by the dash lines on the bottom spectrum, (bottom) the spectrum from the white round dot as shown in the top images. The sample is a PS/PMMA blend.

§ 4.4 STXM Measurements of Protein Covered PS/PMMA Blend Surfaces

The challenges of radiation damage in STXM are similar, but perhaps less severe than in X-PEEM. The photon flux is controlled by slits in STXM532 rather than mask and chopper in X-PEEM. The slits used for this work were typically 75\35\35 (microns) (entrance\horizontal exit\vertical exit). This setup gives adequate spectral resolution and flux for this study. Typically STXM is less surface sensitive than X-PEEM and thus it is important to have a thin polymer substrate in order to improve the ratio of protein to polymer signals. Typically organic samples (density ~ 1 g/ml) are 80 ~ 150 nm thick for OD_{max} = 2.0. For this work we used a thin polymer sample < 50 nm (OD_{max} ~ 0.3) to increase the contrast of protein signals relative to the PS/PMMA film. Minimum thickness used for STXM can be as small as 5 – 10 nm but this could cause problem of bad statistics due to low OD (OD_{max} < 0.1) (See **Table 2.1** for more details of STXM methodology). The advantage of STXM is that it can detect protein adsorption with the sample covered by a thin layer (1~2 μm) of water or aqueous solution. This advantage is what this work focuses on. As in X-PEEM, stack measurements are the best way to map protein distributions on polymer surfaces. Similar stack acquisition strategies as in X-PEEM were used. The challenge of STXM measurements is the sample preparation, which has been discussed in **Chapter 3**.

§ 4.5 Procedure of Spectromicroscopy Data Analysis

The stack analysis procedures in X-PEEM and STXM both follow the general scheme depicted in **Fig. 4.6**. The procedures for X-PEEM and STXM are slightly different due to the differences in the two techniques. If one of the analysis steps shown

in **Fig. 4.6** is not necessary for one technique, a "NO" is indicated, otherwise, a "YES" is indicated. For each stack, thirteen steps need to be considered in order to obtain a quantitative result.

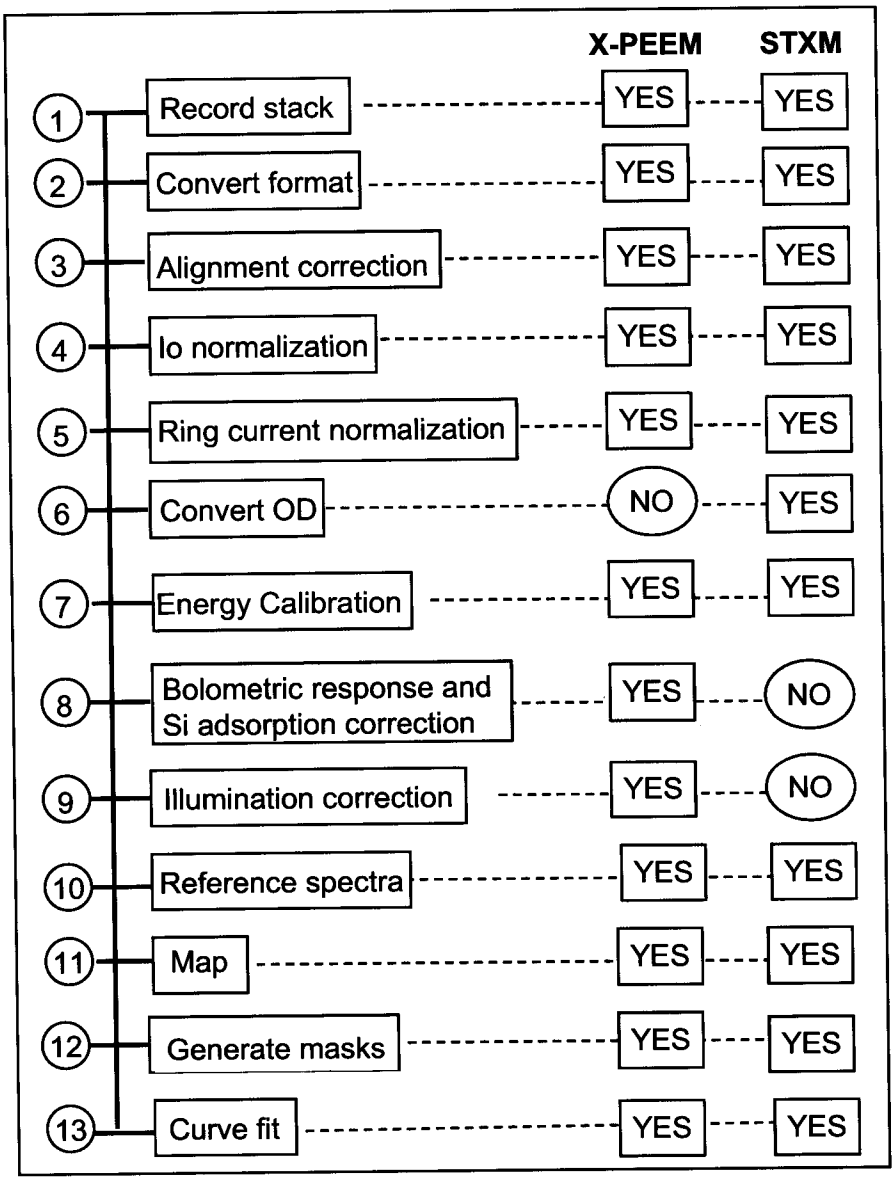

Fig. 4.6 Scheme of the steps used to analyze an image sequence in STXM and PEEM.

STEP 1 is the acquisition of a stack. A sequence of images is recorded and saved individually, together with a header file (STXM) or an energy scanning file (X-PEEM). In **STEP 2**, multiple images are converted to a single file.

STEP 3: Aligning the images of a stack ensures every spatial feature maintains the same *x, y* coordinates at all energies. This step is only necessary for a stack with misalignment issues that can arise from vibration and other factors in X-PEEM. An example of the alignment issue is shown in **Fig. 4.7**, which shows images from a C1s stack at 285.15 eV and 288.45 eV with a red circle centered on a PMMA domain (light) at 288.45 eV. The pixel identification should be in centered of the same PMMA domain (dark) at 285.1 eV but instead is found at the edge of the dark PMMA domain due to misalignment. The spectra from the red-spot region before alignment and after alignment are compared in **Fig. 4.7**. Before alignment the intensity at 285.1 eV is higher since the red region drifts around with scanning energy and thus the spectrum contains PS signals from part of PS domains around the red PMMA domain. This alignment issue can be resolved in two ways: automatically by the zstack_align routine in aXis2000 software or 'manually' using other routines in aXis2000 involving user identification of fiducials in each image. The automatic method uses an image cross correlation technique implemented with 2-D Fourier transforms to identify shifts between successive images. The manual method uses one or more fiducials (easily identified features present in each image) which are manually selected on each image. All images of the stack are then aligned relative to the fiducials. Both methods, with many options, are implemented in aXis2000 [aX00].

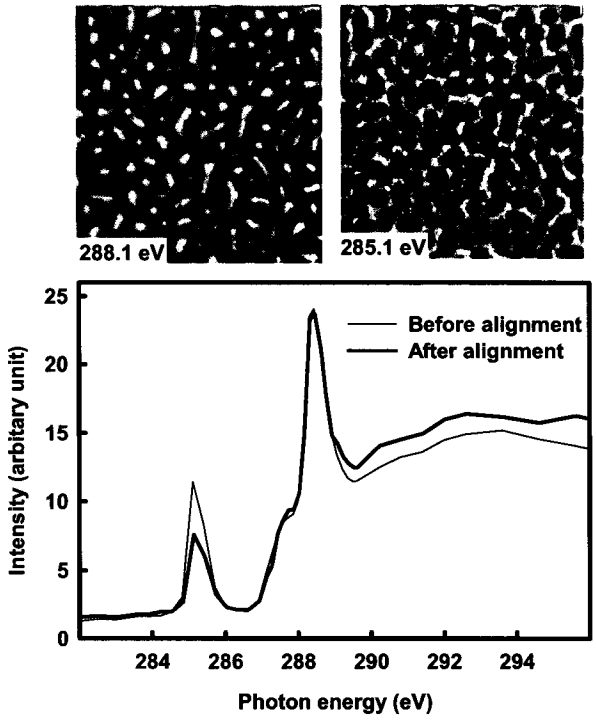

Fig. 4.7 Misalignment of the C1 stack of the 0.01 mg/ml albumin covered PS/PMMA.

The alignment can equally be performed anytime before **STEP 10**. It is recommended to perform alignment in **STEP 3** since if one has any problems with any procedures between **STEP 2** and **STEP 10**, one can repeat such steps starting from an aligned stack. Alignment needs lots of careful work particularly in this system where the PS/PMMA pattern is only clear at a few energies near 285.15 and 288.45 eV.

In X-PEEM, image movement is caused by charging; when the electrons are released from the surface, their trajectories are altered and the whole image "moves" [M04]. For the data presented in this thesis, there were only 2~3 stacks that have such

alignment issues. In STXM, misalignment issue is caused by a misalignment of the sample and zone plate as the zone plate moves in *z*.

STEP 4 consists of normalization of the stack to the photon flux (I_0). The I_0 normalization corrects for structure in the incident photon flux and ideally gives intensities which are proportional to sample composition (although there are additional factors in X-PEEM). For X-PEEM, there are two methods used to acquire an I_0, the internal I_0 method and external I_0 method. The internal I_0 measurement uses the signal at a scratch which exposes the underlying Si wafer. However, it is hard to make a clean scratch on a polymer-covered Si wafer without a build up of any polymer. The signal from residual polymers will contribute to the I_0 and cause spectral distortions. Although one may think to remove such signals by subtraction it is hard to do such subtraction due to the unknown strength of such signals. The external I_0 measurement is more reliable although it is more complicated and slower. The external I_0 measurement is done on a HF-etched SiOx wafer. **Fig. 4.8** compares the internal I_0 (obtained from a square region on the scratch shown in a)) and external I_0 (b), and the spectra (from a round region of a)) normalized to the internal and external I_0 (c). An external I_0 measurement was performed for each beamtime (2-3 days) to account for the instability of the energy scale of X-PEEM and the I_0 signal. For the work presented in this thesis all X-PEEM stacks were normalized to an external I_0.

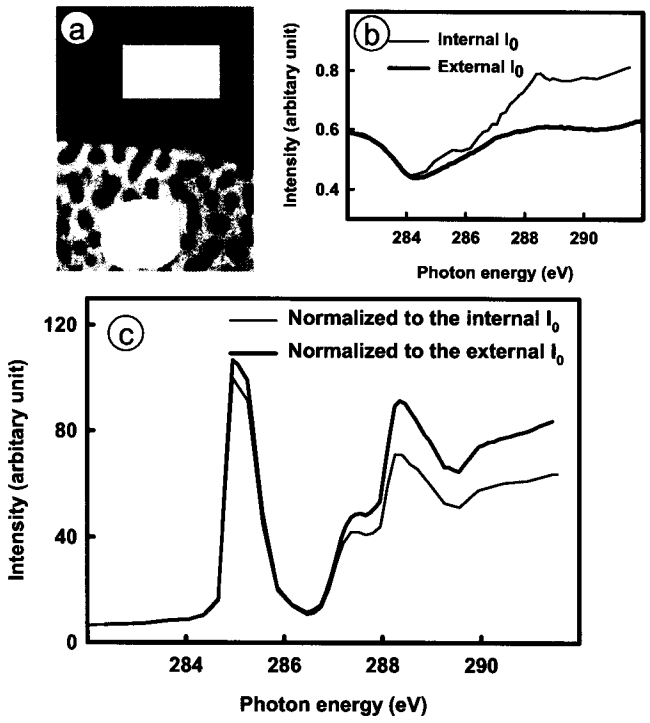

Fig. 4.8 a) Image at 295.15 eV of a stack. b) comparison of external I_0 and internal I_0 obtained from the square area of a) on a scratch; c) comparison of the spectra [from the round region of a)] normalized to external and internal I_0.

For STXM, one can also use either an internal I_0 or an external I_0. The internal I_0 is usually acquired by recording a 2-region stack with one region being an area off the polymer section. The latter works only if part of the Si_3N_4 window is not covered by a polymer film or other composites and those bare areas are within 10 μm of the area of interest. However, this method is not practical when the I_0 region is far away (> 10 μm) from the area of interest defined for the stack. In other cases, where the Si_3N_4 window is completely covered by a polymer film, the I_0 must be acquired at least either before or after the stack on a bare Si_3N_4 window loaded on the same sample holder.

STEP 5: Correction for the ring current decay which occurred during the acquisition of a stack. The ring current in 2-bunch mode decays much faster than multi-bunch mode (**Fig. 4.9**) and thus this correction is very important in analysis of 2-bunch mode data.

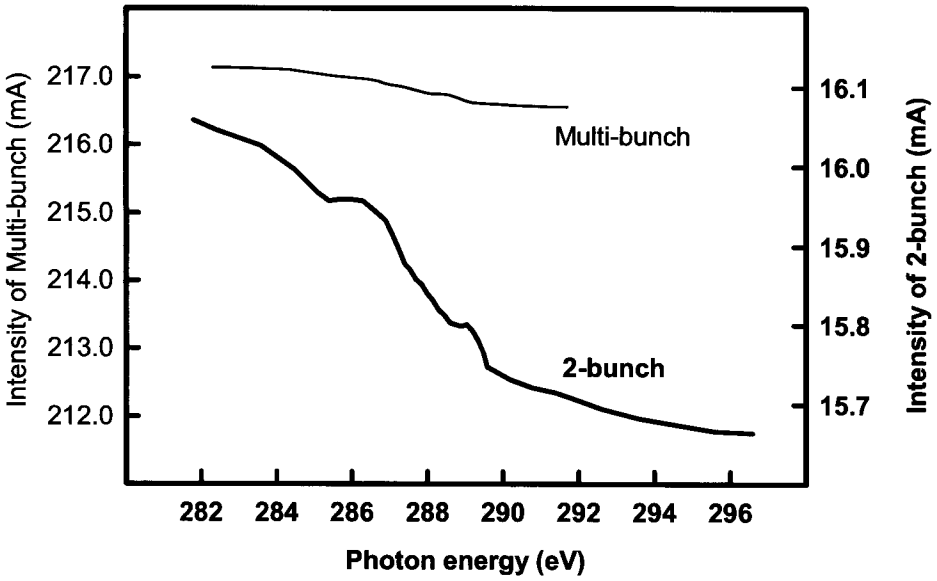

Fig. 4.9 Ring current of 2-bunch and multi-bunch of X-PEEM [Note different Y-axis scales are used for multi-bunch (left) and 2-bunch (right)].

STEP 6: Conversion of the raw data into a linear absorption optical density (OD) scale. STXM detects transmitted light and it is necessary to convert the raw data to a OD scale using the I_0 and Beers law [$OD=A=-\ln (I/I_0)$]. X-PEEM is a form of total electron yield detection which does not require this conversion.

STEP 7: Calibration of energy scale. This step is crucial for the data analysis in this study due to the similarity of the C1s excitation spectra of PMMA and proteins. The ALS X-PEEM bending magnet beamline (7.3.1) does not have entrance or exit slits and

thus the energy scale depends on the position of the electron beam in the storage ring (stable to ~1-2 μm in one fill but can change from fill to fill). It also can be affected by the mechanical stability of beamline optics and the position of the exit slit. The ALS STXM bending magnet beamline (5.3.2) has a much more stable energy scale but it is still possible to have small energy shifts up to ~0.2 eV. The energy calibration is done using the C 1s(C=C) $\rightarrow \pi^*_{C=C}$ transition at 285.15 eV of PS as a standard. The corresponding PS peak from the stack is aligned to the centre of the peak of the model spectrum of PS.

STEP 8: Corrections for bolometric response and Si adsorption. This step is only applied to X-PEEM data. The I_0 of X-PEEM is obtained from an HF-etched piece of Si. The Io signal (or an X-PEEM stack) is divided by the intrinsic X-ray absorption of Si for correction of spectral shape. The bolometric correction is to normalize to a linear energy term to account for the bolometric response function of detection of X-PEEM [S92]. This step should be applied to a stack after energy calibration since the functions used for the corrections are in the right energy scale.

STEP 9: Correction for non-uniform illumination in X-PEEM which arises because the spot on the sample is not uniform. The illumination correction is done by dividing a heavily smoothed (×99) version of the average image from the stack after setting the mean of that illumination map to one (See **Fig. 4.10**).

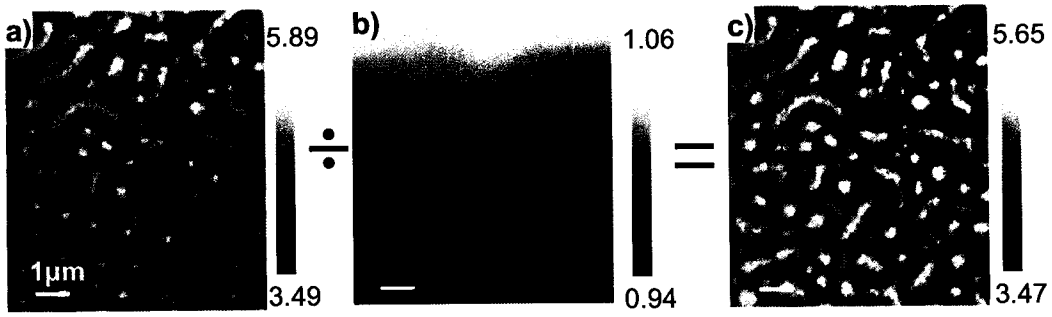

Fig. 4.10 a) Stack average image before the illumination correction; b) image used for the illumination correction; c) stack average image after the illumination correction.

After all corrections mentioned above, the data is properly conditioned for generation of chemical component maps. In order to do this reference spectra are needed. Preparation of reference spectra should be done before one starts data analysis but it is numbered as **STEP 10** since it is only needed for chemical mapping (STEP 11). **Fig. 4.11** shows the reference spectra used in this work. The spectra of PS, PMMA, albumin and fibrinogen were recorded using STXM on free standing thin films (PS, PMMA) or as a solvent cast deposit on a silicon nitride window (albumin and fibrinogen). The spectra were set to an absolute linear absorption scale by scaling to match the elemental response of one nm at bulk densities (ρ_{PS} = 1.05, ρ_{PMMA} = 1.18, $\rho_{albumin}$ = 1.0, $\rho_{fibrinogen}$=1.2 [BIG99]), computed from standard tables of elemental X-ray absorption ([HLT&82], [HGD93]). The computed elemental responses are plotted in the dark-grey lines. The optical linear absorption spectra were the reference spectra used in fitting a stack of protein covered PS/PMMA. Although the energy resolution of STXM (~0.2 eV) is better than X-PEEM (~0.6 eV), the sharpest features in the X-PEEM spectra of the samples studied in this work have the same width as their counterparts in the STXM reference

spectra due to the natural breadth of the peaks. Furthermore, as discussed above, the recorded X-PEEM stack was normalized to the intrinsic X-ray absorption of Si [HGD93] and also to a linear energy term to account for the bolometric response function of X-PEEM detection [S92]. Such normalizations correct for the systematic distortions in X-PEEM lineshape compared to STXM lineshape. For these reasons it is reasonable to use the STXM reference spectra for the analysis of the X-PEEM measurements.

Fig. 4.11 (left) presents the optical linear absorption spectra of pure PS, PMMA, albumin and fibrinogen thin films in the C 1s region. All three materials exhibit distinct C 1s spectra. The PS spectrum is dominated by the strong C 1s(C=C) $\rightarrow \pi^*_{C=C}$ transition at 285.1 eV. The albumin and PMMA spectra are each dominated by strong C 1s(C=O) $\rightarrow \pi^*_{C=O}$ transitions. However the $\pi^*_{C=O}$ peak in albumin occurs at 288.20(6) eV, 0.25(8) eV below the $\pi^*_{C=O}$ peak in PMMA which occurs at 288.45(6) eV. The 0.25 eV energy shift is mainly associated with the change in energy of the C 1s level since the carbonyl carbon is in a less electronegative environment in the amide (R-CONH) than in the ester (R-COOMe). This shift is small but clear and has been documented previously [MHC&04]. It forms the basis for chemical differentiation of albumin (and other proteins) from PMMA (and other esters). In addition, the shape of the low energy side of the $\pi^*_{C=O}$ peak is different in the two species. These differences assist differentiation of PMMA and proteins.

Fig. 4.11 (middle) presents the optical linear absorption spectra of pure PS, PMMA, albumin and fibrinogen thin films in the N 1s regions. The N 1s signal is a good indicator of the amount of protein present in a protein covered PS/PMMA surface since

protein is the only species with a N 1s spectrum, with a characteristic N 1s $\rightarrow \pi^*_{CONH}$ transition at 401.2 eV. However the N 1s signal is much weaker than the C 1s signal, and thus the N1s edge is less sensitive than the C1s edge for quantitative measurements. In addition, the N 1s signals do not give a specific measure of the PS and PMMA components of the substrate, although the morphology is readily visible due to the differences in elemental composition of PS and PMMA.

Fig. 4.11 (right) presents the optical linear absorption spectra of pure PS, PMMA, albumin and fibrinogen thin films in the O 1s regions. At the O 1s edge, PMMA and Fg each are dominated by O 1s $\rightarrow \pi^*_{C=O}$ transitions at 531.6 eV, but PMMA has an extra transition at 535.5 eV arising from O 1s (O–CH3) $\rightarrow \pi^*_{C=O}$ transitions, specific to esters.

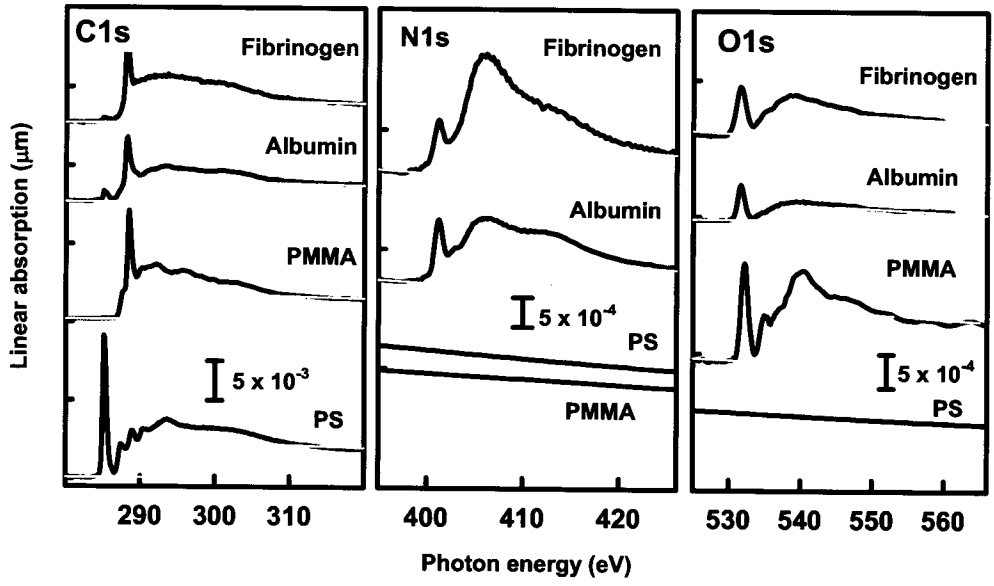

Fig. 4.11 C 1s, N 1s and O 1s of X-ray absorption spectra of PS, PMMA, albumin and fibrinogen recorded from pure materials. The spectra are plotted on an absolute linear absorption scale (with offsets). The grey lines indicate the elemental response [HGD93].

STEP 11 uses the prepared stack and reference spectra to generate quantitative chemical component maps. The reference spectra are used in fitting a stack at either the C1s, N1s or O1s edge to derive component maps. There are three types of mapping available in aXis2000: "SF (stack-fit)", "SVD" (singular value decomposition) ([AZC&92], [ZBM&96], [KHM&02]) and "CGO" (conjugate gradient optimization) [LP01]. All three compute a least squares fit of the intensity at each pixel - $S(j,k)$ - to a linear combination of reference spectra for each component (S_i, each on a quantitative linear absorption scale).

$$S(j,k) = a_0(j,k) + \Sigma_i\, a_i(j,k) * S_i \qquad (4.1)$$

In the SF approach, an energy independent term, (a_o), is included, which accounts for energy independent offsets (backgrounds) in the reference or the image sequence spectra. In the SVD and CGO approach, there is no a_o term. Both SF and SVD use the singular value decomposition routine in IDL. In the CGO approach, a non-matrix algorithm is implemented on a pixel-by-pixel, iterative curve fit basis, using a novel method to control convergence.

For STXM data, the fit coefficient, a_i, is the equivalent thickness in nm of the i^{th} component at the (j,k) pixel since the reference spectra are set to the elemental response for 1 nm thickness. For X-PEEM data, the fit coefficient is a relative contribution of each component to the detected photoemitted yield. The thickness of each component is not obtained directly from X-PEEM measurements. However the thickness can be obtained by normalizing the sum of the component map to the sampling depth which was

estimated from measurements of a series of PS films with different thickness. See **Section 4.6.1** for details.

As an example, the result of a SF analysis of the C1s stack of 0.005 mg/ml albumin (unbuffered water solution, pH7.3, adsorption for 20 min at room temperature) covered PS/PMMA is shown in **Fig.4.13**. The SF generates the maps for each component (PS, PMMA, and albumin), a constant map and a map of residual fit (or chi-square map, the least squares measure of the mis-match between the actual spectrum and the fit at each pixel). The sum map is obtained by adding the maps of all components. The histograms of the thicknesses for each component and the sum are derived from corresponding maps. The gray scale limits are the minimum and maximum thickness. Lighter intensities indicate locations where there is more of that component. The color-coded map, which reveals the spatial correlation of the chemical components, is also presented in **Fig. 4.12**. This is obtained by combining the component maps of PS, PMMA and albumin, with the PS signal in red, the PMMA signal in green, and the albumin signal in blue.

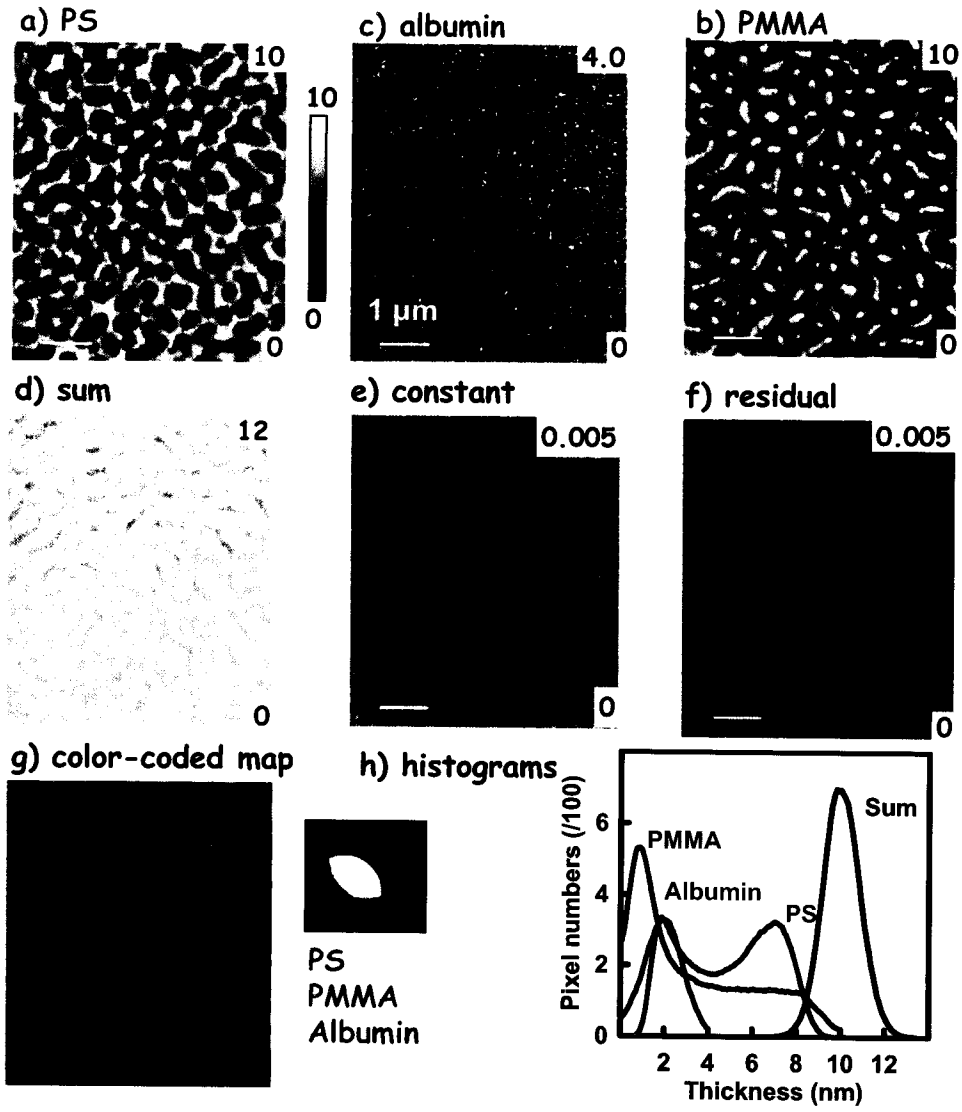

Fig. 4.12 SF of the C1s stack of 0.005mg/ml albumin (unbuffered water solution, pH7.3, adsorption for 20 min at room temperature) covered PS/PMMA. a) PS component map; b) PMMA component map; c) albumin component map; d) sum of each component maps; e) constant map; f) chi-square map; g) color-coded map (red is PS, green is PMMA and blue is albumin; the color combination beside the map shows the color changes with albumin adsorption on the red PS/green PMMA domains; h)histograms of the PS, PMMA, albumin and sum of all components.

For C 1s stacks, the component maps derived from the three approaches are very similar, and the color-coded map is also the same. The maps from SVD and CGO are not shown here since they look the same as those from SF. If interested, please see [M04].

STEP 12: Isolation of spectra from chemical similar areas using threshold masking of component maps. In order to get quantitative results for the amounts (thickness) of each component in a specific region, i.e., PS, PMMA, and the PS/PMMA interface regions, masks defining the spatial location of each region are generated by using threshold masking of the component maps to select only those pixels where the signal was above a defined threshold. The masks of PS and PMMA are shown with the white highlighted regions in a) and b) in **Fig. 4.13** respectively. The interface mask is a ~80 nm wide band at the PS-PMMA interface, as shown in the white highlighted region in c) of **Fig. 4.13**, obtained by selecting those pixels not present in either the masked PS or masked PMMA maps. The three different regions: PS, PMMA and the PS/PMMA interfaces are coded into a single image in d) of **Fig. 4.14** in different colors (red is PS, green is PMMA and blue is the interfaces).

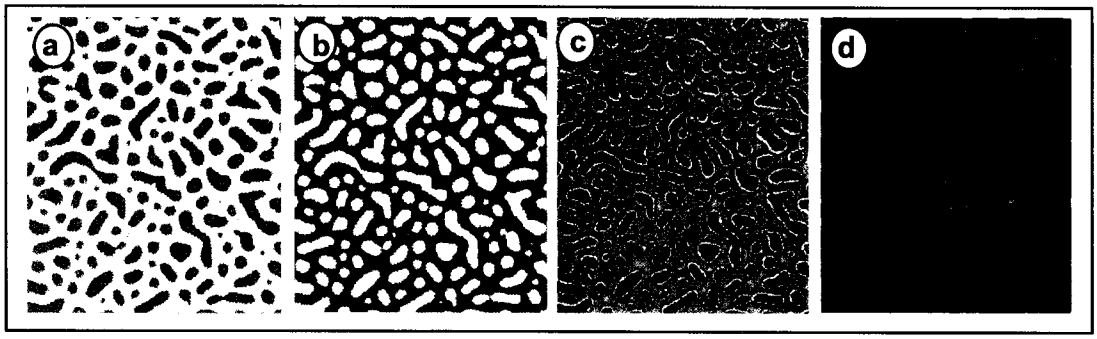

Fig. 4.13 The mask of PS (a), PMMA (b), the PS/PMMA interface (c), and the color-coded map of the three different regions: red is PS, green is PMMA and blue is the interfaces

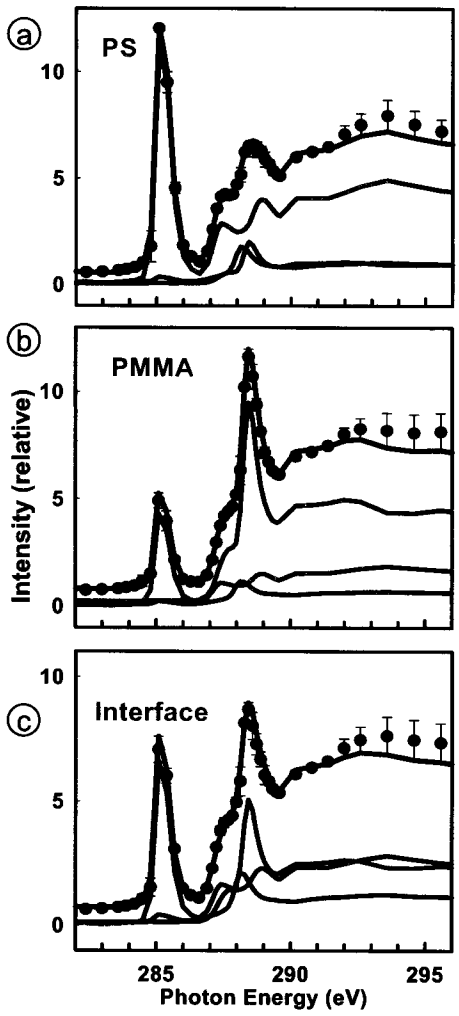

Fig. 4.14 Linear regression curve fit of the masked spectra of PS (a), PMMA(b), and PS/PMMA interface (c) from the C1s stack of 0.005mg/ml albumin covered PS/PMMA: data - points, fit - thick solid line, components – thin lines in color (red for PS, green for PMMA and blue for albumin).

STEP 13: Curve fitting of spectra extracted from masked regions to reference spectra. There are two approaches for fitting: linear regression (which includes the a_o constant) and CGO. **Fig. 4.14** shows the linear regression fitting of the masked spectra from the C1s stack of 0.005mg/ml albumin covered PS/PMMA. The curve fitting gives the thickness of each component on a region. The results of curve fittings shown in **Fig 4.14** are tabulated in Table 4.2 in the following section.

§ 4.6 Optimization of Spectromicroscopy Data Analysis

The procedure of data analysis of a stack has been discussed in detail above but there are some issues that need further exploration.

Firstly, the fit coefficient of X-PEEM data is a relative contribution of each component to the detected photoemitted yield. How to obtain the thickness of each component? **Section 4.6.1** discusses this issue in detail.

Secondly, can we have a more detailed visualization on how proteins adsorb a surface? **Section 4.6.2** deals with how to generate a map for protein distributions on a surface and a corresponding distribution histogram curve.

Thirdly, it is mentioned that there are several approaches for mapping and curve fitting. Which of them is best? Here the different approaches are compared and the optimum choice is identified. All these issues are discussed in **Section 4.6.3**.

Finally, analysis of C 1s stacks was used to illustrate the procedures. Can similar quantitative information be obtained from stacks at N 1s or O 1s edges? **Sections 4.6.4**, **4.6.5** and **4.6.6** explore the analysis of N 1s and O 1s stacks in the content of this study.

§ 4.6.1 Normalization of X-PEEM Signals to The Total Sampling Depth

The thickness scales for component maps are obtained by normalizing the sum of all components to the estimated total sampling depth of X-PEEM in the system. The sampling depth was measured using a series of PS films with different thicknesses: 2, 5, 16 and 32 nm. (See Chapter 3 for sample preparation). The spectra of the PS films with different thickness are plotted in **Fig. 4.15 a)**. Photoemitted intensities at two energies (285.1 eV and 282 eV) were obtained from the spectra and are plotted in **Fig. 4.15 b)**.

The signals saturate around 10 nm which is estimated to be the total sampling depth of PS film.

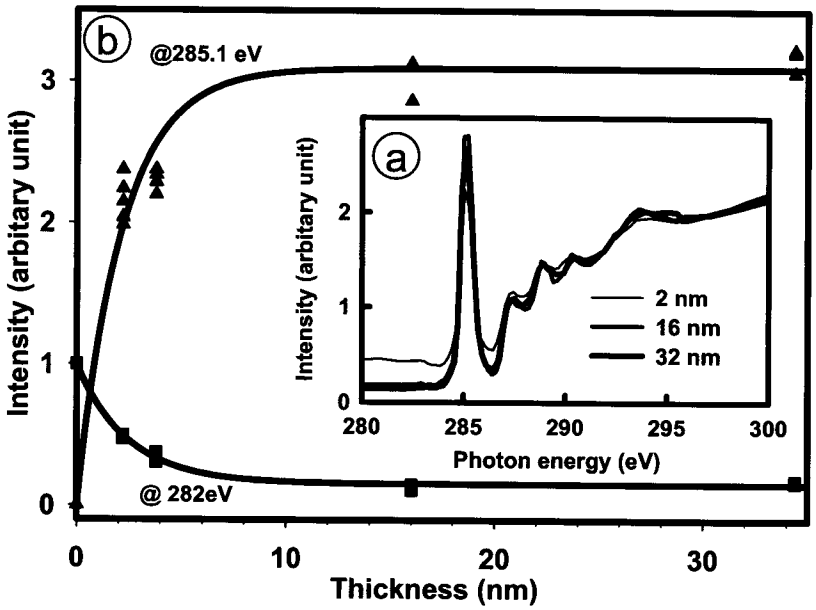

Fig. 4.15 a) Spectra of PS films with different thicknesses; b) photoemitted intensities of bare PS film at 285.1 eV (triangle) and 282 eV (square) as a function of the thickness of the films.

To derive absolute signals from X-PEEM data, each component map is added to give the map for the sum of components (sum-map). The centroid of the histogram of the sum-map is then normalized to 10 nm and the same normalization factor is used to normalize each component map, and the original intensity of the stack images. As shown in Fig. 4.12 h) the centroid of the histogram of sum-map is 10 nm after normalization. The thickness of each component is obtained by applying the same normalization factor.

The curve fit of X-PEEM data normalized to the sampling depth gives the thickness of each component in each region. For example, **Table 4.1** is the result for C 1s

Table 4.1 Thickness of each component from linear regression curve fit of the masked spectra from PS, PMMA and PS/PMMA interface regions, from the C1s stack of 0.005 mg/ml albumin covered PS/PMMA (uncertainty ± 0.1 nm).

Area	Component	Thickness (nm/pixel)		
		PS region	PMMA region	PS/PMMA interface
ROI-A (1)	PS	6.5	2.4	3.8
	PMMA	1.6	6.4	3.8
	Albumin	**1.9**	**1.1**	**2.3**
	Sum	10.0	10.0	10.0
ROI-A (2)	PS	6.5	2.2	3.7
	PMMA	1.3	6.4	3.6
	Albumin	**2.2**	**1.4**	**2.6**
	Sum	10.0	10.0	10.0
ROI-A (3)	PS	6.5	2.3	3.8
	PMMA	1.5	6.5	3.7
	Albumin	**2.0**	**1.2**	**2.5**
	Sum	10.0	10.0	10.0
ROI-A (4)	PS	6.5	2.2	3.7
	PMMA	1.3	6.3	3.6
	Albumin	**2.3**	**1.5**	**2.7**
	Sum	10.0	10.0	10.0
ROI-A (Whole area)	PS	6.5	2.3	3.8
	PMMA	1.4	6.4	3.7
	Albumin	**2.1**	**1.3**	**2.5**
	Sum	10.0	10.0	10.0
ROI-B	PS	6.7	2.2	3.7
	PMMA	1.1	6.4	3.7
	Albumin	**2.2**	**1.4**	**2.6**
	Sum	10.0	10.0	10.0
Standard deviation of albumin thickness		0.12	0.11	0.11

X-PEEM analysis of 0.005 mg/ml albumin covered PS/PMMA (unbuffered water solution, pH 7.2, 20 min adsorption at room temperature). These results are the analysis of stacks recorded on two regions of interest (ROI): ROI-A (~ 10 × 10 μm^2) and ROI-B (~ 5 × 5 μm^2). To check the uniformity of protein adsorption over a certain ROI, the ROI-A was divided into four nearly equal areas (~5 × 5 μm^2): (1), (2), (3), and (4). The results from the four sub-areas of ROI-A are also listed in **Table 4.1**. We can see that the albumin thickness on each region (PS, PMMA, or PS/PMMA interfaces) obtained from either different areas of a ROI [ROI-A (1), (2), (3), (4), and (whole area)] or different ROIs (ROI-A, ROI-B) are almost the same. The standard deviation of the reported albumin thickness on each was calculated based on all the results on this region from different ROIs and different areas of a ROI. These standard deviations (~ 0.1 nm) are listed in the last row of the table. The uncertainty of ± 0.1 nm, based on this and similar analysis of other samples, was estimated for albumin thickness measurements of all samples.

§ 4.6.2 Protein Distribution On a Region

Besides the protein thickness on a region, it is also possible to obtain the histogram of protein distribution on a region which helps to visualize how protein molecules distribute on that region.

The sample of 0.005 mg/ml albumin (unbuffered water solution, pH 7.3, adsorption for 20 min at room temperature) covered PS/PMMA is used to illustrate how to obtain the histogram of albumin distribution on a region, for example, the PS region.

As shown in **Fig. 4.16.**, by multiplying the albumin component map in a) and the PS component mask in b), one can obtain the map for the albumin distribution on the PS region (alb_on_PS) in c). The histogram of the alb_on_PS map is the histogram of albumin distribution on the PS region. This histogram is plotted in d), compared with the histogram of the albumin distribution on the whole surface which was derived from the map in a).

The maps and histogram of alb_on_PMMA and alb_on_interface can be obtained in a similar way. By coding the albumin distribution maps in different colors, one can get the albumin distribution on the whole surface, as shown in panel e) of **Fig. 4.16**, the red is albumin on the PS region, green is albumin on the PMMA region and blue is albumin on the interfacial region. The dark regions contain little albumin. A magnified view of the color-coded map for albumin distribution is shown in panel f) of **Fig. 4.16**. It shows that there is more albumin on the edges of the PMMA domains rather than the centers while albumin molecules are distributed more uniformly on the PS region. As seen in **Fig. 3.4**, the AFM of a PS/PMMA blend surface shows that the surface is very smooth. So I expect that different albumin distributions are mostly due to the chemical differences of the surface, different driving forces for protein adsorptions on different regions, protein structures, or other factors but not the surface roughness.

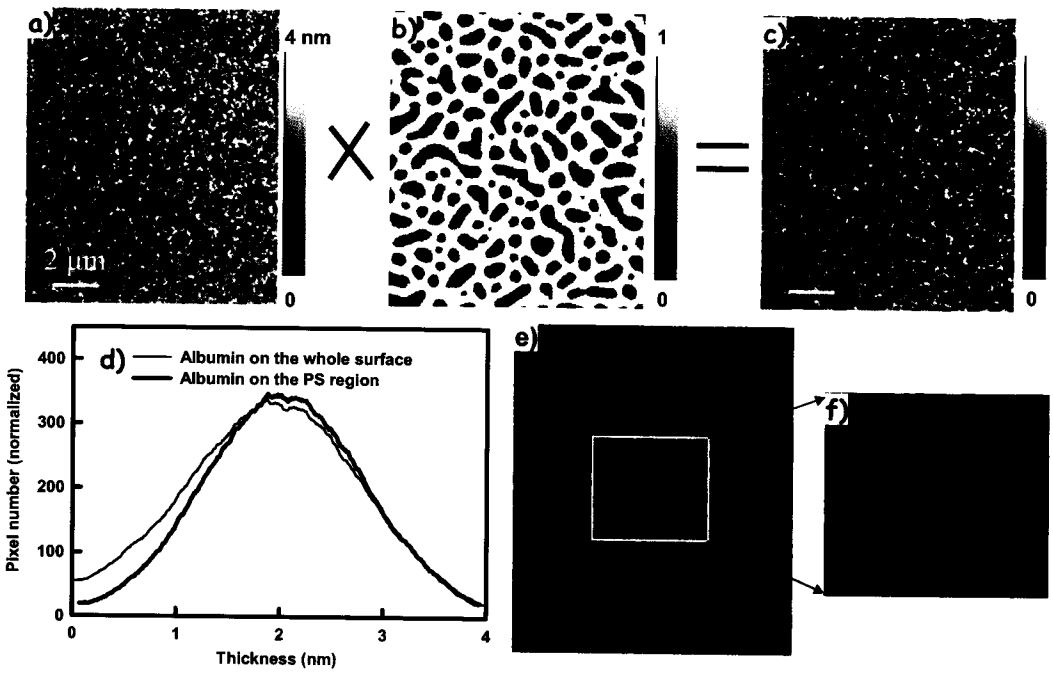

Fig. 4.16 a) albumin component map; b) PS component mask; c) Alb_on_PS map; d) histogram of album distribution on the whole surface (thinner curve) and on the PS region (thicker curve); e) color-coded albumin distribution map: red is alb_on_PS, green is alb_on_PMMA and blue is alb_on_interface. The dark regions have no albumin; f) a clearer view of color-coded albumin distribution map, cropped from a region in e).

§ 4.6.3 C1s Stacks: Different Mapping Fitting Approaches

As discussed above, there are three approaches for mapping: SF, SVD, and CGO. There are two approaches for curve fit: linear regression and CGO. Which approach is the best choice? The adsorption of 0.005 mg/ml albumin from de-ionized water onto a PS/PMMA blend is chosen as an example. The C1s stack is 327_049 (2-bunch, March 27th, 2005).

The component maps from the three approaches look almost the same (not presented here but they are all similar to **Fig. 4.12**). However the different approaches of

fitting give different quantitative results. The results from different mappings and curve fittings are summarized in **Table 4.2.** The histograms of albumin thickness from different mapping approaches are plotted in **Fig. 4.17**. The centroid numbers of albumin thickness histograms are also listed in **Table 4.2** for comparison.

Table 4.2 Albumin thickness of 0.005mg/ml albumin covered PS/PMMA, obtained by different mapping and curve fit approaches.

Map	**Curve fit**	**Alb_on_ PS**		**Alb_on_ PMMA**		**Alb_on_ Interface**		**Preference factors[a] of albumin on PS/PMMA/Interface**	
		Fit	**Hist**	**Fit**	**Hist**	**Fit**	**Hist**	**Fit**	**Hist**
SF	Linear	2.1	2.1	1.3	1.3	2.5	2.5	1.6/1.0/1.9	1.6/1.0/1.9
	CGO	2.5		1.9		3.1		1.3/1.0/1.6	
	CGO[b]	2.1		1.3		2.5		1.6/1.0/1.9	
SVD or CGO	Linear	2.1	2.5	1.3	2.0	2.5	3.1	1.6/1.0/1.9	1.3/1.0/1.6
	CGO	2.5		1.9		3.1		1.3/1.0/1.6	
	CGO[b]	2.1		1.3		2.5		1.6/1.0/1.9	

[a] The thicknesses are scaled so that the thickness of albumin on PMMA is equal to one;
[b] with linear background subtraction.

Based on **Table 4.2** and **Fig.4.16**, a few observations can be made:

a) SVD and CGO derived maps have similar histograms of albumin distributions, but SF is different from both.

b) For different mapping methods, the same curve fit method has the same results. For example, the linear regression fit of the masked spectra from both SF and SVD maps has the same results.

c) CGO and linear regression curve fits have different results but CGO curve fit with linear background subtraction has the same results as linear regression fit.

d) For SF mapping, only the results from the linear regression (or CGO with linear subtraction) are consistent with the result from the histograms.

d) For SVD and CGO maps, only the results from the CGO curve fit are consistent with the result from the histograms.

For the same curve fit method, either linear regression or CGO, different mappings have the same results. This is because the masked spectra derived from the composite maps obtained by the different mapping methods are the same for each region. However, linear regression and CGO fittings give different results. Using histograms as a criterion, the centroid of protein distribution histogram curve on a region should be equal to the protein thickness on this region derived from curve fit. When SF is used for mapping, the linear regression curve fit is the more reasonable choice (both have the a_0 term and thus the curve fit has the same result as histograms). When SVD or CGO is used for mapping, the CGO curve fit is the more reasonable choice (no a_0 term). However, based on C 1s stacks it is hard to justify which mappings is the best, SF or SVD/CGO? SF combined linear regression curve fit shows larger differences in albumin preference over different regions (1.6/1.0/1.9) than SVD/CGO mapping combined with CGO curve fit (1.3/1.0/1.6).

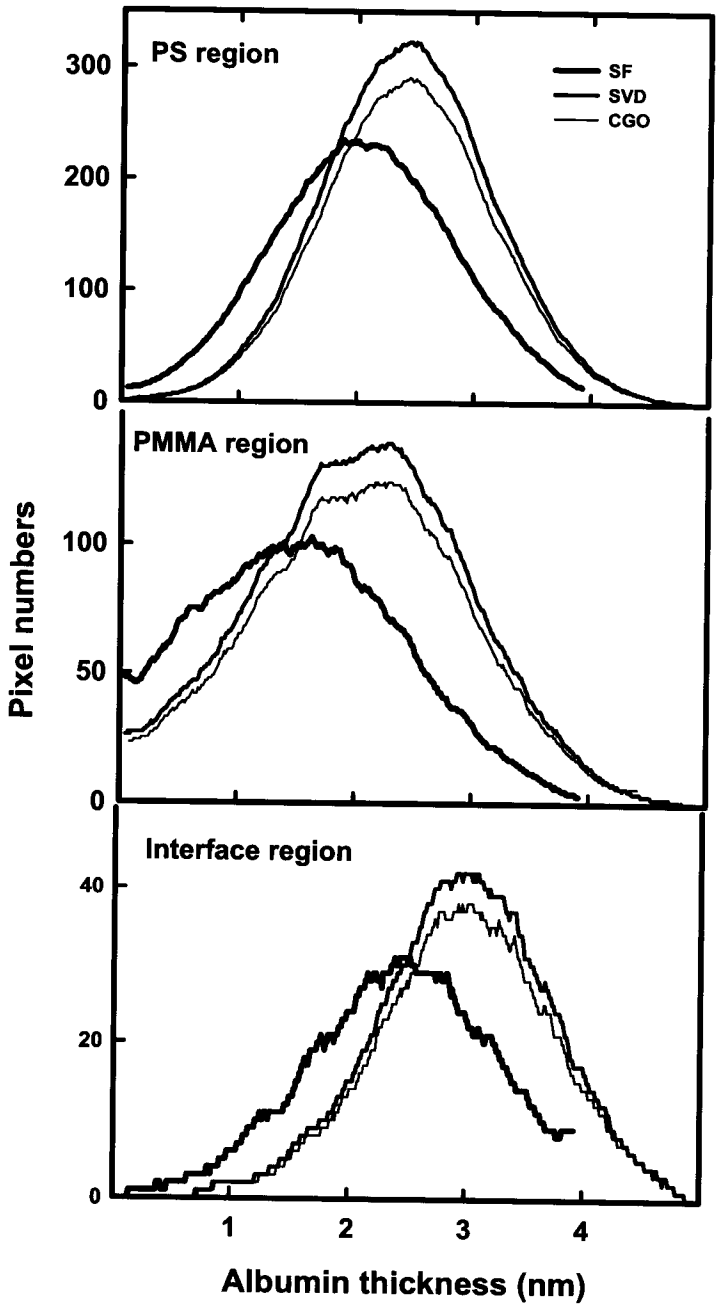

Fig. 4.17 Histograms of albumin thickness on different regions, obtained by different mapping approaches. (0.005 mg/ml albumin covered PS/PMMA blend.)

§ 4.6.4 N1s Stacks: Different Fitting Approaches

N 1s data from the same sample (adsorption of 0.005 mg/ml albumin from de-ionized water onto a PS/PMMA blend), and the same AOI is used to explore the relative merits of N 1s and C 1s signals for protein mapping.

The reference spectra used for the N 1s edge are shown in **Fig. 4.11**. The component maps generated from SF and SVD mapping of N 1s data are presented in **Fig.4.18**. The numbers shown in the right hand side of each component map are the thickness of this component. The color-coded maps of PS /PMMA (red) and albumin (blue) are also presented in the bottom row of **Fig.4.18**, along with the histograms of PS/PMMA, albumin components and the sum of each components. The centroid of the sum of each component is normalized to the total sampling depth of 10 nm. As shown in **Fig.4.11**, PS and PMMA do not have nitrogen and thus their spectra are a similarly sloping curve at the N1s edge. The mapping was done using a computed PS reference spectrum and the experimental albumin reference spectrum. The 'PS' map derived in this fit is thus the sum of PS and PMMA signals since it is impossible to differentiate PS and PMMA at N 1s edge. After normalizing the sum of all components to the total sampling depth of 10 nm, the thickness of PS/PMMA from SF is abnormal large (much larger than the total sampling depth of 10 nm) but the corresponding thickness from SVD is in the normal range. The color-code maps from SF and SVD show similar albumin distributions but the quality of the map from SVD is much better. These differences result from the additional "constant" term in SF. The spectra of PS and PMMA in the N 1s region do not have any spectral structure and thus an additional constant makes the

mapping in SF overly flexible (constant and the PS spectrum are very similar) and produces problems. Thus, for N 1s (and also O 1s), SVD (or CGO) is preferred over SF for mapping.

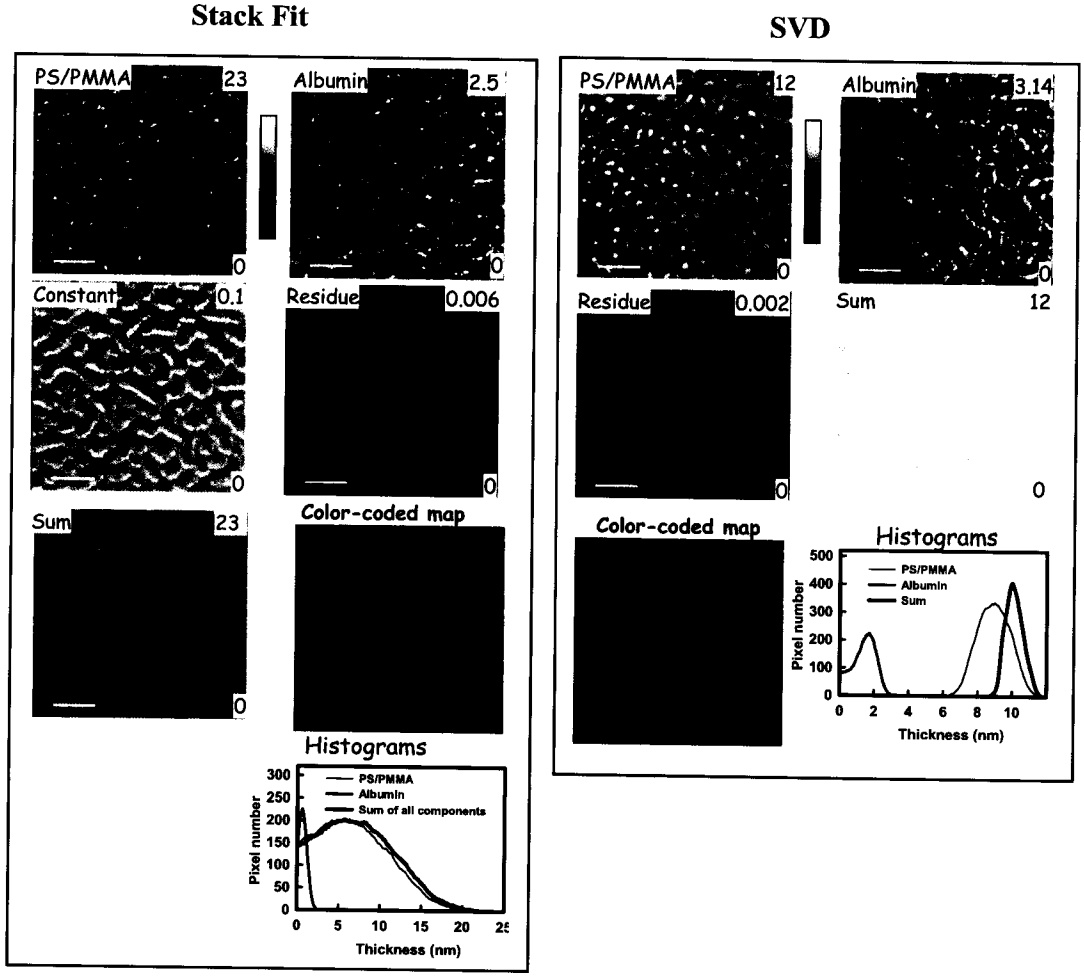

Fig. 4. 18 The composition maps of the N1s stack of 0.005mg/ml albumin covered PS/PMMA: maps from stack fit (left) and SVD (right). The bottom row is the color-coded maps of PS/PMMA (red) and albumin (blue), and the histograms of different components: PS/PMMA, albumin and sum of each component.

The curve fits (left) of masked N 1s spectra are shown in Fig.**4.19**, along with the masks of each region (right). Here the fitting curves from different fitting methods are compared with the experimental spectra. It is clear that the linear regression curve fit gives a much better fit to the experimental spectra than CGO curve fit. **Fig. 4.20** shows the fitting curve and the contributions from each component.

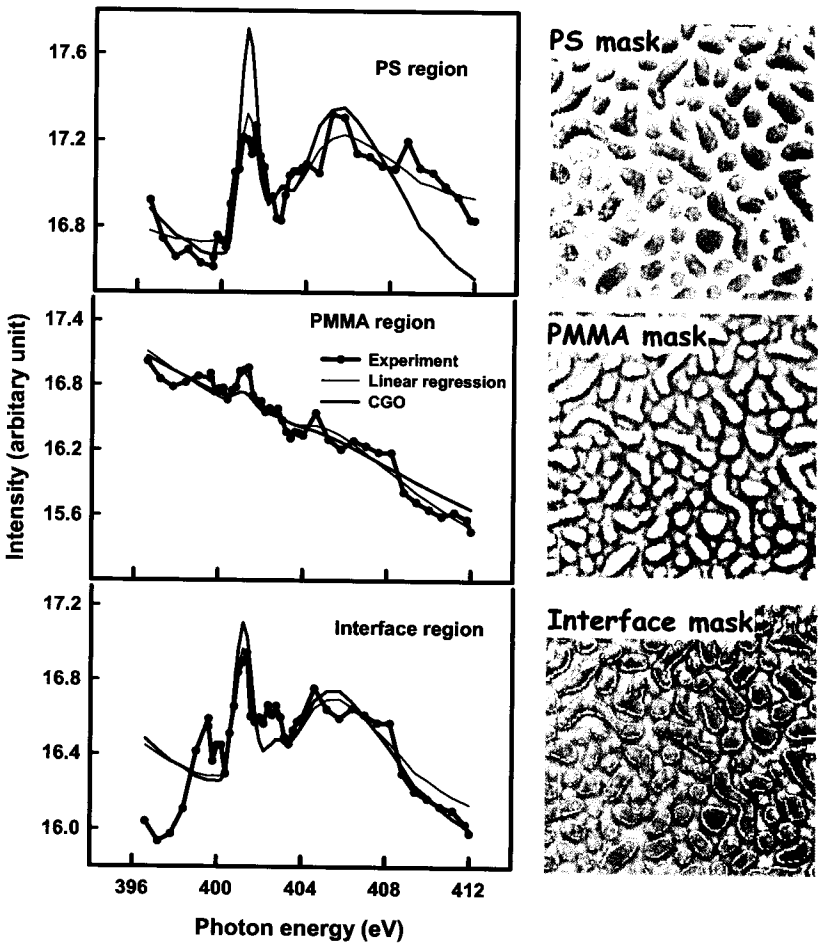

Fig. 4.19 Experimental N 1s spectra and fitting curves by linear regression and CGO fittings in different regions (PS, PMMA and interface) (left) and corresponding masks of the different regions (right). (0.005 mg/ml albumin covered PS/PMMA blend.)

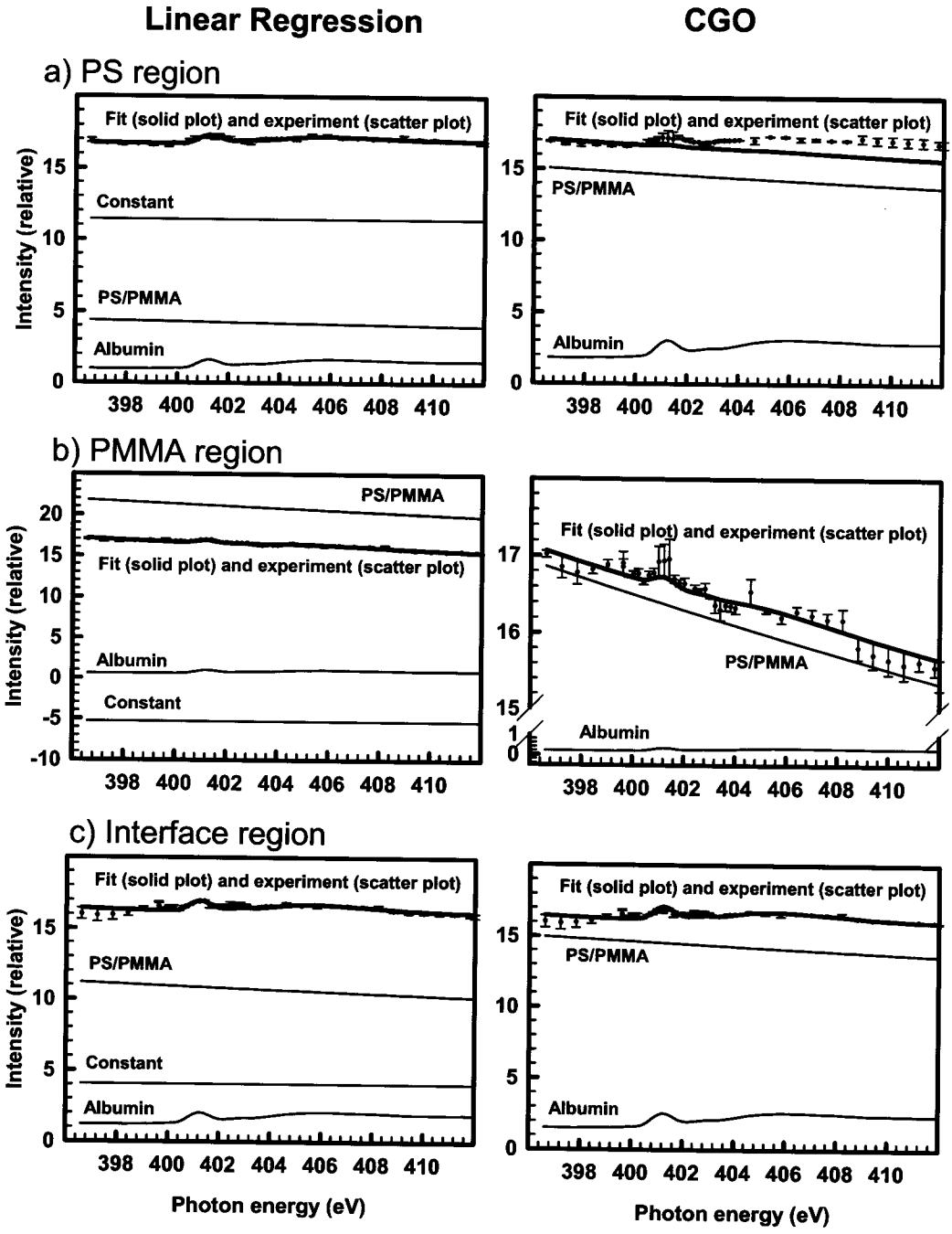

Fig. 4.20 Curve fit of the masked spectra of PS (a), PMMA(b), and PS/PMMA interface (c) from the N 1s stack of 0.005mg/ml albumin covered PS/PMMA: data – points with error bar; fit - thick solid line; components – thin lines as labeled.

§ 4.6.5 O 1s Stacks: Different Fitting Approaches

The same sample as used for illustrating C 1s and N 1s stacks is chosen to explore the O 1s stack analysis: adsorption of 0.005 mg/ml albumin from de-ionized water onto a PS/PMMA blend. The N 1s stack 327_051 (2-bunch, March 27th, 2005) was recorded on the same AIO, following the C 1s and N 1s stacks.

The reference spectra used for the O 1s edge are shown in **Fig. 4.11**. The component maps generated from SF and SVD mapping are presented in **Fig. 4.21**. The numbers shown in the right hand side of each component map is the minimum and maximum of the thickness of this component. The color-coded maps of PS (red), PMMA (green) and albumin (blue) are also presented in the bottom row of **Fig. 4.21**. SF mapping gives the wrong map and thickness for PS component (domains are discontinuous in the PS map). The constant map of SF mapping shows strong PS patterned domains. As with the N 1s case, SVD mapping is better than SF mapping for O 1s signals. However, the color-coded map from SVD mapping shows different albumin preference compared with the map from the C1s stack in **Fig. 4.12** and the N1s stack in **Fig. 4.18**.

The curve fits (right) of masked spectra at the O1s edge are shown in **Fig. 4.22**, along with the masks of each region (left). Different from the N1s edge, the different approaches of curve fits give similar fitting curves at the O1s edge.

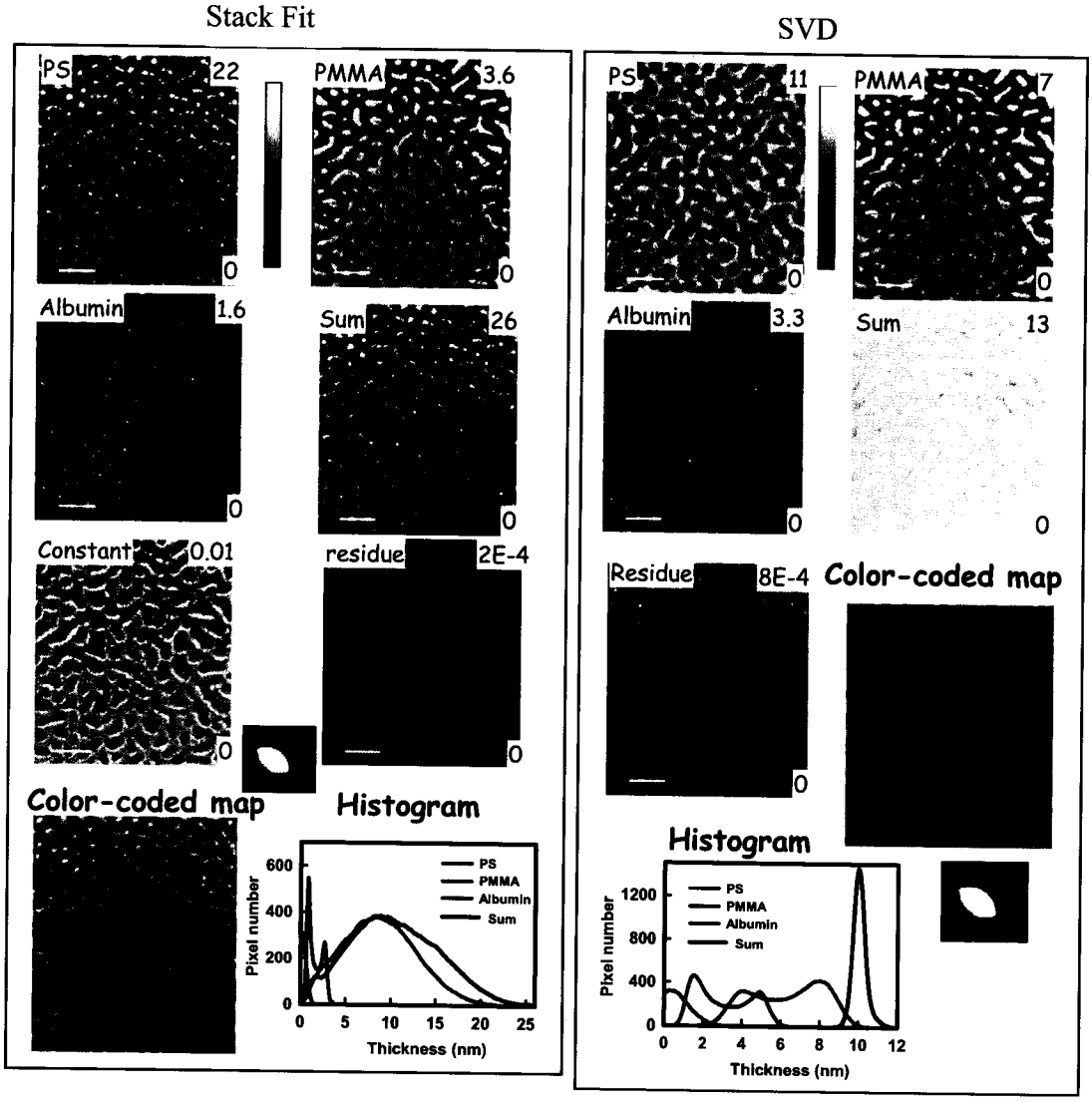

Fig. 4. 21 Composition maps of the O1s stack of 0.005mg/ml albumin covered PS/PMMA: maps from stack fit (left) and SVD (right). In the color-coded maps, red is PS, green is PMMA and blue is albumin. The distribution histograms of each component (PS, PMMA and albumin) and sum of each component are shown in the bottom row.

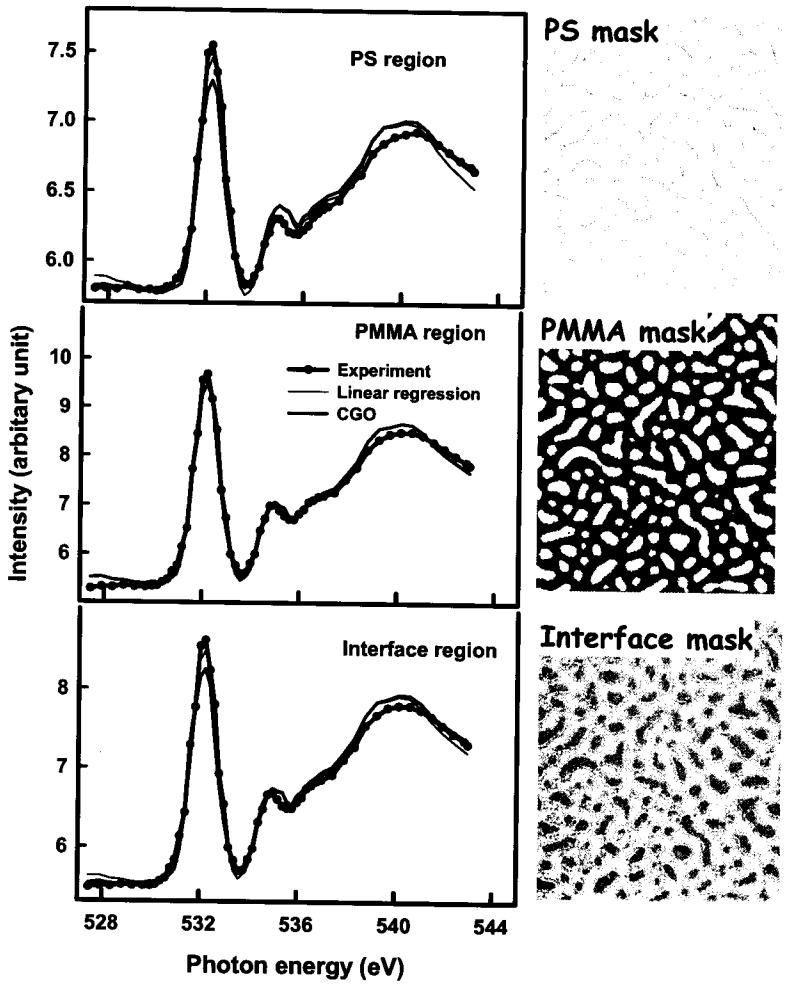

Fig. 4.22 Experimental O1s spectra and fitting curves by linear regression and CGO fittings in different regions (PS, PMMA and interface) (left) and corresponding masks of the different regions (right). (0.005 mg/ml albumin covered PS/PMMA blend.)

§ 4.6.6 Comparison of Results from C 1s, N 1s, and O 1s Signals From The Same AOI

The same sample (adsorption of 0.005 mg/ml albumin from de-ionized water onto a PS/PMMA blend) was used to explore the different mapping and fitting approaches at the C 1s, N 1s and O1s edges.

When going from one edge to another edge, the AOI can move (misalignment of the stacks at different edges) due to changed trajectory of the photon beam. As shown in **Fig. 4.23**, the interface mask generated from the C1s stack is used to monitor such misalignment. When the C1s mask is superimposed on the N1s and O1s stacks, the interface C1s mask does not match to the interface of the PS/PMMA in the N1s and O1s stacks. There are two ways to solve such issues: the first way is to align the images of different stacks at different edges and the second way is to generate individual masks for each stack at different edges. However the second way is not practical since the mapping for the N1s stack does not give reasonable PS/PMMA pattern. **Fig. 4.24 (a)** shows the mask of PMMA generated from the PS/PMMA map (SVD) of an **N 1s** stack (see **Fig. 4.18** for the component maps). By aligning the N1s stack with two images at 285.1 and 288.5 eV from the C1s stack (the two images at 285.1 and 288.5 eV in the C1s stack are chosen since they give the pattern of the PS and PMMA domains). **Fig. 4.24 (b)** shows the PMMA mask generated from the aligned image (aligned with N1s stack) at 288.5 eV. These two masks are quite different from each other and the difference is shown in **Fig. 4.24 (c)**. The two masks only share the common regions in white-highlighted. The yellow-highlighted region only belongs to the mask in (a) while the blue-highlighted region only belongs to the mask in (b). Therefore it is necessary to use the C1s stack to

define the mask in the N1s stack. This is because the contrast of PS and PMMA are strong enough in the PS/PMMA map from solely the N1s stack. The masks generated from the C 1s images after alignment are good masks for the N 1s stack, as shown in the right hand side of **Fig. 4.19**.

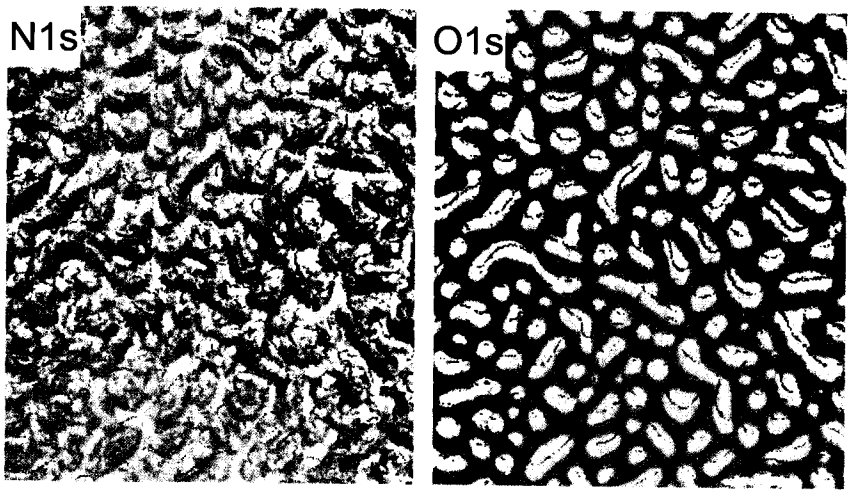

Fig. 4.23 Interface mask (green) from the C1s stack superimposed on a N1s and O1s stack.

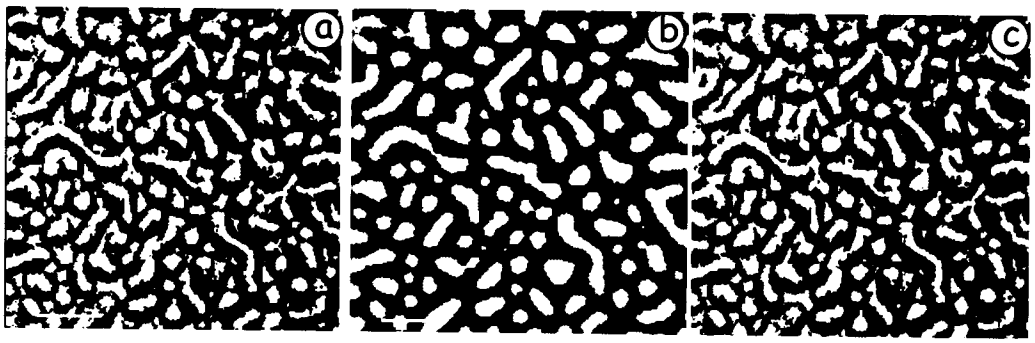

Fig. 4.24 Masks of PMMA from two different ways: a) from the N1s stack; b) from the C1s image, and c) the comparison of the two masks: white- the overlapped mask of the two masks in a) and b); blue- the mask from b) only; yellow-the mask from a) only.

Table 4.3 summarizes the quantitative results from fitting at C1s, N1s and O1s edges. The albumin thickness on each region (PS, PMMA and interface) of the same surface is NOT consistent between the stacks at recorded the three different edges. From the ratio of albumin distribution on different regions, the C 1s stack or the N 1s stack is qualitatively consistent but the O1s stack is not qualitatively consistent with either of the C 1s stack or the N 1s stack. Why does the O 1s stack show qualitatively different albumin preference to those of the C 1s and N 1s stacks? One explanation is that the O 1s stack is damaged since it was recorded after the successive measurements of the C 1s and N 1s stacks on the same AOI.

Table 4.3 Signals of albumin on different regions at different edges recorded under the same AOI.

Region		**C 1s (SF)**	**N 1s (SVD)**	**O 1s (SVD)**
	Component	**Thickness (nm)**	**Thickness (nm)**	**Thickness (nm)**
PS	PS	6.5	7.4	7.8
	PMMA	1.4		2.0
	Album	**2.1**	**2.6**	**0.2**
PMMA	PS	2.3		4.4
	PMMA	6.4	9.6	4.8
	Album	**1.3**	**0.4**	**0.8**
Interface	PS	3.8	8.5	5.6
	PMMA	3.7		3.5
	Album	**2.5**	**1.5**	**0.9**
Preference factor of albumin on PS/PMMA/Interface		**1.6/1.0/1.9**	**6.5/1.0/3.8**	**0.2/1.0/1.1**

Based on the above explorations, C 1s stacks are the best stacks for quantitative analysis for our system since each component have its characteristic absorption structure at C 1s edge.

Chapter 5
Concentration and exposure-time dependence for albumin adsorption

Reprinted with permission from *Journal of Physical Chemistry B* **2006**, 110, 16763-16773, Li Li, Adam P. Hitchcock, Nicholas Robar, Rena Cornelius, John L. Brash, Andreas Scholl, and Andrew Dora, "X-ray Microscopy Studies of Protein Adsorption on a Phase-Segregated Polystyrene/Polymethyl Methacrylate Surface. 1. Concentration and Exposure-Time Dependence for Albumin Adsorption" Copyright 2006, American Chemical Society"

The published paper contains totally 11 pages (Page 117~127). Including this cover page (Page 116), Chapter 5 then contains totally 12 pages.

X-ray Microscopy Studies of Protein Adsorption on a Phase-Segregated Polystyrene/Polymethyl Methacrylate Surface. 1. Concentration and Exposure-Time Dependence for Albumin Adsorption

Li Li,[†] Adam P. Hitchcock,*[,†] Nicholas Robar,[†,⊥] Rena Cornelius,[‡] John L. Brash,[†,‡,§] Andreas Scholl,[∥] and Andrew Doran[∥]

BIMR, McMaster University, Hamilton, ON, Canada L8S 4M1, Chemical Engineering, McMaster University, Hamilton, ON, Canada L8S 4L7, School of Biomedical Engineering, McMaster University, Hamilton, ON, Canada L8S 4K1, and Advanced Light Source, Berkeley Lab, Berkeley, California 94720

Received: April 20, 2006; In Final Form: June 26, 2006

X-ray photoemission electron microscopy using synchrotron radiation illumination has been used to measure the spatial distributions of albumin on a phase-segregated polystyrene/poly(methyl methacrylate) (PS/PMMA) polymer thin film following adsorption from unbuffered, deionized aqueous solutions under a range of solution concentrations and exposure times. Chemical mapping of the albumin, PS, and PMMA shows that the distribution of albumin on different adsorption sites (PS, PMMA, and the interface between the PS and PMMA domains) changes depending on the concentration of the albumin solution and the exposure time. The preferred sites of absorption at low concentration and short exposure are the PS/PMMA interfaces. Albumin shows a stronger preference for the PS domains than the PMMA domains. The exposure-time dependence suggests that a dynamic equilibrium between albumin in solution and adsorbed on PS domains is established in a shorter time than is required for equilibrating albumin between the solution and the PMMA domains. The explanation of these preferences in terms of possible adsorption mechanisms is discussed.

1. Introduction

Protein adsorption on solid surfaces is a very complex process that depends on various interactions between protein and substrate, as well as the state of hydration of the protein and the surface, the structure of the protein, and the presence of other components such as buffer salts, coadsorbed species.[1] Understanding and controlling protein adsorption is an important issue in biomaterials since it is known that protein adsorption is the first event in the interaction of tissue with a material. Different techniques have been used to study protein adsorption, including Fourier transform infrared spectroscopy (FTIR),[2] surface plasmon resonance (SPR),[3−5] ellipsometry,[5,6] atomic force microscopy (AFM),[7,8] surface matrix-assisted laser desorption ionization mass spectrometry (MALDI-MS),[9] secondary ion mass spectrometry (SIMS),[10,11] X-ray photoelectron spectroscopy (XPS),[12,13] quartz crystal microbalance (QCM),[14,15] and radiolabeling.[16] While these techniques provide good analytical sensitivity, in many cases they do not provide chemically specific identification, and in others, they are not able to visualize and thus locate sites of protein adsorption on laterally heterogeneous surfaces. AFM has excellent spatial resolution but only limited chemical sensitivity. SIMS combines both chemical identification and mapping, but its spatial resolution is currently of the order of 1 μm. In many biomaterials applications a major effort is underway to control protein adsorption by structuring and/or chemical patterning the surface at a sub-micrometer scale.[17−19] Analytical tools such as that described in this work can provide useful feedback to assist such developments. At a more fundamental level, it is of interest to understand protein−surface interactions in more detail, particularly as related to the role of surface properties such as hydrophobicity and chemical functionality. The use of surfaces that present distinct regions having different surface properties in close proximity gives the possibility to investigate the effect of these properties "simultaneously" in a single material, on a competitive basis. Adsorption site preference on such surfaces is of interest from both kinetic and thermodynamic viewpoints. A kinetics perspective raises questions such as location of first attachment and the evolution of regional preference over time as the surface fills. This has been studied previously with much more limited spatial sensitivity using protein adsorption on surfaces with a compositional and thus hydrophobicity gradient.[20,21] In this work the ability of X-ray spectromicroscopy to map protein distributions relative to surface domains at high resolution is used to study competitive adsorption on a chemically heterogeneous surface.

Recently, we demonstrated that synchrotron-based soft X-ray microscopy techniques can provide the required combination of chemical sensitivity, spatial resolution, and surface sensitivity. Specifically, we have shown that scanning transmission X-ray microscopy (STXM) can detect protein on complex polymer surfaces, both in the dried state and fully hydrated state.[22] We have also shown that X-ray photoemission electron microscopy (X-PEEM) can map polymer surfaces at high spatial resolution (~80 nm).[23] X-PEEM was shown to be capable of identifying preferred sites of fibrinogen attachment at submonolayer levels

* Corresponding author. Tel.: 905-525-9140 ext. 24749. Fax: 905-521-2773. E-mail: aph@mcmaster.ca.
[†] BIMR, McMaster University.
[‡] Chemical Engineering, McMaster University.
[§] School of Biomedical Engineering, McMaster University.
[∥] Advanced Light Source, Berkeley Lab.
[⊥] Summer student from Department of Biology, Mount Allison University, Sackville, NB, Canada.

10.1021/jp062442o CCC: $33.50
Published on Web 08/02/2006

on a phase-segregated polystyrene/poly(methyl methacrylate) (PS/PMMA) blend surface.[24]

Here we report the first of a series of papers describing a systematic investigation by X-PEEM and STXM of the adsorption of human serum albumin (HSA) on the surface of a PS/PMMA blend at different conditions of concentration, exposure time, pH, temperature, ionic strength, and competitive adsorption. This first paper focuses on methodological issues, and the use of X-PEEM to probe the location of HSA on the PS/PMMA blend surface when adsorbed from deionized water solutions of various concentrations and after different exposure times.

2. Experimental Section

2.1. Materials. 2.1.1. Substrate. PS (MW = 1.07 M, δ = 1.06) and PMMA (MW = 312 K, δ = 1.01) were obtained from Polymer Source Inc. and were used without further purification. A 30:70 w/w PS/PMMA (1 wt %) toluene (Aldrich, 99.8% anhydrous) solution was spun cast (4000 rpm, 40 s) onto clean 0.8 × 0.8 cm native oxide Si wafers (111) (Wafer World, Inc.), which had previously been degreased with trichloroethylene (Aldrich, +99.5% pure), acetone (Burdick & Jackson, HPLC grade), and methanol (Caledon), and then rinsed under running deionized water. The PS:PMMA/Si substrates were annealed at 160 °C for 12 h in a vacuum oven at a pressure of $\sim 10^{-4}$ Torr. Noncontact mode atomic force microscopy (AFM) measurements were used to measure the thickness of the PS:PMMA polymer film. The step height in the region of a fine scratch showed the film to be 40−50 nm thick. The discrete domains are ovoid PMMA islands with 500−800 nm width, separated by a similarly sized continuous domain of PS. Both the PS and PMMA domains also contain microdomains at the 10−200 nm size scale, amounting to ~20% of the majority domain. It is not clear why the minority PS component (30 wt %) forms the continuous domain, but the same morphology is observed for this type of spun-coat sample over a range of PS/PMMA compositions and molecular weights.[23]

2.1.2. Albumin. Human serum albumin (HSA) was obtained from Behringwerke AG, Marburg, Germany, and found to be homogeneous as judged by sodium dodecyl sulfate polyacrylamide gel electrophoresis (SDS-PAGE). All the albumin solutions used in this work were prepared from deionized (DI) water. The 0.005, 0.01, and 0.05 mg/mL albumin solutions were prepared by successive dilution from a 0.1 mg/mL albumin stock solution. Albumin is highly soluble and does not denature in deionized water unless heated above 70 °C and under strong alkaline conditions.[25] The pH of the unbuffered albumin solutions was measured to be 7.2 ± 0.2, slightly more acidic than physiological pH. We have also studied the adsorption of albumin from phosphate saline buffer (PSB) solutions. It is well-known that the change in ionic strength of a solution will affect the range of electrostatic interactions. Indeed, as will be presented elsewhere, changing from deionized water to PSB leads to some differences in the adsorption site preferences for albumin, although smaller than those found in our previous study on fibrinogen adsorption.[24] We present these results for adsorption from DI water as a base for comparison to the other aspects of this extended study.

2.2. Protein Exposure. To prepare samples for the concentration-dependence study, three wells of a Fisher multiwell plate (1 cm diameter well) were filled with albumin solutions of different concentrations. The remaining wells were filled with deionized water. A piece of the PS/PMMA/Si substrate was introduced into each albumin solution and then the plate was shaken gently in the horizontal direction to expel any air bubbles that may have formed on the substrate surfaces. After 20 min exposure, each substrate was taken out of the albumin solution and incubated in fresh deionized water in another well. After 2 min, the substrate was moved to another cell with fresh deionized water. This washing procedure was repeated four times for each substrate. The albumin-covered PS/PMMA sample was then removed from the final well and dried by carefully touching the edge of the Si wafer with lens paper. For the exposure-time-dependence study, the PS/PMMA sample was exposed to a 0.01 mg/mL albumin solution for times of 5, 20, and 60 min.

2.3. X-PEEM. The X-PEEM (PEEM2) at ALS bending magnet beamline 7.3.1[26] was used for this study. The principles and performance of the instrument have been presented extensively elsewhere.[26] A schematic of the instrument is given in Figure 1 of ref 23. Briefly, the sample is illuminated by monochromatic X-rays, and the photoejected electrons are extracted into an electrostatic imaging column by a high electric field between the sample and the objective lens and transported with controlled magnification to a CCD camera. From the perspective of X-ray absorption, X-PEEM is a variant of the total electron yield method, which strongly emphasizes low kinetic energy secondary electrons. The sampling depth (1/e) of X-PEEM for polymers has been measured as 4 nm,[27] with signals effectively being integrated over the outer 10 nm of the sample. In this work, the light employed was elliptically polarized with 70−80% right circularly polarized light. The electrostatic field at the sample was 9 kV/mm. The projector voltage was then adjusted such that the resulting field-of-view was between 40 and 60 μm.

Image sequences[28] at the C 1s edge were recorded from several different areas of the sample and analyzed using techniques described below to derive quantitative maps of the PS, PMMA, and HSA distributions. In contrast to X-PEEM of hard materials, there are many challenges of X-PEEM measurements of radiation-sensitive organic soft matter. Since the previous X-PEEM work on PS/ PMMA[23] and fibrinogen-covered PS/PMMA,[24] we have optimized sample preparation, data acquisition, and data analysis procedures extensively. The PS:PMMA layer is kept thin (<50 nm) and flat (~10 nm rms) in order to avoid discharges. A 100 nm thick Ti filter is used to reduce second-order light in the C 1s region. The radiation damage rates for all three components have been characterized.[27] To reduce radiation exposure, a fast shutter has been implemented which, when used to blank the beam between successive data points, reduces exposure to <50% of that used during previous acquisition protocols. The incident flux was reduced to minimize damage while still providing adequate spectral resolution (the mechanism to reduce flux involves masking prior to the grating which reduces the grating illumination and, if done excessively, leads to degradation of the spectral resolution). With these improvements, our implementation of X-PEEM to these biomaterials studies has evolved to the point where radiation-sensitive systems such as PMMA can be measured with minimal artifacts.

3. Data Analysis

3.1. Reference Spectra. The spectra of PS, PMMA, and human serum albumin (HSA) were recorded using scanning transmission X-ray microscopy (STXM) on free-standing thin films (PS, PMMA) or as a solvent-cast deposit on a silicon nitride window (HSA). The STXM energy scale was calibrated using the sharp C 1s → Rydberg lines in CO_2.[29] The calibrated spectra were set to an absolute linear absorption scale by scaling

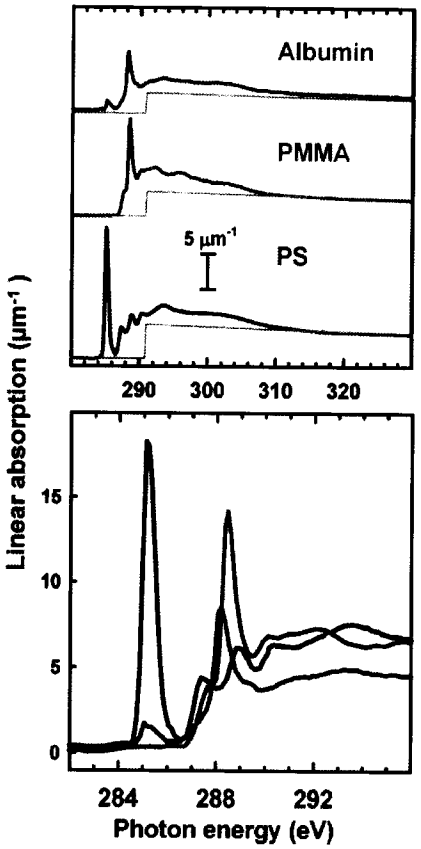

Figure 1. (a) C 1s X-ray absorption spectra of polystyrene (PS, red), poly(methyl methacrylate) (PMMA, green), and human serum albumin (HSA, blue) recorded from pure materials. The spectra are plotted on an absolute linear absorption scale (with offsets). The gray lines indicate the elemental response.[32] (b) Expanded comparison of the near edge region.

to match the elemental response of 1 nm at bulk densities (ρ_{PS} = 1.05, ρ_{PMMA} = 1.18, ρ_{HSA} = 1.0[30]), computed from standard tables of elemental X-ray absorption.[31,32] These linear absorption spectra were the reference spectra used in fitting the C 1s image sequences of HSA-covered PS/PMMA. Although the energy resolution of STXM (0.1−0.2 eV) is better than that of X-PEEM (0.4−0.5 eV), the sharpest features in the X-PEEM spectra of the samples studied in this work have the same width as their counterparts in the STXM reference spectra due to the natural breadth of the peaks. Furthermore, as discussed in the next section, the recorded X-PEEM stacks are Io-normalized using corrections for systematic line shape distortions that would otherwise give different X-PEEM and STXM line shapes. For these reasons it is reasonable to use the STXM reference spectra for the analysis of the X-PEEM measurements.

Figure 1 presents the optical linear absorption spectra of pure PS, PMMA, and albumin thin films in the C 1s regions. The dark-gray lines are the computed elemental response.[32] All three materials exhibit distinct C 1s spectra. The PS spectrum is dominated by the strong C 1s(C=C) → $\pi^*_{C=C}$ transition at 285.1 eV. The albumin and PMMA spectra are each dominated by strong C 1s(C=O) → $\pi^*_{C=O}$ transitions. However, the $\pi^*_{C=O}$ peak in albumin occurs at 288.20(6) eV, 0.25(8) eV below the $\pi^*_{C=O}$ peak in PMMA which occurs at 288.45(6) eV. The 0.25 eV energy shift is mainly associated with the change in energy of the C 1s level since the carbonyl carbon is in a less electronegative environment in the amide (R-CONH) than in the ester (R-COOMe). This shift is small but clear and has been documented previously.[24] It forms the basis for chemical differentiation of albumin (and other proteins) from PMMA (and other esters). In addition, the shape of the low-energy side of the $\pi^*_{C=O}$ peak is different in the two species. These differences assist differentiation of PMMA and albumin and thus the accuracy of the mapping is improved when longer range image sequences are used.

There are many factors in addition to the X-ray absorption coefficient that determine the signal strength from a given point on a surface, and thus the image contrast in X-PEEM. However, for a flat sample, with materials likely to have similar work function and similar scattering and propagation properties for low-energy electrons, and in the absence of any charging effects (all the case here), the X-ray absorption factor should dominate the response. Thus, although fully quantitative results require accurate information about the material dependence of sampling depth and electron propagation, we believe the approach used in this work, which uses quantitative reference spectra of the pure materials and a measured sampling depth, will give results for which the relative quantization of albumin on different parts of the surface is meaningful, and that the quantization will suffer at most from small systematic errors.

3.2. Chemical Mapping. Each image sequence was normalized to ring current and the Io signal from an HF etched Si wafer recorded under the same acquisition conditions. The Io signal was divided by the intrinsic X-ray absorption of Si[32] and also by a linear energy term to account for the bolometric response function of this type of detection.[33] Since the energy scale of the ALS 7.3.1 beamline can change significantly from day to day, each image sequence was carefully calibrated to set the position of the peak of the (asymmetric) C 1s → $\pi^*_{C=C}$ transition of the PS domains to 285.15 eV.

The normalized image stack was analyzed using the "stack fit" routine[34] implemented in the analysis package, aXis2000.[35] This routine performs a least-squares fit to the spectrum at each pixel in an image sequence to a linear combination of the reference spectra of the pure materials, and to an additional "constant" (energy-independent) term. The fit coefficients are then assembled to form component maps which are maps of the spatial distribution of each component in the area imaged. Because the reference spectra are quantitative (the intensity scale of each one is the signal expected from 1 nm of the material at bulk density), the intensities of the component maps are correct relative to each other. To give an absolute "thickness" scale to the component maps, it is necessary to set the scale for the total thickness. This is estimated to be 10 nm, based on the results of X-PEEM measurements of a series of pure PS thin films of varying thickness.[28] In the case of the albumin map it is important to note that thickness is "quantized" by the finite size of the molecule. If albumin is aligned with its smallest dimension (4 nm) normal to the surface, a thickness of 1 nm in a given region should be interpreted as one-fourth of the surface of that region being covered by a monolayer of albumin while the other three-fourths of the region is bare. Effectively, the thickness scale for the albumin component can be re-interpreted as a coverage scale, with a value of 4 nm representing saturated monolayer coverage.

As an example of this process, the results from a stack fit analysis of the C 1s X-PEEM data for albumin adsorption from a 0.005 mg/mL solution for 20 min are presented in Figure 2

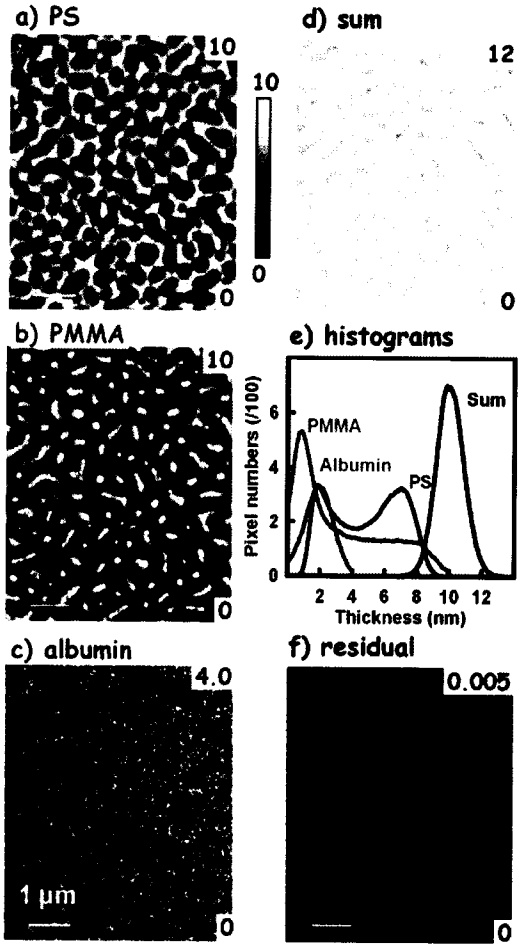

Figure 2. Component maps of (a) PS, (b) PMMA, and (c) albumin for a PS/PMMMA blend substrate exposed to a 0.005 mg/mL HSA aqueous solution for 20 min, derived from pixel-by-pixel curve fits of a C 1s image sequence. The numbers in the upper and lower right of each component map are limits of the thickness gray scales in nm. (d) Sum of the PS, PMMA, and albumin thickness component maps. (e) Histograms of the component and sum maps. The narrow distribution of the sum supports our assumption of similar work function and sampling depth for the various surface regions (PS, PMMA, and interface). The average value of the sum was set to 10 nm to set the thickness scale. (f) Map of the residual of the fit. The gray scale in the latter case is the deviation of the fit and the measured signal, averaged over all energies.

in the form of maps of each component: (a) PS, (b) PMMA, (c) albumin, as well as (d) the sum of these components, (e) histograms of the thicknesses for each component and the sum, and (f) the residual of the fit. The grayscale limits are the minimum and maximum thickness per pixel. Lighter intensities indicate locations where there is more of that component. The thickness values were obtained by normalizing the sum of all three component map signals to the estimated total sampling depth of 10 nm. Note that the summed signal (Figure 2d) is quite constant over the field of view, with a variation of about 15%. This supports our assumption that the sampling depth is similar in the chemically different regions. The component maps show that the PS domains are continuous and the PMMA domains are discontinuous, as found in previous studies of PS/PMMA blends prepared from high MW PS and PMMA.[23] At neutral pH, the HSA molecule has a size of ~4 × 4 × 14 nm in its folded form. Surface plasmon resonance studies of albumin adsorbed on a pure polystyrene surface[36] have been interpreted in terms of a preferred adsorption geometry with the albumin molecule aligned with its long axis parallel to the surface. Thus, the albumin thickness values of <4 nm found for all of the surfaces studied in this work correspond to adsorption at less than one monolayer. This is also consistent with radio-labeling results from similar preparations.[37]

Figure 3a displays a color-coded composite map, which reveals the spatial correlation of the chemical components. This is obtained by combining the component maps of PS, PMMA, and albumin, with the PS signal in red, the PMMA signal in green, and the HSA signal in blue. In Figure 3a the intensity scale for each color is set so that the full range of each component is mapped to the full 0−255 range. Note that, to see details more clearly, Figure 3 displays only the central 17 μm × 17 μm region of the full image shown in Figure 2. The color-coded map shows a distinct blue band at the interface between the PS and PMMA domains. The discontinuous PMMA domains are turquoise rather than green, indicating the presence of HSA on their surface, while the continuous PS domains are purple, indicating significant HSA also on the PS domains. Fibrinogen was also found to show interface preference when it adsorbed on to similar PS/PMMA substrates from unbuffered aqueous solutions.[24]

To obtain the amount of albumin on different regions, signals specific to the PS and PMMA domains were extracted by using threshold masking of the component maps to select only those pixels where the signal was above a defined threshold. The interface signal from a ~80 nm band at the PS−PMMA interface was obtained by selecting those pixels not present in either the masked PS or masked PMMA maps. The amount of each component (PS, PMMA, and albumin) in each region [PS, PMMA, and interface] was then obtained by fitting the extracted spectrum using the same reference spectra used in generating the component maps by the stack fit. Figure 3b displays the masks while panels (c−e) of Figure 3 display the curve fit to each extracted spectrum. The intensities in these spectra are those obtained after adjusting the spectral intensity scale by the same factor which gave a thickness of 10 nm for the average of the sum of the component maps. The points with estimated uncertainties are the experimental spectra. The dark solid curves are the fits to the masked experimental spectra and the color curves are the weighted reference spectra. The results of these fits are reported in Table 1.

3.3. Histogram Analysis of the Albumin Distributions. To further investigate the changes in albumin thickness on the different regions with changes in concentration and exposure times, the albumin maps were segmented into three regions [PS, PMMA, and interface] and then histograms of those signals were derived. The same masks of the PS, PMMA, and PS/PMMA interface regions used to extract the spectra subjected to the curve fit were used to subdivide the albumin component map into three parts—albumin-on-PS, albumin-on-PMMA, and albumin-on-interface—by taking the product of the albumin component map with each mask. The histograms of each of those spatially segregated albumin signals are presented and discussed in the Results section.

3.4. Verification of Precision and Accuracy. Since the contributions of the albumin signal to the total signal are small and the changes in the amounts of absorbed HSA with exposure conditions are relatively even smaller, to build confidence in

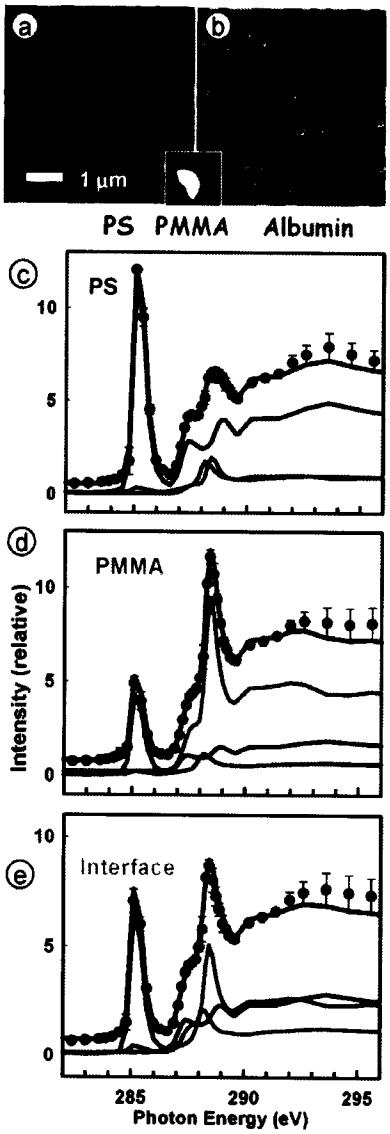

Figure 3. (a) Color-coded component map (left top, rescaled) for the (0.005 mg/mL, 20 min) albumin-covered PS/PMMA blend sample. The color wheel which allows the viewer to determine the composition in mixed regions. (b) Masks used to extract spectra of specific regions. [red = PS > 4 nm, green = PMMA > 4 nm, blue = PS/PMMA interface (all pixels not identified in the masks of the PS and PMMA domains)]. (c−e) Curve fits to the average C 1s spectra extracted from the masked regions (data, points; fit, thick solid line; components, thin lines).

our results, we carefully examined the various steps used to optimize the analytical methodology.

First, at least two measurements were made for each of the adsorption conditions. To minimize the radiation damage, each measurement was performed on a fresh area. The albumin distributions derived from the repeat results were in agreement within the estimated uncertainties.

Second, the spatial distribution of albumin on the surface has also been evaluated by measuring the N 1s edge. The N 1s signal is a good indicator of the amount of albumin present since albumin is the only species with a N 1s signal. However, the N 1s signal is much weaker than the C 1s signal, and thus the N 1s edge is less sensitive than the C 1s edge for quantitative measurements. In addition, the N 1s signals do not give a specific measure of the PS and PMMA components of the substrate, although the morphology is readily visible due to the differences in elemental composition of PS and PMMA. The N 1s results (not shown in this work) are generally in agreement with those from the C 1s edge, especially in terms of trends, but there are some quantitative disagreements. Given that the C 1s signal has a balanced sensitivity to all three chemical components, we have chosen to present only the C 1s results. We are still exploring how to improve the accuracy and reliability of the N 1s measurement. We are also exploring how to optimize O 1s edge measurements as an additional source of chemical mapping information. PS is spectroscopically silent at the O 1s edge, and the radiation damage rate is higher at the O 1s edge than the C1s edge. Thus, of the three possible edges, the O 1s edge provides the least specific and most unreliable information about this particular system.

Third, in addition to the threshold masking technique described in the preceding paragraph, which provides a convenient "single number" evaluation of spatial distributions, the spatial distributions on the three chemically distinct regions of the sample were characterized by examining the histograms of pixel values of albumin thickness. The method was described in detail in the previous section. Here, we note that these distributions are broad relative to the mean thickness. This width reflects the distribution of albumin thicknesses and not the statistical uncertainty. When the spectra from a grouping of pixels at a particular thickness level are selected, and the spectrum of each of those pixels is analyzed independently, the standard deviation of the derived albumin thickness from those repeat analyses is of the order of 0.1 nm, whereas the histogram peaks have widths (fwhm) of the order of 1.5 nm.

Fourth, there are a number of parameters in the analysis which can potentially affect the results. These include choice of fitting method (stack-fit versus SVD[34]), the fine details of the reference spectra used (e.g., from PEEM versus from STXM, compensation for differences in energy resolution of PEEM versus STXM, elimination of small effects of radiation damage in the reference spectra, etc.), and the energy range of the spectral data employed (ideally, one wants to have as many energies where the X-ray absorption of the components differ substantially, but relatively few energies where the X-ray absorption of the components is the same; however, if too few energies are used, the statistical quality is reduced). All these factors were investigated in considerable detail. All reasonable choices gave similar quantitative results, and the same qualitative trends. The results presented herein represent the best choice of methodology, which is based on an extensive exploration of a complex and highly coupled parameter space.

In summary, we believe these results and the estimated errors cited represent a "best case" analysis. Clearly, systematic errors are possible. For example, if one changed the depth to which the total thickness is normalized, the amounts of protein would change in proportion. We justify the choice of 10 nm as the *total* depth contributing to the measured signal because the sampling depth for PS (thickness for which the signal drops by 1/e) has been measured to be 4 ± 1 nm.[27] As is typical of systematic errors, selection of a different value to normalize the total thickness would change the reported albumin thicknesses by an amount larger than our estimated precision.

TABLE 1: Concentration Dependence of Adsorption of HSA on PS/PMMA from De-ionized Water Solution: Composition of PS, PMMA, and PS/PMMA Interfaces (Uncertainty: ±0.1 nm[a])

region	composite (nm/pixel)	0.005 mg/mL fit[b]	0.005 mg/mL hist.[c]	0.01 mg/mL fit	0.01 mg/mL hist.	0.05 mg/mL fit	0.05 mg/mL hist.
PS region	PS	6.5		6.5		5.8	
	PMMA	1.4		1.3		1.6	
	albumin	**2.1**	**2.1**	**2.2**	**2.2**	**2.6**	**2.6**
PMMA region	PS	2.3		1.9		2.3	
	PMMA	6.4		6.7		5.6	
	albumin	**1.3**	**1.3**	**1.4**	**1.4**	**2.1**	**2.1**
interfacial region	PS	3.8		3.7		3.7	
	PMMA	3.7		3.7		3.5	
	albumin	**2.5**	**2.5**	**2.6**	**2.6**	**2.8**	**2.8**
ratio (alb. on PS/PMMA/interface)		**1.6/1.0/1.9**		**1.6/1.0/1.9**		**1.2/1.0/1.3**	

[a] See text. [b] Results from curve fit. [c] Centroid of the albumin distribution histograms. See text.

However, such errors affect the scale, not the qualitative trends with changes in adsorption conditions, and it is the latter we stress in the rest of this presentation.

4. Results

4.1. Concentration Dependence of Albumin Adsorption. The adsorption of albumin from deionized water solutions was studied at three different concentrations: 0.005, 0.01, and 0.05 mg/mL, in each case for a fixed exposure time of 20 min. Figure 4 presents the color-coded composite maps for these three systems, derived from stack fits of C 1s image sequences. The maps on the left are not rescaled, which means a common thickness scale (min/max over all three components) is used for all three components. The maps on the right are rescaled, which means that the intensity of each color is adjusted to fill the full scale of the associated component map. The nonrescaled maps show there is a small but systematic increase in the amount of albumin adsorbed on the surface with increasing albumin concentration. The rescaled maps better show how the spatial distribution of the albumin changes with increasing concentration.

As the albumin concentration increases, the nonrescaled maps show that the color of the continuous PS domains changes from "red rather than purple" to "purple rather than red" and the discontinuous PMMA domains also change from pure green to a more turquoise color. These results show that the thickness of albumin on both the PS and PMMA domains increases with concentration. The rescaled maps clearly show that the interface of the PS and PMMA remains blue in all three cases. These results indicate that, under these adsorption conditions, the preferred adsorption site of albumin is the PS/PMMA interface.

Using the component map masking technique described above, spectra of the PS, PMMA, and interface were extracted and fit to obtain the relative amount of each component in each region. Table 1 presents the results of this quantitative analysis. There is around 15−20% PMMA in the masked PS region and 20−25% PS in the masked PMMA region, which is associated mostly with microdomains.[23] The interfacial region contains about the same amount of PS and PMMA, as expected from the spatial location. What interests us most is the amount of albumin on the chemically different regions of the surface. These values are highlighted in Tables 1 and 2 in bold. The last row of Table 1 shows the ratio of albumin on different regions for the three concentrations studied. This analysis is consistent with the qualitative information in the color-coded maps (Figure 4). The preferred site of albumin adsorption at lowest concentration (0.005 mg/mL) is the PS/PMMA interface, which implies this is the one with a kinetic or thermodynamic advantage relative to adsorption on the PS or the PMMA domains. The albumin thickness at the PS/PMMA interface increased by only 0.3 nm as the concentration was increased from 0.005 to 0.05 mg/mL, suggesting these sites get saturated at very dilute conditions. Albumin shows a stronger preference for PS domains than for PMMA domains at all three concentrations but the preference gets smaller with increasing concentration. The albumin thickness on the PS domains remains almost the same as the concentration changes from 0.005 to 0.01 mg/mL, but increases by 0.4 nm from 0.01 to 0.05 mg/mL. The albumin thickness on the PMMA domains also remains almost the same as the concentration changes from 0.005 to 0.01 mg/mL while it increases by 0.7 nm as the albumin solution concentration is increased from 0.01 to 0.05 mg/ml. Table 1 also shows that as the albumin amount increases, the strength of the PS signal decreases. This is consistent with the fixed sampling depth and thus the blocking of electrons from ionization of the polymer substrate by the overlayer of adsorbed protein.

Figure 5 plots the histograms of albumin distributions on different regions—PS, PMMA, and the PS/PMMA interfaces—for the three different concentrations. Each curve shows a Gaussian-like distribution. The centroids of the histograms are listed in Table 1. These numbers are very similar to the average of the albumin thickness from the curve fit, as expected. The widths of the distributions reflect the stochastic nature of the adsorption process, which means that various areas of each domain type are not covered equally. When the spectra from individual pixels with similar values on each histogram curve are isolated and curve fit, the variation in the thicknesses from those fits is of the order of 0.1 nm, which is the basis for our estimated statistical precision reported in the tables.

4.2. Exposure-Time Dependence. The adsorption of albumin from 0.01 mg/mL deionized water solutions was also studied for three different exposure times: 5, 20, and 60 min. The results for 20 min adsorption from 0.01 mg/mL albumin solution are the same as those in the previous section. We show the result here again in order to give a systematic description of exposure-time dependence. The (rescaled) color-coded maps of the three different exposure times are presented in Figure 6. In this case, the color of the discontinuous PMMA domains changes dramatically from pure green to green-blue and even turquoise in some locations. In the case of the 5 min exposure, the strong blue signal in the color composite map is located at the PS/PMMA interfaces but the blue at the interface becomes lighter with increasing exposure time.

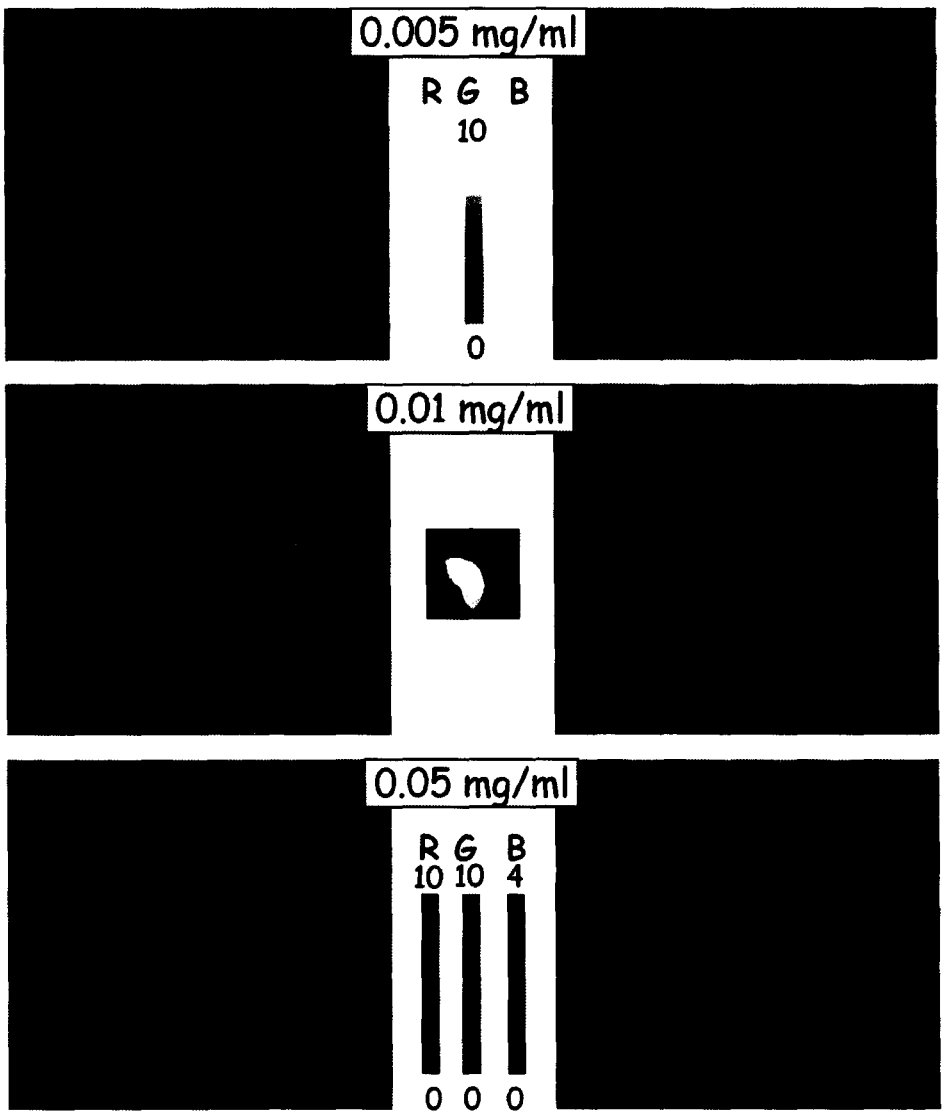

Figure 4. Concentration dependence (0.005, 0.010, and 0.050 mg/mL) of albumin adsorption on PS/PMMA: Color-coded component maps of albumin-covered PS/PMMA for the indicated solution concentrations and an exposure time of 20 min. (left) Nonrescaled maps on a single thickness scale for all three colors indicated by the upper scale; (right) rescaled maps with thickness limits as indicated by the lower intensity scales. The size of each image is 10 μm × 10 μm.

The results from curve fits to the extracted PS, PMMA, and interface spectra are shown in Table 2. These verify the trends presented visually in the color-coded composite maps of Figure 6. Similar to the concentration-dependence study, there is around 20−30% PMMA in the masked PS region and around 20−30% PS in the masked PMMA region due to micro domains.[23] In the case of the 5 min exposure, albumin has a very strong preference for PS and PS/PMMA interfaces. This indicates that the first sites of adsorption are the PS/PMMA interfaces at short exposure times, consistent with the result of the 20 min adsorption from dilute albumin solution. The albumin thickness on the PS domains increases slightly from 5 to 20 min and then remains the same after 20 min. This suggests that adsorption onto the PS domains saturates in less than 20 min. The thickness of albumin on the PMMA domains increases dramatically from near zero at 5 min to 1.4 nm at 20 min and still keeps increasing to 1.9 nm at 60 min. This suggests that adsorption of albumin on the PMMA domains requires a longer time to saturate than that on the PS domains. The albumin thickness on the PS/PMMA interfaces shows a maximum of 3.0 nm for 5 min exposure but then decreases to 2.6 nm after 20 min, with no further change at longer exposure times.

Figure 7 plots the histograms of the albumin distributions on the different regions—PS, PMMA, and the PS/PMMA interfaces—for the three different exposure times. Each curve follows a quasi-Gaussian distribution except the histograms of albumin distributions for 5 min adsorption, where the albumin distribution on the PMMA domains follows a decaying linear curve and a peak is not observed. The average albumin thickness on the PMMA domains is nearly zero. The albumin distributions

TABLE 2: Exposure-Time Dependence of Adsorption of HSA on PS/PMMA from De-ionized Water Solution: Composition of PS, PMMA, and PS/PMMA Interfaces (Uncertainty: ±0.1 nm[a])

region	composite (nm/pixel)	5 min		20 min		60 min	
		fit[b]	hist.[c]	fit	hist.[c]	fit	hist.[c]
PS region (nm/ pixel)	PS	5.8		6.5		4.9	
	PMMA	2.3		1.3		2.9	
	albumin	**1.9**	**1.9**	**2.2**	**2.2**	**2.2**	**2.2**
PMMA region (nm/pixel)	PS	2.6		1.9		2.7	
	PMMA	7.2		6.7		5.4	
	albumin	**0.2**	**d**	**1.4**	**1.4**	**1.9**	**1.9**
interfacial region (nm/pixel)	PS	3.5		3.7		3.7	
	PMMA	3.5		3.7		3.7	
	albumin	**3.0**	**3.0**	**2.6**	**2.6**	**2.6**	**2.6**
ratio (alb. on PS/ PMMA/interface)		**9/1.0/15**		**1.6/1.0/1.9**		**1.2/1.0/1.4**	

[a] See text. [b] Results from curve fit. [c] Centroid of albumin distribution histograms. [d] No peak in the histogram.

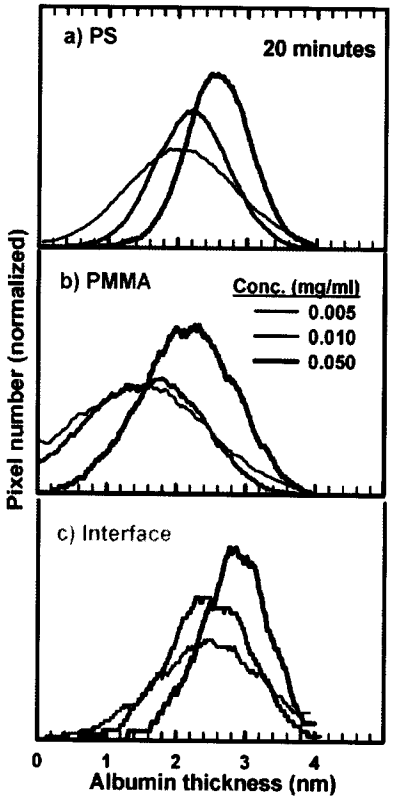

Figure 5. Histograms of the thickness of albumin thickness on different regions for adsorption for 20 min from solutions of concentrations of 0.005, 0.01, and 0.05 mg/mL. (a) Albumin on PS, (b) albumin on PMMA, and (c) albumin on the interface. The sum of pixels for each region for each exposure condition was set to a common value to take into account the fact that differently sized regions were imaged in the various samples.

on the PS and PS/PMMA domains for 5 min exposure have long tails into the thicker albumin region. The centroids of the histograms are listed in Table 2 as an alternate estimate of the average albumin thickness.

5. Discussion

The major finding of this study is that the preferred first site of albumin adsorption (at short time and low concentration) on micro phase-separated PS/PMMA blends is the domain boundary, which we refer to here as the interface between the domains (our limited lateral spatial resolution precludes exact identification of the location of the albumin within the domain boundary region). At longer exposures, there is a redistribution of the protein away from the interfaces and toward the PS and PMMA domains (especially the PS domains). These trends, based on the data in Tables 1 and 2, are presented in Figure 8 in the form of log−log plots. As can be seen, the plots in Figure 8a are linear, thus suggesting in the case of the concentration dependence that adsorption on the different surface regions follows the Freundlich isotherm model.[38] Adsorption on the PS domains appears to achieve equilibrium quickly as indicated by the very small variation in albumin coverage with either concentration or exposure time. As seen in Figure 8b, adsorption to the interface at 0.01 mg/mL decreases and adsorption to the PMMA domains increases with time. Indeed, the form of the time variation suggests that there may be exchange of protein between these two regions. The reversibility of albumin adsorption on the PS/PMMA interfaces indicates that absorbed albumin molecules are not denatured. Why does this initial localization and subsequent redistribution happen? Clearly, the answer to this question depends on the mechanisms of adsorption that are in play, and their dependence on the surface properties of both the protein and the adsorbing surface.

Globular proteins, including albumin, consist of hydrophobic (nonpolar) and hydrophilic (polar, charged) regions, and thus can engage in multiple mechanisms of adsorption including hydrogen bonding, electrostatic interactions, and hydrophobic interactions. Norde and Lyklema[38] have discussed these mechanisms and the driving forces behind them. Hydrophobic interactions play a major role in protein−surface systems; these are driven by entropy gain due to loss of structured water at the interacting surfaces, and conformational re-ordering. Examples where the adsorption is endothermic and/or where protein and surface have net charge of the same sign are common. In an aqueous environment, a protein adopts conformations where the hydrophilic (polar, charged) amino acid residues tend to be located externally and the hydrophobic residues located internally. However, not all of the hydrophobic groups are "hidden" in the interior and not all of the hydrophilic groups are exposed externally to water.[39] Thus, proteins in aqueous solution tend to have both hydrophobic and hydrophilic patches on the exterior surface, although the surface must be predominantly hydrophilic (or have a sufficient charge density) if the protein is to remain molecularly dispersed.[40]

Given the amphipathic character of proteins as described, it is perhaps not surprising that albumin prefers to locate initially

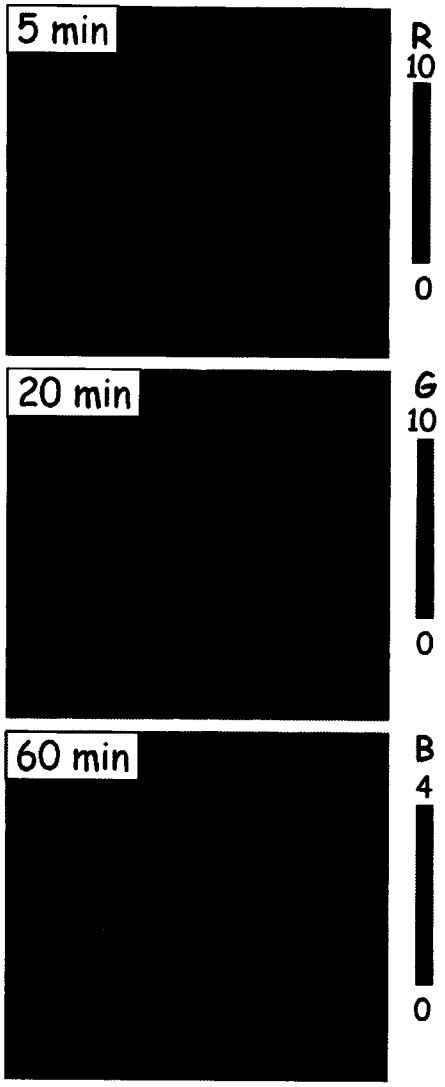

Figure 6. Exposure-time dependence (5, 20, and 60 min) of albumin adsorption on PS/PMMA: Color-coded component maps of albumin-covered PS/PMMA for the indicated times of exposure to an HSA solution of 0.01 mg/mL. Only rescaled maps are displayed, with thickness limits as indicated. The size of each image is 10 μm $\times$ 10 μm.

at the boundaries of the PS and PMMA domains. The difference in surface energy between PS and PMMA is significant as indicated by water contact angles of 97° and 76°,[41] respectively. Thus, the more hydrophobic regions of albumin should tend to bind to the PS domains while the more hydrophilic regions should bind to the PMMA domains. This preference is most easily accommodated by adsorption at the interfaces, as found here.

As the surface fills, sites which are kinetically most accessbile, and/or those of lowest free energy, will be occupied first. In the present case the preferred interfacial locations will at some point be fully occupied and further adsorption will, perforce, occur on the domain surfaces. From the data at short time and low albumin concentration it appears that the more hydrophobic

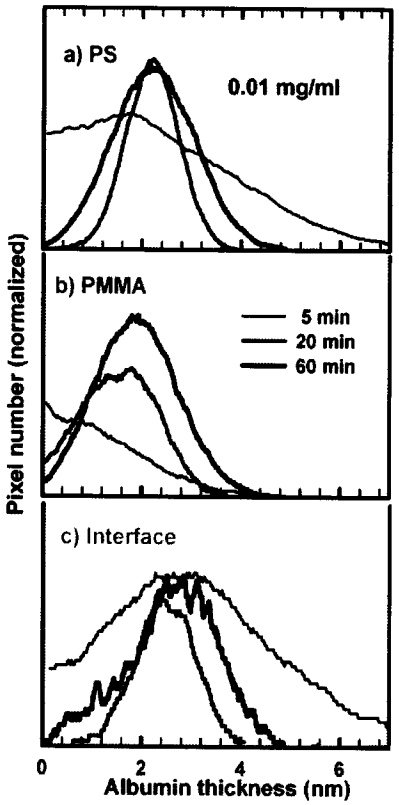

Figure 7. Histograms of the albumin thickness on different regions for adsorption from a 0.01 mg/mL solution for exposure times of 5, 20, and 60 min. (a) Albumin on PS, (b) albumin on PMMA, and (c) albumin on the interface. The sum of pixels for each region for each exposure condition was set to a common value to take into account the fact that differently sized regions were imaged in the various samples.

PS domains are favored initially over the PMMA domains, thus suggesting that the hydrophobic interactions expected to predominate between PS and albumin provide greater binding energy than the interactions that occur when albumin adsorbs on PMMA. As well as hydrophobic interactions, the latter may involve hydrogen bonding between the carbonyls of PMMA and the amide nitrogens of albumin. Dipole−dipole interactions may also occur.

The redistribution of protein on the surface at higher concentrations and longer times involving an apparent net loss of protein from the interface regions is intriguing, though perhaps counter-intuitive. The driving force for such a process is not clear from an energy standpoint, but it suggests either that desorption/re-adsorption is taking place which results in redistribution of albumin over the surface, or redistribution is occurring by surface diffusion (not involving desorption) as has been shown in other systems.[42,43] It might be possible to distinguish between these possibilities by investigating whether redistribution occurs if the protein solution is replaced with solvent after, say, an adsorption time of 5 min. If it does, then the diffusion rather than the desorption−resorption mechanism would be favored.

Other work on protein adsorption where surfaces of deliberately varied chemical composition have been investigated includes that of Elwing and others using hydrophobicity

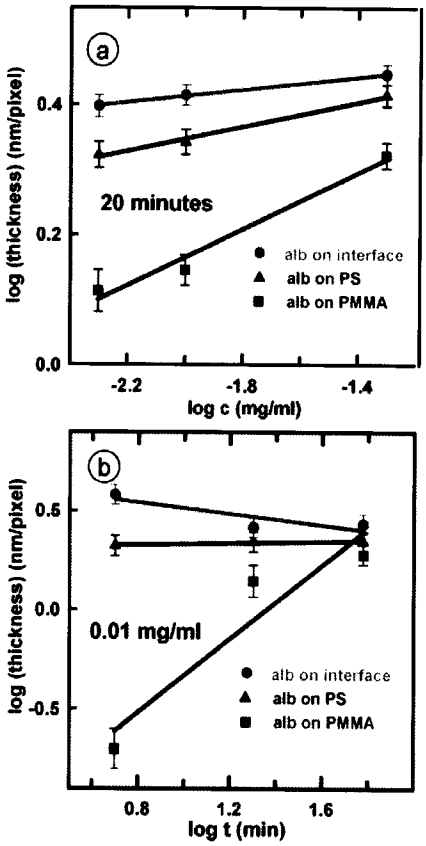

Figure 8. Log−log plots of the albumin thickness on the PS (red), PMMA (green), and PS/PMMA interface (pink) regions versus (a) concentration (for 20 min exposure time) and (b) exposure time (for adsorption from a 0.01 mg/mL solution).

gradients formed by differential deposition of silanes on silicon, to form a surface with a water contact angle which varied continuously from 90° to 10° along the length of the sample. In one study[20] it was shown that adsorption of fibrinogen from buffer and of proteinaceous material from plasma decreased monotonically from the hydrophobic to the hydrophilic end of the gradient, thus providing convincing evidence that proteins have stronger affinity for hydrophobic than for hydrophilic surfaces. In general the spatial resolution in these studies was of the order of 0.5 mm, 4 orders of magnitude lower than the ~80 nm spatial resolution of the present work.

A potential application of the X-PEEM methodology is to assist development of patterned polymer surfaces for microarrays and biochips which are being developed for rapid screening and high throughput analysis for proteomics and other applications.[44] Åsberg et al.[45] achieved hydrophobic patterning on a hydrophilic substrate with surface features of the order of 50 μm using polydimethyl siloxane (PDMS) stamping on a glass substrate. These surfaces were used to control the adsorption patterning of peptides and proteins. Interestingly, they allowed distinction between different conformations of the attached biomolecules. Bouaidat et al.[46] created patterns of protein adsorbing (glass) and nonadsorbing (PEO-like) areas using plasma polymerization combined with photolithography methods. Patterns with features of the order of 50 μm were achieved. In contrast to the work reported in the present paper, none of this patterning work addresses the issues of differential adsorption kinetics and redistribution of protein over the surface as a function of time, although the latter may be important for biochip applications where the dimensional stability of protein arrays may be critical.

6. Summary

Albumin adsorption on a patterned PS/PMMA blend has been studied with X-PEEM at a spatial resolution better than 100 nm. The concentration and exposure-time dependence data are consistent with each other, showing that the preferred adsorption site at low concentration, and for short exposure, is the PS/PMMA interfacial region. We suggest that competition between polar and nonpolar interactions controls the first site of adsorption since it can be established on a short time scale. The X-PEEM results indicate there is reversible adsorption on the PS/PMMA interface. At longer exposure times, the system adopts a configuration in which the amount of albumin on the PMMA and PS domains increases significantly and there is a more even distribution over all three types of adsorption sites.

Acknowledgment. This research is supported by Natural Science and Engineering Research Council (NSERC, Canada) and the Canada Research Chair programs. X-ray microscopy was carried out using PEEM2 at the ALS. The ALS is supported by DoE under Contract DE-AC03-76SF00098.

References and Notes

(1) Malmsten, M. *Biopolymers at interfaces*; Marcel Dekker: Basel, 2003.
(2) Chittur, K. K. *Biomaterials* **1998**, *19*, 357−369.
(3) Green, R. J.; Frazier, R. A.; Shakesheff, K. M.; Davies, M. C.; Roberts, C. J.; Tendler, S. J. B. *Biomaterials* **2000**, *21*, 1823−1835.
(4) Sigal, G. B.; Mrksich, M.; Whitesides, G. M. *J. Am. Chem. Soc.* **1998**, *120*, 3464−3473.
(5) Höök, F.; Kasemo, B. *Anal. Chem.* **2001**, *73*, 5796−5804.
(6) Elwing, H. *Biomaterials* **1998**, *19*, 397−406.
(7) Siedlecki, C. A.; Marchant, R. E. *Biomaterials* **1998**, *19*, 441−454.
(8) Ta, T. C.; McDermott, M. T. *Anal. Chem.* **2000**, *72*, 2627−2634.
(9) Kingshott, P.; StJohn, H. A. W.; Chatelier, R. C.; Griesser, H. J. *J. Biomed. Mater. Res.* **2000**, *49*, 36−42.
(10) Lhoest, J.-B.; Wagner, M. S.; Tidwell, C. D.; Castner, D. G. *J. Biomed. Mater. Res.* **2001**, *57*, 432−440.
(11) Mantus, D. S.; Ratner, B. D.; Carlson, B. A.; Moulder, J. F. *Anal. Chem.* **1993**, *65*, 1431−1435.
(12) Ratner, B. D.; Horbett, T. A.; Shuttleworth, D.; Thomas, H. R. *J. Colloid Interface Sci.* **1981**, *83*, 630−642.
(13) Sundgren, J.-E.; Bodo, P.; Ivarsson, B.; Lundstrom, I. *J. Colloid Interface Sci.* **1986**, *110*, 9−20.
(14) Höök, F.; Rodahl, M.; Brzezinski, P.; Kasemo, B. *Langmuir* **1998**, *14*, 729−734.
(15) Höök, F.; Kasemo, B. *Anal. Chem.* **2001**, *73*, 5796−5804.
(16) Archambault, J. G.; Brash, J. L. *Colloids Surf B: Biointerfaces* **2004**, *33*, 111−120.
(17) Castner, D. G.; Ratner, B. D. *Surf. Sci.* **2002**, *500*, 28−60.
(18) Tirrell, M.; Kokkoli, E.; Biesalski, M. *Surf. Sci.* **2002**, *500*, 61−83.
(19) Ostuni, E.; Chapman, R. G.; Liang, M. N.; Meluleni, G.; Pier, G.; Ingber, D. E.; Whitesides, G. M. *Langmuir* **2001**, *17*, 6336−6343.
(20) Elwing, H.; Askendal, A.; Lundström, I. *J. Biomed Mater Res.* **1987**, *21*, 1023.
(21) Gölander, C.-G.; Pitt, W. G. *Biomaterials* **1990**, *11*, 32−35.
(22) Hitchcock, A. P.; Morin, C.; Heng, Y. M.; Cornelius, R. M.; Brash, J. L. *J. Biomater. Sci., Polym. Ed.* **2002**, *13*, 919−938.
(23) Morin, C.; Ikeura-Sekiguchi, H.; Tyliszczak, T.; Cornelius, R.; Brash, J. L.; Hitchcock, A. P.; Scholl, A.; Nolting, F.; Appel, G.; Winesett, A. D.; Kaznacheyev, K.; Ade, H. *J. Electron Spectrosc.* **2001**, *121*, 203−224.
(24) Morin, C.; Hitchcock, A. P.; Cornelius, R. M.; Brash, J. L.; Scholl, A.; Doran, A. *J. Electron Spectrosc.* **2004**, *137−140*, 785−794.
(25) Peters, T., Jr. *All About Albumin: Biochemistry, Genetics, and Medical Applications*; Academic Press: New York, 1995.

(26) Anders, S.; Padmore, H. A.; Duarte, R. M.; Renner, T.; Stammler, T.; Scholl, A.; Scheinfein, M. R.; Stöhr, J.; Séve, L.; Sinkovic, B. *Rev. Sci. Instrum.* **1999**, *70*, 3973−3981.

(27) Jacobsen, C.; Wirick, S.; Flynn, G.; Zimba, C. Soft X-ray spectroscopy from image sequences with sub-100 nm spatial resolution. *J. Microsc.* **2000**, *197*, 173−184.

(28) Wang, J.; Li, L.; Morin, C.; Hitchcock, A. P.; Doran, A.; Scholl, A. *J. Electron Spectrosc.*, in preparation.

(29) Ma, Y.; Chen, C. T.; Meigs, G.; Randall, K.; Sette, F. *Phys. Rev. A* **1991**, *44*, 1848−1858.

(30) Brandrup, J.; Immergut, E. H.; Grulke, E. A.; Bloch, D. *Polymer Handbook*; Wiley-Interscience: New York, 1999.

(31) Henke, B. L.; Lee, P.; Tanaka, T. J.; Shimabukuro, R. L.; Fujikawa, B. K. *At. Nucl. Data Tables* **1982**, *27*, 1−256.

(32) Henke, B. L.; Gullikson, E. M.; Davis, J. C. *At. Data Nucl. Data Tables* **1993**, *54*, 181−298.

(33) Stohr, J. *NEXAFS Spectroscopy*; Series in Surface Science, Vol. 25; Springer: Berlin, 1992.

(34) Hitchcock, A. P.; Morin, C.; Zhang, X.; Araki, T.; Dynes, J. J.; Stöver, H.; Brash, J. L.; Lawrence, J. R.; Leppard, G. G. *J. Electron Spectrosc. Relat. Phenom.* **2005**, *259−269*, 144−147.

(35) aXis2000 is free for noncommercial use. It is written in Interactive Data Language (IDL) and available from http://unicorn.mcmaster.ca/aXis2000.html.

(36) Green, R. J.; Davies, J.; Davies, M. C.; Robert, C. J.; Tendler, S. J. B. *Biomaterials* **1997**, *18*, 405−413.

(37) Li, L.; Hitchcock, A. P.; Cornelius, C.; Brash, R. J., in preparation.

(38) Norde, W.; Lyklema, J. *J. Biomater. Sci. Polym. Ed.* **1991**, *2*, 183−202.

(39) Klotz, I. M. *Arch. Biochem. Biophys.* **1970**, *138*, 704−706.

(40) Kuhn, L. A.; Swanson, C. A.; Pique, M. E.; Tainer, J. A.; Getzoff, E. D. *Proteins: Struct., Funct., Genet.* **1995**, *23*, 536−547.

(41) Liu, Y.; Messmer, M. C. *J. Phys. Chem. B* **2003**, *107*, 9774−9779.

(42) Axelrod, D.; Koppel, D. E.; Schlessinger, J.; Elson, E.; Webb, W. W. *Biophys. J.* **1976**, *16*, 1055−1069.

(43) Cole, N. B.; Smith, C. L.; Sciaky, N.; Terasaki, M.; Edidin, M.; Lippincott-Schwartz, J. *Science* **1996**, *273*, 797−801.

(44) Weibel, D. B.; Garstecki, P.; Whitesides, G. M. *Curr. Opin. Neurobiol.* **2005**, *15*, 560−567.

(45) Åsberg, P.; Nilsson, K. P.; Inganäs, O. *Langmuir* **2006**, *22*, 2205−2211.

(46) Bouaidat, S.; Berendsen, C.; Thomsen, P.; Guldager Petersen, S.; Wolff, A.; Jonsmann, J. *Lab Chip* **2004**, *4*, 632−637.

Chapter 6

Effect of pH on albumin adsorption

This chapter reports results of an X-PEEM analysis of albumin adsorption on a PS/PMMA blend from 0.05 mg/ml aqueous solutions with pHs of 2.0, 4.0, 7.0, 8.6 and 10.0. Albumin is found to have maximum adsorption at pH = 2 when it is fully extended. The minimum adsorption was found at pH 8.6, where albumin is contracted. Changes in the PS/PMMA preference with pH are interpreted in terms of conformational changes which modify the hydrophobic fraction of the albumin surface.

§ 6. 1 Introduction

Chapter 5 reported the concentration and exposure-time effect on albumin adsorption on a PS/PMMA blend surface. This chapter focuses on another effect in the albumin adsorption – pH effect. HSA consists of 585 amino acids in a single polypeptide chain. The molecule is known to exist in different conformations depending on the pH. Foster [F77] reported the relationship of isomeric forms of albumin at different pH, as shown in **Fig. 6.1a.** Under neutral pH, HSA shows a compact heart-shaped three-dimensional structure with three homologous domains (I, II, and III). Each domain contains two subdomains. With changes in pH, the compact "native" albumin structure undergoes reversible conformational isomerization leading effectively to unfolding of the molecule. The N-F transition involves the unfolding of domain III. The F form is characterized by a dramatic increase in viscosity, much lower solubility, and a significant

loss in alpha helix content. At pH values lower than 4, albumin undergoes additional expansion with additional loss of alpha helix content. This expanded form, known as the E form, has increased intrinsic viscosity, and an increase in the hydrodynamic axial ratio from ~4 to above 9. At pH 9, albumin changes conformation to the basic form (B). At pH above 10, another reversible isomerization occurs to create the A form. The diagrams of the F and E forms were proposed by Carter et al [CH94] are shown in **Fig. 6.1b**, compared with that of the N form. Recently, Qiu et al [QZO&06] used a single intrinsic

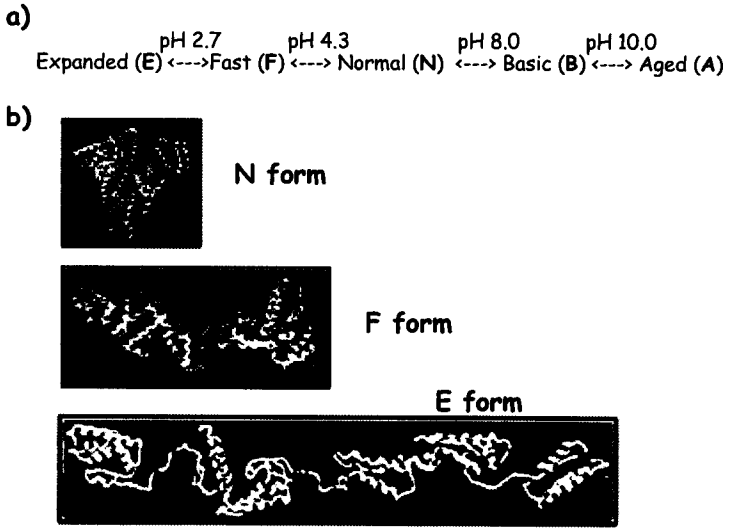

Fig. 6.1 (a) Names of conformations of albumin at different pH and corresponding transition points [F77]; (b) Structures of albumin in normal, fast and extended forms [CH94] [1].

tryptophan residue as a local molecular probe to study albumin conformational changes at different pH using a femtosecond-resolved fluorescence method. The different conformations proposed for the different pH conditions are shown in **Fig. 6.2**

[1] Reprinted with permission from *Advances in Protein Chemistry* 45 (**1994**) 153-203, Carter, D. C.; Ho, J. X, Copyright (1994), Academic Press.

([QZO&06]). Albumin adopts a contracted configurations at basic pH, a flexible globular structure at near-neutral pH, and extended forms at acidic pH.

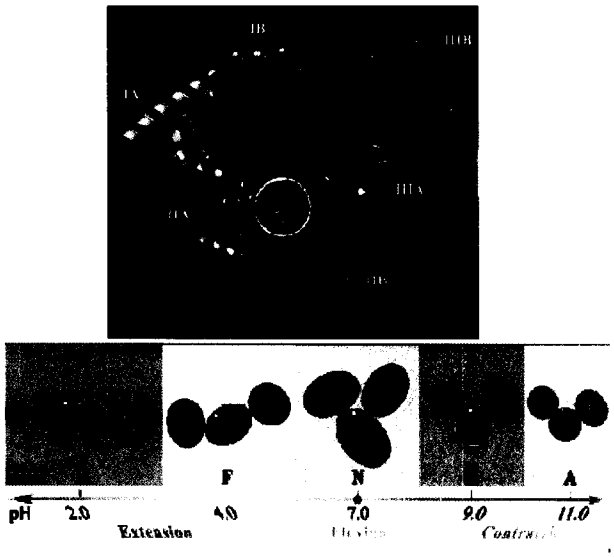

Fig. 6.2 Top: X-ray crystallographic structure of HSA at neutral pH condition. The structure in yellow is the tryptophan molecular probe. Bottom: schematic representation of conformational transitions, from the contracted configuration in basic pH, to the flexible globule structure at neutral pH, and to the extended form in acidic pH. The location of molecular probe is indicated by the white dot in domain IIA [QZO&06][1].

The present chapter analyzes the adsorption of albumin from aqueous solutions of different pH onto a phase segregated PS/PMMA blend surface. From the measured distributions of albumin on chemically distinct regions of the surface (PS, PMMA domains and the PS/PMMA domain interfaces), we are able to identify the preferred sites for HSA adsorption from solutions of different pH. The results are rationalized in terms

[1] Reprinted with permission from *Journal of Physical Chemistry B*, **2006**, Vol.110, Page 10540-10549, Qiu, W.; Zhang, L.; Okobiah, L.; Yang, Y.; Wang, L.; Zhong, D.; Zewail, A.H., Copyright (2006) American Chemical Society.

of changing amounts of exposed hydrophobic/hydrophilic domains as the albumin unfolds and contracts at different pH.

§ 6. 2 Experimental

The preparation of PS/PMMA blend films was described in **Chapter 3**. Protein solutions of 0.05 mg/ml albumin at four different pH were prepared. The solution of pH 2 and pH 4 were prepared by adding HCl drop wise, and the solutions of pH8.6 and pH10 were prepared by adding NaOH drop wise. The neutral pH solution was prepared from unbuffered deionized water and the pH of the solution was measured to be 7.0 ± 0.1.

The sample exposure method described in **Chapter 3** was used. The incubation of PS/PMMA substrate in the albumin solutions was performed in a cell of a Fisher multiwell plate (1 cm diameter well). The incubation time for each sample was 20 minutes. After incubation, each substrate was washed using water of the same pH.

The X-PEEM at ALS bending magnet beamline 7.3.1 [APD&99] was used, following the procedure discussed in **Chapter 4**. Image sequences (stacks) [CSG&00] at the C 1s edge (282 – 296 eV) were recorded in several different areas. These C 1s image sequences were analysed to generate quantitative maps of the PS, PMMA and protein distributions. The chemical mapping is based on the differences among the reference spectra of three components in each system: albumin, PS and PMMA at the C 1s edge [LHR&06]. Since different data sets are used in this work some examples of the mapping and curve fit analysis are presented.

§ 6. 3 Results

As an example, the fitting result from a C1s stack of 0.05 mg/ml (pH = 4.0) albumin adsorption is presented in **Fig. 6.3** in the form of maps of each component: (a) PS, (b) PMMA, (c) albumin, as well as (d) the sum of these components, (e) the residual of the fit, and (f) the color-coded map. The component maps are the fitting coefficients obtained from curve fits of the spectrum at each pixel to a linear combination of the reference spectra and an additional 'constant' (energy-independent) term using the 'stack fit' procedure [HMZ&05]. Each component map is the quantitative spatial distribution of that component with the gray scale limits set to the minimum and maximum thickness per pixel over the whole map. Note that in each of the pH conditions measured in this work the summed signal was constant within 7% over the whole field of view, supporting the underlying assumption of our procedure that the sampling depth is similar in the chemically different regions.

By combing the component maps of PS, PMMA and albumin, a color-coded composite map can be obtained to reveal the spatial correlation of the chemical components, as shown in **Fig. 6.3f**. The PS signal is mapped to red, the PMMA signal is mapped to green, and the albumin signal is mapped to blue. The color-coded map shows a strong blue band which matches the interfaces between the PS and PMMA domains. This indicates a preference for albumin adsorption at the PS/PMMA interfaces.

To obtain the relative amount of albumin on different regions, signals specific to the PS and PMMA domains and the PS/PMMA interface (~ 80 nm band) were extracted by using threshold masking of the component maps to select only those pixels where the

signal was above a defined threshold. The amount of each component (PS, PMMA and albumin) in each region [PS, PMMA, interface] was then obtained by fitting the extracted spectrum using the same reference spectra used in generating the component maps by the stack fit. **Fig. 6.4a** displays the masks while panels (**b-d**) display the curve fit to each extracted spectrum. The points with estimated uncertainties are the experimental spectra. The dark solid curves are the fits to the masked experimental spectra and the color curves are the weighted reference spectra. The results of these fits are reported in **Table 6.1**, along with the results obtained in the same way for other pH studies.

Fig. 6.5 presents color-coded composite maps derived from stack fits of C 1s image sequences measured for albumin on PS/PMMA samples generated by a 20 minute adsorption of albumin from 0.05 mg/ml solutions with pH adjusted to 2.0, 4.0, 7.2, 8.6 and 10.0 respectively. The maps show the variation in the spatial distributions of the protein on the various chemically different parts of the surface. The "purer" the red (green) color, the smaller the amount of protein that is present on the PS (PMMA) domains. The bluish-purple color of the continuous PS domains indicates that there is a significant amount of protein on the PS domains. Similarly, the turquoise color of the discontinuous PMMA domains indicates there is protein on the PMMA domains. The clear blue color at the PS/PMMA boundaries shows that albumin prefers the PS/PMMA interfaces on all of the surfaces examined.

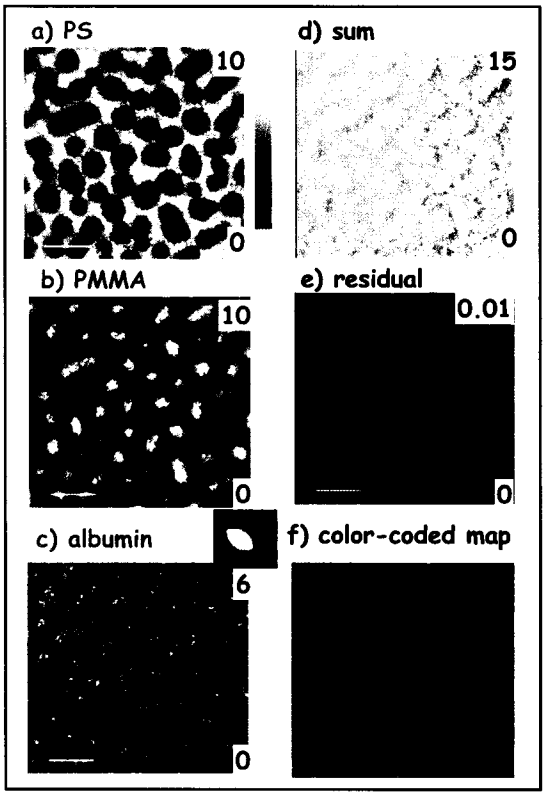

Fig. 6.3 Component maps of (a) PS, (b) PMMA and (c) albumin for a PS/PMMMA blend substrate exposed to a 0.05 mg/ml HSA at pH 4, derived from pixel-by-pixel curve fits of a C 1s image sequence. The numbers in the upper and lower right of each component map are limits of the thickness gray scales in nm. (d) sum of the PS, PMMA and albumin thickness component maps. (e) map of the residual of the fit. The gray scale in the latter case is the deviation of the fit and the measured signal, averaged over all energies. (f) color-coded component map (red is PS, green is PMMA and blue is albumin).

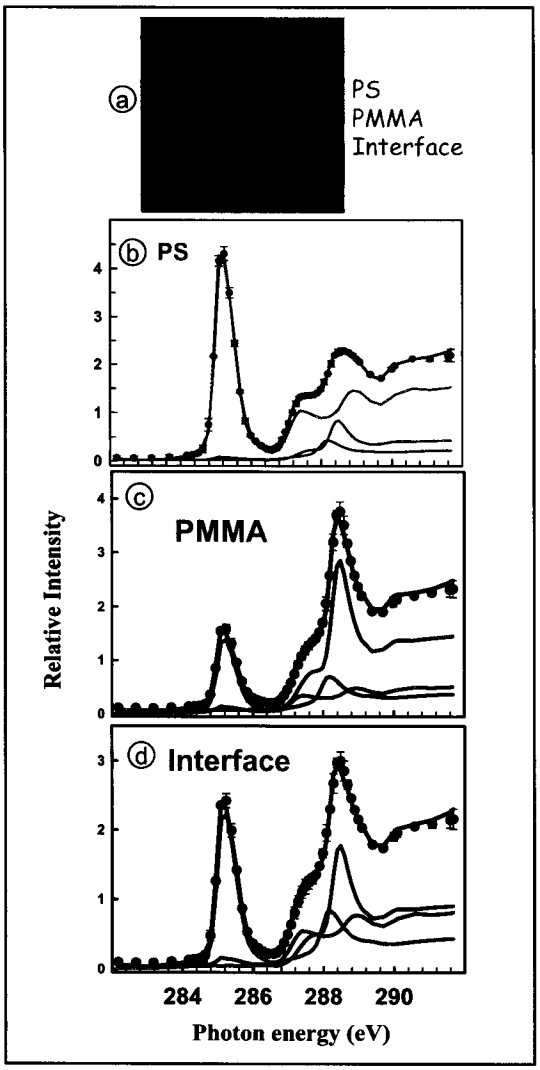

Fig. 6.4 (a) Masks used to extract spectra of specific regions. [red = PS > 4 nm, green = PMMA > 4 nm, blue = PS/PMMA interface (all pixels not identified in the masks of the PS and PMMA domains)]. (b-d) Curve fits to the average C1s spectra extracted from the masked regions (data - points, fit - thick solid line, components – thin lines).

Table 6.1 Adsorption of albumin on PS/PMMA film as f(pH): protein thickness (nm/pixel) on the PS, PMMA and PS/PMMA interfaces (uncertainty: ± 0.1 nm*).

Region	Composite (nm /pixel)	pH 2.0	pH 4.0	pH 7.0	pH 8.6	pH 10.0
PS region	PS	6.0	6.9	5.8	7.2	6.3
	PMMA	1.0	1.7	1.6	2.0	1.8
	Albumin	**3.0**	**1.4**	**2.6**	**0.8**	**1.9**
PMMA region	PS	1.8	2.1	2.3	2.4	2.5
	PMMA	5.0	5.6	5.6	7.2	5.3
	Albumin	**3.2**	**2.3**	**2.1**	**0.4**	**2.2**
Interfacial region	PS	2.8	3.6	3.7	3.7	3.7
	PMMA	2.7	3.6	3.5	3.7	3.6
	Albumin	**4.5**	**2.8**	**2.8**	**2.6**	**2.7**

* See **Section 4.6.1**.

As shown in **Table 6.1**, there is around 10-20% PMMA in the masked PS region and around 20-25% PS in the masked PMMA region, which is associated mostly with microdomains [M IT &01]. The interfacial region contains about the same amount of PS and PMMA, as expected from the spatial location. What is of most interest is the amount of albumin on the chemically different regions of the surface; these values are highlighted in bold in **Table 6.1**. In agreement with the color-coded maps, there is a preference for the albumin to adsorb at the PS/PMMA interface at all pH conditions. At neutral pH (7.2) albumin shows a slightly stronger preference for PS relative to the PMMA domains. At extreme acidic pH (2.0) and basic pH (10) adsorption to the PS and PMMA domains is similar. However at the moderate acidic and basic pH conditions (4.0, 8.6), albumin shows different behavior. At pH 4.0, albumin adsorption to the PMMA domains is ~1.6

times larger than that to the PS domains (PMMA preference), while at pH 8.6 albumin adsorption on PMMA is around half less than that on the PS domains (PS preference).

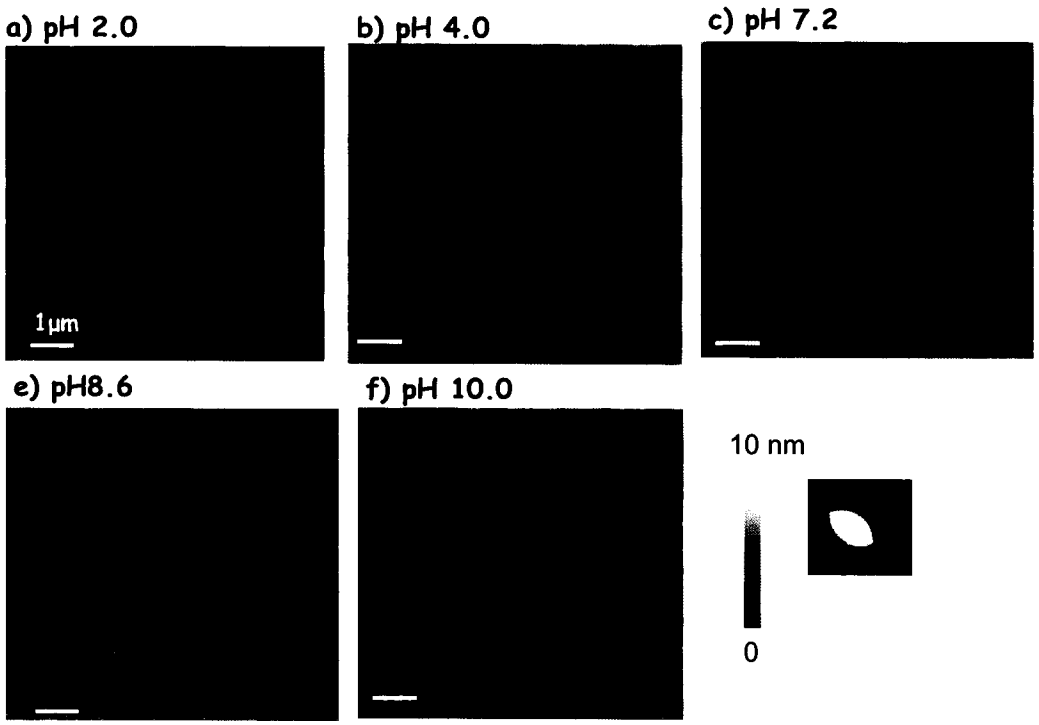

Fig. 6.5 Color-coded component maps of albumin covered PS/PMMA for the indicated pH media.

§ 6. 4 Discussion

Fig. 6.6 summarizes the results of the X-PEEM study in terms of pie charts. The area of each pie is proportional to the total amount of adsorbed albumin (mean thickness, corrected for the relative amounts of each chemically different part of the surface). The relative size of each section is proportional to the albumin thickness (nm/pixel) adsorbed on the PS, PMMA and PS/PMMA interface regions. As the relative area of the gray

region indicates, the PS/PMMA interface was the preferred adsorption site at all values of pH studied. The relative proportions adsorbed on the PS and PMMA regions were similar at pH values of 7.2, 2 and 10.0. However a completely different situation was observed at pH = 4, where PMMA was strongly preferred, and at pH = 8.6 where PS was strongly preferred.

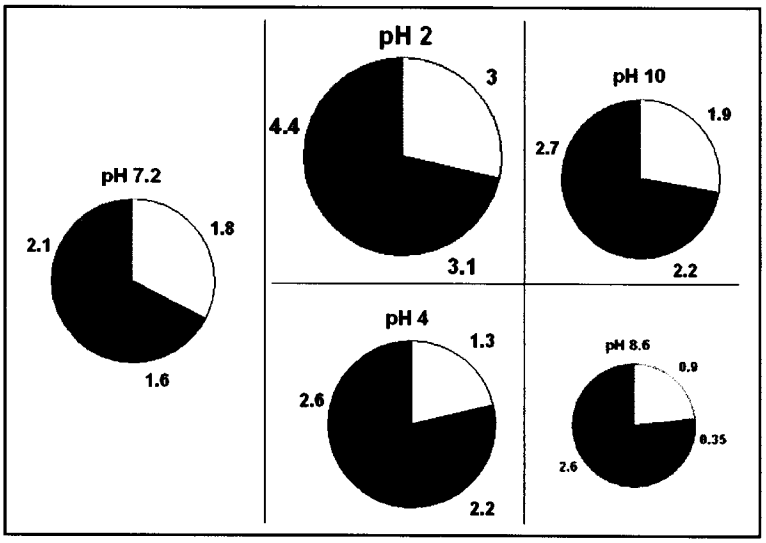

Fig. 6.6 Albumin adsorption on different regions (white—PS, black—PMMA, grey—interface) as a function of pH. The numbers are mean thickness (nm) on each region.

The interface preference has been explained in **Chapter 5** in terms of the cooperative effects of hydrophobic interactions between the hydrophobic fragments of HSA and the PS combined with hydrogen bonding between the hydrophilic fragments of HSA and PMMA.

To explain the pH dependence of the albumin distribution preference on PS and PMMA regions, the surface properties of the PS/PMMA blend should be considered first.

Polymer surfaces usually have low surface charge density. The PS and PMMA polymers used in this work should not have any charges on their surface, because they are prepared by living anionic polymerization, and the introduction of any surface active materials was carefully avoided in the sample preparation. The net charge of albumin varies with pH. The isoelectric point of albumin, where the molecule has zero net charge, is 4.7 [P05]. The net charge of albumin is >+20, +10, -15, -22 and -27 at pH 2.0, 4.0, 7.0, 8.6 and 10.0, respectively [MZ98].

The electrostatic interactions between charged albumin and polymer surfaces are not the dominant driving force for protein adsorption since PS/PMMA surfaces are not charged. However the charges on albumin at different pHs are involved in determining the albumin conformation. The structural changes with pH [F77, CH94, QZO&06] can explain the differences in the adsorption preference at different pHs. Albumin undergoes contraction [QZO&06] when the pH changes from 7.0 to 10.0. Our study shows that albumin has similar adsorption preference for PS and PMMA regions at pH 7.0 and 10.0, but much stronger adsorption preference for PS over PMMA regions at pH 8.6 (although a much smaller amount is actually adsorbed – see **Fig. 6.6**). I interpret this to indicate that albumin has similar amounts of exposed hydrophobic and hydrophilic residues at pH 7.0 and pH 10.0. However in the course of contraction, which could be driven by internal hydrogen bonding, the fraction of hydrophobic residues at the surface of the contracted albumin at pH 8.6 can become relatively larger. If so, a more hydrophobic albumin surface at pH 8.would result in stronger adsorption preference to PS. This interpretation is supported by a recent report that albumin has a larger hydrophobicity at pH 9 than at

pH 7 [AL00]. This also suggests that hydrophobic interactions dominate over electrostatic interactions for albumin adsorption onto the PS/PMMA surface at pH 7.0, 8.6 and 10. Based on this study, I propose that albumin is hiding more hydrophilic groups internally to stabilize its secondary structure through hydrogen bonds among the albumin hydrophilic residues in the course of contraction. Therefore relatively more hydrophobic groups are exposed to the surface, resulting in stronger adsorption on the PS domains.

Albumin undergoes extension (unfolding) [F77, CH94] when pH goes from 7.0 to 2.0. Our study shows that albumin has similar adsorption preference to PS and PMMA regions at pH 7.0 and 2.0, but much stronger adsorption preference to PS over PMMA regions at pH 4.0 (see **Fig. 6.6**). This indicates that albumin exposes similar amounts of hydrophobic and hydrophilic residues at pH 7.0 and pH 2.0. However in the course of extension (unfolding) at pH 4.0, albumin exposes more hydrophilic residues than hydrophilic residues. The lower hydrophobicity of the albumin surface at pH 4.0 results in a weaker adsorption preference to PS regions than PMMA regions. This is consistent with the fact that the hydrophobicity of albumin is less at pH 4.0 than that at pH 7.0 [AL00]. In analogy to the assumption that hydrophilic residues are 'hidden' when albumin contracts in basic media, I propose that when albumin is partly unfolded at pH = 4 [F77, CH94, QZO&06] it exposes more hydrophilic residues by breaking the hydrogen bonds between the hydrophilic residues.

It is conventional wisdom that the pH for maximum amount of protein adsorption is at the isoelectric point, which occurs at pH = 4.7 for albumin[P95]. In this study the

maximum albumin adsorption was observed at pH = 2.0 rather than pH = 4.0, which is closer to the isoelectric point of albumin. I suggest this is because the hydrophobic effect dominates over the electrostatic effect and the fully extended albumin structure at pH 2.0 provides the maximum number of interaction sites for the surface.

In conclusion, the pH dependent results are consistent with hydrophobic interactions dominating over electrostatic interactions for albumin adsorption onto the PS/PMMA surface At pH 8.6, albumin contracts by hiding more hydrophilic groups internally to stabilize its secondary structure through hydrogen bonding. At pH 4.0, albumin is partly unfolded which exposes more hydrophilic residues.

Chapter 7

Effect of incubation temperature on albumin adsorption

This chapter describes the results of albumin adsorption on PS/PMMA blend surface from 0.004 mg/ml aqueous solutions at different adsorption temperatures: 15, 37, and 60°C. The main result is that albumin shows a dramatic increase in the adsorbed amount at 60°C adsorption temperature with unfolding of albumin.

§ 7.1 Introduction

It is important to study the adsorption behavior of albumin at different temperatures for clinical use. For example, albumin is heated to 60°C for about 10 h to inactivate the hepatitis virus. However, most research studies albumin adsorption at room temperature. Sakiyama et al. [STN&98] studied the adsorption and desorption behavior of bovine serum albumin (BSA) on the surface of stainless steel particles. It was found that the amount of BSA adsorbed increases significantly with temperature above 60°C which was attributed to thermal aggregation of albumin molecules at the surface through intermolecular thiol-disulfide interchange reactions.

Following up the study of albumin adsorption at different concentrations and exposure times (**Chapter 5**), and pHs (**Chapter 6**), this chapter studies the adsorption behavior of albumin on a PS/PMMA surface at three different incubation temperatures: 15, 37, and 60°C at a concentration of 0.004 mg/ml unbuffered water solutions.

§ 7.2 Experimental

All the albumin solutions used in this work were prepared from unbuffered de-ionized water. A 0.004 mg/ml solution, diluted from stock 0.1 mg/ml solution, was used for adsorption study with 20 min exposure time at three different solution temperatures: 15, 37, and 60°C.

Fig. 7.1 shows the setup for temperature-controlled protein adsorption. A water bath with a beaker of ~100 ml de-ionized water was heated to a specific temperature using a hot plate. Two glass vials filled with the same amount of protein solutions were then introduced into the water bath. One vial was used for preparation of the protein covered sample while the other was used to observe the temperature under the same condition as protein adsorption to avoid any contamination from the thermometer. A thermometer was inserted into the protein solution in one of the glass vial. When the protein solution stabilizes at the specific temperature (in ~15 min), a piece of PS/PMMA sample was placed into the solution of each glass vial. The temperature varied by < 0.2°C with the introduction of the PS/PMMA sample. After 20 min, the glass vial without thermometer was taken out from the water bath and the protein solution was removed partly using glass pipet from the vial until the solution level is down to the upper edge of the Si wafer covered with PS/PMMA film. The heated de-ionized water was added into the vial to dilute the protein solution and then was removed in the same way. During the third time of adding de-ionized water, the solution was removed completely from the vial. Another two washings were performed in the same way and then the PS/PMMA sample was taken out from the vial to dry and cool down at room temperature. The

sample in the other vial with thermometer was discarded. For the protein adsorption at 15°C, ice was used to control the temperature. For each case, the temperature was stable within 0.3°C.

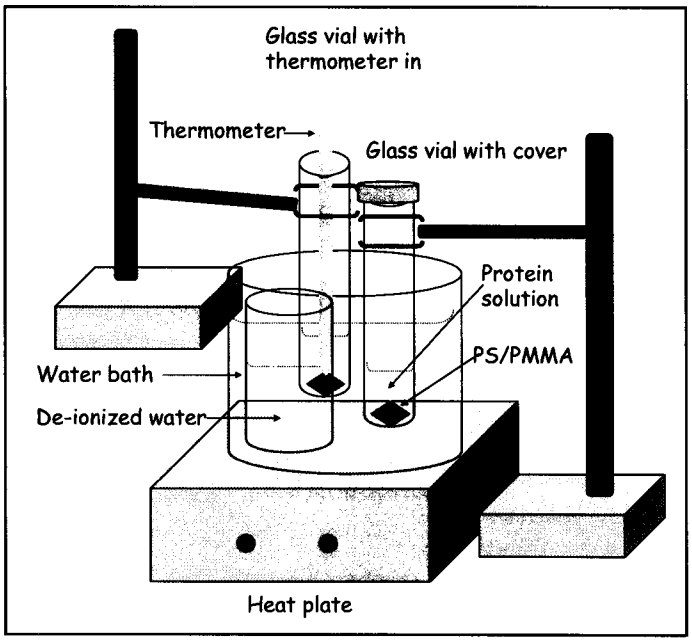

Fig. 7.1 Experimental setup of protein adsorption at a controlled temperature.

§ 7.3 Data analysis and results

The results from a stack fit analysis of the C 1s X-PEEM data for albumin adsorption at 15°C are presented in **Fig. 7.2** in the form of maps of each component: (a) PS, (b) PMMA, (c) albumin, as well as (d) the sum of these components, (e) the residual of the fit, and (f) the color coded composite map (red is PS, green is PMMA, and blue is albumin). The details of the analysis method were discussed in **Chapter 5**. The gray scale limits are the minimum and maximum thickness per pixel. Lighter intensities indicate locations where there is more of that component. The component maps show that

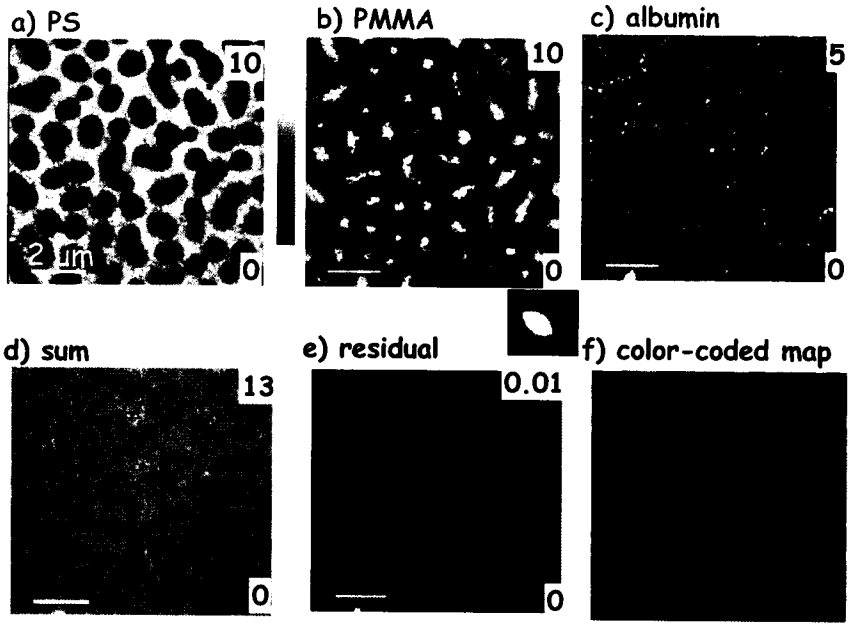

Fig. 7.2 Component maps of (a) PS, (b) PMMA and (c) albumin for a PS/PMMMA blend substrate exposed to a 0.004 mg/ml HSA at 15°C, derived from pixel-by-pixel curve fits of a C 1s image sequence. The numbers in the upper and lower right of each component map are limits of the thickness gray scales in nm. (d) sum of the PS, PMMA and albumin thickness component maps. (e) map of the residual of the fit. The gray scale in the latter case is the deviation of the fit and the measured signal, averaged over all energies. (f) color-coded component map (red is PS, green is PMMA and blue is albumin).

the PS domains are continuous and the PMMA domains are discontinuous, as found in previous studies of PS/PMMA blends prepared from high MW PS and PMMA [M IT &01]. The color-coded composite map reveals the spatial correlation of the chemical components. This is obtained by combining the component maps of PS, PMMA and albumin, with the PS signal in red, the PMMA signal in green, and the HSA signal in blue. The color-coded map shows a distinct blue band at the interface between the PS and PMMA domains. The discontinuous PMMA domains are turquoise rather than green

indicating the presence of HSA on their surface, while the continuous PS domains are nearly red, indicating there was very little HSA on the PS domains.

The color-coded composite maps for the other samples (37 and 60°C) were obtained in a similar way as that for albumin adsorption at 15°C. **Fig. 7.3** shows the color-coded composite maps for albumin adsorption at three temperatures: 15, 37, and 60°C. The maps on the left column are not rescaled, which means a common thickness scale (min/max over all 3 components) is used for all three components. The maps on the right column are rescaled, which means that the intensity of each color is adjusted to fill the full-scale of the associated component map. The non-rescaled maps show there is a dramatic increase in the amount of albumin adsorbed on the surface at the adsorption temperature of 60°C compared with other cases. The rescaled maps better show how the spatial distribution of the albumin changes with adsorption temperatures.

The non-rescaled maps show that the color of the continuous PS domains remains 'almost red' and PMMA domains also remains 'almost green' at the adsorption temperature of 15 and 37°C. However, at adsorption temperature of 37°C, the PS and PMMA domains change to 'purple rather than red' and 'turquoise rather than green', respectively. These results show that there is relatively little albumin on both the PS and PMMA domains for 15 and 37°C adsorption, while the albumin component becomes much thicker at 60°C adsorption. In all cases, the interfaces of the PS and PMMA show a distinct blue color, indicating strong adsorption at the PS/PMMA interfaces. The blue band around the interfaces of the PS and PMMA domains is much clearer in the rescaled

map. These results indicate that, under these adsorption conditions, the preferred adsorption site of albumin is the PS/PMMA interface.

To obtain the relative amount of albumin on different regions, signals specific to the PS and PMMA domains were extracted by using threshold masking of the component maps to select only those pixels where the signal was above a defined threshold. The interface signal from a ~80 nm band at the PS-PMMA interface was obtained by selecting those pixels not present in either the masked PS or masked PMMA maps. The amount of each component (PS, PMMA and albumin) in each region [PS, PMMA, interface] was then obtained by fitting the extracted spectrum using the same reference spectra used in generating the component maps by the stack fit. As an example, the analysis of albumin adsorption at 15°C is shown in **Fig. 7.4**. **Fig. 7.4 a** displays the masks while panels **(b-d)** display the curve fit to each extracted spectrum. The points with estimated uncertainties are the experimental spectra. The dark solid curves are the fits to the masked experimental spectra and the color curves are the weighted reference spectra. The results of these fits are reported in **Table 7.1**, along with the results obtained in similar way from other samples of different adsorption temperatures.

Table 7.1 lists the thicknesses of different components [PS, PMMA, and albumin] on each region [PS domains, PMMA domains and PS/PMMA interfaces] at each adsorption temperature. There are around 15-20% PMMA on the PS region while there is around 20-25% PS on the PMMA region due to the microdomains [M IT &01] associated with incomplete phase separation of PS and PMMA. The interface region consists of similar amounts of PS and PMMA.

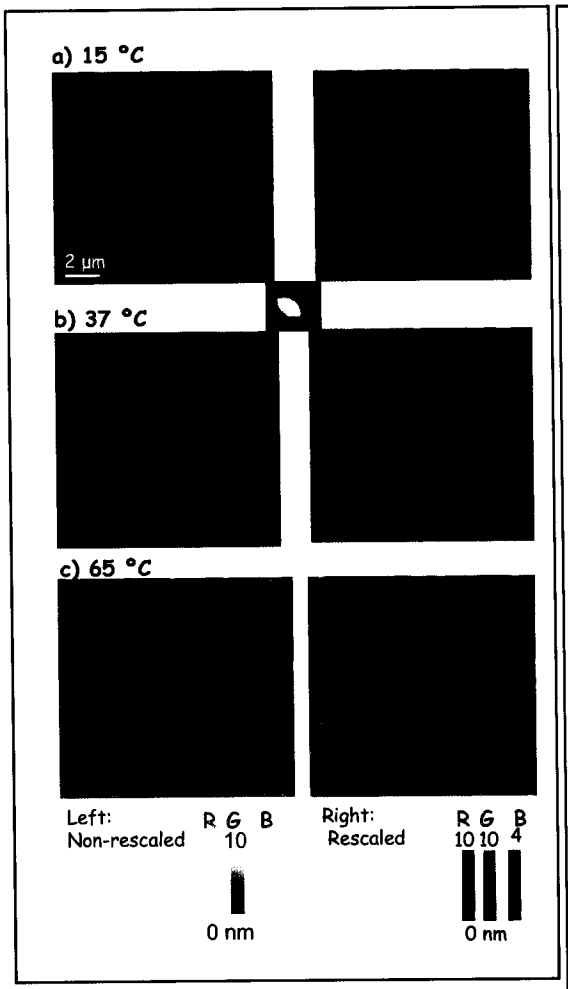

Fig. 7.3 Color-coded component maps of albumin covered PS/PMMA for the indicated adsorption temperature. Left column: non-rescaled map; Right column: rescaled map

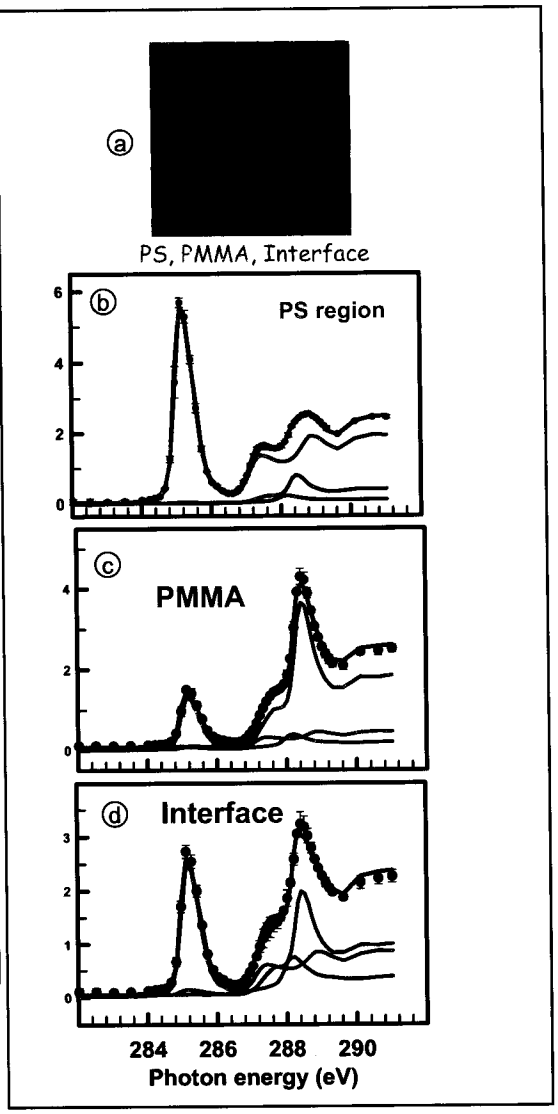

Fig. 7.4 (a) Masks used to extract spectra of specific regions. [red = PS > 4 nm, green = PMMA > 4 nm, blue = PS/PMMA interface (all pixels not identified in the masks of the PS and PMMA domains)]. (b-d) Curve fits to the average C1s spectra extracted from the masked regions (data - points, fit - thick solid line, components – thin lines).

Consistent with the color-coded maps, the adsorbed amount of albumin on both the PS and PMMA domains are much smaller at 15 and 37°C adsorption temperatures than that at 60°C. At 15 and 37°C adsorption temperatures, the amount of albumin on the PMMA domains is also nearly the same but larger than that on the PS domains. Both adsorptions show strong preference to the PS/PMMA interfaces. However, the amount of albumin adsorbed on each region increases dramatically when the adsorption increases to 60°C but the difference in the preference on different regions gets smaller.

Table 7.1 Temperature dependence of adsorption of HSA on PS/PMMA from de-ionized water solution: Composition of PS, PMMA and PS/PMMA interfaces (uncertainty: ± 0.1 nm*).

Region	Composite (nm /pixel)	15°C	37°C	60°C
PS region	PS	7.9	7.6	5.8
	PMMA	1.5	1.6	1.7
	Albumin	**0.6**	**0.8**	**2.5**
PMMA region	PS	1.9	2.5	2.2
	PMMA	7.0	6.5	4.9
	Albumin	**1.1**	**1.0**	**2.9**
Interfacial region	PS	3.8	4.1	3.5
	PMMA	3.8	4.0	3.5
	Albumin	**2.0**	**1.9**	**3.3**
Preference factor of albumin on PS/PMMA/Interface		0.5/1.0/1.8	0.8/1.0/1.9	0.9/1.0/1.1

* See **Section 4.6.1**.

§ 7.4 Discussion

It was reported that HSA denatures around 60°C [GV92]. Consistently, HSA was found to unfold suddenly in a very narrow temperature range of 58-60°C over the studied temperature range of 45-80°C [WCM&00]. The unfolding of HSA at 60°C can explain the dramatic increase in the adsorbed amount of albumin at 60°C adsorption temperature found in our study (See **Fig. 7.5**) since the unfolded HSA has a larger surface area available for interacting with the substrate. Upon unfolding, albumin exposes more hydrophobic residues to the solution [WCM&00], and thus the albumin adsorbed on the hydrophobic PS domains increases. Furthermore, more water species are released from

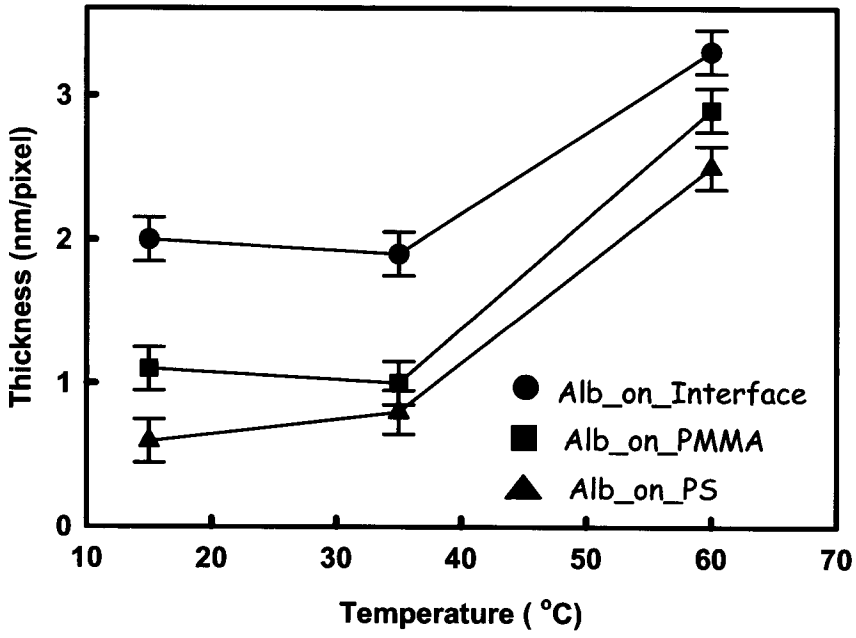

Fig. 7.5 Adsorbed amount thickness (nm/pixel) on different regions of the PS/PMMA blend surface: triangle (▲) is albumin_on_PS, rectangle (■) is albumin_on_PMMA and round (●) is albumin_on_interface. The two adsorbed data points on each region are connected by a strange line.

the hydrogen bonds inside the albumin [WCM&00]. The released hydrogen binding sites inside the albumin result in increasing hydrogen bonding between the albumin and PMMA domains.

Chapter 8

Comparison of albumin and fibrinogen adsorption

This chapter compares the adsorption of two proteins (human serum albumin and fibrinogen) onto a PS/PMMA blend surface from 0.05 and 0.01 mg/ml phosphate buffered saline (PBS) solutions (pH 7.2). The main result is that fibrinogen shows weaker adsorption and it undergoes conformation changes when the concentration increases from 0.01 to 0.05 mg/ml.

§ 8. 1 Introduction

Due to its significance in biotechnology in designing blood-compatible surfaces and devices, adsorption of blood proteins has been extensively studied with many different experimental techniques in an attempt to understand the complex process of protein adsorption (See **Chapter 5**). In the context of this chapter, recently Roach et al [RFP05] have compared adsorption of albumin and fibrinogen (0.05~1.0 mg/ml phosphate-buffered saline solutions) on model hydrophobic hetanethiol and hydrophilic mercaptoethanol surfaces using a quartz crystal microbalance (QCM) and grazing angle infrared spectroscopy. It was found that albumin has a much higher binding affinity to the hydrophobic surface than to the hydrophilic surface. Fibrinogen has much stronger absorption to both surfaces than albumin. Albumin was found to have a lower degree of ordered structure on the hydrophobic surface than on the hydrophilic surface and albumin shows a single stage adsorption process within the concentration 1.0 mg/ml. Fibrinogen

was found to have greater conformation deformation induced by adsorption on the hydrophobic surface than on the hydrophilic surface and fibrinogen undergoes a multistage adsorption process at concentration higher than 0.5 mg/ml. Johnson et al [JWC05] have used sum frequency generation (SFG) spectroscopy to study fibrinogen adsorption from 1 mg/ml phosphate-buffered saline solution on a PS surface, PMMA surface and 1:1 PS/PMMA blend surface in order to investigate the property of the blend surface. It was found the fibrinogen structure changes slightly on the PS surface whereas it changes significantly on the PMMA surface within a 65 min adsorption time. The adsorption of fibrinogen on the PS/PMMA blend surface was dominated by contributions from fibrinogen molecules adsorbed on the PMMA domains within a 30 min adsorption time.

In this work I compare adsorption of two different proteins, human serum albumin and fibrinogen, from two concentrations of phosphate buffered saline (PBS) solutions onto the same type of PS/PMMA surface as used for other studies in this thesis. Albumin is the most abundant protein in blood with a molecular weight of 66 kDa. It has an ellipsoid shape with size of 4 by 14 nm. Fibrinogen is the key structural glycoprotein in blood clotting with a molecular weight of 340 kDa. It is rod shaped with a long dimension of 46 nm [RFP05].

In addition to X-PEEM, ^{125}I-labeling results of the adsorption isotherms of the two proteins onto pure PS, pure PMMA and the PS/PMMA blend surfaces are presented. Details of that technique were presented in **Chapter 3**. By combining the results of the two different studies, the differences in adsorption of HSA and fibrinogen on this surface

have been derived and interpreted. To our knowledge, this is the first time that a large difference in the adsorption behavior of different proteins has been measured using X-ray microscopy and also the first time for a competitive adsorption study using X-ray microscopy.

§ 8. 2 Experimental

The preparation of PS/PMMA blend films have been discussed in **Chapter 3**. Protein solutions were prepared from phosphate buffered saline (PBS, PH=7.2) at two concentrations: 0.05 and 0.01 mg/ml, by diluting 0.5 mg/ml solutions. The mixtures of the two proteins were prepared by mixing the two single protein solutions at the same concentration with volume ratio of 1:1.

The sample exposure method and ^{125}I –label technique have been discussed in **Chapter 3**.

The X-PEEM at ALS bending magnet beamline 7.3.1 [APD&99] was used for this work. The same experimental condition used in the work of [LHR&06] was used in this work. Image sequences (stacks) [CSG&00] of the C1s edge were recorded at several different areas for analysis in order to map the PS, PMMA and albumin distributions.

§ 8. 3 Data analysis

As an example, the fitting result from a C1s stack of 0.01mg/ml PBS fibrinogen adsorption is presented in **Fig. 8.1** in the form of the maps of each component: a) PS, b) PMMA, c) albumin, d) sum of all components, and e) residue of the fit, as well as f) the

color-coded composite map of PS, PMMA and albumin (red is PS, green is PMMA and blue is albumin). The numbers showed on the right hand side of each map are the minimum and maximum thicknesses of 10 nm (See **Chapter 5**) based on normalizing the total signal to a sample depth of 10 nm of X-PEEM in our system. The color-coded map shows a strong blue band at the interface between the PS and PMMA domains. This indicates a preference for albumin adsorption at the PS/PMMA interfaces.

To obtain the relative amount of albumin on different regions, signals specific to only the PS domains, only the PMMA domains, and to a ~80 nm band at the PS-PMMA interface were extracted by using threshold masking. The masks of the PS, PMMA and interface are shown in **Fig. 8.2 a**. The masks of the PS, PMMA and interfacial regions are mapped with red, green and white colors individually. The extracted spectrum from each masked region was fit using the reference spectra to obtain the average amount of each component (PS, PMMA and protein) in each type of surface region. The curve fit to each extracted spectrum is shown in **Fig. 8.2 (b)-(d)**. The points with estimated uncertainties are the experimental spectrum. The dark solid curve is the fitting curve and the color curves are the weighted reference spectra. The fitting results are reported in **Table 8.1**.

As shown in **Table 8.1**, there is around 15-20% PMMA in the masked PS region and 20-25% PS in the masked PMMA region, which is associated mostly with microdomains [M IT &01]. The interfacial region contains about the same amount of PS and PMMA, as expected from the spatial location. The amount of albumin on the chemically different regions of the surface, which is of most interest, is highlighted in

Table 8.1 in bold font. The last column of the tables shows the ratio of albumin on different regions. Similarly, the same information can be generated for other samples and summarized in **Table 8.2** in the section of 'Results and discussions'.

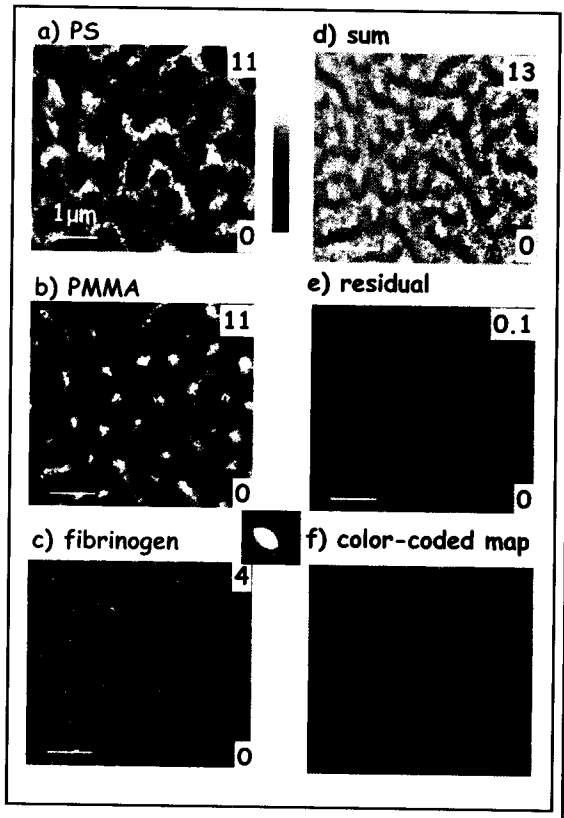

Fig. 8.1 Maps of PS, PMMA and albumin produced by stack fit of a C1s image sequence of 0.01 mg/ml PBS fibrinogen adsorption (the scale bar is 1 μm). The numbers at the lower and upper right-hand side of each component map are the maximum and minimum thickness per pixel with a linear color gradient as indicated by the grayscale bar. Lighter intensities indicate locations where there is more of that component. The color-coded map is rescaled.

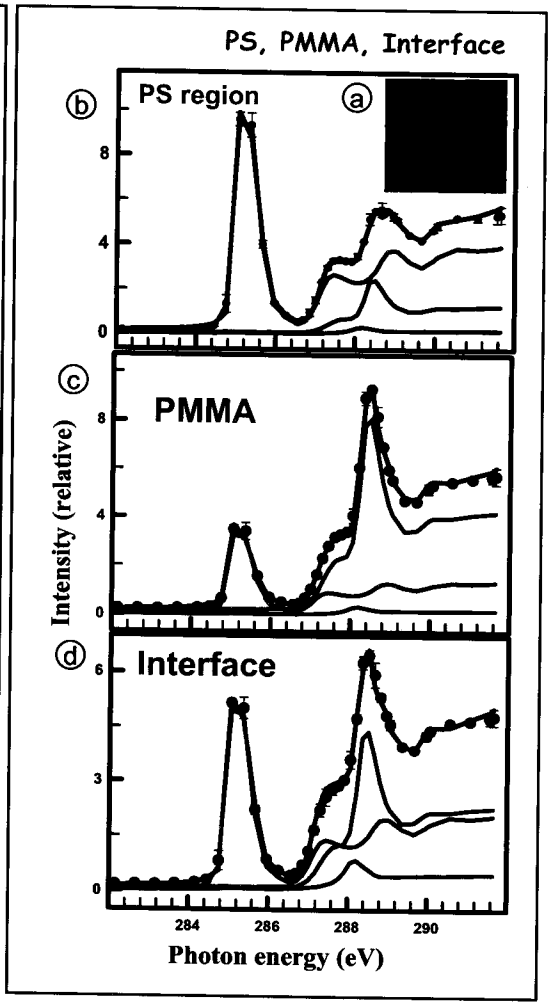

Fig. 8.2 Masked maps (a) of PS, PMMA and interface of PS/PMMA and the corresponding curve fittings (b-d) of the C1s spectrum extracted from the masked region.

Table 8.1 Adsorption of albumin on PS/PMMA film from 0.01mg/ml PBS solution: Composition of PS, PMMA and PS/PMMA interfaces (nm/pixel) (uncertainty ±0.1 nm*)

ROI A	PS composition	PMMA composition	HSA composition	Preference factor of HSA on PS/PMMA/Interface
PS region	6.5	1.7	**1.8**	**1.1/1.0/1.3**
PMMA region	2.3	6.1	**1.6**	
Interfacial region	3.9	3.9	**2.1**	

- See **Section 4.6.1**.

§ 8. 4 Results and Discussions

§ 8. 4. 1 ^{125}I-labeled Adsorption Isotherms of HSA and Fibrinogen

Fig. 8.3 shows isotherms for adsorption of ^{125}I-labeled fibrinogen and HSA from phosphate buffer onto pure PS, to pure PMMA and to the PS/PMMA blend surface. Different from the albumin adsorption isotherm in **Fig 3.6**, the absorbed amounts of proteins in mass per unit are converted to molar per unit area in **Fig. 8.3**. The protein concentrations are in unit of mg/ml in **Fig. 8.3a** while in unit of mol/ml in **Fig. 8.3b**. The fibrinogen adsorption results are from the measurements conducted by Rena Cornelius and Cynthia Morin. The amount of HSA or fibrinogen adsorbed onto the PS/PMMA blend as a function of exposure time is fit with a Langmuir-like isotherm formula (**Equation 8.1**) (HSA – black; Fibrinogen – blue).

$$\theta = aC/(b+C) \qquad (8.1)$$

where θ is the fraction of surface coverage, a and b are constants, and C is the concentration of protein solution (See Equation 3.2 for Langmuir equation). Since the two constants *a* and *b* do not have any physical meanings, then their fitting values are not presented here.

The adsorptions of two proteins onto either the PS or the PMMA surfaces also follow the Langmuir-like model and the fitting results are plotted as thinner curves. In the radio-labeling isotherms in **Fig. 8.3b**, the protein concentrations in the X-axis are in units of mol/ml while the adsorbed amounts in the Y-axis are in units of mol/cm^2. The isotherms show that the molar (i.e number) of adsorbed albumin molecules is larger on each studied surface (PS, PMMA and PS/PMMA blend) than the molar per area (i.e number per area) of adsorbed fibrinogen molecules when adsorption from the solutions with the same concentrations in units of mol/ ml. This indicates that albumin has stronger adsorption than fibrinogen. Furthermore, HSA shows a larger difference than fibrinogen in the amount adsorbed on different surfaces (PS, PMMA and PS/PMMA blend).

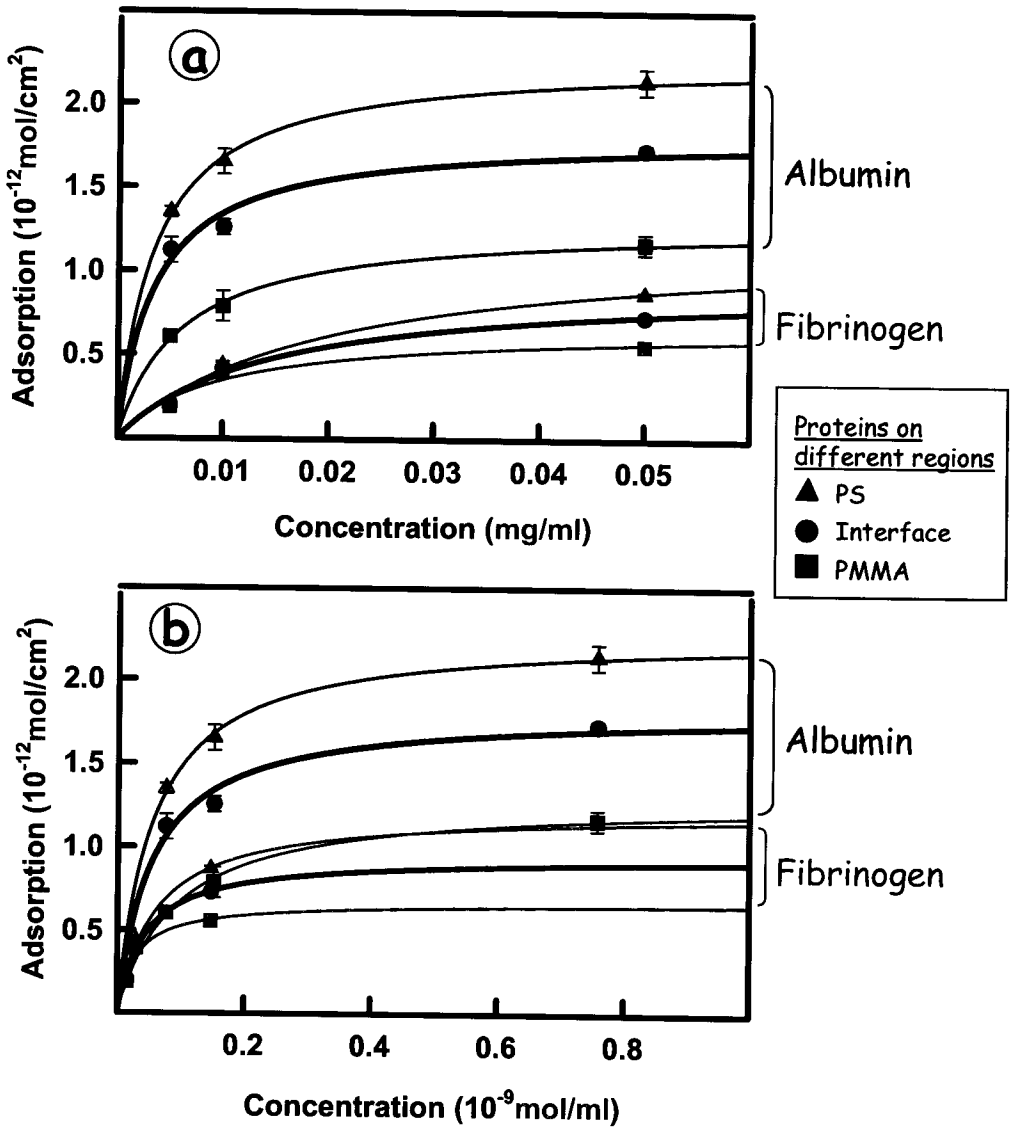

Fig. 8.3 Isotherms for adsorption of fibrinogen and albumin on pure PS, pure PM and the blend measured using ^{125}I radiolabeling. **a)** Adsorption amount in mole/area versus concentration in mg/ml; **b)** Adsorption amount in mole/area versus concentration in mol/ml. The lines are fits to the Langmuir-like isotherm model. Black lines are used for albumin adsorption on different surfaces [PS (triangle), PMMA (rectangle) and PS/PMMA blend (round), while the blue lines are used for fibrinogen adsorption on different surfaces [PS (triangle-dot), PMMA (rectangle-dot) and PS/PMMA blend (round-dot)]. The error is estimated from the four repeat measurements.

§ 8. 4. 2 X-PEEM Study of Adsorption of HSA and Fibrinogen

The adsorption of albumin and fibrinogen from 0.01 and 0.05 mg/ml PBS solutions was studied. **Fig. 8.4** presents color-coded composite maps for these four systems, derived from stack fits [HM&05] of C 1s image sequences. Within the presentation for each protein solution concentration, the maps in the top row are not rescaled and a common thickness scale is used across all three components. The maps on the bottom row are rescaled and the intensity of each color is adjusted to fill the full-scale of the associated component map. The non-rescaled maps show the absolute protein thickness in the different systems, while the rescaled maps show the variation in the spatial distributions of the proteins.

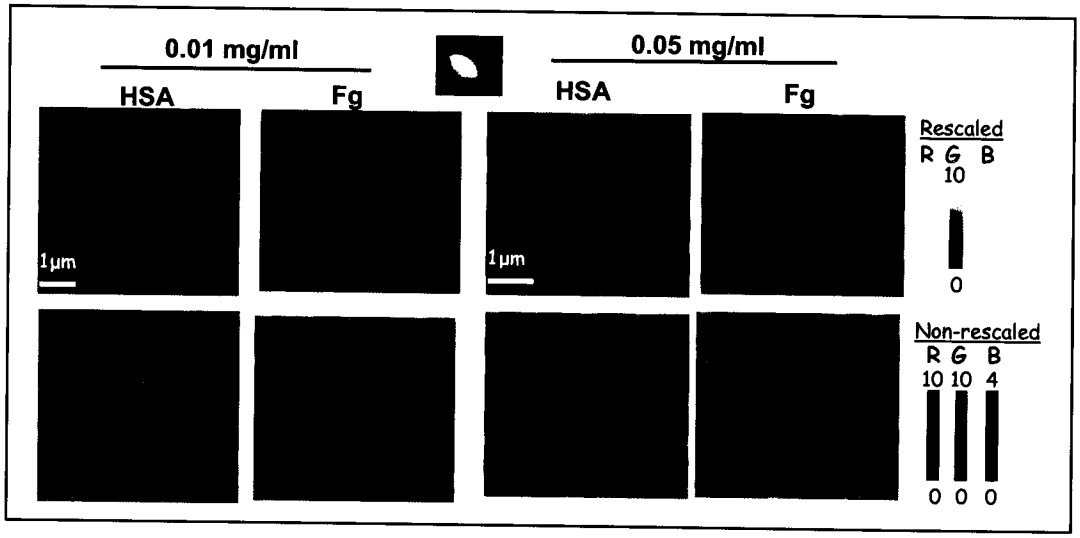

Fig. 8.4 Color-coded component maps of albumin and fibrinogen covered PS/PMMA at concentrations of 0.01 and 0.05 mg/ml. Top: rescaled maps; Bottom: non-rescaled maps.

The non-rescaled maps show that the thicknesses of the adsorbed proteins increase with concentrations. The rescaled maps show that both proteins have strongest preference to the PS/PMMA interfaces in all cases, especially for the case of 0.01mg/ml fibrinogen.

The protein thicknesses obtained from fitting are summarized in **Table 8.2**. Fibrinogen shows strong absorption preference onto the PS/PMMA interfaces at 0.01mg/ml while only a slight preference to the PS/PMMA interfaces at 0.05 mg/ml.

Table 8.2 Adsorptions of albumin and fibrinogen on PS/PMMA film from PBS solutions: thickness (nm/pixel) of each component (PS, PMMA and protein) on the regions of PS, PMMA and PS/PMMA interfaces (uncertainty: ± 0.1 nm*).

Thickness of each component on different region (nm/pixel)		**0.01 mg/ml**		**0.05 mg/ml**	
		HSA	**fibrinogen**	**HSA**	**fibrinogen**
PS region	PS	6.5	7.6	5.7	5.4
	PMMA	1.7	1.9	1.1	1.2
	protein	**1.8**	**0.5**	**3.2**	**3.4**
PMMA region	PS	2.3	2.6	1.5	1.7
	PMMA	1.6	6.9	4.5	4.1
	protein	**1.6**	**0.5**	**4.0**	**4.1**
Interfacial region	PS	4.0	4.5	3.0	2.8
	PMMA	3.9	4.4	2.9	2.7
	protein	**2.1**	**1.1**	**4.2**	**4.4**
Preference factor of proteins on PS/PMMA/Interface		**1.1/1.0/1.3**	**1.0/1.0/2.2**	**0.8/1.0/1.0**	**0.8/1.0/1.1**

* See **Section 4.6.1**.

§ 8. 4. 3 Comparison of ^{125}I-label and X-PEEM Studies

Radio-labeling detects the number density of absorbed protein without spatial resolution, while X-PEEM detects the thickness of absorbed protein in a spatially resolved manner. Radio-labeling cannot differentiate the contributions from the separate types of surface adsorption sites (PS domains, PMMA domains, or PS/PMMA interdomainal interfaces). However, some information can be derived by comparison of the results from the two different techniques.

Fig. 8.4 compares the adsorption of albumin and fibrinogen from the studies of radio-labeling (a) and X-PEEM (b) at the two concentrations (0.01 and 0.05 mg/ml). For 0.01 mg/ml albumin, the radio-labeling study shows that the amount of absorbed albumin molecules is largest on the PS surface, smaller on the PS/PMMA blend surface, and smallest on the PMMA surface. The X-PEEM study also shows than the albumin thickness on the PS domains is thicker than that on the PMMA domains of the PS/PMMA bend. This is consistent with the radio-labeling result that more adsorbed albumin molecules are on the PS surface than on the PMMA surface (starts from the same mg/ml solutions) but the difference in the thickness (i.e. surface coverage in the sub-monolayer adsorption in our case) detected by X-PEEM is smaller than the difference in the number adsorbed albumin molecules detected by radio-labeling technique.

For 0.01 mg/ml fibrinogen, the radio-label study shows that the number per area of absorbed albumin molecules is almost the same on the PS, PMMA and PS/PMMA blend surfaces. Consistently, X-PEEM study shows that the albumin thickness on the PS and PMMA domains of the blend is identical. However, the albumin thickness on the

PS/PMMA interfaces is around twice of that on the PS or PMMA domains. This indicates that the PS/PMMA interfaces are the first binding sites, as found in the previous study [LHR&06].

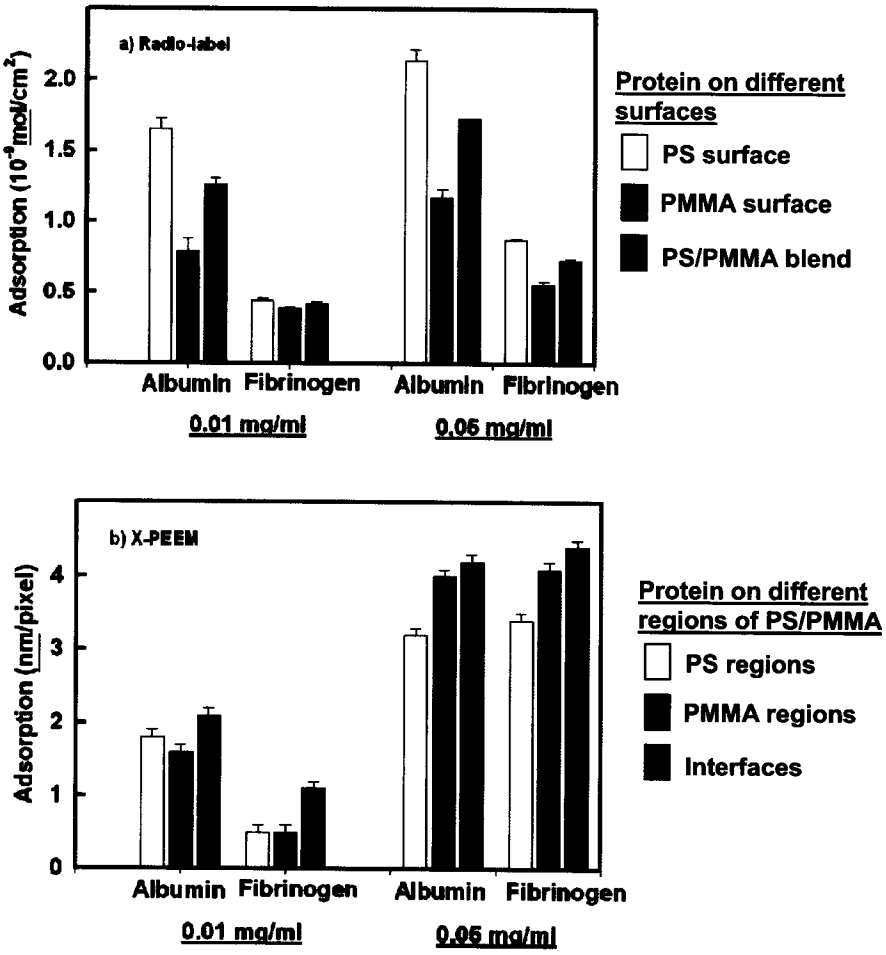

Fig. 8.5 (a) Radio-label measurement of albumin and fibrinogen adsorption onto the PS (white bar), PMMA (black bar) and PS/PMMA blend (grey bar) surfaces from 0.01 and 0.05 mg/ml PBS solutions. The error is estimated from the four repeat measurements (b) X-PEEM measurement of albumin and fibrinogen adsorption onto the PS (white bar), PMMA (black bar) and PS/PMMA interface (grey bar) regions of the PS/PMMA blend at 0.01 and 0.05 mg/ml PBS concentrations. See Sections 3.3 and 4.6.1 and for the estimate of error bar.

Interestingly, for 0.05 mg/ml albumin and fibrinogen adsorption, the radio-label study shows that the adsorbed number of both albumin and fibrinogen molecules on the PS surface is larger than that on the PMMA surface, while X-PEEM study shows an opposite case: the adsorbed thickness on the PS domains is smaller than that on the PMMA domains.

§ 8. 4. 4 Discussion

As has been discussed previously [LHR06], the interface preference can be explained as a result of cooperative action of the hydrophobic interactions between the hydrophobic fragments of a protein and the PS and the hydrogen bonding between the hydrophilic fragments of a protein and the PMMA.

A fibrinogen molecule ($6\times6\times45$ nm^3) is larger than an albumin molecule ($4\times4\times14$ nm^3). It has been reported that albumin has a preference to adsorb with the long axis parallel to the surface and thus the maximum thickness is 4 nm under submonlayer adsorption level [JJC&97]. The adsorption of fibrinogen is more complex. Roach et al. [RFP05] proposed that fibrinogen undergoes a multistage adsorption process at high concentration ((> 0.5mg/ml) based on studies in the concentration range of 0.05-1.0 mg/ml. Roach [RFP05] propose that fibrinogen initially adsorbs rapidly with its long axis parallel to the surface to cover the surface quickly, and then the adsorbed fibrinogen undergoes rearrangement to a perpendicular orientation to allow further adsorption onto newly free adsorbed sites. The proposed mechanism for the rearrangement is the resulting increased hydrophobic interactions between fibrinogen molecules when

fibrinogen molecules align with long axis parallel to each other but not the surface (See Fig. 8.6).

In our study, when the concentration increases from 0.01 to 0.05 mg/ml, the number of absorbed **albumin** per area detected by radio-labeling increases by a factor of ~1.3 on the PS surface and ~1.5 on the PMMA surface. The thickness of adsorbed **albumin** per pixel detected by X-PEEM increases by a factor of ~1.8 on the PS domains and ~2.5 on the PMMA domains. For fibrinogen, the number of adsorbed **fibrinogen** per area increases by a factor of ~2 on the PS surface and ~1.4 on the PMMA surface which is similar to that of albumin. However the thickness of adsorbed **fibrinogen** per pixel detected by X-PEEM increase by ~7 factor on the PS domains and ~8 factor on the PMMA domains which is much larger than that for albumin. This indicates that a multistage adsorption process can occur in the adsorption of fibrinogen onto the PS/PMMA surface at a low concentration of 0.05 mg/ml (compared with the concentration of 0.5 mg/ml reported by Roach et al. [RFP05]). As sketched in **Fig. 8.6**, at 0.01 mg/ml, both fibrinogen and albumin align their long axes parallel to the surface but fibrinogen shows lower affinity to the surface (less adsorbed number per area when starts from the same mol/ml solution). At 0.05 mg/ml, fibrinogen undergoes rearrangement to align the long axis normal to the surface to allow more fibrinogen to adsorb onto the surface. The rearranged fibrinogen may also align on the surface with the long axis against the surface at an angle smaller than 90° (see **Fig. 8.6**). This can explain why the thickness of adsorbed fibrinogen has an unusual increase rate when the concentration increases from 0.01 to 0.05 mg/ml.

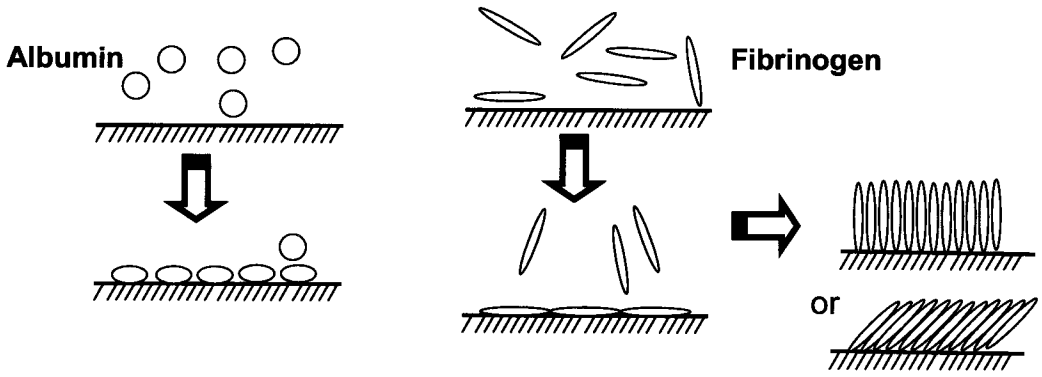

Fig. 8.6 Adsorption process of albumin and fibrinogen.

Following up the comparison of the adsorptions of fibrinogen and albumin, I explored application of X-PEEM to study competitive adsorptions of the two proteins – ie exposure to a mixed fibrinogen and albumin solution. This part of the work is not presented in this thesis since it needs more analysis.

Chapter 9

Albumin adsorption in presence of solution

This chapter describes a Scanning Transmission X-ray Microscopy (STXM) study of albumin adsorption onto a PS/PMMA blend surface, where the sample is in a wet cell with a residual aqueous layer of the 0.05 mg/ml human serum albumin (HSA) solution. The result is consistent with X-PEEM in that the first adsorption site is the PS/PMMA interfaces but the difference in the adsorbed amount on the PS and PMMA domains is larger than that detected by X-PEEM. This is possibly due to sample heating by the strongly focused X-rays which could excite motion of the albumin molecules.

§ 9.1 Introduction

Albumin adsorption on the PS/PMMA blend surface under a variety of solution conditions has been investigated using X-PEEM, as discussed in **Chapter 5** through **Chapter 8**. A major concern and limitation of X-PEEM is that the sample is in an ultrahigh vacuum ($P < 10^{-8}$ torr) which could lead to denaturation. STXM is less surface sensitive than X-PEEM but it has the advantage of being able to measure the C 1s signals from samples which have up to ~ 2μm of aqueous solution in the path of the X-rays. This makes it possible to study protein adsorption under very natural conditions, namely in the presence of the protein solution. Such measurement is closer to the real protein adsorption issue in biological science. This is the first X-ray microscopy study of protein adsorption on a PS/PMMA blend surface in solution. An earlier study by Cynthia Morin

[HMH&02] presented STXM results for fibrinogen adsorption on a filled polyurethane sample, in the presence of an aqueous overlayer solution.

§ 9.2 Experimental

§ 9.2.1 Sample Preparation

For the preparation of PS/PMMA blend films, please see Chapter 5. Human serum albumin (HSA) was obtained from Behringwerke AG, Marburg, Germany, and found to be homogeneous as judged by sodium dodecyl sulphate polyacrylamide gel electrophoresis (SDS-PAGE). The 0.05 mg/ml albumin solution used in this work were prepared from unbuffered de-ionized water, diluted from 0.1 mg/ml albumin solution,

Two Si_3N_4 windows were used for making a wet cell. One window was covered with PS/PMMA blend (see **Chapter 3** for how to float a PS/PMMA blend film onto a Si_3N_4 window). One side of a Si_3N_4 window is flat while the other side is a 200 micron deep well, created by the back etching used to make the 100 nm free standing Si_3N_4 membrane. The flat sides of the windows are used for the inner surfaces of the wet cell. **Fig. 9.1** shows the procedure used to make a wet cell for STXM measurements. A drop of ~ 10 μl albumin solution was put on a Si_3N_4 window using the micropipette. The outer perimeter (~1 cm) of the Si_3N_4 window was glued with epoxy. A second Si_3N_4 window was placed on the first window and then the two windows were aligned. A needle was then used to clear away the epoxy squeezed out from the windows. The epoxy was allowed to dry before putting the wet cell into the experimental chamber of STXM. In

order to avoid the contamination of epoxy to the sample, a Si_3N_4 window with larger frame is recommend.

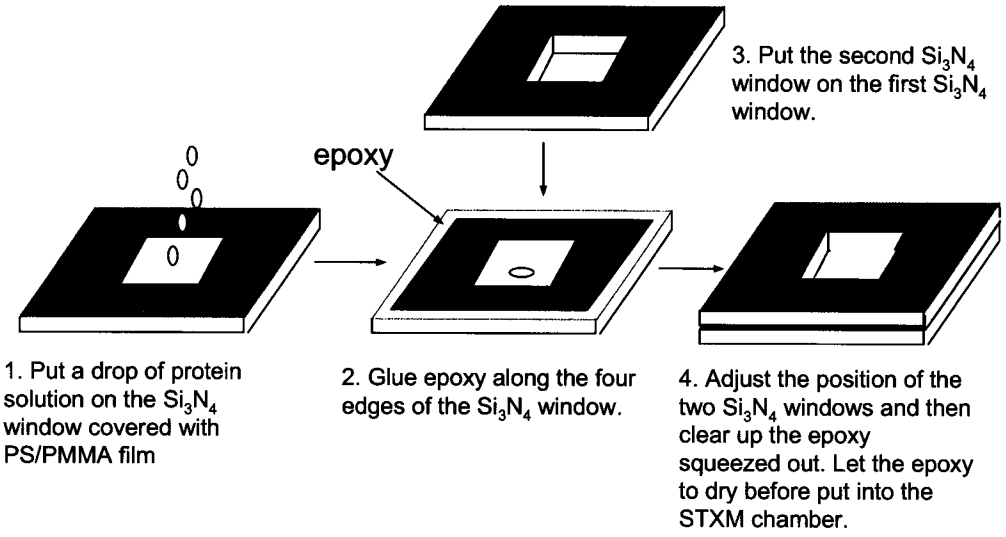

Fig. 9.1 Diagram of making a wet cell for STXM measurement.

§ 9.2.2 STXM

The measurements were carried out on the interferometrically controlled STXM [KTS&03] located at bend magnet beamline 5.3.2 [WAK&02] at the Advanced Light Source (ALS). The very thin (100 nm) Si_3N_4 member can be easily broken by gas/liquid pressure if the STXM chamber is pumped. Thus the sample loading procedure used was as follows. Before the wet cell was put into the STXM chamber, the chamber was pumped and then filled with He gas to one atmosphere pressure until the O 1s signal leveled off. The gas was left flowing while the wet cell was placed into the chamber. After that the He gas was flowed for another 10 minutes without any pumping. The level

of the N_2 signal at 401.1 eV was monitored to ensure minimal residual air, although in fact there was significant signal from the O_2 of the residual air in the results.

Image sequences [JWF&00] were used in this work. However, before recording an image sequence, an O 1s point spectrum was measured to check if the wet cell was still wet, by comparing that spectrum to the O1s spectrum of water. In **Fig. 9.2a**, the thicker curve is the O 1s point spectrum recorded on the sample. The sharp peak at around 531 eV shown is due to the overlap of the 1s $\rightarrow \pi^*$ transition in O_2 (530.8 eV) and the peaks of O 1s (O=C)$\rightarrow \pi^*_{O=C}$ transitions of PMMA and albumin. The peaks at around 539 and 542 eV are due to the presence of O_2, as indicated by the O 1s spectrum of O_2 in the thinner curve shown in **Fig. 9.2a**. The O_2 signal is from the residue of O_2 that was not replaced by the flowing He gas. The O_2 signal can be subtracted from the recorded sample spectrum. The corrected sample spectrum (with O_2 signal subtraction) is plotted in **Fig. 9.2b** in the thicker curve, which also plots the O 1s spectrum of water expected from 160 nm thickness (thinner curve). **Fig. 9.2c** is the ratio of the corrected spectrum to the O 1s spectrum of water. The ratio curve has a nearly flat line above 533 eV, corresponding to a thickness of ~130 nm water layer on the sample, as indicated by the dashed line.

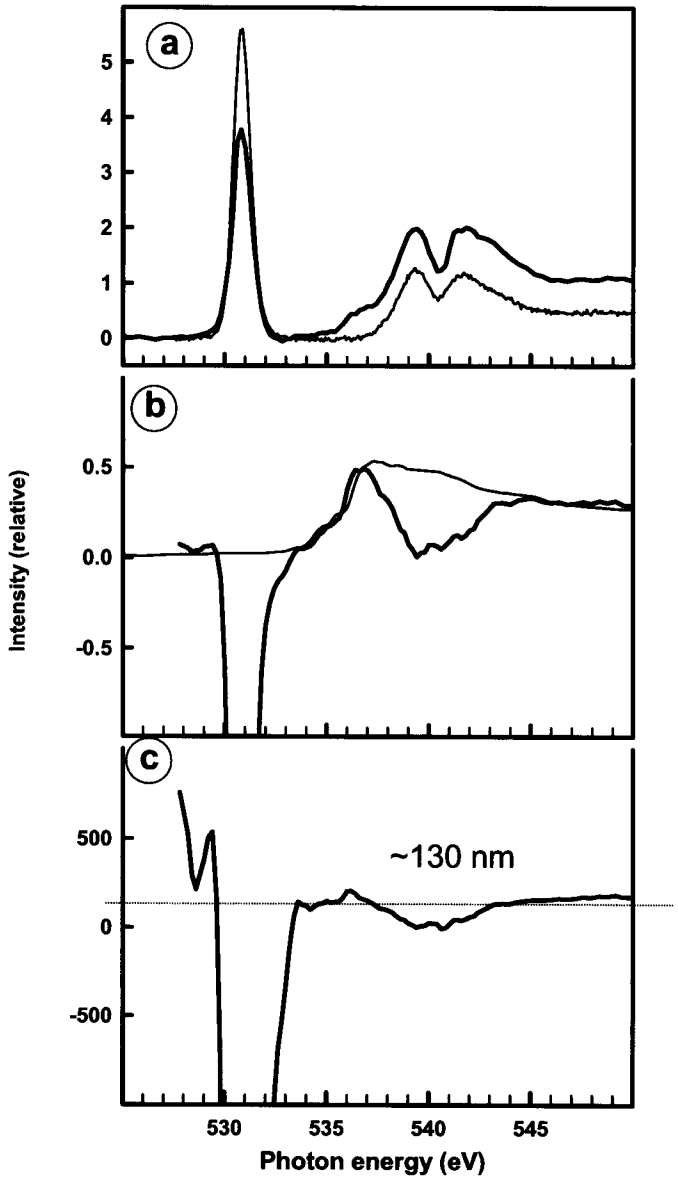

Fig. 9.2 (a) The O 1s point spectrum on the sample (heavy curve) and the O 1s spectrum of O_2 with a quantitative linear absorbance scale (thinner curve); (b) the sample spectrum subtracted with the O_2 signal (thicker curve) and the 130 fold of the O 1s spectrum of water (a) (thinner curve); (c) the ratio of the corrected sample spectrum with O_2 signal subtraction to the spectrum of water with a quantitative linear absorbance scale.

§ 9.3 Results and Discussion

The quantitative chemical maps derived from a stack fit analysis of the C 1s STXM data for albumin adsorption in presence of 0.05 mg/ml unbuffered water solution are presented in **Fig. 9.3** in the form of maps of each component: (a) PS, (b) PMMA, (c) albumin, as well as (d) the sum of these components, (e) the residual of the fit, and (f) the color coded composite map (red is PS, green is PMMA, and blue is albumin). The details of the analysis method were presented in **Chapter 5**. In contrast to PEEM data, STXM detects the X-rays transmitted through samples and the OD from STXM is quantitatively related to the amount of each compound present in the column at each pixel. The gray scale limits are the minimum and maximum thickness per pixel. Lighter intensities indicate locations where there is more of that component. The color-coded map shows a distinct blue on the interfaces between the PS and PMMA domains and on the PS domains. It indicates that most albumin molecules are sitting on the continuous PS and the interfaces of PS/PMMA.

To obtain the relative amount of albumin on different regions, signals specific to the PS and PMMA domains were extracted by using threshold masking of the component maps to select only those pixels where the signal was above a defined threshold. The interface signal from a ~80 nm band at the PS-PMMA interface was obtained by selecting those pixels not present in either the masked PS or masked PMMA maps. The amount of each component (PS, PMMA and albumin) in each region [PS, PMMA, interface] was then obtained by fitting the extracted spectrum using the same reference spectra used in generating the component maps by the stack fit. The analysis of albumin adsorption is

shown in **Fig. 9.4**. **Fig. 9.4 a** displays the masks while panels **(b-d)** display the curve fit to each extracted spectrum. The points with estimated uncertainties are the experimental spectra. The dark solid curves are the fits to the masked experimental spectra and the color curves are the weighted reference spectra. **Table 9.1** reports the results of these fits.

The thicknesses of different components [PS, PMMA, and albumin] on each region [PS domains, PMMA domains and PS/PMMA interfaces] and the total thickness of each region are summarized in **Table 9.1**. There are large PMMA signals (around 47%) on the PS region, different from the X-PEEM measurement [LHR&06].

As we can calculated from **Table 4.1**, X-PEEM study shows that the ratio of PMMA to PS on a PS region on the surface of PS/PMMA is ~0.21, while the ratio of PS to PMMA on a PMMA region is ~0.36, due to the microdomains [MIT&01] associated with incompletely phase separation of PS and PMMA. The comparison of X-PEEM and STXM studies suggests that there is an underlying PMMA layer on the PS region in addition the PMMA microdomains on the surface. The amount of PMMA on PS regions is much smaller (~20-30%) in the X-PEEM due to its limited sampling depth (~10 nm) that prevents the detection of underneath PMMA layer. This underneath PMMA layer can also explain why the surface area ratio of PS to PMMA is two (measured by X-PEEM), although PMMA is the major component in the blend (PS/PMMA =30/70 weight ratio). As a result of signal from the underlying PMMA layer, the interface region consists of much less of PS than PMMA. However, the total thickness of each region of PS/PMMA film is almost the same (~ 2 nm difference).

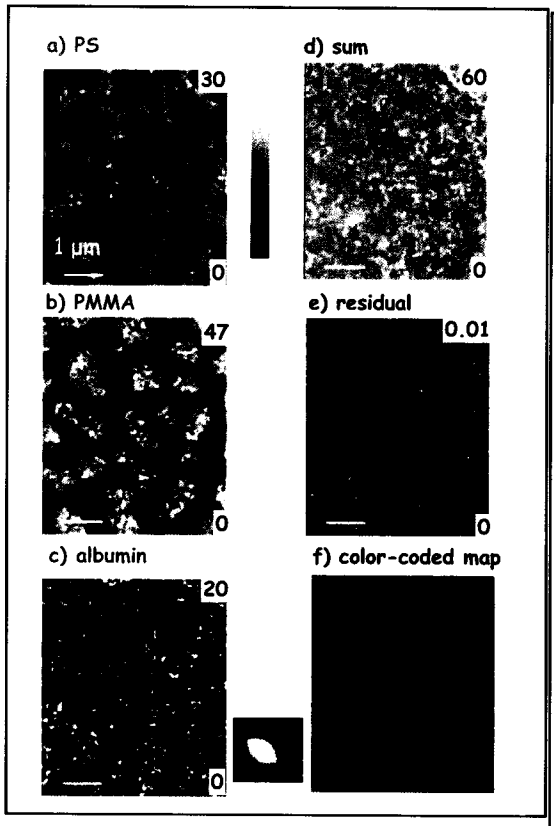

Fig. 9.3 Component maps of (a) PS, (b) PMMA and (c) albumin for a PS/PMMMA blend substrate exposed to a 0.05 mg/ml HSA unbuffered water solution, derived from pixel-by-pixel curve fits of a C 1s image sequence. The numbers in the upper and lower right of each component map are limits of the thickness gray scales in nm. (d) sum of the PS, PMMA and albumin thickness component maps. (e) map of the residual of the fit. The gray scale in the latter case is the deviation of the fit and the measured signal, averaged over all energies. (f) color-coded component map (red is PS, green is PMMA and blue is albumin).

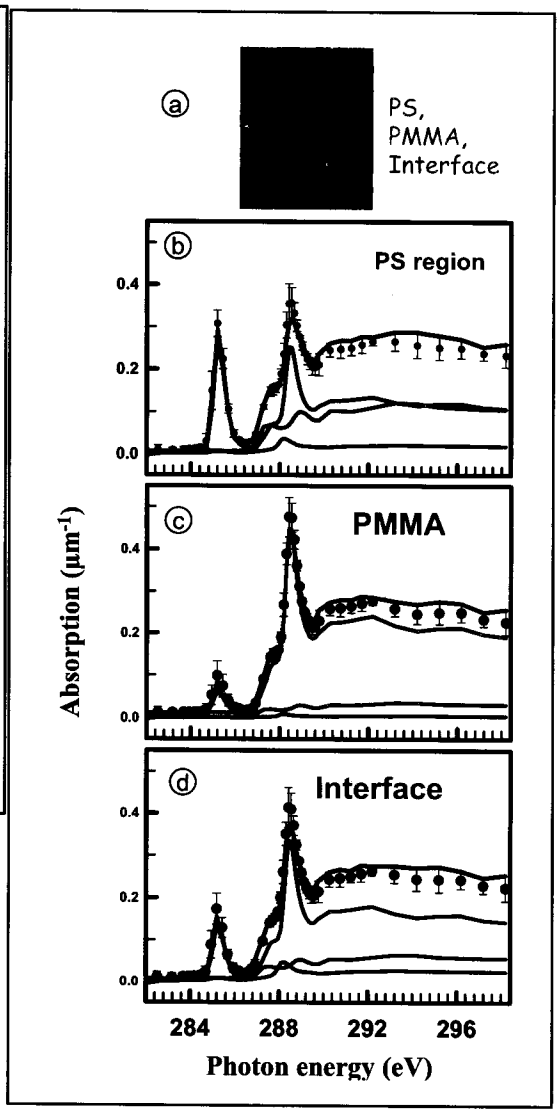

Fig. 9.4 (a) Masks used to extract spectra of specific regions. [red = PS > 11 nm, green = PMMA > 16 nm, blue = PS/PMMA interface (all pixels not identified in the masks of the PS and PMMA domains)]. (b-d) Curve fits to the average C1s spectra extracted from the masked regions (data - points, fit - thick solid line, components – thin lines).

Table 9.1 Adsorption of HSA on PS/PMMA in presence of 0.05 mg/ml unbuffered de-ionized water solution: Composition of PS, PMMA and PS/PMMA interfaces (uncertainty: ± 0.5 nm).

Composite (nm/pixel)	**PS region**	**PMMA region**	**Interface region**
PS	16.4	4.8	8.8
PMMA	18.6	30.9	24.7
Albumin	**4.3**	**1.0**	**5.6**
Surface PMMA *	3.4	13.5	8.4
Underneath PMMA*	15.2	17.4	16.3
Total thickness of polymer film (PS and PMMA)	35.0	35.7	33.5

* Not from the direct stack analysis but from the calculations based on some assumptions (see text for detail).

Assuming that the ratio of PS microdomains on PMMA regions (~0.21) or the ratio of PMMA microdomains on PS regions (~0.36) detected by X-PEEM is near the same for each PS/PMMA blend system in our work, we can estimated the thickness of the postulated underneath PMMA layer. Also as shown in **Table 9.1**, on the PS region, we can calculate that there is 3.4 nm surface-PMMA microdomains associated with 16.3 nm PS. On the PMMA region, we also can calculate that there is 13.5 nm surface-PMMA associated with 4.8 nm PS microdomains. By subtracting the surface-PMMA microdomains from the total PMMA film (the second row of the table), we can estimate the thickness of underneath PMMA layer, which is 15.2 nm on the PS region and 17.4 nm on the PMMA region. The average of the underneath PMMA layer on PS and PMMA regions is then 15.2 nm. By subtracting this from the total PMMA thickness on the

interface, we get 8.4 nm surface-PMMA on the interface which is similar to the thickness of PS on the interface (8.8 nm), as expected.

Based on **Table 9.1**, **Fig. 9.5** is proposed as the structure of the PS/PMMA blend.

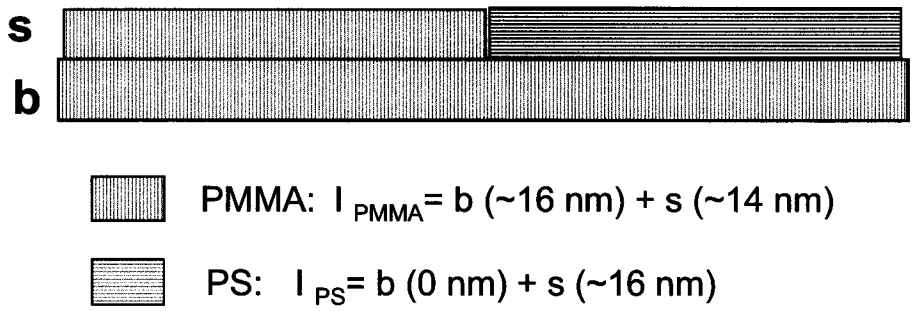

Fig. 9.5 The scheme of the phase separation of PS/PMMA blend (only show one repeat unit of the surface).

The amount of albumin on different regions is highlighted in bold font in **Table 9.1**. Consistent with the color-coded maps, the amount of albumin on the PMMA domains is very small (1.0 nm) compared with the amount on PS domains (4.3 nm) and the amount on the PS/PMMA interfaces (5.6 nm). Therefore albumin shows stronger absorption on the PS region and the interface of PS/PMMA domains. This strong preference to the PS/PMMA interface for albumin adsorption is consistent with all other cases where albumin adsorption under different conditions was measured by X-PEEM. The stronger preference to the PS domains than to the PMMA domains is also consistent with what was found for albumin adsorption at similar conditions detected by X-PEEM (See **Chapter 5**). However the difference between the adsorption on the PS and PMMA

detected in presence of albumin solution is much larger than that detected for the dried sample by X-PEEM. This is possibly due to sample heating by the strongly focused X-rays which could excite motion of the albumin molecules. This results in a weak hydrogen bonding between albumin molecules and the PMMA since hydrogen bonding needs to look for specific binding sites and is stabilized by multiple bindings. However the hydrophobic interactions between albumin molecules and PS are driven by the entropy gain from the dehydration of both albumin and PS surface, as discussed in **Chapter 5**. The albumin adsorption difference between X-PEEM dried sample and STXM wet cell measurements are also possibly due to the different sample preparations.

Chapter 10

Summary and further work

§ 10. 1 Summary

The work presented in this thesis shows that XRM can detect protein adsorption on a patterned PS/PMMA blend surface at sub-monolayer levels with a spatial resolution of 50-70 nm. This confirms the original work in this area by my predecessor Cynthia Morin [M04]. The technique and its applications have been extended as follows. Albumin adsorption under different conditions (concentration, pH, ionic strength and temperature) has been studied using X-PEEM. The adsorption of two different proteins (albumin and fibrinogen) has been compared. Furthermore HSA adsorption in presence of solution has been studied using STXM.

Under all the adsorption conditions studied, the proteins (albumin or fibrinogen) always show the strongest preference for adsorption at the PS/PMMA interfaces. However different preferences for the PS and PMMA domains were observed under different adsorption conditions.

This work has significant impact to the biological world, including: development of two quantitative techniques, further understanding of protein adsorption behavior theoretically and potential for contribution to the development of improved biomaterials.

§ 10. 2 Suggestion for Further Work

§ 10. 2. 1 Clarification of Issues Raised in Thesis

There are still some issues which require more exploration.

The area ratio of PS to PMMA is 60/30 on the surface of a PS/PMMA blend studied in this work although the mass ratio of PS to PMMA is 30/70. Why? As discussed in Chapter 9, I suspect that there is a thin layer of PMMA between the substrate and the PS/PMMA blend surface. Is this really true? This question could be addressed by making a series of PS/PMMA blend films on a Si wafer with different thicknesses (for example, 2, 5, 16, 32, 50 nm) by controlling the concentrations of PS/PMMA solutions used for spin coating and the spin coating speed, as what was done for the preparation of PS films with different thicknesses. From the ratio of the intensities of the two peaks at 285.15 eV (specific to PS) and 288.45 eV (specific to PMMA) in the spectrum of each film, it may be possible to determine if there is an underlying PMMA layer at the Si surface. This issue can also possibly be solved by floating the polymer films onto a Si wafer from the mica with the underlying side up, as was done to make the samples for STXM measurements discussed in **Chapter 3** and then examining them by X-PEEM. If the signal of this polymer film is dominated by PMMA signals then it is true that there is an underlying layer of PMMA.

§ 10. 2. 2 Extension in New Directions

There are a number of possible studies extending from work shown in the thesis.

- **Different substrates for protein adsorption study.**

The work presented in this thesis used a PS/PMMA blend film as a substrate for protein study. It would be of interest to study different substrates. I did some research of this type. Unfortunately there were some problems with all of the alternate substrates I explored. The criteria used for selecting different substrates are: (1) they are a patterned surface with domain sizes larger than the spatial resolution of XRM (~50 nm); (2) they form a flat, conducting surface (<10 nm rms, < 50 nm thick, with no asperities); (3) the chemical components are able to be differentiated from each other, and from protein by NEXAFS spectroscopy. Following these criteria, the first substrate I explored was a blend of polystyrene/polyethyleneoxide (PS/PEO) since PEO was reported to resist protein adsorption. However the PEO used was water-soluble (MW = 1×10^5 Dalton) and thus the PEO was washed away during protein exposure. The second substrate I explored was polystyrene grafted butanol (PS-g-butanol). I expected that butanol groups and PS would be phase-separated after annealing due to their different properties. However it was found that the sample I ordered from a commercial supplier (Polymer Source) was impure and that the grafted percentage (~4%) was too low. I think this system deserves further exploring if a sample with a graft percentage of 50% or higher could be obtained. The third substrate I explored was a polystyrene/ polysulfone (PS/PSF) blend since polysulfone is used widely in medical devices. The blend phase separated after annealing but the polysufone dewetted from the substrate. This system is also worth further studying by exploring how to eliminate the dewetting issue.

- **Protein competitive adsorption.**

I did study the competitive adsorption of albumin and fibrinogen although the result is not presented in this thesis. It would be much more exciting if one used two proteins whose NEXAFS are more different for a competitive adsorption study. Jacob Stewart-Ornstein (in Dr. Hitchcock's group) has developed a program to predict the NEXAFS spectrum of a protein from its amino acid sequence. This tool will be useful to identify pairs of proteins with distinguishable NEXAFS spectra.

- **Protein patterning.**

Protein patterning can be used for biosensors and other biomaterials applications. This is another new direction for applying the tools used in this work. There are a few ways to pattern proteins and other biomolecules onto material surfaces, such as photolithography [CYH&96, SRR&98], soft lithography [KAK&95, XW98, KTO&99], spotting techniques [MM99], and microcontact printing techniques [LOW99, YC00].

- **AFM study of protein adsorption.**

In practice, there are lots of issues in the application of AFM to biological science. The limitation and solutions for achieving high spatial resolution remain poorly understood despite rapidly growing applications. Many factors contribute to an AFM image in addition to the topography of the sample surface. These include the size and shape of the tip, properties of the feedback loop, and the mechanical and chemical properties of the sample and imaging environment. For small molecules such as proteins or other polymers with a radius of 5-20 nm, the interacting part of tip is often larger than

the scanned structures. In such cases, the image is as much a representation of the tip as it is a representation of the probed molecules. Therefore it is important to have a sharp tip for AFM studies of protein molecules. For adsorbed protein molecules, if a constant morphology is observed over an entire image, it suggests that there are contributions of tip structure to the image of the sample since adsorbed protein molecules are typically rotationally disordered. Furthermore, more than one tip on the same scale (multiple tipping) during the examination of a sample can cause shadowing of the image and other artificial structure in the images.

Chapter 3 shows an AFM image of the albumin covered PS/PMMA blend surface. I did try to image the albumin structure on the PS and PMMA domains of the blend but the results are not presented in this thesis since more work needs to be done in order to have reliable AFM images. This would include careful characterization of the AFM tip and optimizing the scanning parameters.

- **Operation of PEEM 3.**

This work used the second generation of X-PEEM microscope at the ALS (PEEM 2). The third generation of X-PEEM (PEEM 3) is being commissioned and Dr. Hitchcock's group has requested beam time with it. It is predicted and designed to have much better spatial resolution: 5 nm spatial resolution at comparable transmission to PEEM 2 (a few %) and 50 nm resolution at almost 100% transmission. This improved performance will be very beneficial for the study of our very radiation-sensitive samples. PEEM 3 will also use a better beamline equipped with an elliptically polarizing undulator (EPU) with

higher energy resolution ($E/\Delta E = 3000\sim10000$), polarization control, and better control of the flux.

In summary, starting from the work presented in this thesis, there are many follow-up experiments that could be potentially productive.

References

[A90] Peter William Atkins, *Physical Chemistry*, W. H. Freeman and Company, New York, **1990**.

[AB04] J.G. Archambault, J.L. Brash, *Colloids Surf B: Biointerfaces*, 33 (**2004**) 111-120.

[ABN86] T. Arnebrant, K. Barton, T. Nylander, *J. Colloid, Interface Sci.*, 119 (**1986**) 383-390.

[AL00] N. Alizadeh-Pasdar, E. C. Y. Li-Chan, *J. Agric. Food Chem.*, 48 (**2000**)328-334.

[AN86] T. Arnebrant, T. Nylander, *J. Colloid, Interface Sci.*, 111 (**1986**) 529-533.

[AN88] T. Arnebrant, T. Nylander, *J. Colloid Interface Sci.* 122 (**1988**) 557-566.

[APD&99] S. Anders, H. A. Padmore, R. M. Duarte, T. Renner, T. Stammler, A. Scholl, M. R. Scheinfein, J. Stöhr, L. Séve, Boris Sinkovic, *Rev. of Sci. Instrum.* 70 (**1999**) 3973-3981.

[AU00] H. Ade, S. G. Urquhart, *NEXAFS Spectroscopy and Microscopy of natural and Synthetic Polymers*, in "Chemical Application of Synchrotron Radiation" edited by T.K. Sham, World Scientific, Singapore, **2000**.

[AWS&98] H. Ade, D. A. Winesett, A. P. Smith, S. Anders, T. Stammler, C. Heske, D. Slep, M. H. Rafailovich, J. Sokolov, J. Stöhr, *Appl. Phys. Lett.* 73 (**1998**) 3775.

[aX00] aXis2000 is free for non-commercial use. It is written in Interactive Data Language (IDL), and available from http://unicorn.mcmaster.ca/aXis2000.html.

[AZC&92] H. Ade, X. Zhang, S. Cameron, C. Costello, J. Kirz, and S. Williams, Science 258 (**1992**) 972.

[B70] A. Benninghoven, *Z Phys.* 230 (**1970**) 403-417.

[B73] A. Benninghoven, *Surf. Sci.* 35 (**1973**) 427-457.

[B94] A. Benninghoven, *Angew. Chem. Int. Ed. Engl.* 33 (**1994**) 1023.

[B98] E. Bauer, *Surface Review and Letters*, 5(6) (**1998**)1275-86

[BBL&96] J. Buijs, P. A. W., van den Berg, J. W. Th., Lichtenbelt, W. Norde, J. Lyklema, *J. Colloid Interface Sci.* 178 (**1996**) 594.

[BGC03] A. M. Belu, D. J. Graham, D. G. Castner, *Biomaterials* 24 (**2003**), 3635-3653.

[BH99] E. Bordini, M. Hamdan, *Rapid Commun. Mass Spectrom.* 13 (**1999**) 1143.

[BIG99] Brandrup, J.; Immergut, E. H.; Grulke, E. A.; Bloch, D. *Polymer Handbook*, Wiley-Interscience, **1999**.

[BMA&96] L. Bergstrom, A. Meurk, H. Arwin, D. J. Rowcliffe, *J. Am. Chem. Soc.* 79 (**1996**) 339-348.

[BNL96] J. Buijs, W. Norde, J. W. T. Litchenbelt, *Langmuir* 12 (**1996**) 1605-1613.

[BO93] M. Brigham-Burke, D. J. O'Shannessy, *Chromatographia, 35*(**1993**) 45- 49.

[BQG86] G. Binnig, C. F. Quate , C. Gerber. *Phys. Rev. Lett.,* 56 (**1986**) 930.

[BR98] A. S. Blawas, W. M. Reichert, *Biomaterials*, 19 (**1998**) 595-609.

[BS90] D. Briggs, M. P. Seah, *Practical Surface Analysis. Vol. 1: Auger and X-Ray Photoelectron Spectroscopy*. 2nd edition John Wiley & Sons Ltd, Chichester, England, **1990**.

[BWN97] J. Buijs, D. D. White, W. Norde, *Colloid Surf. B* 8 (**1997**) 239.

[C87] Y. D. Clonis, *Bio/Technology*, *5* (**1987**)1290-1293.

[CA85] T. M. Cotton in *Surface and Interfacial Aspects of Biomedical Polymers, 2*, J. D. Andrade Ed., Plemum Press, New York, **1985**.

[CB81] B.M.C. Chan, J.L. Brash, *J. Colloid Interface Sci.* 82 (**1981**) 217.

[CB84] B. M. Chan, J. L. Brash, *J. Colloid, Interface Sci.*, 82 (**1984**) 217-225.

[CCD92] T. –W. Chan, A. W. Cilburn, P. J. Derrick, *Org. Mass Spectrom.* 27 (**1992**) 53-56.

[CDL&98] A. Cossy-Favre, J. Diaz, Y. Liu, H. R. Brown, M. G. Samant, J. Sto¨hr, A. J. Hanna, S. Anders, T. P. Russel, *Macromolecules* 31 (**1998**) 4957.

[CH94] Carter, D. C.; Ho, J. X.; *Adv. Protein Chem.* 45 (**1994**) 153-203.

[CHH78] P. A. Cuypers, W. T. Hermens, H. C. Hemker, *Anal. Biochem.* 84 (**1978**) 56-67.

[CR02] D. G. Castner, B.D. Ratner, *Surf. Sci.* 500 (**2002**) 28.

[CSG&00] Jacobsen, C.; Wirick, S.; Flynn, G.; Zimba, C. Soft X-ray spectroscopy from image sequences with sub-100 nm spatial resolution. *J. Microscopy*, 197 (**2000**) 173-184.

[CT01] J. Caslavska, W. Thomann, *J. Microcol.*, 13 (**2003**) 69-83.

[CYH&96] M. Chee, R.Yang, E. Hubbell, A. Berno, X. C. Huang, D. Stern, J. Winkler, D. J. Lockhart, M. S. Morris, S. P. A. Fodor, *Science*, 274 (**1996**)610.

[DBS&97] J. L. Dewez, V. Berger, Y. J. Schneider, P.G. Rouxhet, *J. Colloid Interface Sci.*, 191 (**1997**) 1-10.

[DCL&98] G. De Stasio, M. Capozi, G.F. Lorusso, P. A. Baudat, T. C. Droubay, P. Perfetti, G. Margaritondo, B. P. Tonner, *Rev. Sci. Instrum.,* 69 (**1998**) 2062

[DMT&97] T. Droubay, G. Mursky, B. P. Tonner, *J. Electron Spectrosc. Relat. Phenom.* 84 (**1997**) 159.

[DN83] P. van Dulm, W. Norde, *J. Colloid Interface Sci.* 91 (**1983**) 248.

[EBC&97] C. Eriksson, E. Blomberg, P. Clasesson, H. Nygren, *Colloids Surf. B*, 9 (**1997**) 67-79.

[EDL84] H. J. van Enckevort, D. V. Dass, A. G. Langdon, *J. Colloid Interface Sci.* 98, (**1984**) 138.

[EKR&91] W. Engel, M.E. Kordesch, H.H. Rothermund, S. Kubala, and A. von Oertzen, *Ultramicroscopy*, 36 (**1991**) 148

[ELC&97] P. L. Edminston, L.J. E. Lee, S. S. Cheng, S. S. Saavedra, *J. Am. Chem. Soc.*, 119 (**1997**) 560.

[EPS&96] U. M. Elofsson, M. A. Paulsson, P. Sellers, T. Arnebrant, *J. Colloid Interface Sci.*, 183 (**1996**) 408-415.

[F77] Foster, J. F., In "Albumin Structure, Function and Uses" (V. M. Rosenoer, M. Oratz, and M. A. Rothschild, eds), pp. 53-84, Pergamon, Oxford, **1977**.

[F96] G. D. Fasman, *Circular Dichroism: The Comformational Analysis of Biomolecules.* Plenum Press, New York, **1996**.

[FJ80] B. D. Fair, A. M. Jamieson, *J. Colloid Interface Sci.* 77 (**1980**) 525-534.[FLE&92] H. Fitzpatrick, P. F. Luckham, S. Eriksen, K. Hammond, *J. Colloid Interface Sci.*, 149 (**1992**) 1-9.

[FSL&04] N. Faucheux, R. Schweiss, K. Lutzow,; C. Werner, T. Groth, *Biomaterials* 25 (**2004**) 2721-2730.

[G04] J. J. Gray, *Curr Opin Biotechnol* 14 (**2004**) 110-115.

[GDD&97] R. J.Green, J. Davies, M. C. Davies, C. J. Roberts, S. J. B. Tendler, *Biomaterials*, *18* (**1997**) 405-413.

[GFS&00] R. J. Green, R. A. Frazier, K. M. Shakesheff, M. C. Davies, C. J. Roberts and S.J. B. Tendler, *Biomaterials* 21 (**2000**) 1823-1835.

[GK88] C. G. Golander, E. Kiss, *J. Colloid Interface Sci.* 240 (**1988**) 121.

[GKM&04] H. J. Griesser, P. Kingshott, S. L. McArthur, K. M. McLeanb, G. R. Kinsele, R. B. Timmonse, *Biomaterials* 25 (**2004**) 4861–4875.

[GMC&93] R. Guidon, S. Maurel, N. Chakfe, T. How, X. Xhang, M. Therrien, M. Formichi, C. Gosselin, *Biomaterials* 14 (**1993**) 694-704.

[GNJ&03] Joseph Goldstein, Dale E. Newbury, David C. Joy, Charles E. Lyman, Patrick Echlin, Eric Lifshin, L.C. Sawyer and J.R. Michael, *Scanning Electron Microscopy and X-ray Microanalysis*, Springer, 3 edition, **2003**.

[GRA&95] G. W. Gross, B. K. Rhoades, H. M. E. Azzazy, M. –C. Wu, *Bioelectron.* 10 (**1995**) 553-567.

[GV92] G. Barone, C. Giancola, A. Verdoliva, *Thermochimica Acta*, 199 (**1992**) 197-205.

[GW87] E. V. Groman, M. Wilchek, *Trends Biotechnol.*, *5* (**1987**) 220-223.

[H48] D.C. Harris, *Quantitative Chemical Analysis, 3rd Edition*, W.H. Freeman and Company, New York, **1948**.

[H97] Y. Hwu, *J. Electron Spectrosc. Relat. Phenom.* 84 (**1997**) 149.

[HG&93] B. L. Henke, E. M. Gullikson, J. C. Davis, *At. Data Nucl. Data Tables*, 54 (**1993**) 181-298.

[HGD93] Henke, B.L.; Gullikson, E.M.; Davis, J.C. *At. Data Nucl. Data Tables* **1993**, 54, 181-298.

[HH&06] Hernández Cruz, D.; Hitchcock, A. P.; West, M. M.; Rousseau, M.-E.; Pézolet, M.; *Biomacromolecules* (accepted Jan 2006).

[HK01] F. Höök, B. Kasemo, *Anal. Chem.*, 73 (**2001**) 5796.

[HLN&04] J. Hyun, W-K. Lee, N. Nath, A. Chilkoti, S. Zauscher, *J. Am. Chem. Soc.*, 126 (**2004**) 7330-7335.

[HLT&82] B. L. Henke, P. Lee, T. J. Tanaka, R. L. Shimabukuro, B. K. Fujikawa, *At. Nucl. Data Tables*, 27 (**1982**)1-256.

[HLT&93] B. L. Henke, P. Lee, T. J. Tanaka, R. L. Shimabukuro, B. K. Fujikawa, *At. Nucl. Data Tables*, 27 (**1982**)1-256; B. L. Henke, E. M. Gullikson, J. C. Davis, *At. Data Nucl. Data Tables*, 54 (**1993**)181-298.

[HM&05] A. P. Hitchcock, C. Morin, X. Zhang, T. Araki, J. J. Dynes, H. Stöver, J. L. Brash, J. R. Lawrence, G. G. Leppard, *J. Electron. Spectrosc. and Relat. Phenom.* 144-147 (**2005**) 259-269.

[HMH&02] A.P. Hitchcock, C. Morin, Y.M. Heng, R.M. Cornelius, J.L. Brash, *J. Biomaterials Science, Polymer Ed.* 13 (**2002**) 919-938.

[HMZ&05] A. P. Hitchcock, C. Morin, X. Zhang, T. Araki, J. Dynes, H. Stover, J. Brash, J. R. Lawrence, G. G. Leppard, *J. Electron. Spectrosc. Relat. Phenom.* 144–147 (**2005**) 259–269.

[HN94] C. A. Haynes, W. Norde, *Colloids Surf. B.* 2 (**1994**) 517.

[HRA86] V. Hlady, D. R. Reinecke, J. D. Andrade, *J. Colloid Interface Sci.* 111 (**1986**) 555.

[HRB&98] F. Höök, M. Rodahl, P. Brzezinski, B. Kasemo, *Langmuir*, 14 (**1998**) 729.

[HTG&00] A. C. Henry, T. J. Tutt, M. Galloway, Y. Davidson, C.S. McWhorter, S. A. Soper, R. L. McCarley, *Anal. Chem.* 72 (**2000**)5331-5337.

[HU92] M. Hanson, K. K. Unger, *Trends Anal. Chem., 11* (**1992**) 368-373.

[INT&95] H. Itoh, A. Nagata, T. Toyomasu, T. Sakiyama, T. Nagai, T. Saeki, K. Nakanishi, *Biosci Biotech. Biochem.*, 59 (**1995**) 1648-1651.

[JJC&97] Green, R.J.; Davies, J.; Davies, M.C.; Robert, C.J.; Tendler, S.J.B. *Biomaterials*, 18 (**1997**) 405-413.

[JWC05] Johnson, W.C.; Wang,J.; Chen, Z, *J. Phys. Chem. B*, 109 (**2005**) 6280-6286.

[JWF&00] C. Jacobsen, S. Wirick, G. Flynn, C. Zimba, *J. Microscopy, 197* (**2000**) 173-184.

[JYL00] C. A. Johnson, Y. Yuan, A. M. Lenhoff, *J. Colloid Interface Sci.*, 223 (**2000**) 261-272.

[K02] B. Kasemo, *Surf. Sci.* 500 (**2002**) 656.

[KAK&95] A. Kumar, N. Abbott, E. Kim, H. Biebuyck, G. M. Whitesides, *Acc. Chem. Res.*, 28 (**1995**) 219.

[KBR02] D. T. Kim, H. W. Blanch, C. J. Radke, *Langmuir* 18 (**2002**) 5841-5850.

[KF98] A. Kondo, H. Fukuda, *J. Colloid Interface Sci.*, 198 (**1998**) 34.

[KH02] Peter Kingshott, Hartwig Höcker, *Encyclopedia of Surface and Colloid Science*, Dekker **2002**.

[KH04] B. Kirby, E. F. Hasselbrink Jr., *Electrophoresis*, 25 (**2004**) 203-213.

[KH88] M. Karas and F. Hillenkamp, *Anal. Chem.* 60 (**1988**) 2299.

[KHM&02] I.N. Koprinarov, A.P. Hitchcock, C. McCrory, R.F. Childs, J. Phys. Chem. B 106 (**2002**) 5358.

[KKH&88] D. Kleinfeld, K. H. Kahler, P. E. Hockberger, *J. Neurosci.* 8 (**1988**) 4098-4120.

[KL89] H. G. Kessler, D. B. Lund, *Fouling and Clearing in Food Processing*, Tu Munich, Germany **1989**.

[KM99] S. Kidoaki, T. Matsuda, *Langmuir* 15 (**1999**) 7639.

[KMH93] A. Kondo, S. Oku, F. Murakami, K. Higashitani, *Colloid Surf. B*, 1 (**1993**) 197-201.

[KPE&96] T. Klonisch, G. Panayotou, P. Edward, A. M. Jackson, P. Berger, P. J. Delves, T. Land, I. M. Roitt, *Immunology, 89* (**1996**)165-171.

[KSC&00] P. Kingshott, H. A. W. StJohn, R. C. Chatelier, H. J. Griesser, *J. Biomed. Mater. Res.* 49 (**2000**) 36.

[KTO&99] R. S. Kane, S. Takayama, E. Ostuni, D. E. Ingber, G. M. Whiteside, *Biomaterials*, 20 (**1999**) 2363-2376.

[KTS&03] A.L.D. Kilcoyne, T. Tyliszczak, W.F. Steele, S. Fakra, P. Hitchcock, K. Franck, E. Anderson, B. Harteneck, E.G. Rightor, G.E. Mitchell, A.P. Hitchcock, L. Yang, T. Warwick and H. Ade, *J. Synchrotron Rad.*, 10 **(2003)** 125

[LCA&04] T. L. Lasseter, B. H. Clare, N. L. Abbott, R. J. Hamers, *J. Am. Chem. Soc.* 126 (**2004**) 10220-10221.

[LCH04] T. L. Lasseter, W. Cai, R. Hamers, *J. Analyst*, 129 (**2004**) 3-8.

[LDA&98] J. B. Lhoest, E. Detrait, P.v.d. B. d. Aguilar, P. Bertrand, *J. Biomed. Mater. Res.* 41 (**1998**) 95-103.

[LHR&06] Li, L.; Hitchcock, A. P.; Robar, N.; Cornelius, R.; Brash, J.L.; Scholl, A.; Doran, A.; *J. Phys. Chem. B* **2006** in press.

[LLT96] J. R. Lu, E. M. Lee, R. K. Thomas, *Acta Cryst.* A52 (**1996**) 42.

[LM03] Liu, Y.; Messmer, M. C. *J. Phys. Chem. B*, 107 (**2003**) 9774-9779.

[LOW99] J. Lahiri, E. Ostuni, G. M. Whitesides, *Langmuir*, 15 (**1999**) 2055.

[LM03] Liu, Y.; Messmer, M. C. *J. Phys. Chem. B*, 107 (**2003**) 9774-9779.

[LM96] B. Lassen, M. Malmsten, *J. Colloid Interface Sci.*, 180 (**1996**) 339-349.

[LP91] D. R. Lu, K. Park, *J. Colloid Interface Sci.* 144 (**1991**) 271-281.

[LT98] J. R. Lu, P. K. Thomas, *J. Chem. Soc. Faraday Trans.* 94 (**1998**) 995.

[LWT&01] J. B. Lhoest, M S. Wagner, C. D. Tidwell, D. G. Castner, *J. Biomed. Mater. Res.* 57 (**2001**) 432-440.

[LWT&01] J. -B. Lhoest, M. S. Wagner, C. D. Tidwell, D. G. Castner, *J. Biomed. Mater. Res.* 57 (**2001**) 432.

[LZZ98] F. Liu, M. Zhou, F. Zhang, *Appl. Radiat. lsot.*,49 (**1998**) 67-72.

[M03] Martin Malmsten, *Biopolymers at interfaces*, Marcel Dekker, Inc., Basel, **2003**

[M04] C. Morin, PhD thesis, *Soft X-ray Spectromicroscopy of Proteins on Patterned Polymer Films*, McMaster University, **2004**.

[M98] M. Malmsten, *J. Colloid Interface Sci.*, 207 (**1998**) 186-199.

[MA88] G. Meyer, N. M. Amer, *Appl. Phys. Lett.*, 53 (**1998**)1045-1047.

[MBL&97] E.L. Montei, V.W. Ballarotto, M.E. Little, M.E. Kordesch, *J. Electron. Spectrosc. Rel. Phenom.*, 84 (**1997**) 129

[MD00] B. S. Murray, C. Deshaires, *J. Colloid Interface Sci.*, 227 (**2000**) 32-41.

[MH&04] Morin, C.; Hitchcock, A. P.; Cornelius, R. M.; Brash, J. L.; Scholl, A.; Doran, A. *J. Electron Spectrosc.*, 137-140 (**2004**)785-794.

[MHC&04] C. Morin, A. P. Hitchcock, R. M. Cornelius, J. L. Brash, A. Scholl, A. Doran, *J. Electron Spectroscopy* 137-140 (**2004**) 785-794.

[MIT&01] C. Morin, H. Ikeura-Sekiguchi, T. Tyliszczak, R. Cornelius, J.L. Brash, A.P. Hitchcock A. Scholl, F. Nolting, G. Appel, A. D. Winesett, K. Kaznacheyev and H. Ade, *J. Electron Spectrosc* 121 (**2001**) 203.

[MLW&96] M. Malmsten, B. Lassen, J. Westin, C.-G. Golander, R. Larsson, U. R. Nilsson, *J. Colloid Interface Sci.* 179 (**1996**) 163-172.

[MM99] V. N. Morozov, T. Y. Morozova, *Anal. Chem.* 71 (**1999**) 3110.

[MMJ&01] S. L. McArthur, K. M. Mclean, H. A. W. S. John, H. Griesser, *J. Biomaterials* 22 (**2001**) 3295-3304.

[MNV&97] M. C. L. Maste, W. Norde, A. J. W. G. Visser, *J. Colloid Interface Sci.* 196 (**1997**) 224-230.

[MRC&93] D. S. Mantus, B. D. Rater, B. A. Carlson, J. f. Moulder, *Anal. Chem.* 65 (**1993**) 1431.

[MS00] G. MacBeath, S. L. Schreiber, *Science*, 289 (**2000**) 1760-1763.

[MW74] C. R. McMillin, A. G. Walton, *J. Colloid Interface Sci.*, 48 (**1974**) 345.

[MW95] M. Mrksich, G. M. Whitesides, *Trends Biotechnol.*, 13 (**1995**) 228-235.

[MZ98] M. K. Menon, A. L. Zydney, *Anal. Chem.*, 70 (**1998**)1581-1584.

[N86] W. Norde, *Adv. Colloid Interface Sci.* 25 (**1986**) 267.

[NA92] W. Norde, A. C. Anusiem, *Colloid Surf.*, 66 (**1992**) 73.

[NL91] W. Norde, J. Lyklema, *J. Biomater. Sci. Polymer Edn*, 2 (**1991**)183-202.

[MA95] J. Martensson, H. Arwin, *Langmuir* 11 (**1995**) 963-968.

[NAG97] T. Nylander, T. Arnebrant, P. -O. Glantz, *Colloids Surf. A* 129-130 (**1997**) 339-344.

[NGP95] W. Norde, M. Giesbers, H. Pingsheng, *Colloid Surf. B* 5 (**1995**) 255.

[NL91] Willem Norde, Johannes Lyklema, *J. Biomater. Sci. Polymer Edn*, 2 (**1991**)183-202.

[NLS&94] E. Nice, M. Lackmann, F. Smyth, L. Fabri, A. W. Burgess, *J. Chromatogr., A*, 660 (**1994**)169-185.

[NM01] Jens Als-Nielsen and Des McMorrow, *Elements of Modern X-ray Physics*, John Wiley & Sons, **2001**.

[NSI01] K. Nakanishi, T. Sakiyama, K. Imamura, *J. BioSci. Bioeng.*, 91 (**2001**) 233-244.

[OKH91] A. Overberg, M. Karas and F. Hillenkamp, *Rapid Commun. Mass Spectrom.* 5 (**1991**) 128.

[OYW99] E. Ostuni, L. Yan, G. M. Whitesides, *Colloids Surf. B*, 15 (**1999**) 3-30.

[P95] Theodore Peters, Jr.,, *All About Albumin: Biochemistry, Genetics, and Medical Applications*; Academic Press: NY, **1995**.

[PB62] G. A. Parks, P. L. de Bruyn, *J. Phys. Chem.*, 66 (**1962**) 967-973.

[PCC93] Pierce Chemical Company, IODO-GEN Iodination Reagent, **1993**.

[PHL&01] Y. V. Pan, Y. Hanein, D. Leach-Scampavia, K. F. Böhringer, B. D. Ratner, D. D. Denton, *IEEE Conference on Micro Electro Mechanical Systems (MEMS)*, **2001**

[PR85] R. W. Paynter, B. D. Ratner, In *Surface and Interface Aspects of Biomedical Polymers*, J. D. Andrade, Ed., Plenum Press, New York, **1985**, pp 189-216.

[PSP&91] C. Pale-Grosdemange, E. S. Simon, K. L. Prime, G. M. Whitesides, *J. Am. Chem. Soc.*, 113 (**1991**) 12-20.

[PT90] J. Penfold, R. K. Thomas, *J. Phys. Cond. Matter*, 2 (**1990**) 1369.

[QZO&06] Qiu, W.; Zhang, L.; Okobiah, L.; Yang, Y.; Wang, L.; Zhong, D.; Zewail, A.H.; *J. Phys. Chem. B*, 110 (**2006**)10540-10549

[R84] E. Regoeczi, Iodine-Labeled Plasma Proteins, vol. 1, CRC Press, Boca Raton, FL, **1984**.

[R95] B. D. Ratner, *Surf. Interface Anal.* 23 (**1995**) 521-528.

[REC&96] J. Revilla, A. Elaissart, P. Carriere, C. Pichot, *J. Colloid Interface Sci.*, 180 (**1996**) 405-412.

[RFP05] Roach, P.; Farrar, D.; Perry, C. C. *J. AM. Chem. Soc.* 127 (**2005**)8168-8173.

[RH90] R.J. Rapoza, T.A. Horbett, *J. Biomed. Mater. Res.* 24 (**1990**) 1263.

[RHS&81] B. D. Ratner, T. A. Horbett, D. Shuttleworth, H. R. Thomas, *J. Colloid Interface Sci.* 83 (**1981**) 630.

[S92] J. Stohr, *NEXAFS Spectroscopy*, Series in Surface Science, Vol. 25, Springer, Berlin, **1992**.

[SA96] A. P. Smith and H. Ade, *Appl. Phys. Lett.* 69 (**1996**) 3833.

[SBI85] J. –E. Sundgren, P, Bodo, b. Ivarsson, I. Lundstrom, *J. Colloid Interface Sci.* 113 (**1985**) 530.

[SBY93] V. I. Silin, G. A. Balchytis, V. A. Yakovlev, *Opt, Comm.*, *97* (**1993**) 19-24.

[SFJ02] J. S. sharp, J. A. Forrest, R. A. Jones, *Biochemistry* 41 (**2002**) 15810-15819.

[SGF98] G. Sagvolden, I. Giaever, J. Feder, *Langmuir* 14 (**1998**) 5984.

[SHA&00] T. Sulchek, R. Hsieh, J. D. Adams, S. C. Minne, C. F. Quate, *Review of Sci. Instru.*, 71 (**2000**) 2097-2099.

[SHK95] P. W. Stevens, M. R. Hansberrry, D. M. Kelso, *Anal. Biochem.*, 225 (**1995**) 197-205.

[SHV&02] S. A. Soper, A. C. Herry, B. Vaidya, M. Galloway, M. Wabuyele, R. L. McCarley, *Anal. Chim. Acta*, 470 (**2002**) 87-99.

[SJD99] S. Sharma, R. W. Johnson, T. A. Desai, *Langmuir*, 20 (**2004**) 348-356.

[SL92] C. T. Shibata, A. M. Lenhoff, *J. Colloid Interface Sci.* 148 (**1992**) 485.

[SLT&98] T. J. Su, J. R. Lu, R. K. Thomas, Z. F. Cui, J. Penfold, *J. Phys. Chem. B.*, 102 (**1998**) 8100-8108.

[SLT&99] T. J. Su, J. R. Lu, R. K. Thomas, Z.F. Cui, *J. Phys. Chem. B.*, 103 (**1999**) 3727-3736.

[SM97] G. De Stasio G. Margaritondo, J. *Electron Spectrosc. Relat. Phenom.* 84 (**1997**) 137.

[SM98] C. A. Siedlecki, R. E. Marchant, *Biomaterials* 19 (**1998**) 441.

[SMC&96] Z. Shao, J. Mou, D.M. Czajkowsky, J. Yang, J.-Y., Yuan, *Advances in Physics*, 45 (**1996**) 1-86.

[SMW98] G. B. Sigal, M. Mrksich, G. M. Whitesides, *J. Am. Chem. Soc. 120* (**1998**) 3464.

[SRR&98] (9) A. Schwarz, J. S. Rossier, E. Roulet, N. Mermod, M. A. Roberts, H. H. Girault, *Langmuir*, 14 (**1998**) 5526.

[SSC&98] J. Stöhr, M. Samant, A. Cossy-Favre, J. Diaz, Y. Momoi, S. Odahara, T. Nagata, *Macromolecules* 31 (**1998**) 1942.

[SSK&98] D. Spanke, V. Solinus, D. Knabben, F. U. Hillebrecht, F. Ciccacci, L. Gregoratti, M. Marsi, *Phys. Rev. B* 58 (**1998**) 5201.

[SSS89] H. Shirahama, K. Susuki, Y. Suzawa, *J. Colloid Interface Sci.*, 129 (**1989**) 483-490.

[SSK&97] S. Singh, H. Solak, N. Krasnoperov, F. Cerrina, A. Cossy, J. Diaz, J. Stöhr, M. Samant, *Appl. Phys. Lett.* 71 (**1997**) 55.

[SRR&98] (9) A. Schwarz, J. S. Rossier, E. Roulet, N. Mermod, M. A. Roberts, H. H. Girault, *Langmuir*, 14 (**1998**) 5526.

[STN&98] T. Sakiyama, T. Toyomasu, A. Nagata, K. Imamura, K. Nakanishi, T.Takahashi, T. Nagai, *J. of Chem. Eng. of Japan*, 31(**1998**) 208-213.

[TCG&01] C. D. Tidwell, D. G. Castner, S. L. Golledge, B. D. Ratner, K. Meyer, B. hagenhoff, A. Benninghoven, *Surf. Interface Anal.* 31 (**2001**) 724-733.

[TDD&95] B.P. Tonner, D. Dunham, T. Droubay, J. Kimuna, J. Denliger, E. Rotenberg, A. Warwick, *J. Electron. Spectrosc. Relat. Phenom.*, 75 (**1995**) 309.

[TIG04] Kouichi Tsuji, Jasna Injuk, and René Van Grieken, *X-Ray Spectrometry:Recent Technological Advances* , John Wiley & Sons, **2004.**

[TM00] T. C. Ta, M. T. McDermott, *Anal. Chem.* 72 (**2000**) 2627.

[TR91] R. M. Tromp, M.C. Reuter, *Ultramicroscopy*, 36 (**1991**) 99.

[VDS&05] T. Volz, S.Dürr, N. Syassen, G. Rempe, E. van Kempen, S. Kokkelmans, *Phy. Rev. A*, 72 (**2005**) 010704.

[WAK&02] T. Warwick, H. Ade, A.L.D. Kilcoyne, M. Kritscher, T. Tylisczcak, S. Fakra, A.P. Hitchcock, H.A. Padmore, *J. Synchrotron Radiat.* 9 (**2002**) 254.

[WAL95] M. Wahlgren, T. Arnebrant, I. Lundstrom, *J. Colloid Interface Sci.* 506 (**1995**) 175.

[WC01] M. S. Wagner, D. G. Castner, *Langmuir* 17 (**2001**) 4649-4660.

[WCM&00] Y. Wu, B. Czarnik-Matusewicz, K. Murayama, Y. Ozaki, *J. Phys. Chem. B*, 104 (**2000**) 5840-5847.

[WHC03] M. S. Wagner, T. A. Horbett, D. G. Castner, *Langmuir* 19 (**2003**) 1708-1715.

[WML&06] J. Wang, C. Morin, L. Li, A. P. Hitchcock, A. Doran, A. Scholl, *J. Electron Spectrosc.*, in preparation.

[WPA98] T. Warwick, H. Padmore, H. Ade, *Proc. SPIE*, 3449 (**1998**) 12-18.

[WSH&03] M S. Wagner, M. Shen, T. A. Horbett, D. G. Castner, *J. Biomed. Mater. Res.* 64A (**2003**) 1-10.

[WTC02] M S. Wagner, B. J. Tyler, D. G. Castner, *Anal. Chem.* 74 (**2002**) 1824-1835.

[WTL99] H. Wang, K. Tseng and C. B. Lebrilla, *Anal. Chem.* 71 (**1999**) 2014.

[XW98] Y. Xia, G. M. Whitesides, *Angew. Chem., Int. Ed. Engl.*, 37 (**1998**) 550.

[YBM&01] Q. Yu, J. M. Bauer, J. S. Moore, D. J. Beebe, *Appl. Phys. Lett.*, 78 (**2001**) 2589-2591.

[YC00] Z. Yang, A. Chilkoti, *Adv. Mater.* 12 (**2000**) 413.

[YPC88] B. R. Young, W. G. Pitt, S. L. Cooper, *J. Colloid Interface Sci.* 124 (**1988**) 28.

[ZBM&96] X. Zhang, R. Balhorn, J. Mazrimas, J. Kirz, *J. Struc. Biol.*, 116 (**1996**) 355.

[ZMH&05] Z. Zhang, H. Ma, D. B. Hausner, A. Chilkoti, T. P. Beebe Jr., *Biomacromolecules* 6 (**2005**) 3388-3396.

Appendix A

This appendix gives a list all the software packages I used for my PhD.

1. aXis2000 (versions between Jun 2005 , Jan 2006)

aXis2000 is a freeware program written in Interactive Data Language (IDL) by Adam Hitchcock, and it is available from *http://unicorn.mcmaster.ca/aXis2000.html*. It was used for the spectromicroscopy data analysis: images, stack and spectral analyses.

2. Nanoscope III V5.12r2

This software, by Digital Instruments, was used to acquire and analyse the AFM images that were generated with the Digital Instruments, Nanoscope IIIA. This instrument is located in the Brockhouse Institute for Materials Research at McMaster.

3. PaintShop Pro, version 4

PaintShop Pro, from JASC Incorporated, was used to write images as jpeg files for presentations. These images were either screen saved from the aXis2000 software, pasted from constructed figures in powerpoint, or read from other image formats from aXis2000 and other software.

4. Sigma Plot 6.0

Sigma Plot 6.0 (by Jandel Scientific) was used for graphical representations.

5. Microsoft Office, versions 97, 2000, XP and 2003

Word and Powerpoint were used to write reports and prepare oral and poster presentations. Excel was used for organizing data sets and cataloguing samples,

performing regression analyses (on data not shown in this thesis) and making graphical representations.

6. STXM Control

This software was initially written by Dr. Tolek Tyliszczak (McMaster) and Peter Hitchcock, and extensively further developed from 2002-2006 by Dr. Tyliszczak (ALS). It controls the beamline (slit sizes and monochromator), the STXM microscope motors, and acquires the data at STXM 5.3.2.

7. X-PEEM software packages

The software used for operating the X-PEEM at the ALS, PEEM2, are detailed in the following table. Except for Image Pro 4.0, the commercial camera software, these programs were written by various members of the PEEM2 team.

Table A.1 List of PEEM2 software

Program	Function	Computer
Frontend	monochromator, stigmator control, ring current recording	***bl7-49.als.lbl.gov (SUN)***
PEEM2power	PEEM power supplies, Hotdeck power supply	***bl7-49.als.lbl.gov (SUN)***
Image Pro 4.0	camera software, image analysis	**Peem2 (PC)**
Connect Sun	spectromicroscopy, interfaces PC – SUN	**Peem2 (PC)**